TECHNISCHE UNIVERSITÄT MÜNCHEN
Lehrstuhl für Baumechanik

ITM-Based FSI-Models for Rooms with Absorptive Boundaries

Martin Buchschmid

Vollständiger Abdruck der von der Fakultät für Bauingenieur- und Vermessungswesen der Technischen Universität München zur Erlangung des akademischen Grades eines

Doktor-Ingenieurs

genehmigten Dissertation.

Vorsitzender: Univ.-Prof. Dr.-Ing. K.-U. Bletzinger

Prüfer der Dissertation:

1. Univ.-Prof. Dr.-Ing. habil. G. H. Müller
2. Univ.-Prof. Dr. rer. nat. habil. P. Rentrop
3. Univ.-Prof. Dr.-Ing. H. Grundmann, em.

Die Dissertation wurde am 17.10.2011 bei der Technischen Universität München eingereicht und durch die Fakultät für Bauingenieur- und Vermessungswesen am 13.12.2011 angenommen.

Abstract

Models for Fluid Structure Interaction (FSI) in room acoustical calculations are used in many different fields of engineering like automotive industry or civil engineering. For simulations of the spatial resolution of the sound field within acoustic cavities very often techniques based on Finite Element formulations are used.

In order to reduce the number of degrees of freedom and therefore the numerical effort, a model reduction method, based on a Component Mode Synthesis (CMS), is applied in this thesis. Macrostructures are assembled out of single substructures applying shape functions at the interfaces. These substructures contain acoustic components like absorbers or resonators. They are calculated separately in the frame of the CMS approach. The acoustic fluid is modeled with the Spectral Finite Element Method (SFEM) and coupled with plate-like compound absorbers at the interfaces via wavenumber- and frequency-dependent impedances using *Hamilton*'s Principle and a *Ritz* approach, where phase correct coupling conditions are ensured. The porous foam in the absorber is modeled with the Theory of Porous Media (TPM) and the impedances are calculated with the help of the Integral Transform Method (ITM).

Acknowledgments

First of all I want to express my deep gratitude to my supervisor Prof. Gerhard Müller for giving me the opportunity to create the thesis at the Lehrstuhl für Baumechanik and for granting me all the scientific freedom during this work. His open-minded and unreserved support led to many valuable and fruitful discussions. Besides his support and his encouragement, I also thank him for the friendly and familiar atmosphere at the chair as well as the companionable relationship, which grew over the years.

I would like to thank Prof. Peter Rentrop and Prof. Harry Grundmann for the revision of the thesis and for their valuable advices in their specific areas of expertise.

To all my colleagues at the Lehrstuhl für Baumechanik of the Technische Universität München I would like to express my thanks for their support. I want to thank especially Martina Pospiech and Jovana Sremčević for the scientific discussions, their great support and the congenial atmosphere within our research group.

To my family I would like to thank for their patience with me during the final stages of writing this thesis.

dedicated to
Sabine and Maximilian

Table of Contents

Table of Symbols

General

λ	[m]	wavelength
ω	[rad/s]	natural circular frequency
Ω	[rad/s]	circular frequency of excitation
k_x, k_y	[rad/m]	wavenumbers in x- and y-direction
$Z(k_x, k_y, \Omega)$	[Ns/(m^3)]	wave impedance
U	[Nm]	potential energy
T	[Nm]	kinetic energy
L	[Nm]	Lagrangian
c	[Nm/s]	damping coefficient
D^{Lehr}	[−]	damping ratio
η^D	[−]	damping loss factor
A - E	[−]	coefficients in the formulation of the absorber
$\mathscr{A}$ - $\mathscr{D}$	[−]	abbreviations in the formulation of the absorber
$\mathcal{A}$ - $\mathcal{C}$	[−]	coefficients in the FSI-formulation

Technical Acoustics/FSI

ρ_A	[kg/m^3]	density of the air	$\left(\rho_A = 1.204\,\frac{kg}{m^3}\text{ at }20°\text{C}\right)$
c_A	[m/s]	speed of sound of the air	$\left(c_A = 343.4\,\frac{m}{s}\text{ at }20°\text{C}\right)$
k_A	[rad/m]	wavenumber in the air	
Z_0	[Ns/(m^3)]	plane wave impedance	$\left(Z_0 = 413.5\,\frac{Ns}{m^3}\text{ at }20°\text{C}\right)$
r	[−]	reflection factor	
α	[−]	absorption coefficient	
ϱ	[−]	reflection coefficient	
δ	[−]	dissipation coefficient	

$\boldsymbol{\lambda}$		vector of *Lagrange* multipliers
Φ_A	$[\mathrm{m}^2/\mathrm{s}]$	velocity potential in the acoustic fluid
$\mathbf{v}_A$	$[\mathrm{m}/\mathrm{s}]$	velocity in the acoustic fluid
$\mathbf{u}_A$	$[\mathrm{m}]$	displacement in the acoustic fluid
p_A	$[\mathrm{N}/\mathrm{m}^2]$	pressure in the acoustic fluid
$\hat{\Phi}_A$	$[\mathrm{m}^2/\mathrm{s}]$	velocity potential in the *Fourier*-domain
$\hat{\mathbf{v}}_A$	$[\mathrm{m}/\mathrm{s}]$	velocity in the *Fourier*-domain
$\hat{\mathbf{u}}_A$	$[\mathrm{m}]$	displacement in the *Fourier*-domain
$\hat{p}_A$	$[\mathrm{N}/\mathrm{m}^2]$	pressure in the *Fourier*-domain
$\psi_n(y,z)$		trial function for the absorber
$\hat{\psi}_n(y,z)$		*Fourier* approximation of $\psi_n(y,z)$

Theory of Porous Media

ϕ_α		denotes the constituent α ($\alpha = S$ for the solid- and $\alpha = G$ for the gas-phase)
dv_α	$[\mathrm{m}^3]$	partial volume element of the constituent α
dv	$[\mathrm{m}^3]$	total volume element
B_α		domain of the constituent α
n_α	$[-]$	volume fraction of the constituent α
$\rho_{\alpha\,R}$	$[\mathrm{kg}/\mathrm{m}^3]$	macroscopic real density
ρ_α	$[\mathrm{kg}/\mathrm{m}^3]$	macroscopic partial density
$\mathbf{x}$	$[\mathrm{m}]$	position vector in the actual configuration
$\mathbf{X}$	$[\mathrm{m}]$	position vector in the reference configuration
$\boldsymbol{\chi}_\alpha$		function of placements
$(\ldots)'$		material time derivative
$\mathbf{u}_\alpha$	$[\mathrm{m}]$	displacement of the constituent α
$\mathbf{v}_\alpha$	$[\mathrm{m}/\mathrm{s}]$	velocity of the constituent α
$\mathbf{a}_\alpha$	$[\mathrm{m}/\mathrm{s}^2]$	acceleration of the constituent α
$\mathbf{w}$	$[\mathrm{m}/\mathrm{s}]$	seepage velocity between the phases
$\mathbf{w}_F$	$[\mathrm{m}/\mathrm{s}]$	filter velocity
$\hat{\mathbf{u}}_\alpha$	$[\mathrm{m}]$	displacements in the *Fourier*-domain
$\hat{\mathbf{v}}_\alpha$	$[\mathrm{m}/\mathrm{s}]$	velocities in the *Fourier*-domain
g	$[\mathrm{m}/\mathrm{s}^2]$	gravitational acceleration
Φ_α	$[\mathrm{m}^2]$	scalar potential for the displacement field
$\boldsymbol{\Psi}_\alpha$	$[\mathrm{m}^2]$	vector potential for the displacement field

$\hat{\Phi}_\alpha$	$[\mathrm{m}^2]$	scalar potential in the *Fourier*-domain
$\hat{\mathbf{\Psi}}_\alpha$	$[\mathrm{m}^2]$	vector potential in the *Fourier*-domain
k_x, k_y	[rad/m]	wavenumbers
k_{11}, k_{12}	[rad/m]	wavenumbers of the compressional waves
k_2	[rad/m]	wavenumber of the shear wave
$\mathbf{F}_\alpha$	$[-]$	deformation gradient
$\mathbf{H}_\alpha$	$[-]$	displacement gradient
$\mathbf{C}_\alpha$	[m]	right *Cauchy-Green* deformation tensor
$\mathbf{B}_\alpha$	[m]	left *Cauchy-Green* deformation tensor
$\mathbf{E}_\alpha$	$[-]$	*Green* strain tensor
$\mathbf{A}_\alpha$	$[-]$	*Almansi* strain tensor
e_S	$[-]$	volumetric strain of the solid component
e_{SR}	$[-]$	part of e_S belonging to the real material
e_{SN}	$[-]$	part of e_S belonging to the change of pores
$\mathbf{T}_\alpha$	$[\mathrm{N/m}^2]$	*Piola-Kirchhoff* stress tensor of the constituent α
$\mathbf{T}_\alpha^E$	$[\mathrm{N/m}^2]$	tensor of effective stresses of the constituent α
$\mathbf{T}_S^D$	$[\mathrm{N/m}^2]$	deviatoric part of the stress tensor
$\hat{\mathbf{T}}_\alpha$	$[\mathrm{N/m}^2]$	*Piola-Kirchhoff* stress tensor in the *Fourier*-domain
σ_α, τ_α	$[\mathrm{N/m}^2]$	physical normal and shear stresses
$\hat{\sigma}_\alpha$, $\hat{\tau}_\alpha$	$[\mathrm{N/m}^2]$	physical stresses in the *Fourier*-domain
$\tilde{\lambda}_S$	$[\mathrm{N/m}^2]$	1^{st} macroscopic *Lamé* constant
μ_S	$[\mathrm{N/m}^2]$	2^{nd} macroscopic *Lamé* constant
$\tilde{\lambda}_S^c$, μ_S^c	$[\mathrm{N/m}^2]$	complex macroscopic *Lamé* constants
p	$[\mathrm{N/m}^2]$	pore pressure
$\hat{p}$	$[\mathrm{N/m}^2]$	pore pressure in the *Fourier*-domain
p_α^E	$[\mathrm{N/m}^2]$	effective stresses of the constituent α
p_α	$[\mathrm{N/m}^2]$	partial hydrostatic stresses of the constituent α
K_{SR}	$[\mathrm{N/m}^2]$	compression modulus of the real solid material
K_{SN}	$[\mathrm{N/m}^2]$	compression modulus of the solid skeleton
$\widehat{p}_\alpha^E$	$[\mathrm{N/m}^3]$	interaction forces between the constituents
$\mathbf{S}_G$	$[\mathrm{Ns/m}^4]$	permeability tensor
γ_{GR}	$[\mathrm{N/m}^3]$	effective fluid weight
k^G	[m/s]	*Darcy* flow coefficient
K^G	$[\mathrm{m}^4/(\mathrm{Ns})]$	specific permeability/conventional saturated permeability

K^S	[m^2]	intrinsic permeability
η_G	[Ns/m^2]	partial dynamic fluid viscosity
η_{GR}	[Ns/m^2]	effective dynamic fluid viscosity
Ξ	[Ns/m^4]	specific flow resistance $\left(1\,\frac{Rayl}{cm} = 10^3\,\frac{Ns}{m^4}\right)$
θ	[K]	temperature
R	[J/(kg K)]	specific gas constant ($R = 287.058$ for dry air)

Theory of Elasticity

ρ_H	[kg/m^3]	density of the elastic material
$\mathbf{u}_H$	[m]	displacement vector for the elastic material
$\mathbf{v}_H$	[m/s]	velocity
$\mathbf{a}_H$	[m/s^2]	acceleration
$\hat{\mathbf{u}}_H$	[m]	displacements in the *Fourier*-domain
$\hat{\mathbf{v}}_H$	[m/s]	velocities in the *Fourier*-domain
Φ_H	[m^2]	scalar potential for the displacement field
$\mathbf{\Psi}_H$	[m^2]	vector potential for the displacement field
$\hat{\Phi}_H$	[m^2]	scalar potential in the *Fourier*-domain
$\hat{\mathbf{\Psi}}_H$	[m^2]	vector potential in the *Fourier*-domain
k_x, k_y	[rad/m]	wavenumbers
k_3, k_4	[rad/m]	wavenumbers of the compressional and the shear wave
k_r	[rad/m]	circular wavenumber
$\mathbf{E}_H$	[−]	*Green* strain tensor
$\mathbf{T}_H$	[N/m^2]	*Piola-Kirchhoff* stress tensor for the elastic material
$\hat{\mathbf{T}}_H$	[N/m^2]	*Piola-Kirchhoff* stress tensor in the *Fourier*-domain
σ_H, τ_H	[N/m^2]	physical normal and shear stresses
$\hat{\sigma}_H$, $\hat{\tau}_H$	[N/m^2]	physical stresses in the *Fourier*-domain
λ_H	[N/m^2]	1$^{\text{st}}$ *Lamé* constant of the elastic material
μ_H	[N/m^2]	2$^{\text{nd}}$ *Lamé* constant of the elastic material

Acronyms

BEM	Boundary Element Method
BT	Biot's Theory
CMS	Component Mode Synthesis
EFEM	Energy Finite Element Method
FEM	Finite Element Method
FSI	Fluid-Structure Interaction
FRF	Frequency Response Function
HBEM	Hybrid Boundary Element Method
IRF	Impulse Response Function
ITM	Integral Transform Method
SFEM	Spectral Finite Element Method
SM	Spectral Method
TPM	Theory of Porous Media

1 Introduction

1.1 Motivation

Due to increasing requirements of comfort, acoustic design has become more important during the last years, especially in the field of civil engineering and automotive design. The sound field within rooms or vehicles has to be predicted and then modified in an acoustic optimization process in order to reach an optimal result for the specific use.

The calculation of the sound pressure level inside of acoustic cavities is usually done with the help of energy methods like the Statistical Energy Analysis (SEA) for instance. The SEA is typically applied to vibro-acoustic problems in the high-frequency range. It provides robust results for subsystems with a high modal density and it is based on an averaging over frequency bands, points of excitation and points of observation. However, its performance is limited if a description of the spatial resolution of the response is required and if the influence of boundary conditions has to be described in detail. Impulse Response Functions, which are typically used for the classification of acoustic cavities (e.g. rooms designed for speech or music) and contain information about reflections of the sound waves and also their decay due to damping effects, cannot be predicted sufficiently by the SEA.

The acoustic design of rooms or vehicles is done by placing elements like reflectors or absorbers (e.g. passive absorbers or plate resonators) into the sound field. Therefore a robust method for the phase correct modeling of interior sound fields with a sufficient spatial resolution is needed, where the absorptive behavior of the delimiting surfaces can be considered. Impulse responses could be computed at the basis of frequency response functions for example.

1.2 State of Research

Sound fields in acoustic cavities in buildings or inside vehicles, which are caused by vibrating delimiting surfaces or sound-sources located inside rooms, typically are modeled with energy methods. Among these the Statistical Energy Analysis [Lyon and DeJong 1995] is successfully applied to general vibro-acoustic investigations in the high-frequency range, providing solutions in the frequency domain. Damping is considered by means of the average free path of the sound waves and the energy loss at the surfaces [Cremer and Müller 1982]. Langley [2008] gives an overview over recent advances and remaining challenges in the SEA. The method provides robust results in the high-frequency domain, however with a reduced resolution due to the averaging inherent in the method. It has deficiencies e.g. in case of repetitive structures or point loads. By means of corrections, like response concentration factors for example [see Lyon 1983, 1984; Mohammed and Fahy 1990; Manning 1999], the deficiencies can be "roughly" corrected to a certain extent. In addition, the averaging reduces the possibility to study the impact of measures to affect the sound field e.g. the influence of the position of absorbers in closed spaces. Also if a higher resolution of the spatial distribution of the sound field is of interest, the methods are limited (if the sound field at the position of the drivers head [Langhe 2007] in a vehicle shall be calculated, or if near-field effects have to be considered for example). Furthermore in many applications of vibro-acoustic coupling between structural vibrations and sound fields inside adjacent volumes different modal densities of the substructures require hybrid approaches combining the SEA with the Finite Element Method (FEM) approach. Those approaches have been developed and also implemented in commercial software [see Shorter and Bremner 1999; Shorter and Langley 2005a,b,c].

For investigations in the time domain ray-tracing methods are used complementary to the SEA [Vorländer 2007]. They provide the impulse-response, which is, as mentioned above, of special interest in order to understand room acoustical characteristics as those strongly depend on the initial reflection pattern.

Parallel to those developments the enormous increase of the possibilities related with the development of numerical methods like the FEM and the Boundary Element Method [compare Marburg and Nolte 2008] lead to a continuous expansion of the possibilities to investigate vibro-acoustic problems also in the mid- and high-frequency domain. However, especially for modeling the sound field inside volumes, there are the challenges of tackling the high modal density, the number of singularities and the high number of degrees of freedom, which increase for increasing frequencies. The errors related with the discretization have been investigated by Babuška et al. [1997a,b]. In order to handle the *pollution effect* [see Gerdes and Ihlenburg 1999; Babuška and Sauter 1997], the h- and p- version of the FEM, applied

to the *Helmholtz*-equation for simple systems, has been investigated by Mehdizadeh and Paraschivoiu [2003]; Farhat et al. [2002]. For the solution of the system of equations Padé expansion solvers [Franck and Hafner 2005; Franck 2006] are suitable and already implemented in commercial codes. Infinite Finite Element approaches, which are applied in order to avoid errors due to reflecting waves in infinite models, are discussed by von Estorff et al. [2008] for instance.

Freymann [2000] presented a method to investigate the FSI-problem for acoustic volumes with delimiting structures. Measurement results on the scatter in low- and mid-frequency ranges were published by Freymann and Stryczek [2000]. Magalhaes and Ferguson [2005] developed a model for a three-dimensional FSI, which is based on a Component Mode Synthesis.

Naka et al. [2004] reduced the size of the room to investigate and thus the number of degrees of freedom by a *Dirichlet*-to-*Neumann* mapping, introducing an imaginary surface. This is possible, in case the impedances of the separated volume can be found analytically. In [Gaul and Wagner 1998; Wagner et al. 2004] a Hybrid Boundary Element formulation (HBEM) at the basis of hybrid variation principles is derived for the modeling of the FSI-problem for harmonic oscillations. It is verified by the help of various applications.

Hüppe and Kaltenbacher [2009] discussed the limits of FEM in the mid-frequency range. In order to cope with high modal densities Buchschmid et al. [2009a] suggest to apply an averaging technique in the postprocessing of the FEM calculation. Computing energy influence coefficients a SEA-like evaluation can be carried out for the FEM model without fulfilling the SEA-requirements for the modeling. Pospiech, Buchschmid et al. [2010] discussed the application of basic possibilistic and probabilistic concepts on acoustic models to estimate the variation in the frequency response functions resulting from uncertain input data.

For FEM analyses in the high-frequency range Li [2011] provided a scaling approach for the vibration problem of line-coupled plates as an alternate method. Aoutou and Savin [2011] developed a discontinuous FE-model for solutions of transport equations for high-frequency power flows in the time domain.

The error obtained when approximating the *Helmholtz* equation by means of the FEM can be significantly reduced by the use of energy methods (EFEM). In the scope of these methods the primary variables are not pressure or velocity but energy density and energy flow [compare Bitsie 1996; Moens et al. 1998; Mace and Shorter 2000, for example]. However, as a description of the boundary conditions related with various types of absorbers requires

a modeling in terms of velocity and pressure, these methods have to be classified in between the SEA and the FEM/BEM approaches concerning the possibilities of computing spatial characteristics of the sound field. The wavenumber dependent modeling of the boundary conditions is feasible in the scope of this method as far as delimiting surfaces can be described by simple models or partial differential equations like plates for instance. In case of more complex boundary conditions e.g. porous absorbers, it is advantageous to use pressures and velocities as primary variables.

The state of the art concerning the description of typical boundary conditions in the frequency domain, as far as the absorptive and reflective behavior is concerned, can be found in the standard references [Cremer and Müller 1982; Mechel 1989, 1995a; Müller and Möser 2003; Fuchs 2006]. Considering *Helmholtz*-resonators and vibrating plates, the appropriate models, which are available, provide point- or wavenumber dependent boundary-impedances. However, porous absorbers require a more detailed study. Simple methods build up the porous foam with an equivalent fluid, defining characteristic wavenumbers and impedances. The most popular approach is called the *Rayleigh* model in honor of Lord *Rayleigh*, who published this method already in 1878 [Rayleigh 1878]. Whereas the parameters can be defined strictly theoretically in the Rayleigh model, Delany and Bazley [1970] use a similar approach for fibrous materials, which is derived empirically with the help of measurements. Mechel [1976] published an extension of this method for low frequencies. Equivalent fluid models can be used, if the dimension of the pores is small compared to the wavelength, which was discussed by Lafarge [2006]. For porous materials, having a rigid frame, semi-phenomenological models are used, where the bulk modulus and a complex density have to be defined for the equivalent fluid. Different approaches for this effective density and the bulk modulus were suggested by Johnson et al. [1978], Champoux and Allard [1991], Pride et al. [1993], Wilson [1993] as well as by Lafarge et al. [1997] for instance. Performance studies for these models were carried out by Panneton and Olny [2006] and Olny and Panneton [2008]. Langer et al. [2009] discussed the sensitivity of the absorption coefficient depending on changes in the definition of the material parameters for the methods, named above. In order to consider the elasticity of the matrix of the porous material the theory of Biot [1956b,c] is used widely in acoustics. The propagation of acoustic waves was discussed by Biot [1961, 1962]. Depollier et al. [1988] compared the Biot theory with previous continuity equations for sound absorbing materials. They stated a good agreement with the equations proposed by Beranek [1947] and Lambert [1983] and suggested a correction of the formulation, published by Zwikker and Kosten [1949]. A summary over the methods is given by Allard [2009]. Struckmeier [2007] implemented the theory of Biot in a FEM/BEM model for seismically induced liquefaction problems. Larbi et al. [2009] use FEM models for FSI-problems with absorptive boundaries

also based on the Biot model.

Besides the Biot Theory (BT), which was found empirically, there exists another theory for modeling porous foams. A report about the early development of the Theory of Porous Media (TPM) was published by de Boer [1992]. It dates back to the work of Fillunger [1913]. This theory is based on the theory of mixtures [Truesdell and Toupin 1960] and the volume fraction concept [Bowen 1980, 1982]. Many important contributions to the TPM were given in the following years by de Boer and Ehlers [1986], Ehlers [1989], Diebels [2000] and Makert [2005]. The TPM model for acoustic foams, which is presented in the scope of this work, was published in parts already in [Buchschmid and Müller 2008]. Schanz and Diebels [2003] discussed both theories, the BT and the TPM, in a comparative study in case of incompressible and compressible constituents.

The characteristics of many absorbers generally show a wavenumber dependent absorptive behavior, which is typically taken into account in measurements just in an integrative or selective way. Measurements mostly are carried out in a reverberant chamber under a diffuse wave field according to DIN ISO 354 or in an impedance tube in accordance with DIN EN ISO 10534-1 under perpendicularly incident waves. In situ measurements to determine the reflective or absorptive behavior of absorbers under a wave field with a certain angle of incidence are covered by DIN ISO 13472-1. Mommertz [1995] provided an improved method of measuring the complex reflection coefficient in situ for perpendicular and oblique sound incidence.

The radiation of structural elements typically is approximated by the radiation efficiency, describing the coupling with an unbounded medium and thus neglecting the effect of reflected waves on the power balance. A method for computing the radiated sound power and thus the radiation efficiency, which is based on Integral Transform Methods (ITM) and can be applied as a postprocessing step of a FEM computation for instance, was presented by Müller, Buchschmid et al. [2006]. In order to compare results out of numerical computations with measurements, where standardized excitations are applied to the structure, this kind of excitation has to be built up in the model. Rabold, Buchschmid et al. [2010] published different methods for modeling the excitation force of a standard tapping machine on lightweight floor structures.

1.3 Modus Operandi and Layout of the Thesis

In the scope of this thesis a method for a phase correct computation of interior sound fields in the frequency domain, caused by sound sources in the interior or by vibrating delimiting structures, is derived. A special focus is laid on efficient models for absorptive layers at the boundaries of the acoustic cavity.

In the first part a model for compound absorbers, consisting of porous layers, elastic layers and air cushions for instance is deduced. Starting with the description of the different materials, in chapter 2 the model for the porous foam, which is based on the Theory of Porous Media [de Boer 2000; Ehlers and Bluhm 2002] is discussed in detail. The essentials, like the volume fraction concept, the kinematic relations as well as the stress-definition and the special assumptions, linked with the application for acoustic materials, are sketched briefly. The laws of conservation are presented focusing especially on the implementation of the dissipation of the absorber. By the use of Integral Transform Methods the pore pressure can be eliminated in the transformed domain and the fundamental system is derived in terms of the displacements of the individual constituents. In order to specify the coefficients of the fundamental system in the layered model, the displacements and the stresses are defined in the transformed domain.

In an analogous way the elastic material and the air are presented in the following chapters, which are kept short, because the treatment of the *Lamé* equation, which is used for the elastic layers, and the wave equation for the acoustic fluid is similar to the equations of motion for the porous material.

In chapter 4 the fundamental systems for the different materials are combined to build compound absorbers. Obeying the boundary conditions between the individual layers a system of equations is set up, where the system is loaded by incident sound waves. The problem is solved in the transformed domain and characteristic acoustic quantities like the impedance and the absorption coefficient are deduced for infinite plate absorbers. These results are provided depending on frequency and wavenumber and used for the FSI later on. Numerical calculations are presented for several types of absorbers. The mechanical characteristics of the results are discussed against the background of simpler methods, which are often used in practice, and the results are compared to measurements.

In chapter 5 a method for the FSI is derived, which allows to consider absorptive boundary structures not only using simulations for the absorber, but also with results out of practical measurements. For modeling the acoustic fluid in the FSI, a Spectral Finite Element formulation is used, which is very efficient for smooth solutions in acoustic problems. In order

to reduce the calculation time, especially when investigating slight changes in the geometry of the system, a modal approach is applied. Therefore an orthonormal basis is calculated for the fluid, assuming ideal reflective boundary conditions. For the FSI the Component Mode Synthesis is applied in combination with a *Hamilton* approach, assuming a continuity of the displacements normal to the coupling interface. The application of the method was presented in parts by Buchschmid et al. [2009b, 2010]. In the CMS additional coupling modes are added to the normal modes to enable the coupling at the interface [compare Magalhaes 2004]. The efficiency of the algorithm is enhanced considering near-field characteristics, which were discussed for applications in soil dynamics by Müller, Buchschmid et al. [2008], for the definition of the coupling modes. Adequate form functions have to be applied at the interface, which permit to describe the wavenumber dependent relationship between the primary variables at the boundaries via wavenumber- and frequency dependent impedances. The requirements for these trial functions are specified and also verified with examples. Finally results for the coupled FSI-model with an absorptive boundary structure are presented.

2 Porous Material

In the modern era of research two important models for porous materials were developed, which are able to describe these media in an universal way. Both theories were applied to various problems in continuum mechanics. They are used in civil engineering, geophysics, petroleum engineering, material science and biomechanics as well as in automotive design. The methods are adapted for the specific use by defining the individual constituents to be compressible or incompressible, applying elastic or plastic material laws or by specifying permeability parameters for instance.

Biot started to develop his theory in 1941, publishing his work about consolidation problems. He implemented an anisotropic material law and extended the theory to anisotropic viscoelastic solids in the following years. In 1956 Biot presented the application of his method to dynamic problems for low and high frequencies. The respective references are [Biot 1941a,b, 1955, 1956a,b,c]. Coussy [2004] summarizes the fundamentals of this method and depicts the current state of research. The method is widely used in acoustics to model porous materials [compare Mechel 2008; Allard 2009] in absorptive structures.

De Boer [1992] reviewed the development of the Theory of Porous Media, which started with the work of Fillunger [1913] about the uplift problem in saturated rigid porous solids and was accompanied by a heavy and tragically ending dispute between Fillunger and Terzaghi in this early phase [compare de Boer 2005a]. The TPM is predicated on the theory of mixtures [Truesdell and Toupin 1960], a macroscopic approach, where the continuum is assumed to consist of miscible, interacting constituents in combination with the volume fraction concept, which was introduced by Bowen [1980, 1982] and provides information about the microscopic properties of the constituents in an averaged sense, leading to "excellent tools for the macroscopic description of general immiscible multiphasic aggregates" [see Ehlers and Bluhm 2002]. Important contributions to the development of the TPM were done by de Boer and Ehlers [1986], Ehlers [1989], Bluhm [1997] Diebels [2000], Ricken [2002] and Makert [2005] for instance.

The derivation of Biot's poroelastic theory is, in contradiction to the TPM, not strictly based on the principles of mechanics and thermodynamics. In a comparison of both theories

for the linear case Ehlers and Kubik [1994] stated, that an equivalence can be achieved, if the so-called *apparent mass density*, which expresses the dynamic interaction between the constituents in the Theory of Biot, is assumed to be zero. Schanz and Diebels [2003] confirmed this equivalence in their comparative study for the incompressible model neglecting the apparent mass density and depicted, that the interaction between the solid and the gas phase is covered in a different way in both theories. Comparing the models with compressible constituents, they state, that the "constitutive relations derived on micro mechanical models for both theories are not in agreement to each other".

In the scope of this thesis the TPM is used for modeling the porous material of the absorber, but it is stated clearly, that the modus operandi, which is in detail the solution of the equations of motion with the help of Integral Transform Methods in section 2.3.2, the formulation of the layered absorber model in chapter 4 and finally the implementation into the FSI-model, which is presented in chapter 5, could be carried out, without significant changes in the procedure, on the basis of Biot's theory as well.

The nomenclature for the treatise of the porous material in this chapter is chosen with respect to the standard references, published by de Boer [2000, 2005b].

2.1 Fundamentals of the Theory of Porous Media

2.1.1 Volume Fraction Concept

Due to the application of the *volume fraction concept* information about the individual components (e.g. the displacements or the stresses of a phase) is gained in an averaged sense. This is an advantage compared to the classical *theory of mixtures*.

Averaging the microscopic quantities the mixture can be modeled on the macroscale, where the control volume B_S is spanned by the solid component and the gas, which is the air in the absorber model, can leave the control volume through the non-material surface ∂B_S. The pores are distributed statistically over the control volume and both constituents, solid and gas, occur in any arbitrary volume element dv.

The volume fraction n_α of the component ϕ_α, where $\alpha = S$ for the solid and $\alpha = G$ for the gas phase, is defined as

$$n_\alpha(\mathbf{x}, t) = \frac{dv_\alpha}{dv}, \tag{2.1}$$

where dv_α is the partial volume element of the constituent ϕ_α and $\mathbf{x}$ is the position vector at the center of the total volume element dv. Due to the assumption, that the pores are completely filled with gas, the constituents have to meet the *saturation condition*:

$$\sum_{\alpha=1}^{\kappa} n_\alpha = 1 \tag{2.2}$$

In equation (2.2) κ is the number of constituents within the mixture. In room-acoustical applications, where the porous foam consists of a solid S and a gas G in the pores, the saturation condition reads

$$n_S + n_G = 1. \tag{2.3}$$

Using the volume fractions n_α a relation between the macroscopic real and partial densities ($\rho_{\alpha R}$ and ρ_α) is derived in de Boer [2000, 2005b] assuming a spatial constant microscopic mass density.

$$\rho_\alpha(\mathbf{x}, t) = n_\alpha(\mathbf{x}, t)\, \rho_{\alpha R}(\mathbf{x}, t) \tag{2.4}$$

2.1.2 Kinematics and Strains

As mentioned already in section 2.1.1 the control volume is spanned by the solid phase, where the gas phase can leave this volume. Each constituent can move independently and every point $\mathbf{x}$ in the macroscopic description is assumed to be covered by both constituents (solid and gas) at any time.

In the following the kinematic relations are sketched briefly as far as they are resumed in the description of stresses (see 2.1.3) and the Balance Equations (see 2.2). Applying the Lagrangian description of motion, the position vector $\mathbf{x}$ of the material points X_α is defined in equation (2.5) as a function of placements $\boldsymbol{\chi}$, depending on the position vector $\mathbf{X}_\alpha$ in the reference state at $t = 0$.

$$\mathbf{x} = \boldsymbol{\chi}_\alpha\left(\mathbf{X}_\alpha, t\right) \tag{2.5}$$

$$\mathbf{X}_\alpha = \boldsymbol{\chi}_\alpha^{-1}\left(\mathbf{x}, t\right) \tag{2.6}$$

The Eulerian description is given in equation (2.6). Further information about the requirements for the vector fields (e.g. the invertibility of $\boldsymbol{\chi}$) is given by de Boer [2000, 2005b].

Velocities $\mathbf{v}_\alpha$ and accelerations $\mathbf{a}_\alpha$ are gained out of (2.5), carrying out the material time derivatives of the function of placements $\boldsymbol{\chi}_\alpha$.

$$\mathbf{v}_\alpha = \mathbf{x}'_\alpha = \frac{\partial \boldsymbol{\chi}_\alpha(\mathbf{X}_\alpha, t)}{\partial t} \qquad (2.7) \qquad\qquad \mathbf{a}_\alpha = \mathbf{v}'_\alpha = \frac{\partial^2 \boldsymbol{\chi}_\alpha(\mathbf{X}_\alpha, t)}{\partial t^2} \qquad (2.8)$$

The material deformation gradient is defined, similar to the Theory of Elasticity as (2.9a). Introducing the displacement gradient $\mathbf{H}_\alpha = \operatorname{grad}_\alpha \mathbf{u}_\alpha$ the deformation gradient results in (2.9b)

$$\mathbf{F}_\alpha = \operatorname{grad}_\alpha \boldsymbol{\chi}_\alpha \qquad (2.9a) \qquad\qquad \mathbf{F}_\alpha = 1 + \mathbf{H}_\alpha = 1 + \operatorname{grad}_\alpha \mathbf{u}_\alpha, \qquad (2.9b)$$

where $\operatorname{grad}_\alpha$ is the partial derivative with respect to $\mathbf{X}_\alpha$.

As rigid body motions should not cause stresses in the material [see Stein and Barthold 1996, chap. 3.4] the formulation of the strains is based on the right *Cauchy-Green* deformation tensor $\mathbf{C}_\alpha = \mathbf{F}_\alpha^T \mathbf{F}_\alpha$ and on the left *Cauchy-Green* deformation tensor $\mathbf{B}_\alpha = \mathbf{F}_\alpha \mathbf{F}_\alpha^T$ respectively, which results in the *Green* strain tensor $\mathbf{E}_\alpha$ for the Lagrangian description and in the *Almansi* strain tensor $\mathbf{A}_\alpha$ for the Eulerian description.

$$\mathbf{E}_\alpha = \frac{1}{2}\left(\mathbf{C}_\alpha - \mathbf{I}\right) \qquad (2.10) \qquad\qquad \mathbf{A}_\alpha = \frac{1}{2}\left(\mathbf{I} - \mathbf{B}_\alpha^{-1}\right) \qquad (2.11)$$

Inserting (2.9b) in (2.10) the *Green* strain tensor is written in terms of the displacement field:

$$\mathbf{E}_\alpha = \frac{1}{2}\left(\mathbf{H}_\alpha + \mathbf{H}_\alpha^T + \mathbf{H}_\alpha^T \mathbf{H}_\alpha\right) \quad (2.12a) \qquad\qquad \mathbf{E}_\alpha^{\mathrm{lin}} = \frac{1}{2}\left(\mathbf{H}_\alpha + \mathbf{H}_\alpha^T\right) \qquad (2.12b)$$

For room acoustical applications, because of small deformations, the geometrically linearized *Green* strain tensor (2.12b) is used.

In the model of the porous absorber the solid material, building the porous skeleton, is assumed to be incompressible, because it is much stiffer than the air in the pores, which is considered as a compressible gas. Compressibility and incompressibility of the real materials is handled on the microscale in the Theory of Porous Media. Therefore the multiplicative decomposition of the deformation gradient $\mathbf{F}_\alpha$, which was presented by Bluhm and de Boer [1997], is mentioned briefly.

$$\mathbf{F}_\alpha = \mathbf{F}_{\alpha N}\, \hat{\mathbf{F}}_{\alpha R} \qquad (2.13)$$

In (2.13) $\hat{\mathbf{F}}_{\alpha R}$ is the deformation of the real material and $\mathbf{F}_{\alpha N}$ denotes the change of the size and the shape of the pores. Both lead to the deformation of the control volume dv.

The *Green* strain tensor of the solid component $\mathbf{E}_S$ is split up in a volumetric part $(\mathbf{E}_S \cdot \mathbf{I})\ \mathbf{I}$

and a deviatoric part $\mathbf{E}_S^D$

$$\mathbf{E}_S = (\mathbf{E}_S \cdot \mathbf{I})\ \mathbf{I} + \mathbf{E}_S^D. \tag{2.14}$$

As a consequence of (2.13) the volumetric strains of the solid $e_S = \mathbf{E}_S \cdot \mathbf{I}$ are split up into the strains of the real material e_{SR} and the strains of due to the change of the pores e_{SN}.

$$e_S = e_{SR} + e_{SN} \tag{2.15}$$

Further information about the corresponding *Helmholtz* energy function is given by de Boer [2000].

2.1.3 Stresses

Due to the assumption of small deformations and consequently the linearization of the strains (see section 2.1.2) the actual configuration can be approximated by the reference configuration. Therefore the *Cauchy* stresses and the 2nd *Piola-Kirchhoff* stresses coincide. In the following the definition of the stresses for the *binary porous medium model* with incompressible solid and compressible fluid constituents (*hybrid model of second type*), which is based on de Boer [2000, 2005b], is presented.

Stresses in the Solid Phase

The stress tensor of the solid component $\mathbf{T}_S$ is split up in a volumetric part $p_S\,\mathbf{I}$ and a deviatoric part $\mathbf{T}_S^D$ (see equation (2.16)). Baer and Nunziato [1986] stated about the volumetric part in a binary model (solid skeleton filled with gas), that "... the pressure in the solid grains equals the pressure in the gas plus the pressure due to contact forces between the grains" [found in de Boer 2000, chap. 5]. Assuming the solid and the gas phase to have the same temperature $\theta_S = \theta_G$ the partial pressure p_S of the solid phase results in a weighted pore pressure $-n_S\,p$ and the *effective hydrostatic stresses* p_S^E, which is stated in equation (2.17).

$$\mathbf{T}_S = p_S\,\mathbf{I} + \mathbf{T}_S^D \tag{2.16}$$

$$p_S = -n_S\,p + p_S^E \tag{2.17}$$

According to Biot and Willis [1957] equation (2.17) can be specified with the help of *compressibility tests*. With the help of the *unjacketed test*, where "a sample of the material is immersed in a fluid to which is applied a pressure", the weighted pore pressure $-n_S\,p$ can be

specified. The *jacketed test*, where "a specimen of the material is enclosed in a thin impermeable jacket and then subjected to an external fluid pressure" leads to equation (2.18) for the solid extra stresses p_S^E.

$$p_S^E = n_S \, K_{SN} \, e_{SN} \tag{2.18}$$

Using (2.15), equation (2.18) can be written for an incompressible solid phase ($e_{SR} = 0$) as

$$p_S^E = n_S \, K_{SN} \, e_S \qquad \text{with:} \quad e_S = \mathbf{E}_S \cdot \mathbf{I}, \tag{2.19}$$

where K_{SN} is the compression modulus of the empty solid skeleton. The deviatoric part of the stress tensor $\mathbf{T}_S^D$ is built up with

$$\mathbf{T}_S^D = 2 \, \mu_S \, \mathbf{E}_S^D, \tag{2.20}$$

where $\mathbf{E}_S^D$ denotes the deviatoric part of the strain tensor, defined in equation (2.12b), and μ_S is the *Lamé* constant of the solid component. Equations (2.16), (2.17), (2.19) and (2.20) result in the final description of the stress tensor of the solid component

$$\mathbf{T}_S = -n_S \, p \, \mathbf{I} + n_S \, K_{SN} \, (\mathbf{E}_S \cdot \mathbf{I}) \, \mathbf{I} + 2 \, \mu_S \, \mathbf{E}_S^D. \tag{2.21}$$

Substituting $\left(n_S \, K_{SN} = \tilde{\lambda}_S + \frac{2}{3} \, \mu_S \right)$ in (2.21) leads to the well known representation

$$\mathbf{T}_S = -n_S \, p \, \mathbf{I} + \tilde{\lambda}_S \, (\mathbf{E}_S \cdot \mathbf{I}) \, \mathbf{I} + 2 \, \mu_S \, \mathbf{E}_S, \tag{2.22}$$

where $\tilde{\lambda}_S$ and μ_S are the macroscopic *Lamé* constants.

Stresses in the Gas Phase

The air in the pores of the absorber is handled as a gas phase in the TPM-model. It is restricted to volumetric stresses, because no shear stresses are linked with the changes in the shape of the gas phase. The deviatoric part of the 2$^{\text{nd}}$ *Piola-Kirchhoff* stress tensor vanishes and $\mathbf{T}_G$ is defined as

$$\mathbf{T}_G = -n_G \, p \, \mathbf{I} + \mathbf{T}_G^E, \tag{2.23}$$

consisting of a weighted pore pressure and effective stresses for the gas phase $\mathbf{T}_G^E = p_G^E \mathbf{I}$ [see de Boer 2005b]. As suggested by Diebels [2000] and Makert [2005] the fluid extra stresses are neglected in the scope of a macroscopic theory ($\mathbf{T}_G^E = \mathbf{0}$) "assuming, that dissipation only occurs in the wall boundary layers of the pore channels, whereas the fluid behaves more or less inviscid" [see Makert 2005, chap. 3.2.2].

The viscosity is considered by an additional interaction force $\hat{p}_G^E$, which is described in detail in section 2.1.4.

2.1.4 Dissipation of Energy and Interaction Forces

For room acoustical applications the dissipation of energy in porous materials is caused by two mechanisms. At first, frictional effects occur between the solid and the gas phase at the walls of the pores and transform sound energy into heat. At second, periodic temperature fluctuations in the gas, which result out of pressure rarefaction and compression, cause dissipation of sound energy, because a part of the recoverable thermal energy is transformed into non-recoverable thermal energy [see Cremer and Müller 1982].

The viscosity of the gas phase is responsible for the attenuation of the sound field in the pores. Due to friction at the walls the tangential component of the velocity has to vanish. The decrease of this component is determined by the dynamic fluid viscosity η_{GR}, which is $\eta_{GR} = 1.8\ 10^{-5}\ \frac{kg}{m\,s}$ at a temperature of 20° C.

For the description of porous material in acoustical applications the *flow resistance*, which is the relation of the pressure gradient ($\Delta p = p_1 - p_2$) caused by the porous medium, and the exterior velocity v_e calculated out of the flow rate and the macroscopic cross section of the specimen is used. To characterize the porous material independently from the system, the flow resistance is defined in relation to the thickness d_{TPM} of the layer. The so-called *specific flow resistance* Ξ is results in:

$$\Xi = -\frac{\Delta p}{d_{TPM}\, v_e} \tag{2.24}$$

To enable the sound waves to enter the absorptive structure easily the flow resistance should not be too high, which marks an upper limit for Ξ. The lower limit is defined by the fact, that the sound wave should loose as much energy as possible while propagating through the absorber. The range of Ξ, which is interesting for applications in acoustics, is $5\,Rayl/cm = 5 \cdot 10^3 \frac{Ns}{m^4} < \Xi < 100\,Rayl/cm$ [see Möser 2007; Fuchs 2006]. The specific flow resistance is independent from the porosity and therefore cannot be described as a function

of n_α nor modeled easily. With the help of the *Rayleigh* model Ξ can be estimated in case of very simple geometries [see Cremer and Müller 1982] but for more complex structures this is not possible. Therefore in practice these parameters are very often gained out of measurements. A schematic outline of the measurement procedure, which is regulated in DIN EN 29053, as well as a picture of a real measurement set up are given in figure 2.1.

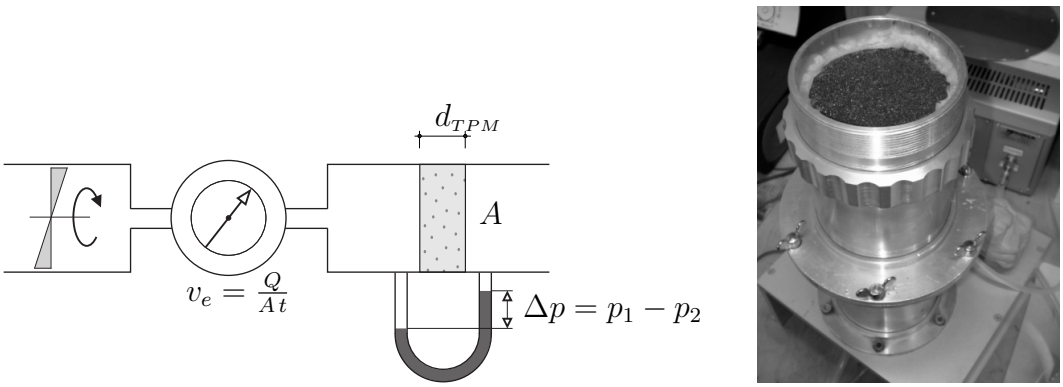

(a) Schematic diagram **(b)** Set up

Figure 2.1: Measurement of the flow resistance [see Cremer and Müller 1982]

The specific flow resistance is measured by means of a steady flow with higher velocities than they occur in room acoustics. In order to overcome disadvantages due to the relation between Δp and v_e, which is nonlinear, either interpolations according to DIN EN 29053 are necessary or measurement devices with oscillating pistons, which work in the velocity range of interest, have to be used.

Several porous absorbers, for example plates of pressed fibers, show anisotropic behavior concerning their specific flow resistance. In this case the flow resistance $\Xi_\parallel$ in and $\Xi_\perp$ normal to the direction of the fibers has to be considered. According to Mechel [1995b] the influence on practical important parameters, the impedance for example, which is introduced in section 4.3, is small. In this work just isotropic materials are considered. Furthermore, due to small displacements in room acoustical applications, it is assumed, that the flow resistance is independent from the deformation of the porous material.

In the Theory of Porous Media the physical exchange processes between the constituents ϕ_α, which builds up these viscous effects, are considered by interaction forces $\hat{p}_\alpha$. Summing up over the mixture they have to vanish, because the sum of the balance equations for the constituents ϕ_α has to result in the balance equations for the mixture.

$$\sum_\alpha \hat{\mathbf{p}}_\alpha = \mathbf{0} \tag{2.25}$$

The interaction forces result out of the formulation of the entropy inequality and they are sketched by de Boer and Didwania [2004] and de Boer [2005b]. For the *hybrid model of second type* they are

$$\hat{\mathbf{p}}_S = p \operatorname{grad} n_S - \mathbf{S}_G (\mathbf{v}_G - \mathbf{v}_S) \tag{2.26}$$

$$\hat{\mathbf{p}}_G = p \operatorname{grad} n_G + \mathbf{S}_G (\mathbf{v}_G - \mathbf{v}_S) \tag{2.27}$$

Due to the *concept of frozen volume fractions* [compare Bowen 1982], which considers constant volume fractions in the scope of a linearized theory, $\operatorname{grad} n_\alpha = \mathbf{0}$ and one obtains:

$$\hat{\mathbf{p}}_S = -\mathbf{S}_G (\mathbf{v}_G - \mathbf{v}_S) = -\mathbf{S}_G \mathbf{w} \tag{2.28}$$

$$\hat{\mathbf{p}}_G = \mathbf{S}_G (\mathbf{v}_G - \mathbf{v}_S) = \mathbf{S}_G \mathbf{w} \tag{2.29}$$

The interaction forces between solid and gas, caused by frictional effects at the walls of the pores, depend on the seepage velocity $\mathbf{w} = (\mathbf{v}_G - \mathbf{v}_S)$, which is the relative velocity between both phases, and on the permeability tensor $\mathbf{S}_G$. It is defined as

$$\mathbf{S}_G = n_G^2 \frac{\gamma_{GR}}{k^G} \mathbf{I} \qquad \text{with: } \gamma_{GR} = \rho_{GR}\, g \tag{2.30}$$

where γ_{GR} denotes the effective fluid weight and k^G is the *Darcy* flow coefficient. The permeability depends on both the solid and the fluid phase of the mixture [see Hall and Hoff 2002]. For Newtonian fluids and a laminar flow in non swelling media a simple relation is given depending on the dynamic fluid viscosity η_{GR}. Introducing the *specific permeability* K^G and the *intrinsic permeability* K^S [compare Makert 2005, for instance]

$$K^G = \frac{k^G}{\gamma_{GR}} = \frac{K^S}{\eta_{GR}} \tag{2.31}$$

$$K^S = \eta_{GR}\, K^G = \frac{\eta_{GR}}{\gamma_{GR}}\, k^G \tag{2.32}$$

the permeability tensor (2.30) can be expressed with

$$\mathbf{S}_G = n_G^2 \left(K^G\right)^{-1} \mathbf{I} \tag{2.33a}$$

or

$$\mathbf{S}_G = n_G^2 \left(\frac{K^S}{\eta_{GR}}\right)^{-1} \mathbf{I}. \tag{2.33b}$$

The specific flow resistance is introduced into the TPM-formulation, comparing equation (2.24) and the general formulation of *Darcy*'s Law

$$\begin{aligned} v_e &= -\frac{1}{\Xi} \frac{\Delta p}{d_{TPM}} \\ v_e &= -K^G \frac{\Delta p}{d_{TPM}}. \end{aligned} \tag{2.34}$$

Equations (2.34) visualize the relation between the specific permeability and the specific flow resistance. The permeability tensor finally reads

$$\mathbf{S}_G \;=\; n_G^2 \,\Xi\, \mathbf{I} \tag{2.35}$$

in the case of isotropic permeability. The scalar value $S_G \;=\; n_G^2 \,\Xi$ is used in the following sections to simplify the equations.

The heat exchange, which is mentioned as the second reason for dissipation, is caused by temperature fluctuations in the gas phase. The compression proceeds isothermal for low frequencies, whereas the adiabatic law is fulfilled just for high frequencies. In spite of small volume fractions of the solid in "acoustical foams", the heat capacity of the skeleton is sufficiently large to generate a heat exchange. Using again the *Rayleigh* model for a simplified pore geometry, a complex bulk modulus can be derived for the gas. The heat conduction losses are subordinate for low frequencies. For high frequencies they are comparable with the dissipation due to viscosity [see Cremer and Müller 1982].

In order to avoid the application of an even more complex thermoelastic theory [see Bluhm 2002], temperature fluctuations are not modeled within the TPM in the scope of this work. To consider the effect of additional dissipation in a simplified way, complex macroscopic *Lamé* constants can be defined for the mixture in equation (2.22).

$$\begin{aligned} \tilde{\lambda}_S^c &= \tilde{\lambda}_S \,\left(1 + i\eta^D\right) \\ \mu_S^c &= \mu_S \,\left(1 + i\eta^D\right) \end{aligned} \tag{2.36}$$

Equation 2.36 considers frequency-independent hysteretic material damping in the TPM-approach, where η^D marks the loss factor. Compared to the damping ratio D^{Lehr}, η^D is defined as:

$$\eta^D = 2\, D^{\text{Lehr}} \tag{2.37}$$

As discussed by Müller [1989], the *Lamé* constants have to be defined in dependence of the sign of the circular frequency of excitation Ω for computations in the *Fourier* domain:

$$\begin{aligned} \tilde{\lambda}_S^c &= \tilde{\lambda}_S \,\left(1 + \operatorname{sgn}(\Omega)\, i\eta^D\right) \\ \mu_S^c &= \mu_S \,\left(1 + \operatorname{sgn}(\Omega)\, i\eta^D\right) \end{aligned} \tag{2.38}$$

2.2 Balance Equations

With regard to Ehlers [1989] and de Boer [2000, 2005b] the balance of mass, momentum and moment of momentum as well as the balance of energy are, based on Truesdell's metaphysical principles [Truesdell 1984, p. 210-236], established in the Theory of Porous Media for each individual constituent ϕ^α considering the interaction forces. The sum of the individual partial balances establishes the balance equation of the mixture as a one-component-body.

2.2.1 Balance of Mass

Without any mass exchange between the constituents and because of the fact, that there is no mass supply in the system the change of mass is equal to zero

$$(M_\alpha)'_\alpha = \left(\int\limits_{B_\alpha} \rho_\alpha \, dv \right)'_\alpha = 0 \tag{2.39}$$

which leads to

$$(\rho_\alpha \, dv)'_\alpha = (n_\alpha \, \rho_{\alpha R} \, dv)'_\alpha = 0. \tag{2.40}$$

The material time derivative $(\ldots)'_\alpha$ describes the time dependent change of a property of an arbitrary material point, which is assumed to be fixed during the observation. It is defined for a scalar function f and a vector valued vector function $\mathbf{f}$ as [see Stein and Barthold 1996, chap. 4]

$$f' = \mathbf{v} \cdot \operatorname{grad} f + \frac{\partial f}{\partial t} \tag{2.41a}$$

$$\mathbf{f}' = \mathbf{v} \cdot \operatorname{grad} \mathbf{f} + \frac{\partial \mathbf{f}}{\partial t}, \tag{2.41b}$$

where the velocity $\mathbf{v}$ was defined in equation (2.7). Applying (2.41a) to ρ_α one obtains:

$$\begin{aligned} (\rho_\alpha)'_\alpha = (n_\alpha \, \rho_{\alpha R})'_\alpha &= \frac{\partial}{\partial t} (n_\alpha \, \rho_{\alpha R}) + \mathbf{v}_\alpha \operatorname{grad} (n_\alpha \rho_{\alpha R}) \\ &= \rho_{\alpha R} \frac{\partial \, n_\alpha}{\partial t} + n_\alpha \frac{\partial \, \rho_{\alpha R}}{\partial t} + \mathbf{v}_\alpha \operatorname{grad} (n_\alpha \, \rho_{\alpha R}) \end{aligned} \tag{2.42}$$

The material time derivative of a volume element is given by the transport theorem

$$(dv)'_\alpha = \operatorname{div} \mathbf{v}_\alpha \, dv. \tag{2.43}$$

Using equations (2.43) and (2.42) and carrying out the product rule, equation (2.40) can be written as:

$$(n_\alpha \, \rho_{\alpha R} \, dv)'_\alpha = \left[\rho_{\alpha R} \frac{\partial n_\alpha}{\partial t} + n_\alpha \frac{\partial \rho_{\alpha R}}{\partial t} + \mathbf{v}_\alpha \operatorname{grad} (n_\alpha \, \rho_{\alpha R}) + n_\alpha \, \rho_{\alpha R} \operatorname{div} \mathbf{v}_\alpha \right] dv = 0 \quad (2.44)$$

The expression $\frac{\partial n_\alpha}{\partial t}$ is extracted out of equation (2.44) using (A.22), which is depicted in the appendix.

$$\frac{\partial n_\alpha}{\partial t} = -\frac{1}{\rho_{\alpha R}} \left(n_\alpha \frac{\partial \rho_{\alpha R}}{\partial t} + \operatorname{div} (n_\alpha \, \rho_{\alpha R} \, \mathbf{v}_\alpha) \right) \quad (2.45)$$

The saturation condition (2.2) is derived with respect to time $\left(\frac{\partial n_S}{\partial t} + \frac{\partial n_G}{\partial t} = 0 \right)$. Inserting expression (2.45) for both constituents (ϕ_S, ϕ_G) and simplifying via (A.12) leads to

$$\frac{n_G}{\rho_{GR}} \frac{\partial \rho_{GR}}{\partial t} + n_G \operatorname{div} (\mathbf{v}_G) + \frac{n_S}{\rho_{SR}} \underbrace{\left(\frac{\partial \rho_{SR}}{\partial t} \right)}_{=0} + n_S \operatorname{div} (\mathbf{v}_S) = 0. \quad (2.46)$$

Taking the incompressibility of the solid phase into account (compare section 2.1.3) equation (2.46) is simplified to

$$n_G \frac{\partial \rho_{GR}}{\partial t} + \rho_{GR} \, n_G \operatorname{div} (\mathbf{v}_G) + \rho_{GR} \, n_S \operatorname{div} (\mathbf{v}_S) = 0. \quad (2.47)$$

The ideal gas equation is used in the scope of the linear theory to relate the real density of the air ρ_{GR} to the pore pressure p

$$\rho_{GR} = \frac{\rho^0_{GR}}{p^0} \, p = \frac{1}{R \, \theta} \, p, \quad (2.48)$$

where R is the specific gas constant and θ denotes the temperature of the gas. ρ^0_{GR} is the constant factor of a Taylor Series expansion. The index 0 is omitted in the following. Diebels [2000] discussed more complex state equations like the law of *Muskat* or the *van der Waals* fluid. Their effects would be eliminated by a consequent linearization [Schanz and Diebels 2003], whereby equation (2.47) results in

$$\frac{n_G}{R \, \theta} \frac{\partial p}{\partial t} + \rho_{GR} \, n_G \operatorname{div} (\mathbf{v}_G) + \rho_{GR} \, n_S \operatorname{div} (\mathbf{v}_S) = 0. \quad (2.49)$$

Substituting the real density ρ^0_{GR} with the partial value ρ_G using (2.4) one finally obtains for the balance of mass

$$\frac{n_G^2}{R\,\theta\,\rho_G}\,\frac{\partial p}{\partial t} + n_G \operatorname{div}(\mathbf{v}_G) + n_S \operatorname{div}(\mathbf{v}_S) = 0. \tag{2.50}$$

2.2.2 Balance of Momentum and Moment of Momentum

The conservation of momentum is expressed in a local form for each constituent ϕ_α considering the interaction forces between the constituents. The momentum of the constituent ϕ_α is defined in equation (2.51).

$$\mathbf{I}_\alpha = \int_{B_\alpha} \rho_\alpha\,\mathbf{v}_\alpha\,dv \tag{2.51}$$

$$(\mathbf{I}_\alpha)'_\alpha = \int_{B_\alpha} \rho_\alpha\,\mathbf{a}_\alpha\,dv \tag{2.52}$$

The material time derivative of the momentum describing the inertia force of the volume element, where $\mathbf{a}_\alpha$ is the acceleration of the constituent ϕ_α $\left(\text{with: } \mathbf{a}_\alpha = (\mathbf{u}_\alpha)''_\alpha\right)$ has to be at equilibrium with the sum of all external forces (consisting of volume forces $\mathbf{b}_\alpha$ and surface forces $\mathbf{t}_\alpha$) and the interaction forces $\hat{\mathbf{p}}_\alpha$, specified in section 2.1.4 and defining the interaction between solid and gas:

$$\int_{B_\alpha} \rho_\alpha\,\mathbf{a}_\alpha\,dv = \int_{B_\alpha} \rho_\alpha\,\mathbf{b}_\alpha\,dv + \int_{\partial B_\alpha} \mathbf{t}_\alpha\,da + \int_{B_\alpha} \hat{\mathbf{p}}_\alpha\,dv \tag{2.53}$$

Applying the divergence theorem the surface integral in equation (2.53) is rewritten with a volume integral

$$\int_{\partial B_\alpha} \mathbf{t}_\alpha\,da = \int_{\partial B_\alpha} \mathbf{T}_\alpha\,\mathbf{n}\,da = \int_{B_\alpha} \operatorname{div}\mathbf{T}_\alpha\,dv. \tag{2.54}$$

Thus equation (2.53) finally results in

$$\operatorname{div}\mathbf{T}_\alpha + \rho_\alpha\,\mathbf{b}_\alpha + \hat{\mathbf{p}}_\alpha = \rho_\alpha\,\mathbf{a}_\alpha. \tag{2.55}$$

External accelerations $\mathbf{b}_\alpha$ are equal to zero in our case. In the following equation (2.55) is established for both, the solid and the fluid component.
The stress- and strain relations (2.22, 2.12b), defined in section 2.1 are used to describe

$\operatorname{div} \mathbf{T}_S$ in equation (2.55):

$$\begin{aligned} \operatorname{div} \mathbf{T}_S = -\operatorname{div}\left(n_S\, p\, \mathbf{I}\right) + \operatorname{div}\left(\tilde{\lambda}_S \left(\frac{1}{2}\left(\operatorname{grad} \mathbf{u}_S + \left(\operatorname{grad} \mathbf{u}_S\right)^T\right) \cdot \mathbf{I}\right) \mathbf{I}\right) + \\ + \operatorname{div}\left(\mu_S \left(\operatorname{grad} \mathbf{u}_S + \left(\operatorname{grad} \mathbf{u}_S\right)^T\right)\right) \end{aligned} \tag{2.56}$$

Simplifying equation (2.56) with the help of (A.13, A.15, A.22 and A.27) and inserting the result in (2.55) using (2.26) leads to equation (2.57) for the conservation of momentum for the solid. Using (2.23) instead of (2.22) one yields equation (2.58) for the gas component in an analogous way:

$$-n_S \operatorname{grad} p + \left(\tilde{\lambda}_S + \mu_S\right) \operatorname{grad} \operatorname{div} \mathbf{u}_S + \mu_S \operatorname{div} \operatorname{grad} \mathbf{u}_S + S_G \left(\mathbf{v}_G - \mathbf{v}_S\right) = \rho_S \mathbf{a}_S \tag{2.57}$$

$$-n_G \operatorname{grad} p - S_G \left(\mathbf{v}_G - \mathbf{v}_S\right) = \rho_G \mathbf{a}_G \tag{2.58}$$

The balance of the moment of momentum is fulfilled, if

$$\mathbf{T}_\alpha = \left(\mathbf{T}_\alpha\right)^T \tag{2.59}$$

holds [see de Boer 2000], which leads to a symmetric stress tensor.

2.3 System of Partial Differential Equations and Fundamental System

Out of the balance equations, discussed in section 2.2, a system of coupled partial differential equations PDEs (2.50, 2.57, 2.58) describing the porous material in the absorber is gained. A potential approach and a transformation in the *Fourier* domain lead to a system of coupled ordinary differential equations ODEs, which can be solved analytically.

2.3.1 Helmholtz Decomposition

According the theorem of *Helmholtz* [compare Arfken 1985] a continuously differentiable three dimensional vector field can be expressed as a sum of a curl-free (irrotational) part, consisting of a scalar potential Φ and a divergence-free (solenoidal) part, built up with a vector potential $\mathbf{\Psi}$. In the following this approach is applied to the displacement field of the solid and the gas component.

$$\mathbf{u}_S = \operatorname{grad} \Phi_S + \operatorname{curl} \mathbf{\Psi}_S \tag{2.60}$$

$$\mathbf{u}_G = \operatorname{grad} \Phi_G + \operatorname{curl} \mathbf{\Psi}_G \tag{2.61}$$

There are three unknowns for each displacement field $\mathbf{u}_\alpha$, describing the spatial directions, whereas four unknowns Φ_α, $\Psi_{\alpha x}$, $\Psi_{\alpha y}$ and $\Psi_{\alpha z}$ are needed for the potential approach.

One component can be chosen arbitrarily without loosing accuracy [Long 1967] for the boundary conditions underlying the problem, discussed in this thesis. The z-component of the vector potential is chosen to $\Psi_{\alpha z} = 0$, leading to a complete system also in case of plane waves in the $x - y$ plane.

A more general approach, where the vector potential is decomposed with the help of two scalar functions and the solenoidal condition is used by Frühe [2011], where the limits of the approach by *Long* are discussed in detail.

Applying the *Helmholtz* decomposition to equations (2.50, 2.57, 2.58) and carrying out a simplification with the help of (A.16, A.24) and (A.26) leads to:

$$\begin{aligned} &\operatorname{grad}\left[-n_S\, p + \left(\tilde{\lambda}_S + 2\mu_S\right)\Delta\Phi_S + S_G\left(\frac{\partial\Phi_G}{\partial t} - \frac{\partial\Phi_S}{\partial t}\right) - \rho_S\frac{\partial^2\Phi_S}{\partial t^2}\right] + \\ &+\operatorname{curl}\left[\mu_S\Delta\boldsymbol{\Psi}_S + S_G\left(\frac{\partial\boldsymbol{\Psi}_G}{\partial t} - \frac{\partial\boldsymbol{\Psi}_S}{\partial t}\right) - \rho_S\frac{\partial^2\boldsymbol{\Psi}_S}{\partial t^2}\right] = \mathbf{0} \end{aligned} \tag{2.62}$$

$$\begin{aligned} &\operatorname{grad}\left[-n_G p - S_G\left(\frac{\partial\Phi_G}{\partial t} - \frac{\partial\Phi_S}{\partial t}\right) - \rho_G\frac{\partial^2\Phi_G}{\partial t^2}\right] + \\ &+\operatorname{curl}\left[-S_G\left(\frac{\partial\boldsymbol{\Psi}_G}{\partial t} - \frac{\partial\boldsymbol{\Psi}_S}{\partial t}\right) - \rho_G\frac{\partial^2\boldsymbol{\Psi}_G}{\partial t^2}\right] = \mathbf{0} \end{aligned} \tag{2.63}$$

$$\frac{n_G^2}{R\,\theta\,\rho_G}\frac{\partial p}{\partial t} + n_G\,\Delta\frac{\partial\Phi_G}{\partial t} + n_S\,\Delta\frac{\partial\Phi_S}{\partial t} = 0 \tag{2.64}$$

The equations for the scalar potentials are extracted out of (2.62) to (2.64)

$$-n_S p + \left(\tilde{\lambda}_S + 2\mu_S\right)\Delta\Phi_S + S_G\left(\frac{\partial\Phi_G}{\partial t} - \frac{\partial\Phi_S}{\partial t}\right) - \rho_S\frac{\partial^2\Phi_S}{\partial t^2} = 0 \tag{2.65}$$

$$-n_G p - S_G\left(\frac{\partial\Phi_G}{\partial t} - \frac{\partial\Phi_S}{\partial t}\right) - \rho_G\frac{\partial^2\Phi_G}{\partial t^2} = 0 \tag{2.66}$$

$$\frac{n_G}{R\,\theta}\frac{\partial p}{\partial t} + \rho_{GR}\,n_G\,\Delta\frac{\partial\Phi_G}{\partial t} + \rho_{GR}\,n_S\,\Delta\frac{\partial\Phi_S}{\partial t} = 0 \tag{2.67}$$

and the pore pressure p is unhinged out of equation (2.66)

$$p = -\frac{S_G}{n_G}\left(\frac{\partial\Phi_G}{\partial t} - \frac{\partial\Phi_S}{\partial t}\right) - \frac{\rho_G}{n_G}\frac{\partial^2\Phi_G}{\partial t^2}. \tag{2.68}$$

Inserting (2.68) in (2.65) and (2.67) and extracting the equations for the vector potentials out of (2.62) to (2.64) leads to the final potential description for the porous material, where the pore pressure p is eliminated.

$$\begin{aligned}\left(\tilde{\lambda}_S + 2\mu_S\right)\Delta\Phi_S + \frac{n_S}{n_G}\rho_G\frac{\partial^2\Phi_G}{\partial t^2} - \rho_S\frac{\partial^2\Phi_S}{\partial t^2} + \left(1+\frac{n_S}{n_G}\right)S_G\left(\frac{\partial\Phi_G}{\partial t} - \frac{\partial\Phi_S}{\partial t}\right) = 0 \\ n_S\Delta\frac{\partial\Phi_S}{\partial t} - \frac{n_G}{R\,\theta}\frac{\partial^3\Phi_G}{\partial t^3} + n_G\Delta\frac{\partial\Phi_G}{\partial t} - \frac{n_G\,S_G}{R\,\theta\,\rho_G}\left(\frac{\partial^2\Phi_G}{\partial t^2} - \frac{\partial^2\Phi_S}{\partial t^2}\right) = 0\end{aligned} \tag{2.69}$$

$$\begin{aligned}\mu_S\,\Delta\boldsymbol{\Psi}_S - \rho_S\frac{\partial^2\boldsymbol{\Psi}_S}{\partial t^2} + S_G\left(\frac{\partial\boldsymbol{\Psi}_G}{\partial t} - \frac{\partial\boldsymbol{\Psi}_S}{\partial t}\right) = \mathbf{0} \\ -\rho_G\frac{\partial^2\boldsymbol{\Psi}_G}{\partial t^2} - S_G\left(\frac{\partial\boldsymbol{\Psi}_G}{\partial t} - \frac{\partial\boldsymbol{\Psi}_S}{\partial t}\right) = \mathbf{0}\end{aligned} \tag{2.70}$$

2.3.2 Fourier Transform and Solution

The system of partial differential equations (2.69 and 2.70) can be transformed into a system of ODEs. The problem is considered in the wavenumber-frequency domain using *Fourier* Transform methods [Föllinger 2003]. The variable t is transformed into the frequency domain ($t \circ\!\!-\!\!\bullet\ \omega$). The spatial coordinates x and y are transformed into the wavenumber domain ($x \circ\!\!-\!\!\bullet\ k_x$), ($y \circ\!\!-\!\!\bullet\ k_y$), initially assuming infinite dimensions in these two directions.

The disadvantage, linked with the transformation is the loss of the possibility to vary the parameters of the system in x- and y- direction. For the applications in acoustics, discussed in the scope of this thesis however, especially for an application in room acoustics, a definition of different layers in z-direction is mostly sufficient.

Carrying out the transformation according to section A.2 leads to:

$$\begin{aligned}\left(\tilde{\lambda}_S + 2\mu_S\right)\left(-k_x^2 - k_y^2 + \frac{\partial^2}{\partial z^2}\right)\hat{\Phi}_S - \omega^2\left(\frac{n_S}{n_G}\rho_G\,\hat{\Phi}_G - \rho_S\,\hat{\Phi}_S\right) + \\ + \left(1+\frac{n_S}{n_G}\right)S_G\,i\omega\left(\hat{\Phi}_G - \hat{\Phi}_S\right) = 0 \\ i\omega\,n_S\left(-k_x^2 - k_y^2 + \frac{\partial^2}{\partial z^2}\right)\hat{\Phi}_S + i\omega^3\frac{n_G}{R\,\theta}\hat{\Phi}_G + \\ + i\omega\,n_G\left(-k_x^2 - k_y^2 + \frac{\partial^2}{\partial z^2}\right)\hat{\Phi}_G + \frac{n_G\,S_G}{R\,\theta\,\rho_G}\,\omega^2\left(\hat{\Phi}_G - \hat{\Phi}_S\right) = 0\end{aligned} \tag{2.71}$$

$$\begin{aligned} \mu_S \left(-k_x^2 - k_y^2 + \frac{\partial^2}{\partial z^2} \right) \hat{\boldsymbol{\Psi}}_S + \omega^2 \rho_S \hat{\boldsymbol{\Psi}}_S + i\omega \, S_G \left(\hat{\boldsymbol{\Psi}}_G - \hat{\boldsymbol{\Psi}}_S \right) = \mathbf{0} \\ \omega^2 \rho_G \hat{\boldsymbol{\Psi}}_G - i\omega \, S_G \left(\hat{\boldsymbol{\Psi}}_G - \hat{\boldsymbol{\Psi}}_S \right) = \mathbf{0} \end{aligned} \tag{2.72}$$

Equations (2.71) and (2.72) are systems of ordinary linear differential equations of second order with constant coefficients. Solving these equations and simplifying the mathematical expressions, the solution for the fundamental systems can be written in the following form:

$$\hat{\Phi}_S = A_1 \, e^{\lambda_{11} \, z} + A_2 \, e^{-\lambda_{11} \, z} + A_3 \, e^{\lambda_{12} \, z} + A_4 \, e^{-\lambda_{12} \, z} \tag{2.73}$$

$$\hat{\Phi}_G = \chi_1 \, A_1 \, e^{\lambda_{11} \, z} + \chi_1 \, A_2 \, e^{-\lambda_{11} \, z} + \chi_2 \, A_3 \, e^{\lambda_{12} \, z} + \chi_2 \, A_4 \, e^{-\lambda_{12} \, z} \tag{2.74}$$

$$\hat{\boldsymbol{\Psi}}_S = \mathbf{B}_1 \, e^{\lambda_2 \, z} + \mathbf{B}_2 \, e^{-\lambda_2 \, z} \quad \text{with } \Psi_{S_3} = 0^1 \tag{2.75}$$

$$\hat{\boldsymbol{\Psi}}_G = \chi_3 \, \mathbf{B}_1 \, e^{\lambda_2 \, z} + \chi_3 \, \mathbf{B}_2 \, e^{-\lambda_2 \, z} \quad \text{with } \Psi_{G_3} = 0^1 \tag{2.76}$$

One observes, that the wavelengths and the directions of propagation coincide for the waves in the solid- and in the gas phase. The ratio in the amplitudes of the potentials of the individual phases is represented by χ_1 to χ_3

$$\chi_1 = -\frac{2 \, \mathscr{A}}{\mathscr{B} + \mathscr{D}} \tag{2.77}$$

$$\chi_2 = -\frac{2 \, \mathscr{A}}{\mathscr{B} - \mathscr{D}} \tag{2.78}$$

$$\chi_3 = \frac{S_G}{S_G + i\omega \, \rho_G}, \tag{2.79}$$

where the abbreviations $\mathscr{A}$, $\mathscr{B}$ and $\mathscr{D}$, defined in equations (2.86) to (2.89), are introduced. For $S_G = 0$ no vector potential exists in the gas phase ($\chi_3 = 0$).

The coefficients λ of the exponential functions result in

$$\lambda_{11} = \sqrt{k_x^2 + k_y^2 - k_{11}^2} \tag{2.80}$$

$$\lambda_{12} = \sqrt{k_x^2 + k_y^2 - k_{12}^2} \tag{2.81}$$

$$\lambda_2 = \sqrt{k_x^2 + k_y^2 - k_2^2}, \tag{2.82}$$

[1] Compare section 2.3.1

with:

$$k_{11}^2 = \omega^2 \frac{\mathscr{C} + \mathscr{D}}{2\left(\tilde{\lambda}_S + 2\,\mu_S\right)} \tag{2.83}$$

$$k_{12}^2 = \omega^2 \frac{\mathscr{C} - \mathscr{D}}{2\left(\tilde{\lambda}_S + 2\,\mu_S\right)} \tag{2.84}$$

$$k_2^2 = \omega^2 \frac{iS_G\left(\rho_S + \rho_G\right) - \omega\,\rho_S\rho_G}{\left(iS_G - \rho_G\,\omega\right)\mu_S} \tag{2.85}$$

The wavenumbers k_{11} and k_{12} specify the compressional waves in the porous material. In contrast to the homogeneous material there occur two different kinds of compressional waves, differing in the phase shift between solid and fluid displacements. The shear wave in the porous foam is represented by k_2. In case of the *hybrid model of second type*, considering the friction between both phases ($S_G \neq 0$), the expressions for the wavenumbers and for the coefficients χ_1 to χ_3 are more complex as for the *binary model* with incompressible solid and fluid constituents.

The abbreviations $\mathscr{A}$ to $\mathscr{D}$, which were introduced to define the fundamental system are:

$$\mathscr{A} = \rho_S\frac{n_S}{n_G} - \frac{i\,S_G}{\omega}\left(\frac{\tilde{\lambda}_S + 2\,\mu_S}{R\Theta\,\rho_G} + \frac{n_S}{n_G} + \left(\frac{n_S}{n_G}\right)^2\right) \tag{2.86}$$

$$\mathscr{B} = \rho_S - \rho_G\left(\frac{n_S}{n_G}\right)^2 - \frac{\tilde{\lambda}_S + 2\,\mu_S}{R\Theta} - \frac{i\,S_G}{\omega}\left(1 - \frac{\tilde{\lambda}_S + 2\,\mu_S}{R\Theta\,\rho_G} - \left(\frac{n_S}{n_G}\right)^2\right) \tag{2.87}$$

$$\mathscr{C} = \rho_S + \rho_G\left(\frac{n_S}{n_G}\right)^2 + \frac{\tilde{\lambda}_S + 2\,\mu_S}{R\Theta} - \frac{i\,S_G}{\omega}\left(\left(1 + \frac{n_S}{n_G}\right)^2 + \frac{\tilde{\lambda}_S + 2\,\mu_S}{R\Theta\,\rho_G}\right) \tag{2.88}$$

$$\begin{aligned}\mathscr{D} = \frac{1}{|\omega|}\Bigg\{ &\left[\omega\left(\frac{\tilde{\lambda}_S + 2\,\mu_S}{R\,\Theta} + \rho_S + \rho_G\left(\frac{n_S}{n_G}\right)^2\right) - i\,S_G\left(\left(1 + \frac{n_S}{n_G}\right)^2 + \frac{\tilde{\lambda}_S + 2\,\mu_S}{R\Theta\,\rho_G}\right)\right]^2 + \\ &+ 4\,\frac{\tilde{\lambda}_S + 2\,\mu_S}{R\,\Theta}\left(i\omega\,S_G\left(1 + \frac{\rho_S}{\rho_G}\right) - \omega^2\,\rho_S\right)\Bigg\}^{\frac{1}{2}}\end{aligned} \tag{2.89}$$

The simple *Binary Model* with incompressible constituents can be derived out of this solution,

carrying out the limits ($R\Theta \to \infty$). The fundamental systems coincide with the results for the incompressible model, which are sketched in Boskovic, Buchschmid et al. [2003] and Boskovic [2005] for $S_G = 0$.

The speed of propagation is derived out of the wavenumbers ($c = \frac{\omega}{k}$). In case of the incompressible model the factor $\mathscr{C}$ is equal to $\mathscr{D}$. Then the propagation speed of the second compressional wave is getting infinite ($c_{12} \to \infty$).

2.3.3 Displacements and Stresses in the Transformed Domain

The displacements $\mathbf{u}_\alpha$ of the individual constituents ϕ_α are obtained from (2.60), (2.61)

$$u_\alpha^x = \Phi_{\alpha,x} - \Psi_{\alpha y,z} \tag{2.90}$$
$$u_\alpha^y = \Phi_{\alpha,y} + \Psi_{\alpha x,z} \tag{2.91}$$
$$u_\alpha^z = \Phi_{\alpha,z} - \Psi_{\alpha x,y} + \Psi_{\alpha y,x} \tag{2.92}$$

and transformed into the *Fourier* domain.

$$\hat{u}_\alpha^x = i\,k_x\,\hat{\Phi}_\alpha - \hat{\Psi}_{\alpha y,z} \tag{2.93}$$
$$\hat{u}_\alpha^y = i\,k_y\,\hat{\Phi}_\alpha - \hat{\Psi}_{\alpha x,z} \tag{2.94}$$
$$\hat{u}_\alpha^z = \hat{\Phi}_{\alpha,z} - i\,k_y\,\hat{\Phi}_{\alpha x} + i\,k_x\,\hat{\Psi}_{\alpha y} \tag{2.95}$$

Inserting the fundamental system (2.73) to (2.76) the displacements are formulated in terms of the unknown coefficients.

$$\begin{bmatrix} \hat{u}_S^x \\ \hat{u}_S^y \\ \hat{u}_S^z \\ \hat{u}_G^x \\ \hat{u}_G^y \\ \hat{u}_G^z \end{bmatrix} = \begin{bmatrix} ik_x & ik_x & ik_x & ik_z & 0 & 0 & -\lambda_2 & -\lambda_2 \\ ik_y & ik_y & ik_y & ik_y & \lambda_2 & -\lambda_2 & 0 & 0 \\ \lambda_{11} & -\lambda_{11} & \lambda_{12} & -\lambda_{12} & -ik_y & -ik_y & ik_x & ik_x \\ ik_x\chi_1 & ik_x\chi_1 & ik_x\chi_2 & ik_x\chi_2 & 0 & 0 & -\lambda_2\chi_3 & \lambda_2\chi_3 \\ ik_y\chi_1 & ik_y\chi_1 & ik_y\chi_2 & ik_y\chi_2 & \lambda_2\chi_3 & -\lambda_2\chi_3 & 0 & 0 \\ \lambda_{11}\chi_1 & -\lambda_{11}\chi_1 & \lambda_{12}\chi_2 & -\lambda_{12}\chi_2 & -ik_y\chi_3 & -ik_y\chi_3 & ik_x\chi_3 & ik_x\chi_3 \end{bmatrix} \mathbf{C}_{TPM}^T \tag{2.96}$$

where

$$\mathbf{C}_{TPM} = \begin{bmatrix} A_1 e^{\lambda_{11} z} & A_2 e^{-\lambda_{11} z} & A_3 e^{\lambda_{12} z} & A_4 e^{-\lambda_{12} z} & B_{1x} e^{\lambda_2 z} & B_{2x} e^{-\lambda_2 z} & B_{1y} e^{\lambda_2 z} & B_{2y} e^{-\lambda_2 z} \end{bmatrix} \tag{2.97}$$

The stresses according to cuttings along the z–axis, which are necessary for the absorber model are extracted out of the stress tensors $\mathbf{T}_\alpha$ for the individual constituents respectively,

carrying out the dot product with the normal vector $\mathbf{n} = [0 \quad 0 \quad 1]^T$, describing the cutting plane.

Starting from equation (2.22) the stresses of the solid phase are described in the *Fourier*-transformed domains as:

$$\begin{bmatrix} \hat{\tau}_S^{xz} \\ \hat{\tau}_S^{yz} \\ \hat{\sigma}_S^{z} \end{bmatrix} = \hat{\mathbf{T}}_S \begin{bmatrix} 0 \\ 0 \\ 1 \end{bmatrix} = \begin{bmatrix} 0 \\ 0 \\ -n_S\,\hat{p} \end{bmatrix} + \mu^S\,\mathbf{M}_{\text{coeff}}\,\mathbf{C}_{TPM}^T \tag{2.98}$$

where

$$\mathbf{M}_{\text{coeff}} = \begin{bmatrix} 2ik_x\lambda_{11} & -2ik_x\lambda_{11} & 2ik_x\lambda_{12} & -2ik_x\lambda_{12} & k_xk_y & k_xk_y & -\lambda_2^2-k_x^2 & -\lambda_2^2-k_x^2 \\ 2ik_y\lambda_{11} & -2ik_y\lambda_{11} & 2ik_y\lambda_{12} & -2ik_y\lambda_{12} & \lambda_2^2+k_y^2 & \lambda_2^2+k_y^2 & -k_xk_y & -k_xk_y \\ 2\lambda_{11}^2-\frac{\lambda^S}{\mu^S}k_{11}^2 & 2\lambda_{11}^2-\frac{\lambda^S}{\mu^S}k_{11}^2 & 2\lambda_{12}^2 & 2\lambda_{12}^2 & -2ik_y\lambda_2 & 2ik_y\lambda_2 & 2ik_x\lambda_2 & -2ik_x\lambda_2 \end{bmatrix}$$

With (2.23) one obtains for the gas phase ϕ_G:

$$\begin{pmatrix} \hat{\tau}_G^{xz} \\ \hat{\tau}_G^{yz} \\ \hat{\sigma}_G^{z} \end{pmatrix} = \hat{\mathbf{T}}_G \begin{pmatrix} 0 \\ 0 \\ 1 \end{pmatrix} = \begin{pmatrix} 0 \\ 0 \\ -n_G\,\hat{p} \end{pmatrix} \tag{2.99}$$

After applying the *Fourier* transform and inserting the *Helmholtz* potentials, for the pore pressure $\hat{p}$, which is defined in (2.68), holds:

$$\hat{p} = \frac{\omega}{n_G} \begin{bmatrix} \rho_G\omega\chi_1 - iS_G(\chi_1+1) & \rho_G\omega\chi_1 - iS_G(\chi_1+1) & \rho_G\omega\chi_2 - iS_G(\chi_2+1) & \rho_G\omega\chi_2 - iS_G(\chi_2+1) & 0 & 0 & 0 & 0 \end{bmatrix}^T C_{TPM}^T \tag{2.100}$$

The stress tensor for the mixture $\hat{\mathbf{T}}_{TPM}$ is decomposed into the stress tensors of the individual phases $\hat{\mathbf{T}}_S$ and $\hat{\mathbf{T}}_G$, which were defined in equations (2.22) and (2.23):

$$\hat{\mathbf{T}}_{TPM} \quad = \quad \hat{\mathbf{T}}_S \quad + \quad \hat{\mathbf{T}}_G \tag{2.101}$$

The *Fourier* transformed physical stresses at horizontal layers are composed to

$$\begin{bmatrix} \hat{\tau}_{TPM}^{xz} \\ \hat{\tau}_{TPM}^{yz} \\ \hat{\sigma}_{TPM}^{z} \end{bmatrix} = \begin{bmatrix} \hat{\tau}_S^{xz} + \hat{\tau}_G^{xz} \\ \hat{\tau}_S^{yz} + \hat{\tau}_G^{yz} \\ \hat{\sigma}_S^{z} + \hat{\sigma}_G^{z} \end{bmatrix}. \tag{2.102}$$

3 Elastic Layers and Air

3.1 Homogeneous Material

3.1.1 System of Partial Differential Equations

The layers, consisting of homogeneous, linear-elastic and isotropic material are described by the *Lamé* equation. Its derivation [compare Stein and Barthold 1996] and also the discussion of kinematics, stresses and strains is very similar to chapter 2 but not as complex. Therefore the relations are just listed in the following.
Assuming the external acceleration to be zero the *Lamé* equation is given in a Cartesian reference frame by

$$(\lambda_H + \mu_H)\,\operatorname{grad}\operatorname{div}\mathbf{u}_H + \mu_H \operatorname{div}\operatorname{grad}\mathbf{u}_H = \rho_H \mathbf{a}_H. \tag{3.1}$$

In (3.1) $\mathbf{a}_\alpha$ is the acceleration of the volume element dv. Stresses are evaluated in arbitrary cutting planes evaluating the 2$^{\text{nd}}$ *Piola-Kirchhoff* stress tensor $\mathbf{T}_H$ (compare section 2.1.3).

$$\mathbf{T}_H = \lambda_H \left(\mathbf{E}_H \cdot \mathbf{I}\right) \mathbf{I} + 2\mu_H \, \mathbf{E}_H \tag{3.2}$$

Here λ_H and μ_H are the *Lamé* constants of the elastic material and $\mathbf{E}_H$ is the *Green* strain tensor (compare section 2.1.2).

$$\mathbf{E}_H = \frac{1}{2}\left(\operatorname{grad}\mathbf{u}_H + (\operatorname{grad}\mathbf{u}_H)^T\right) \tag{3.3}$$

3.1.2 Solution in the Transformed Domain

The *Helmholtz* decomposition is carried out analogously to section 2.3.1, where

$$\mathbf{u}_H = \operatorname{grad}\Phi_H + \operatorname{curl}\boldsymbol{\Psi}_H. \tag{3.4}$$

represents the displacement field. Thus the expression

$$\begin{aligned} & \text{grad} \quad \left[(\lambda_H + 2\mu_H)\, \Delta\Phi_H - \rho_H \tfrac{\partial^2 \Phi_H}{\partial t^2} \right] + \\ + \quad & \text{curl} \quad \left[\mu_H \Delta \boldsymbol{\Psi}_H - \rho_H \tfrac{\partial^2 \boldsymbol{\Psi}_H}{\partial t^2} \right] = \mathbf{0} \end{aligned} \tag{3.5}$$

follows for the Lamé equation (3.1), which finally results in decoupled PDEs for the scalar potential and the vector potentials:

$$\begin{aligned} (\lambda_H + 2\mu_H)\, \Delta\Phi_H - \rho_H \frac{\partial^2 \Phi_H}{\partial t^2} &= 0 \\ \mu_H \Delta \boldsymbol{\Psi}_H - \rho_H \frac{\partial^2 \boldsymbol{\Psi}_H}{\partial t^2} &= \mathbf{0} \end{aligned} \tag{3.6}$$

In analogy to section 2.3.2 the *Fourier* transform from the time- into the frequency domain ($t \circ\!\!-\!\!\bullet\ \omega$) and from the spatial domain into the wavenumber domain ($x \circ\!\!-\!\!\bullet\ k_x$), ($y \circ\!\!-\!\!\bullet\ k_y$) is carried out in order to simplify the problem to the solution of ODEs.

$$\begin{aligned} (\lambda_H + 2\mu_H) \left(-k_x^2 - k_y^2 + \frac{\partial^2}{\partial z^2} \right) \hat{\Phi}_H + \omega^2 \rho_H \hat{\Phi}_H &= 0 \\ \mu_H \left(-k_x^2 - k_y^2 + \frac{\partial^2}{\partial z^2} \right) \hat{\boldsymbol{\Psi}}_H + \omega^2 \rho_H \hat{\boldsymbol{\Psi}}_H &= \mathbf{0} \end{aligned} \tag{3.7}$$

For equations (3.7), describing the homogeneous material, the solution for the scalar and vector potentials is given by

$$\hat{\Phi}_H = C_1\, e^{\kappa_1 z} + C_2\, e^{-\kappa_1 z} \tag{3.8}$$

$$\hat{\boldsymbol{\Psi}}_H = \mathbf{D}_1\, e^{\kappa_2 z} + \mathbf{D}_2\, e^{-\kappa_2 z} \text{ with } \Psi_{H_3} = 0^1 \tag{3.9}$$

with:

$$\kappa_1 = \sqrt{k_x^2 + k_y^2 - k_3^2} \tag{3.10}$$

$$\kappa_2 = \sqrt{k_x^2 + k_y^2 - k_4^2}. \tag{3.11}$$

Here k_3 and k_4 are the wavenumbers of the compressional and the shear wave respectively.

$$k_3^2 = \frac{\omega^2 \rho_H}{(\lambda_H + 2\mu_H)} \tag{3.12a}$$

$$k_4^2 = \frac{\omega^2 \rho_H}{\mu_H} \tag{3.12b}$$

[1] Compare section 2.3.1.

The derivation of displacements and stresses is done in analogy to the porous material (compare section 2.3.3) and therefore not discussed in detail.

The displacements, which were decomposed in (3.4) according to the *Helmholtz* approach, are transformed into the *Fourier* domain

$$\hat{u}_H^x = i\,k_x\,\hat{\Phi}_H - \hat{\mathbf{\Psi}}_{Hy,z} \tag{3.13}$$

$$\hat{u}_H^y = i\,k_y\,\hat{\Phi}_H + \hat{\mathbf{\Psi}}_{Hx,z} \tag{3.14}$$

$$\hat{u}_H^z = \hat{\Phi}_{Hz} - i\,k_y\,\hat{\mathbf{\Psi}}_{Hx} + i\,k_x\,\hat{\mathbf{\Psi}}_{Hy} \tag{3.15}$$

and written in a matrix notation

$$\begin{bmatrix} \hat{u}_H^x \\ \hat{u}_H^y \\ \hat{u}_H^z \end{bmatrix} = \begin{bmatrix} ik_x & ik_x & 0 & 0 & -\kappa_2 & \kappa_2 \\ ik_y & ik_y & \kappa_2 & -\kappa_2 & 0 & 0 \\ \kappa_1 & -\kappa_1 & -ik_y & -ik_y & ik_x & ik_x \end{bmatrix} \underbrace{\begin{bmatrix} C_1\ e^{\kappa_1 z} \\ C_2\ e^{-\kappa_1 z} \\ D_{1x}\,e^{\kappa_2 z} \\ D_{2x}\,e^{-\kappa_2 z} \\ D_{1y}\,e^{\kappa_2 z} \\ D_{2y}\,e^{-\kappa_2 z} \end{bmatrix}}_{\mathbf{C}_H} \tag{3.16}$$

The stresses are derived out of the stress vector, which is computed with the help of the stress tensor $\mathbf{T}_H$ (3.2) and the normal vector $\mathbf{n} = [0 \quad 0 \quad 1]^T$ defining the cutting plane along the z–axis

$$\begin{aligned} \begin{bmatrix} \hat{\sigma}_H^{xz} \\ \hat{\sigma}_H^{yz} \\ \hat{\sigma}_H^{z} \end{bmatrix} &= \hat{\mathbf{T}}_H \begin{bmatrix} 0 \\ 0 \\ 1 \end{bmatrix} = \\ &= \mu_H \begin{bmatrix} 2ik_x\kappa_1 & -2ik_x\kappa_1 & k_xk_y & k_xk_y & -\kappa_2^2 - k_x^2 & -\kappa_2^2 - k_x^2 \\ 2ik_y\kappa_1 & -2ik_y\kappa_1 & \kappa_2^2 + k_y^2 & \kappa_2^2 + k_y^2 & -k_xk_y & -k_xk_y \\ 2k_r^2 - k_4^2 & 2k_r^2 - k_4^2 & -2ik_y\kappa_2 & 2ik_y\kappa_2 & 2ik_x\kappa_2 & -2ik_x\kappa_2 \end{bmatrix} \mathbf{C}_H \end{aligned} \tag{3.17}$$

where

$$k_r = \sqrt{k_3^2 + k_4^2} \tag{3.18}$$

is the circular wavenumber.

3.2 Air as Intermediate Layer and Adjacent Structure

The homogeneous and porous layers, discussed in the previous sections, interact within the model of the porous absorber with the acoustic fluid. The differential equation for the air is the *wave equation*. A detailed derivation is found in Cremer and Müller [1982].

$$\Delta p_A - \frac{1}{c_A^2}\frac{\partial^2 p_A}{\partial t^2} = 0 \tag{3.19}$$

The subscript $(\ldots)_A$ specifies the air. The relation between the primary variables pressure p_A and velocity $\mathbf{v}_A$ is gained, applying *Newton*'s law to a volume element dV of the acoustic fluid

$$\rho_A \frac{\partial \mathbf{v}_A}{\partial t} = -\operatorname{grad} p_A. \tag{3.20}$$

Transforming the problem into the frequency domain, the *Helmholtz* equation results out of (3.19) and, after a transformation of the x- and y-coordinates in the wavenumber domain, one obtains

$$\left(-k_x^2 - k_y^2 + \frac{\partial^2}{\partial z^2}\right)\hat{p}_A + \frac{\Omega^2}{c_A^2}\,\hat{p}_A = 0, \tag{3.21}$$

where $\frac{\Omega}{c_A}$ is the wavenumber k_A of the compressional wave in the fluid. Solving the ODE leads to equation (3.22) for the fundamental system of the acoustic fluid:

$$\hat{p}_A = E_1\, e^{\sqrt{k_x^2+k_y^2-k_A^2}\,z} + E_2\, e^{-\sqrt{k_x^2+k_y^2-k_A^2}\,z} \tag{3.22}$$

The displacements $\hat{\mathbf{u}}_A$ are obtained out of the *Fourier* transformation of equation (3.20):

$$\begin{bmatrix}\hat{u}_A^x\\ \hat{u}_A^y\\ \hat{u}_A^z\end{bmatrix} = \frac{1}{\Omega^2\,\rho_A}\begin{bmatrix} ik_x & ik_x \\ ik_y & ik_y \\ \sqrt{k_x^2+k_y^2-k_A^2} & -\sqrt{k_x^2+k_y^2-k_A^2}\end{bmatrix}\begin{bmatrix} E_1 & e^{\sqrt{k_x^2+k_y^2-k_A^2}\,z} \\ E_2 & e^{-\sqrt{k_x^2+k_y^2-k_A^2}\,z}\end{bmatrix} \tag{3.23}$$

The fundamental systems, derived in the previous sections for the different materials, are composed to define the model for the compound absorber in the following chapter.

4 Compound Absorbers

In rooms, where the walls have a reflective character, which means, that nearly no sound is absorbed or transmitted into adjacent rooms, the sound field has got a strong spatial characteristic. This results in high level differences for the sound pressure in the standing waves and also echoes could appear. The speech intelligibility in offices or conference rooms and the clarity of music in concert halls (measures, which are defined by the early-to-late energy ratio considering specific intervals of integration) suffer from that. The work of employees, delegates and musicians or simply the comfort of the audience is affected negatively if they are not averted by constructive solutions.

To overcome this problem, room acoustical strategies like changing the geometry of the room for instance by inclining the walls to reduce echoes or installing reflectors to modify the early-to-late energy ratio are applied. The sound energy in the room can be controlled in the acoustic cavity installing specific absorptive elements. Absorbers, used in room acoustics, can be classified in passive absorbers and resonators (compare figure 4.1).

One can describe the mode of operation considering a sound wave with the sound pressure p_i, the velocity v_i and the sound power P_i. If its wavelength λ is small compared to the geometry of the "obstacle", the wave is partially reflected P_r, other parts are transmitted P_t or dissipated due to absorption P_a (effects resulting out of sound conduction to adjacent structures are not considered in this work).

$$P_i = P_r + P_t + P_a \tag{4.1}$$

The sound absorption is characterized by the absorption coefficient α, which is defined according to Sabine [1922] as the ratio of "not fully reflected" power and incident power

$$\alpha = \frac{P_a + P_t}{P_i} = \frac{P_i - P_r}{P_i} = 1 - r^2 = 1 - \varrho, \tag{4.2}$$

where r is the reflection factor and ϱ is the reflection coefficient:

$$r = \frac{p_r}{p_i} \tag{4.3}$$

$$\varrho = \frac{P_r}{P_i} = \frac{p_r^2}{p_i^2} \tag{4.4}$$

The ratio of absorbed and incident power is called the dissipation coefficient δ:

$$\delta = \frac{P_a}{P_i} \tag{4.5}$$

It is, following the mechanical description of dissipation, a measure for the energy, which is really dissipated due to transformation of sound energy into thermal energy. In the scope of this work, where the absorptive structures are considered to be mounted on reflective walls α is equal to δ.

Passive absorbers consist of porous materials like foams, mineral wool or cellular glass. The sound waves enter the pores of the absorber and initiate a vibration of the air in the interconnected pores (see figure 4.1a). The kinetic energy of the sound field is reduced due to viscous friction in the pores. Thus it is reasonable to arrange these absorbers in regions with high velocities. Heat exchange effects cause additional dissipative effects within the porous absorber for higher frequencies. The dissipative effects and the way, they are implemented in this model, are depicted in detail in section 2.1.4. Porous absorbers can be covered

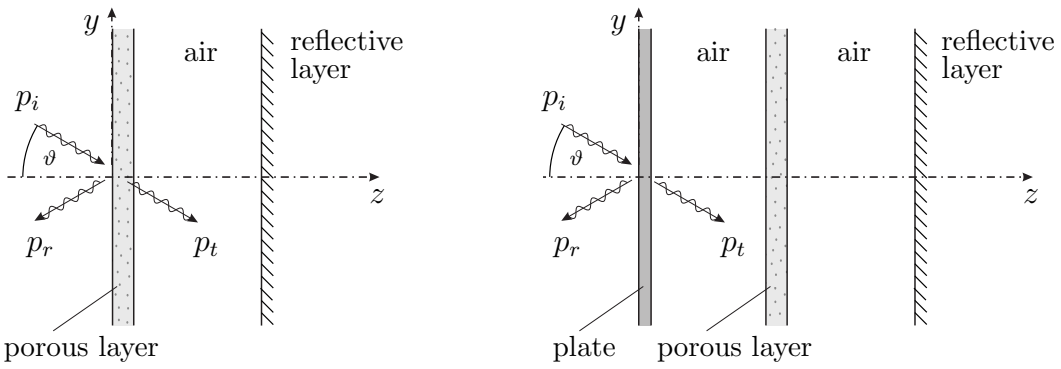

(a) Passive Absorber **(b)** Plate Resonator

Figure 4.1: Classification of absorbers

with acoustically transparent facings like membranes with a small mass surface density or perforated plates.

If the absorptive material is covered with a layer or a membrane having a mass surface density, which is not small compared to the fluid-mass vibrating with the incident wave, the system acts as a plate resonator. Vibrations are excited in the layer by sound waves. Energy is dissipated due to internal damping effects (for instance material damping), which can be

increased by absorption in porous layers, installed in the air cushion behind the vibrating plate, while the plate should not be hindered in vibrating. These resonators work only in a small frequency range (the mass-spring resonance of the system, where the spring is built up by the air cushion). Layers with an appreciable bending stiffness for the plate are used to gain compound absorbers, working in a broader frequency band by activating the bending modeshapes of the plate [see Mechel 1995b; Fuchs 2006]. A schematic sketch of the working principle of a plate resonator is given in figure 4.1b.

If the absorber is covered with a perforated plate, one observes, that the acoustical transparency is becoming worse with increasing frequencies. Already before the distances between the holes of the perforated plate reach dimensions, which are comparable with the wavelength in the acoustic fluid, the air in the holes is starting to act as inert masses (like the membranes, mentioned above) mounted on the air cushion as an elastic support. These *Helmholtz* resonators can be built up with perforated plates or as individual resonators with circular necks. Absorptive material can be applied inside the resonator or in form of a fleece in front of or behind the holes. *Helmholtz* resonators as well as perforated plates are not discussed in this thesis.

Compound absorbers are composed of several layers. These are air volumes, homogeneous layers like membranes or plates and porous layers (figure 4.2). The air in front of the absorber is modeled as a half-space in contrast to the air cushions in the absorber. The simple passive absorber, consisting of a porous layer, mounted either directly on a reflective wall or with an intermediate layer of air, is built up as a special case of compound absorber.

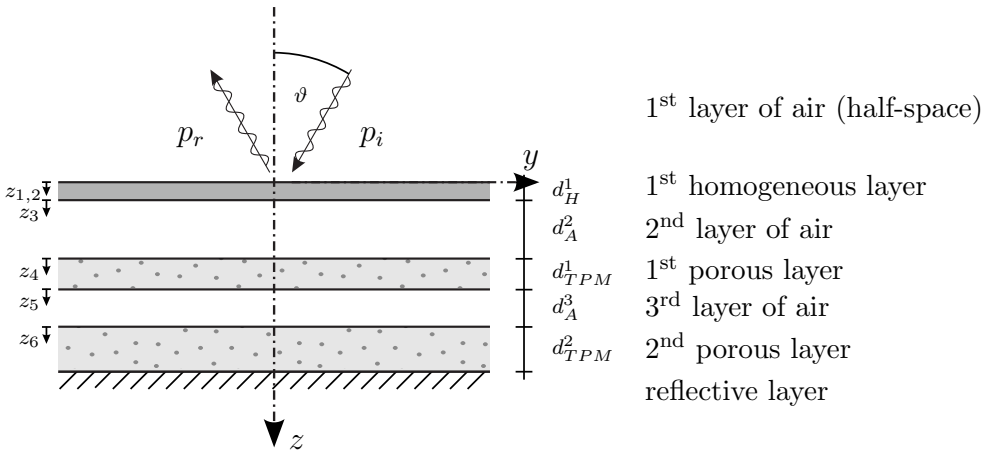

Figure 4.2: Layered model of the compound absorber (schematic sketch)

In the following a layered model, where elastic layers, porous material and air cushions are combined, is derived. The theory, used to model these structures is sketched and the

solution of the systems of differential equations is presented. The boundary conditions and the transition conditions in order to specify the coefficients of the fundamental system for compound structures are discussed. Furthermore the numerical calculation of acoustical parameters, based on this model is presented.

Additional information is found in the standard references, published by Cremer and Müller [1982]; Fahy [2000]; Fuchs [2006]; Heckl and Müller [1995]; Kuttruff [2009]; Mechel [2008]; Möser [2007] as well as Müller and Möser [2003], which are underlying this classification.

4.1 Boundary Conditions and Transition Conditions

Due to the *Fourier* transform in two spatial directions, there exist only horizontal layers in the model, which are defined by a normal vector $\mathbf{n} = \begin{bmatrix} 0 & 0 & 1 \end{bmatrix}^T$ in a Cartesian reference frame.

4.1.1 Lamé-TPM

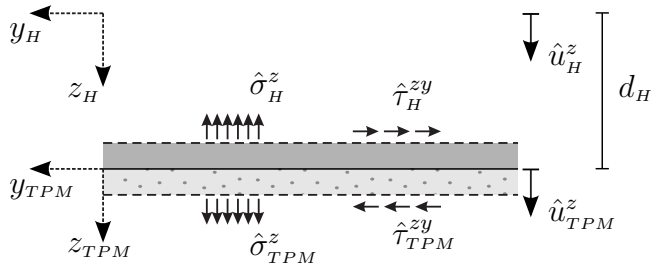

Figure 4.3: Interface between a homogeneous and a porous layer

For a change from a porous to a homogeneous layer as shown in Fig. 4.3, there are seven equations defined for the boundary conditions. Normal and shear stresses have to correspond in both media at the interface $z_{TPM} = 0$

$$\hat{\mathbf{T}}_{TPM}^{z=0}\,\mathbf{n} - \hat{\mathbf{T}}_{H}^{z=d_H}\,\mathbf{n} = \mathbf{0}, \tag{4.6}$$

where, according to equation (2.101), the stresses in the mixture are defined as the sum of the stresses of the constituents.

In contrast to the solid, where all displacements are equated with the displacements of the homogeneous material, for the gas phase only the z-component is coupled:

$$\hat{\mathbf{u}}_S\left(z=0\right)-\hat{\mathbf{u}}_H\left(z=d_H\right)=\mathbf{0} \tag{4.7}$$

$$\hat{u}_G^z\left(z=0\right)-\hat{u}_H^z\left(z=d_H\right)=0, \tag{4.8}$$

where d_H marks the height of the homogeneous layer. In total seven equations are gained for this type of transition.

4.1.2 Helmholtz-TPM

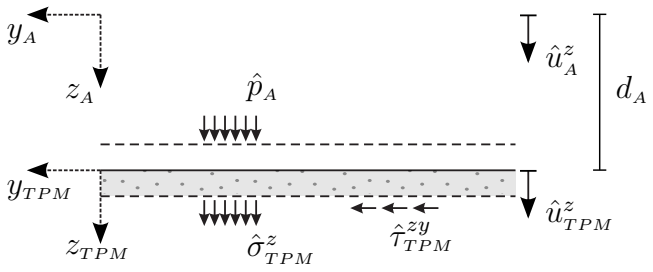

Figure 4.4: Interface between a layer of air and a porous layer

If air is adjacent to a TPM-layer (Fig. 4.4), the normal stresses in the porous medium must be equal to the pressure in the air at the interface $z_{TPM}=0$:

$$\hat{\mathbf{T}}_{TPM}^{z=0}\,\mathbf{n}+\hat{p}_A^{z=d_A}\,\mathbf{n}=\mathbf{0} \tag{4.9}$$

The shear stresses vanish at the interface. Therefore only the z-components of the displacements of the solid and the gas are coupled with the air

$$\hat{u}_S^z\left(z=0\right)-\hat{u}_A^z\left(z=d_A\right)=0 \tag{4.10}$$

$$\hat{u}_G^z\left(z=0\right)-\hat{u}_A^z\left(z=d_A\right)=0, \tag{4.11}$$

which results in five equations.

4.1.3 Helmholtz-Lamé

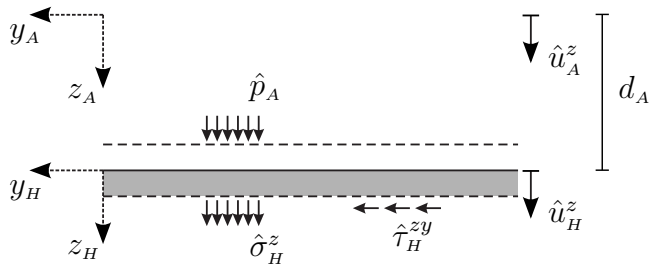

Figure 4.5: Interface between a layer of air and a homogeneous layer

Coupling air to a homogeneous medium (Fig. 4.5) is very similar to the transition *Helmholtz-TPM* in section 4.1.2. The shear stresses of the homogeneous medium vanish at the boundary. This leads to four equations.

$$\hat{\mathbf{T}}_H^{z=0}\,\mathbf{n} + \hat{p}_A^{z=d_A}\,\mathbf{n} = \mathbf{0} \tag{4.12}$$

$$\hat{u}_H^z\,(z=0) - \hat{u}_A^z\,(z=d_A) = 0 \tag{4.13}$$

A survey of the boundary-equations related to the different transitions depicted in table 4.1.

	Stresses	Displacements	Number of eqns.
Lamé-TPM	$\hat{\mathbf{T}}_{TPM}^{z=0}\mathbf{n} - \hat{\mathbf{T}}_H^{z=d_H}\mathbf{n} = \mathbf{0}$	$\hat{\mathbf{u}}_S\,(z=0) - \hat{\mathbf{u}}_H\,(z=d_H) = \mathbf{0}$ $\hat{u}_G^z\,(z=0) - \hat{u}_H^z\,(z=d_H) = 0$	7
Helmholtz-TPM	$\hat{\mathbf{T}}_{TPM}^{z=0}\mathbf{n} + \hat{p}_A^{z=d_A}\mathbf{n} = \mathbf{0}$	$\hat{u}_S^z\,(z=0) - \hat{u}_A^z\,(z=d_A) = 0$ $\hat{u}_G^z\,(z=0) - \hat{u}_A^z\,(z=d_A) = 0$	5
Helmholtz-Lamé	$\hat{\mathbf{T}}_H^{z=0}\mathbf{n} + \hat{p}_A^{z=d_A}\mathbf{n} = \mathbf{0}$	$\hat{u}_H^z\,(z=0) - \hat{u}_A^z\,(z=d_A) = 0$	4

Table 4.1: Summary of the equations resulting out of the boundary conditions

4.1.4 Sommerfeld Radiation Condition

The scalar and vector potentials, defined in sections 2.3, 3.1 and 3.2 are solutions for the *Helmholtz* equation and systems of differential equations, containing *Helmholtz* equations, respectively. Sommerfeld [1949] stated, that “energy which is radiated from the sources must

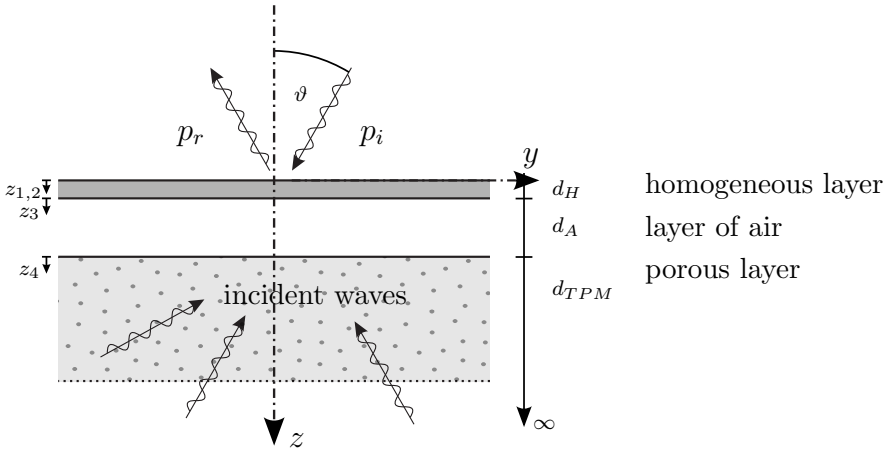

Figure 4.6: Sommerfeld radiation condition – exemplary sketched for an ∞ porous layer

scatter to infinity; no energy may be radiated from infinity into the prescribed singularities of the field".

Therefore in a layer, which is defined as a half-space (see figure 4.6), no incident waves can occur as far-field solutions and the near-field solutions have to decrease exponentially. Müller [1989] pointed out, that for circular frequencies of excitation $\Omega < 0$ the increasing part of the surface waves and the incident spherical waves propagating from infinity to the interface of the layer are described with the same coefficients of the scalar and vector potentials respectively. Therefore the computations are carried out for negative circular frequencies in the following. The corresponding solutions for $\Omega > 0$ are the complex conjugates.

The Sommerfeld radiation condition is fulfilled by skipping the corresponding coefficients in the fundamental systems (compare table 4.2).

	Compressional waves	Shear wave
TPM	$A_2 = 0$ $A_4 = 0$ in (2.73), (2.74)	$\mathbf{B}_2 = \mathbf{0}$ in (2.75), (2.76)
Lamé	$C_2 = 0$ in (3.8)	$\mathbf{D}_2 = \mathbf{0}$ in (3.9)
Helmholtz	$E_2 = 0$ in (3.22)	

Table 4.2: Coefficients to be skipped obeying the Sommerfeld radiation condition

4.1.5 Layers on Reflective Walls

The bottom layer in the compound absorber is a reflective wall for most applications. For practical systems porous layers or air cushions will be connected to the reflective walls. For the sake of completeness the boundary conditions for connections with all three types of material are listed in table 4.3.

	Displacements	Number of eqns.
TPM	$\hat{\mathbf{u}}_S\left(z = d_{TPM}\right) = \mathbf{0}$ $\hat{u}_G^z\left(z = d_{TPM}\right) = 0$ in (2.96)	4
Lamé	$\hat{\mathbf{u}}_H\left(z = d_H\right) = \mathbf{0}$ in (3.16)	3
Helmholtz	$\hat{u}_A^z\left(z = d_A\right) = 0$ in (3.23)	1

Table 4.3: Boundary conditions for connections to reflective walls

4.2 System of Equations

The boundary conditions and the transition conditions for the compound absorber, which are addressed with BC_i in the following, are established using the equations listed in tables 4.1 to 4.3. One obtains a system of linear equations to compute the coefficients of the fundamental systems:

$$\mathbf{K}\,\mathbf{x} = \mathbf{f}, \tag{4.14}$$

where $\mathbf{K}$ is the matrix of coefficients

$$\mathbf{K} = \begin{bmatrix} \dfrac{\partial BC_1}{\partial x_1} & \cdots & \dfrac{\partial BC_1}{\partial x_{n_{tot}}} \\ \vdots & \ddots & \vdots \\ \dfrac{\partial BC_{n_{tot}}}{\partial x_1} & \cdots & \dfrac{\partial BC_{n_{tot}}}{\partial x_{n_{tot}}} \end{bmatrix} \tag{4.15}$$

and $\mathbf{x}$ denotes the vector of unknowns

$$\mathbf{x} = \begin{bmatrix} \mathbf{x}_{TPM}^1 & \cdots & \mathbf{x}_{TPM}^{n_{TPM}} & \mathbf{x}_H^1 & \cdots & \mathbf{x}_H^{n_H} & \mathbf{x}_A^1 & \cdots & \mathbf{x}_A^{n_A} \end{bmatrix}^T \tag{4.16}$$

with:

$$\begin{aligned}\mathbf{x}_{TPM}^{k} &= \begin{bmatrix} A_1^k & A_2^k & A_3^k & A_4^k & B_{11}^k & B_{12}^k & B_{21}^k & B_{22}^k \end{bmatrix}^T \\ \mathbf{x}_{H}^{k} &= \begin{bmatrix} C_1^k & C_2^k & D_{11}^k & D_{12}^k & D_{21}^k & D_{22}^k \end{bmatrix}^T \\ \mathbf{x}_{A}^{k} &= \begin{bmatrix} E_1^k & E_2^k \end{bmatrix}^T .\end{aligned} \tag{4.17}$$

The entries of the vector of unknowns depend on the absorber-type as well as on the number of layers of each material, where n_{TPM}, n_H and n_A mark their maximum number respectively. The total number of unknowns n_{tot} for each combination of k_x, k_y and Ω is

$$n_{tot} = n_{TPM} \cdot 8 + n_H \cdot 6 + n_A \cdot 2 - 1, \tag{4.18}$$

assuming, that for the 1st layer of air (upper layer of the absorber) just the pressure amplitude of the reflected wave p_r is unknown, because the incident wave p_i represents the load $\mathbf{f}$.

$$\mathbf{f} = \begin{bmatrix} f^1 & \cdots & f^n \end{bmatrix}^T \tag{4.19}$$

Due to different magnitudes in (4.14) the system of equations is ill conditioned for higher frequencies, especially if thick layers are defined. Using a preconditioner, as outlined in appendix A.4 provides, for realistic layer thicknesses, a stable system up to a frequency limit, which is sufficient for numerical calculations (about $5\,kHz$). In case of thick layers, which results in large arguments in the exponential functions, it is reasonable to rearrange the definitions of the potentials (see appendix A.4).

4.3 Computation of Acoustic Properties

4.3.1 Impedance

In models of acoustic cavities with compound absorbers as boundary conditions the vibrational characteristics of both, the acoustic fluid in terms of compressional waves and the structure with its body and surface waves, have to be considered. In addition to the individual mechanical properties of the substructures one has to take the interaction at the interfaces into account in the coupled system. Depending on these properties the waves in the fluid are reflected or transmitted and kinetic energy is dissipated.

An efficient possibility to specify substructures for coupling with other structures, which will be discussed at a later stage in this work, is provided by the concept of impedances [see e.g. Fahy 2000, 2007].

If a harmonic time dependent performance of the system can be assumed, which is the case for harmonic analyses for steady state responses, the analysis can be done with a complex exponential description for each circular frequency of excitation Ω. Transient analyses can use this time harmonic assumption too if a spectral decomposition is carried out with *Fourier* transform methods. Applying this complex exponential approach and discussing the conjugate complex quantities individually, the ratio of forces and velocities (in structural systems) or pressure and velocities (in acoustical systems) can be expressed by a complex value, the impedance of the substructure. Depending on the structure and the type of coupling different impedance representations, point impedances for instance, established at the point of excitation for lumped or continuous systems under a single force, or modal impedances, where the ratio of the generalized modal force and the modal velocity is computed, are used.

In this work the differential equations are solved in the wavenumber-frequency domain and a *Fourier* series approach is applied later on for the fluid structure interaction. Thus the acoustic wave impedance is used. It is defined as

$$Z(k_x, k_y, \Omega) = \frac{\hat{p}_A(k_x, k_y, \Omega)}{\hat{v}_A^z(k_x, k_y, \Omega)}, \tag{4.20}$$

where $\hat{p}_A$ and $\hat{v}_A^z$ are the complex values of pressure and normal velocity of the fluid at the interface (surface of the compound absorber). It is evaluated for each set of k_x, k_y and Ω. Müller [1989] showed, that, as the results for the physical quantities have to be real values after applying the inverse transformation, the number of sets can be reduced by a factor two computing just for positive or negative frequencies/wavenumbers and supplementing

the result with the help of the complex conjugate values. As mentioned in section 4.1.4 already, it is convenient to calculate with negative circular frequencies of excitation. In case of computing impedances perpendicular to the compound absorber the results are symmetric with respect to k_x and k_y, which is an additional gain in efficiency.

The application of normal impedances for FSI-problems in combination with absorbers, where the porous material is modeled based on the theory of Biot [1956b,c] and Allard [2009] was done by Deü et al. [2006] and Larbi et al. [2009]. Normal impedances assume plane waves at the surface of the absorber. In this FSI-model the absorber acts as a field of uncoupled single degree of freedom systems.

In order to treat a more complex spatial functionality of the absorptive structure, in equation (4.20) the impedance is computed depending on the wavenumbers k_x and k_y. They are linked to different angles of incidence for the sound waves. Figure 4.7 shows the geometrical relations between wavenumbers, wavelengths and the angle of incidence for the two-dimensional case ($\vartheta_{yz} = 0$, $k_y = 0$), where ($\vartheta_{xz} = \vartheta$).

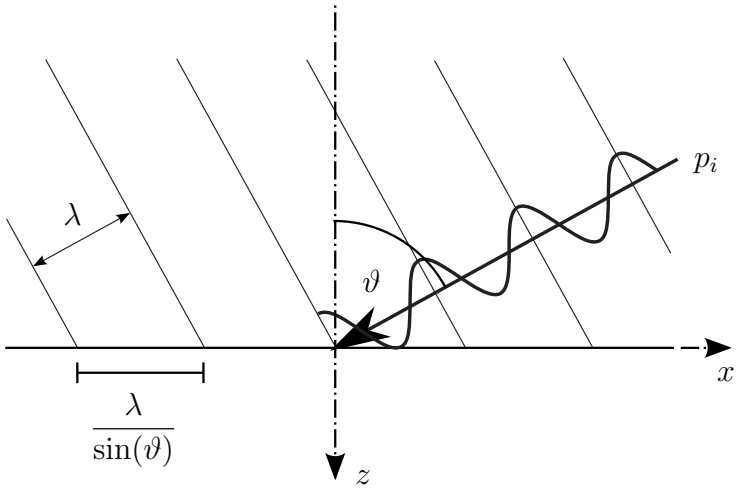

Figure 4.7: Incident sound wave for $\vartheta_{yz} = 0$, $k_y = 0$

The incident sound wave has got a wavelength λ and a wavenumber k_A.

$$\lambda = \frac{2\pi}{\Omega}\, c_A \tag{4.21}$$

$$k_A = \frac{2\pi}{\lambda} = \frac{\Omega}{c_A} \tag{4.22}$$

According to Cremer and Müller [1982] the wavenumber k_A is understood as the absolute value of a vector $\mathbf{k}_A$, which can be decomposed into its components. The periodicity along the surface ($z = 0$) is characterized by the wavenumber k_x. It is called trace wavenumber and calculated out of the trace wavelength $\frac{\lambda}{\sin(\vartheta)}$, as depicted in figure 4.7. The normal wavenumber k_z is calculated out of the normal wavelength $\frac{\lambda}{\cos(\vartheta)}$ analogously.

$$k_z = \frac{2\pi}{\lambda}\cos(\vartheta) = \frac{\Omega}{c_z} = k_A\cos(\vartheta) \quad (4.23) \qquad k_x = \frac{2\pi}{\lambda}\sin(\vartheta) = \frac{\Omega}{c_x} = k_A\sin(\vartheta) \quad (4.24)$$

The three-dimensional case, where the incident sound wave hits the surface with an arbitrary angle, is understood, decomposing the vector of the wavenumber k_A into the components k_x, k_y and k_z.

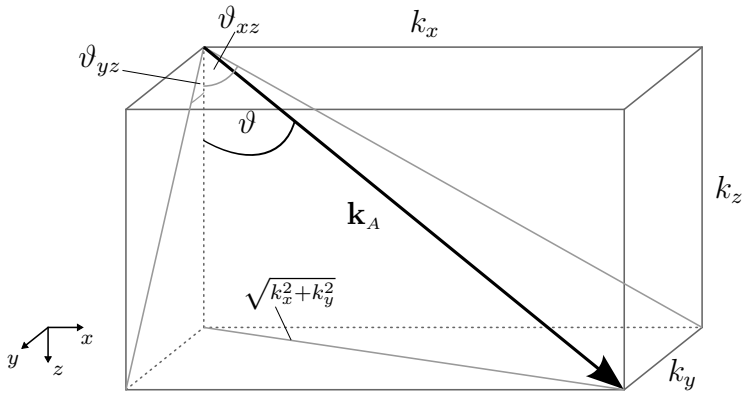

Figure 4.8: Vector decomposition of the wavenumber k_A

Out of figure 4.8 expressions for the spatial angle of incidence ϑ and the angles of the projections of $\mathbf{k}_A$ to the xz-plane (ϑ_{xz}) and to yz-plane (ϑ_{xy}), which build up the two-dimensional case are obtained.

$$\sin(\vartheta) = \frac{\sqrt{k_x^2 + k_y^2}}{k_A} \quad (4.25) \qquad \begin{aligned} \sin(\vartheta_{xz}) &= \frac{k_x}{\sqrt{k_x^2 + k_z^2}} = \frac{k_x}{\sqrt{k_A^2 - k_y^2}} \\ \sin(\vartheta_{yz}) &= \frac{k_y}{\sqrt{k_y^2 + k_z^2}} = \frac{k_y}{\sqrt{k_A^2 - k_x^2}} \end{aligned} \quad (4.26)$$

Substituting $\cos(\alpha) = \sqrt{1 - \sin^2(\alpha)}$ in (4.26) leads to:

$$\cos(\vartheta_{xz}) = \sqrt{1 - \frac{k_x^2}{k_A^2 - k_y^2}} \quad (4.27a) \qquad \cos(\vartheta_{yz}) = \sqrt{1 - \frac{k_y^2}{k_A^2 - k_x^2}} \quad (4.27b)$$

Equations (4.26) as well as (4.27a) and (4.27b) are observed in the literature for the two-dimensional case with $\left(k_y = 0 \rightarrow k_A^2 - k_y^2 = k_A^2\right)$ and $(k_x = 0 \rightarrow k_A^2 - k_x^2 = k_A^2)$. Applying this substitution to equation (4.25) one obtains the relation between the wavenumbers k_x, k_y and the spatial angle of incidence ϑ of the acoustic wave, which will be used in equation (4.33).

$$\cos(\vartheta) = \sqrt{1 - \frac{k_x^2}{k_A^2} - \frac{k_y^2}{k_A^2}} \tag{4.28}$$

Thus the impedances $Z(k_x, k_y, \Omega)$, which are the key values for the description of the compound absorbers in chapter 5, can be evaluated at the basis of equation (4.20) for different types of plate-like compound absorbers.

4.3.2 Absorption Coefficient

The absorption coefficient, specified in equation (4.2), is the ratio of "not fully reflected" power and incident power. It is usually applied in room acoustics for classifying absorbers and can be deduced from the impedances $Z(k_x, k_y, \Omega)$, derived in the last section, in a wave-based consideration.

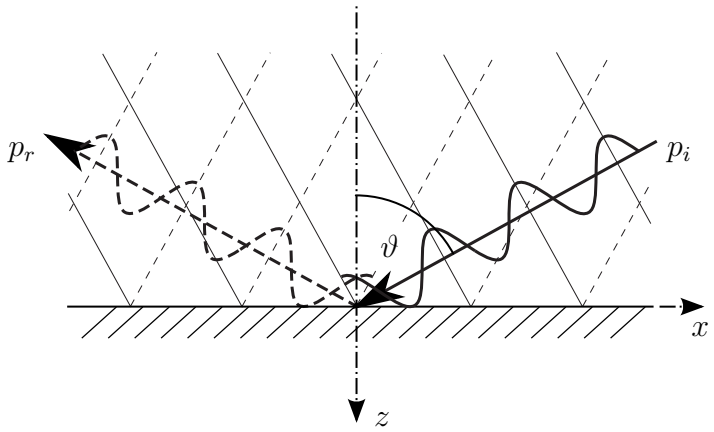

Figure 4.9: Incident and reflective waves

The transformed pressure $\hat{p}$ of the sound wave, defined in equation (3.22), is written in a modified form

$$\begin{aligned} \hat{p}_A &= E_i\, e^{\,i\sqrt{k_A^2 - k_x^2 - k_y^2}\, z} + E_r\, e^{\,-i\sqrt{k_A^2 - k_x^2 - k_y^2}\, z} \\ &= E_i \left(e^{\,i\sqrt{k_A^2 - k_x^2 - k_y^2}\, z} + r\, e^{\,-i\sqrt{k_A^2 - k_x^2 - k_y^2}\, z} \right) \quad \text{with:} \quad r = \frac{E_r}{E_i}, \end{aligned} \tag{4.29}$$

where E_i belongs to the incident and E_r to the reflected sound wave[1] whereas r is the reflection coefficient. The absorption coefficient α can be computed out of the reflectivity

[1] The direction of the traveling wave depends on the sign of Ω [Müller 1989]. The definitions are done for $\Omega < 0$ (compare remark in section 4.1.4).

(4.34) or, as described for plane waves in Möser [2007], it is deduced from the impedance Z of the structure. The velocity perpendicular to the plate is gained out of (3.20):

$$\hat{v}_A^z = \frac{-\sqrt{k_A^2 - k_x^2 - k_y^2}}{\Omega\,\rho_A} E_i \left(e^{i\sqrt{k_A^2-k_x^2-k_y^2}\,z} - r\, e^{-i\sqrt{k_A^2-k_x^2-k_y^2}\,z} \right) \tag{4.30}$$

The impedance Z at the surface of the absorber is obtained to:

$$Z = \frac{\hat{p}_A(0)}{\hat{v}_A^z(0)} = C\,\frac{1+r}{1-r} \qquad \text{with:} \quad C = \frac{-\Omega\,\rho_A}{\sqrt{k_A^2 - k_x^2 - k_y^2}}. \tag{4.31}$$

The factor C is rearranged by the help of (4.28) to visualize the relation between the angle of incidence ϑ of the sound wave and the wavenumbers:

$$C = \frac{-\Omega\,\rho_A}{\sqrt{k_A^2 - k_x^2 - k_y^2}} = -\operatorname{sgn}(\Omega)\,\frac{\rho_A\,c_A}{\sqrt{1 - \dfrac{k_x^2}{k_A^2} - \dfrac{k_y^2}{k_A^2}}} = \frac{Z_0}{\cos(\vartheta)} \tag{4.32}$$

Extracting the reflection coefficient r out of equation (4.31), the absorption coefficient can be determined out of Z, using (4.33) and (4.34)

$$r = \frac{\frac{Z}{C} - 1}{\frac{Z}{C} + 1} \tag{4.33}$$

$$\alpha = 1 - |r|^2 \tag{4.34}$$

and finally results in

$$\alpha = \frac{4\,\mathrm{Re}\left(\frac{Z}{C}\right)}{\left[\mathrm{Re}\left(\frac{Z}{C}\right) + 1\right]^2 + \left[\mathrm{Im}\left(\frac{Z}{C}\right)\right]^2}. \tag{4.35}$$

Equation (4.35) contains the counterpart for the plane wave (for instance in Möser [2007]), if C is set equal to the impedance Z_0 of the air for $\vartheta = 0$.

As one can see, the maximum values for α are gained, if the imaginary part of the impedance vanishes. In the optimum case ($\alpha = 1$) the real part of the wavenumber- and frequency-dependent impedance of the absorptive structure $Z(k_x, k_y, \Omega)$ is equal to the factor C.

In the following section numerical results are presented, where impedances and absorption coefficients were calculated for different types of compound absorbers.

4.4 Numerical Results for Compound Absorbers

In this section important acoustic properties, the impedance Z and the absorption coefficient α, are simulated for various compound absorbers applying the method, derived in the previous sections. These plate-like absorbers consist of different layers of porous material, elastic layers and air cushions. Due to the application of the Integral Transform Method infinite structures are assumed concerning the in-plate dimensions at first. The transition to finite dimensions is done while deriving the calculation scheme for the acoustical FSI–problem in chapter 5.

The formulation of the porous material according to the Theory of Porous Media after de Boer [2000] as well as the layered model based on the ITM is validated with various examples in the following. It is shown, that the method meets fundamental mechanical and acoustical principles but also comparisons with measurements and simple engineering methods, which have already been used for decades in acoustic models, are presented.

4.4.1 Validation with Measurements

At first plane wave conditions are assumed, in order to compare the numerical results for porous foams with measurement results.

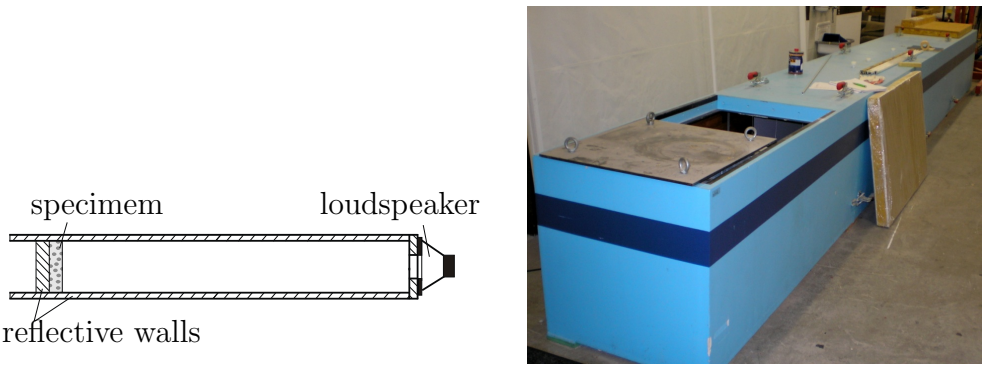

(a) Schematic sketch **(b)** Measurement setup

Figure 4.10: Impedance tube - schematic sketch and measurement setup (Müller-BBM GmbH)

The measurements were carried out in the impedance tube sketched in figure 4.10 in accordance with DIN EN ISO 10534-2:2001-10. This measurement device, which was named *Kundt*'s tube after its inventor *August Kundt*[2], consists of a longitudinal tube with reflective

[2]August Kundt (1839–1894)

walls. It is loaded by a sound source at one end of the tube, whereas the specimen is placed at the opposite end [see e.g. Möser 2007]. Plane waves can be generated in this tube for wavelengths, which are long compared to the cross sectional dimensions of the tube, because the transverse waves show exponentially decaying near-fields along the tube for frequencies below the *cut on frequency*, which is $f_c = \frac{c_A}{2d}$ for the first transverse mode. Thus the upper limit of the frequency range is defined for the setup in figure 4.10b to $275\,Hz$. Using a melamine foam, a polyurethane foam and a mineral wool three different kinds of porous foams were measured.

In the numerical model plane waves are achieved due to the definition of the wavenumbers $k_x = 0$ and $k_y = 0$ in x- and y- direction. The calculations were performed with the material parameters listed in table 4.4.

		Melamin Foam	Polyurethane Foam	Mineral Wool
n_G	$[-]$	0.8	0.8	0.9
ρ_s	$\left[\frac{kg}{m^3}\right]$	15	30	8
E_s	$\left[\frac{N}{m^2}\right]$	5000	9000	7500
ν_s	$[-]$	0.05	0.05	0.05
ρ_g	$\left[\frac{kg}{m^3}\right]$	1.2	1.2	1.2
Ξ	$\left[\frac{N\,s}{m^4}\right]$	4000	10000	5000
d_{TPM}	$[mm]$	72	102	103

Table 4.4: Parameters for the porous material

In addition to the specific flow resistance, which is defined in equation (2.35), a frequency-independent hysteretic material damping loss factor $\eta^D = 0.3$ is defined according to equation (2.38). For the model of the mineral wool just the flow resistance normal to the fibers $\Xi_\perp$ is considered, because plane waves are excited in the material (compare section 2.1.4).

In the following paragraphs the numerical results are depicted compared to the measurement results for the plane wave impedance $Z(\Omega)$ and the absorption ratio α for the materials specified above.

Melamine Foam

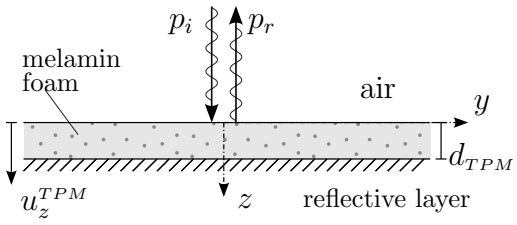

Figure 4.11: Porous layer out of Melamine Foam

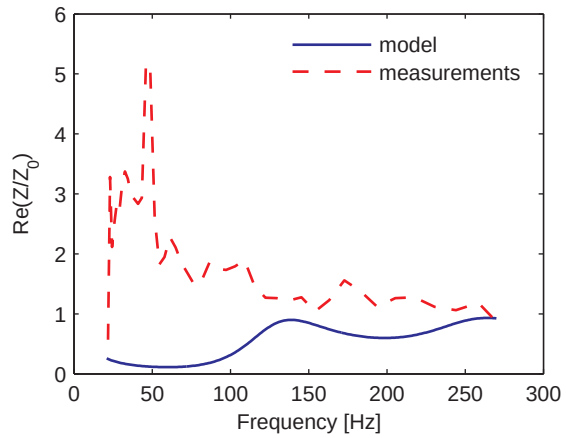

(a) Real part of $\frac{Z}{Z_0}$

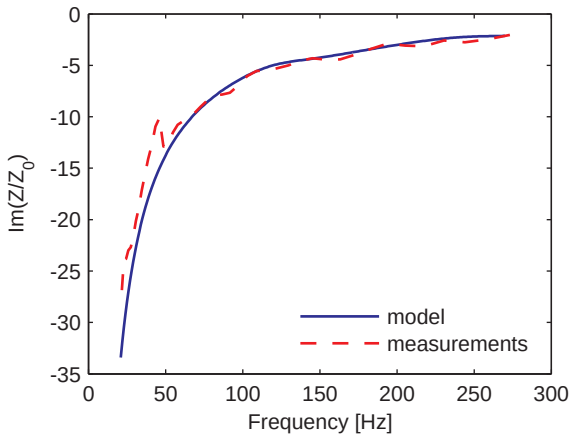

(b) Imaginary part $\frac{Z}{Z_0}$

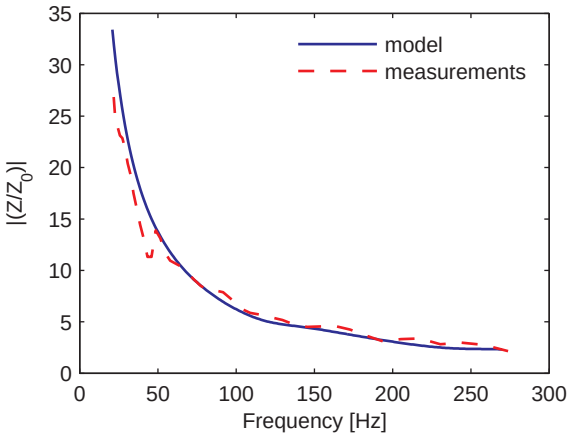

(c) Absolute value $\frac{Z}{Z_0}$

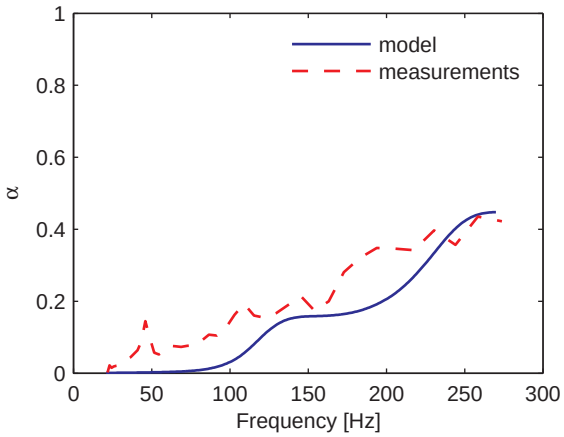

(d) Absorption ratio α

Figure 4.12: Plane wave impedance $Z(\Omega)$ related to $Z_0 = \rho_A\, c_A$ and absorption ratio α for a $7.2\,cm$ layer of Melamine Foam - Comparison against measurements

Polyurethane Foam

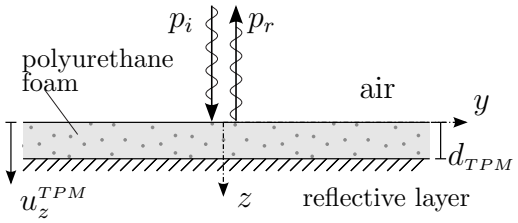

Figure 4.13: Porous layer out of Polyurethane Foam

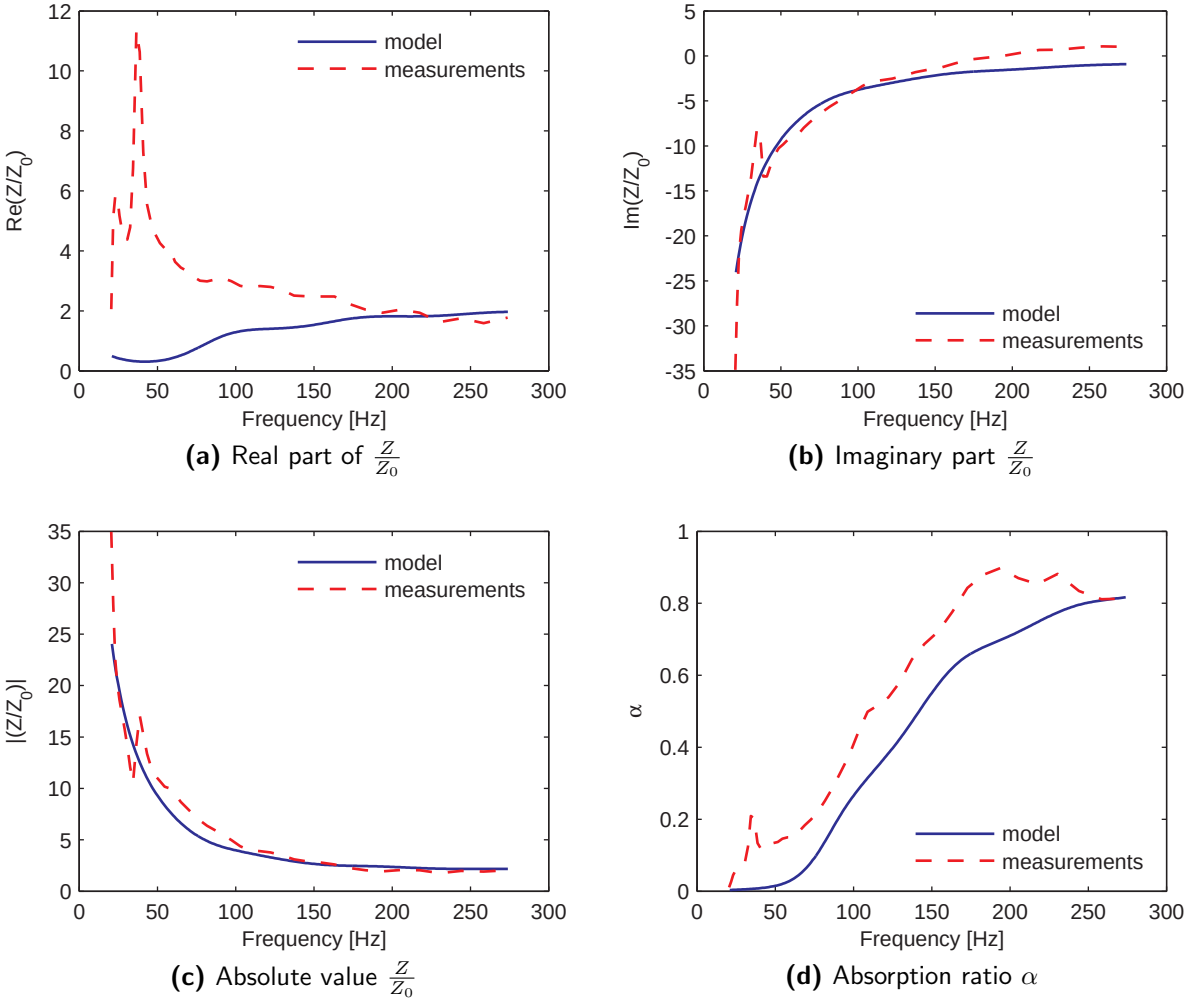

(a) Real part of $\frac{Z}{Z_0}$

(b) Imaginary part $\frac{Z}{Z_0}$

(c) Absolute value $\frac{Z}{Z_0}$

(d) Absorption ratio α

Figure 4.14: Plane wave impedance $Z(\Omega)$ related to $Z_0 = \rho_A\, c_A$ and absorption ratio α for a $10.2\,cm$ layer of Polyurethane Foam - Comparison against measurements

Mineral Wool

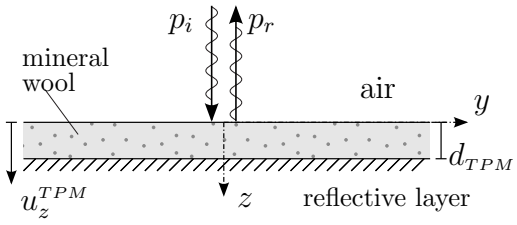

Figure 4.15: Porous layer out of Mineral Wool

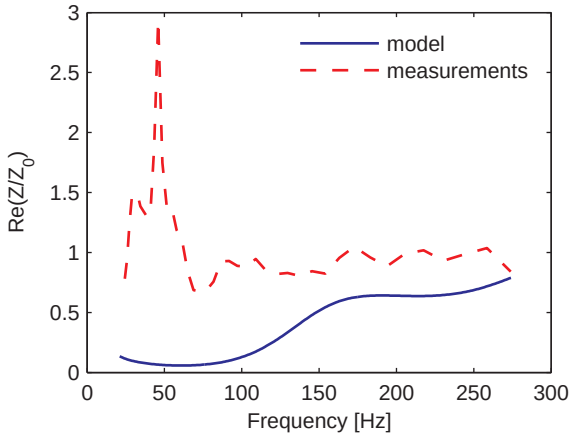

(a) Real part of $\frac{Z}{Z_0}$

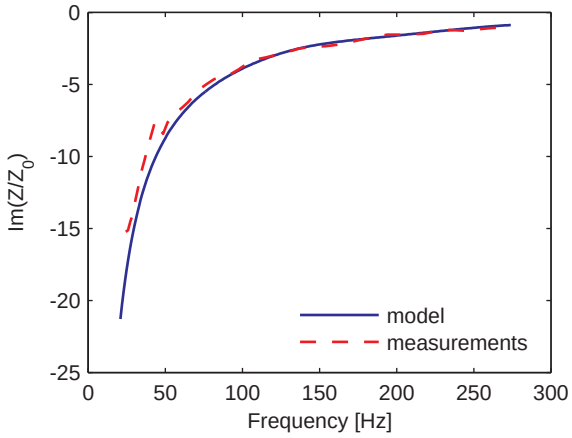

(b) Imaginary part $\frac{Z}{Z_0}$

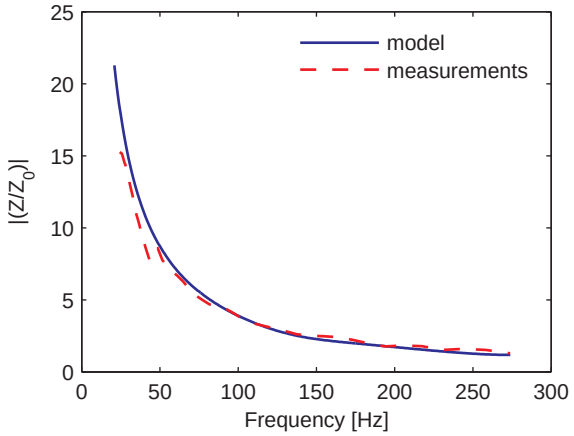

(c) Absolute value $\frac{Z}{Z_0}$

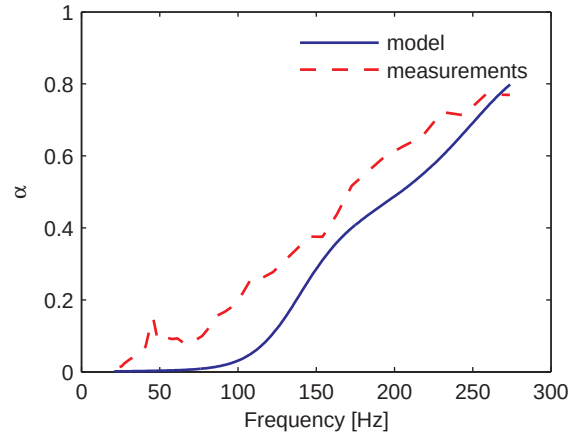

(d) Absorption ratio α

Figure 4.16: Plane wave impedance $Z(\Omega)$ related to $Z_0 = \rho_A\, c_A$ and absorption ratio α for a $10.3\,cm$ layer of Mineral Wool - Comparison against measurements

One observes, that the imaginary part of the impedance $Z(\Omega)$, which characterizes the elastic behavior of the foam, is predicted with a high level of accuracy. The differences, which are

observed at about $40\,Hz$ in figures 4.12b, 4.14b and 4.16b, result out of resonant vibrations of the impedance tube, which has been a tube with a rectangular cross section in this case. In this frequency range the rigid wall assumption of the measurement setup is violated.

Concerning the real part of $Z(\Omega)$, which marks the damping of the porous foam, differences between the simulation and the measurements are observed in the frequency range, where the transverse modes, caused due to the elastic behavior of the measurement setup, disturb the measurement results. The imaginary part is dominating the results for the impedance (note the different scaling of the real and the imaginary part) resulting in very small errors in the absolute values of the impedance.

4.4.2 Comparison with the Rayleigh Model

The simple *Rayleigh* model is used as a reference for plane-wave conditions in the next step. In this model the fibers of the skeleton of the absorptive material are assumed to be parallel to the direction of the propagating waves. The model is based on a formulation of the wave equation for the porous medium, which is very similar to the description of the acoustic fluid. It is discussed by Möser [2007] for instance. A definition of the mass of the skeleton or a specification of macroscopic elastic constants is not possible in contrast to the Theory of Porous Media.

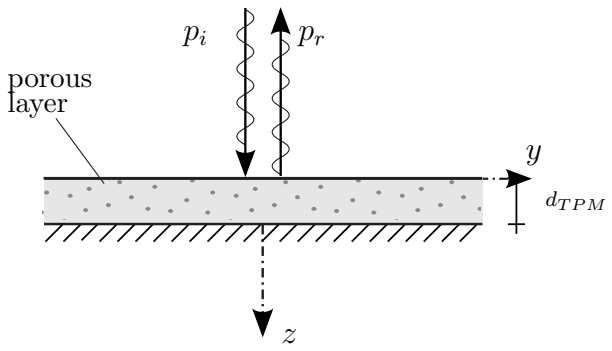

Figure 4.17: Infinite porous layer on a reflective wall considering plane waves

A friction force $\Xi\, A\, dz\, v$, which is responsible for the energy dissipation, is introduced in *Newton*'s law

$$\rho_A \frac{\partial v^z}{\partial t} = -\frac{p}{z} - \Xi\, v_e^z. \tag{4.36}$$

In equation (4.36) v_e is the external velocity referred to the reference volume. The internal velocity v_i, which is defined as the velocity within the pores, is differing ($v_i > v_e$) due to the reduced cross-section and the conservation of the flow-rate. The relation

$$v_e = \frac{n_G}{\kappa}\, v_i \tag{4.37}$$

holds for the velocities, where κ is the *structure factor* ($\kappa \geq 1$), considering, that some of the fibers are ending within the material. In case of a rigid fiber-skeleton the compression of the porous material is described with

$$\frac{\partial v_i^z}{\partial z} = \frac{1}{\rho_A c_A}\frac{\partial p}{\partial t}. \tag{4.38}$$

The *Helmholtz* equation for the porous material is obtained out of (4.37) and (4.38) after a *Fourier* Transform into the frequency domain

$$\frac{\partial^2 p}{\partial z^2} + k_a^2 p = 0 \qquad \text{with: } k_a = k_A\sqrt{\kappa}\sqrt{1 - i\frac{\Xi\, n_G}{\Omega\, \rho_A\, \kappa}}, \tag{4.39}$$

where k_a is the wavenumber of the foam in the *Rayleigh* model. Composing the solution of equation (4.39) out of two waves, traveling in opposite directions, the impedance Z reads for an absorptive layer with a thickness d:

$$Z = k_a \frac{\rho_A\, c_A^2}{n_G\, \Omega}\frac{1 + e^{-i\,2\,k\,d}\, e^{-\frac{\Xi\, d}{\rho_A\, c_A}}}{1 - e^{-i\,2\,k\,d}\, e^{-\frac{\Xi\, d}{\rho_A\, c_A}}} \tag{4.40}$$

In figure 4.18 the plane wave impedances for a porous layer, calculated with the TPM/ITM according to (4.20) and the simple *Rayleigh* model out of equation (4.40) are compared. The real and the imaginary part of the impedance as well as the isolines of the absorption ratio α are sketched for varying circular frequencies of excitation Ω. The results are presented with dimensionless parameters for different ratios $\frac{\Xi d}{Z_0}$. The dimensionless representation in terms of the flow resistance Ξ works for the TPM-model as well, as one expects for a physically correct implementation of the dissipation in section 2.1.4. The figures show, that the general quality of the results is comparable if the parameters occurring in both theories are chosen identically. Of course the *Rayleigh* model is not able to cover as many material parameters as the TPM-model does.

The dependency on the porosity, computed with the TPM-model, is presented in figure 4.19. As one would expect, a lower absorption ratio is obtained for decreasing values of n_g.

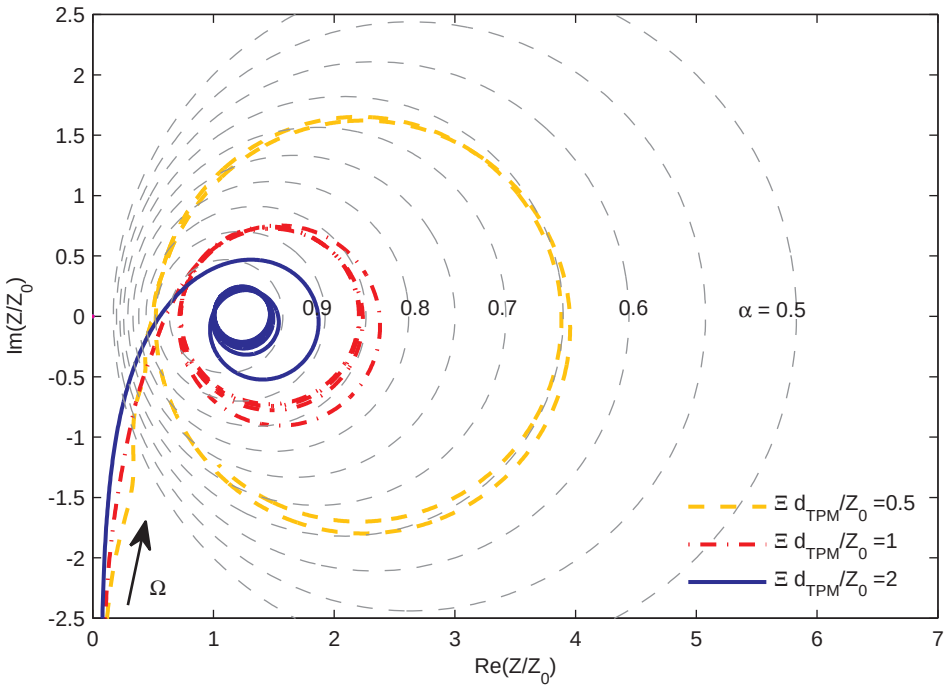

(a) TPM model

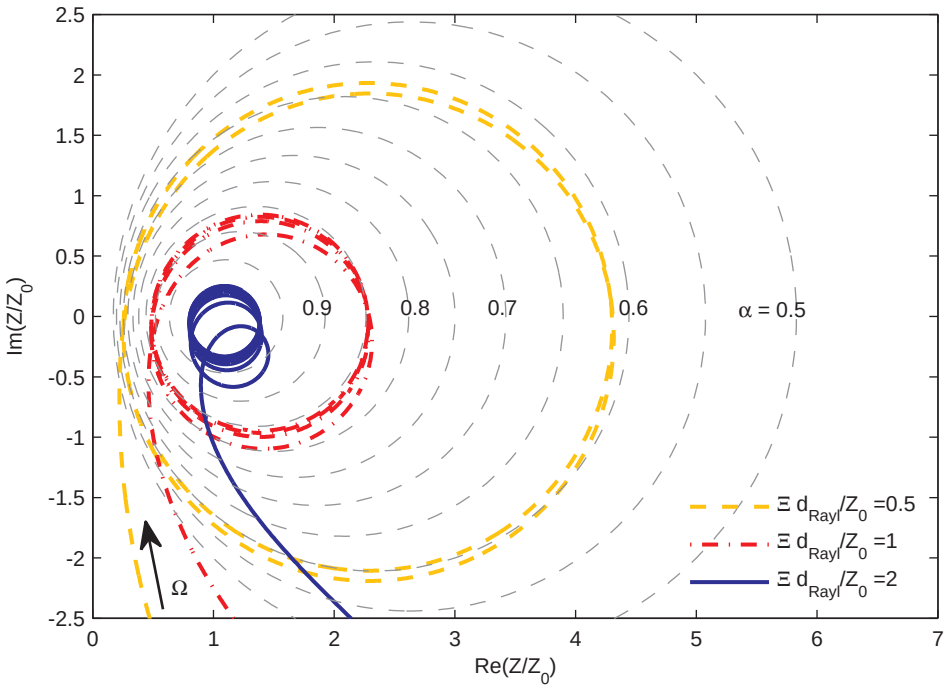

(b) *Rayleigh* model ($\kappa = 1$)

Figure 4.18: Impedance ratio $\frac{Z}{Z_0}$ of porous layers on reflective walls for $\Omega \in [0; 5000]\left[\frac{\text{rad}}{\text{s}}\right]$ ($\vartheta = 0$ and $n_g = 0.95$)

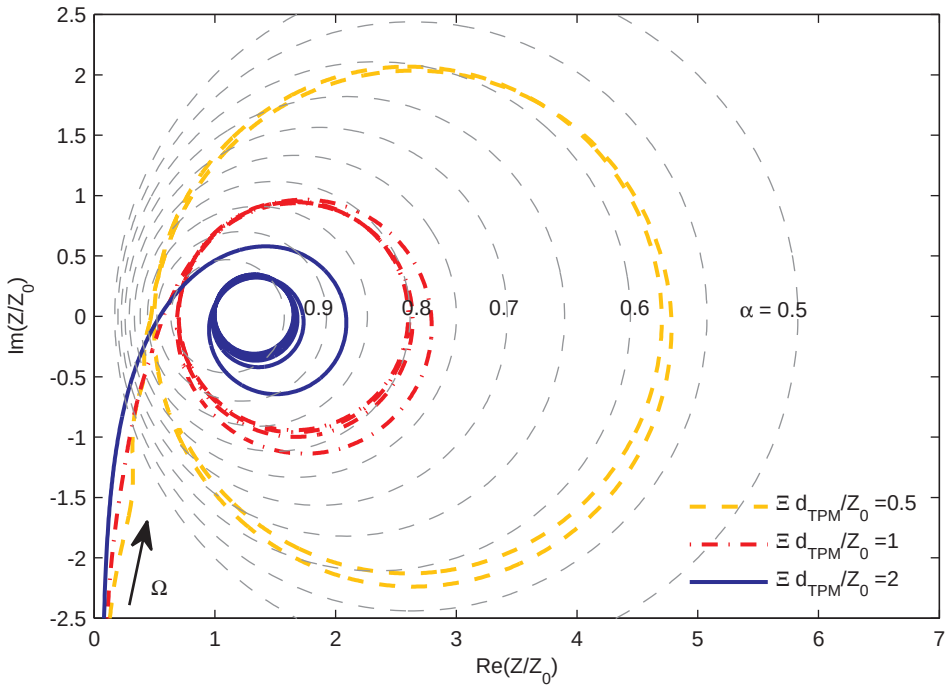

(a) $n_g = 0.90$

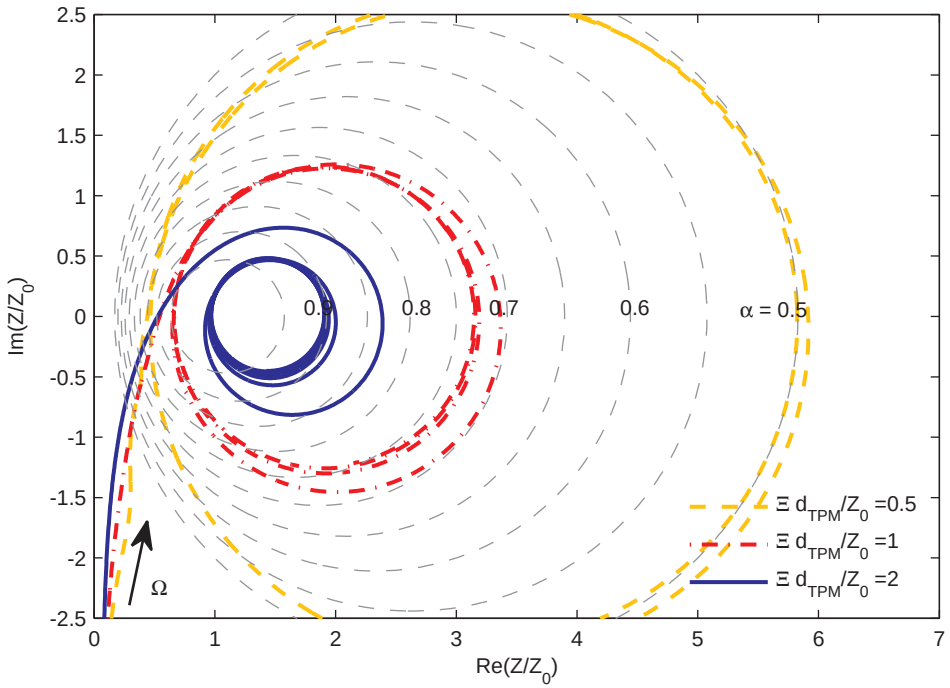

(b) $n_g = 0.85$

Figure 4.19: Absorption ratio α of porous layers on reflective walls for $\vartheta = 0$ computed with the TPM-model - Variation of the porosity for $\Omega \in [0; 5000]\left[\frac{\text{rad}}{\text{s}}\right]$

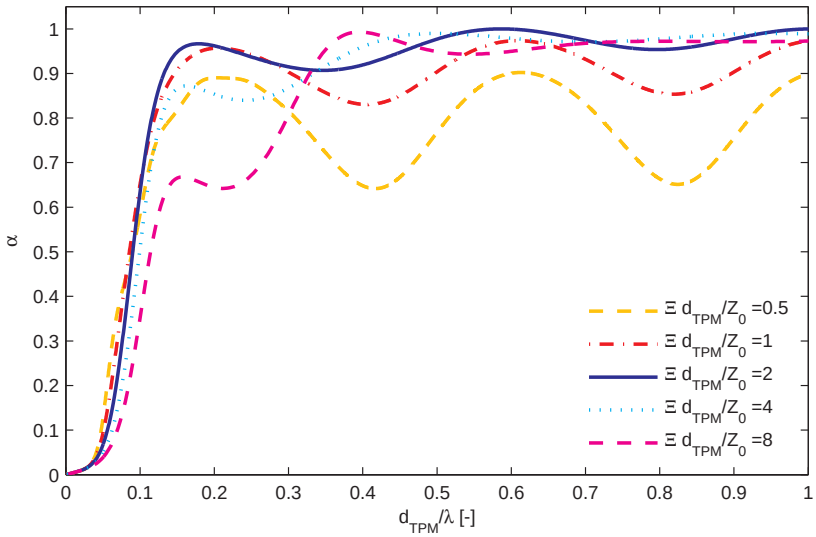

(a) TPM model

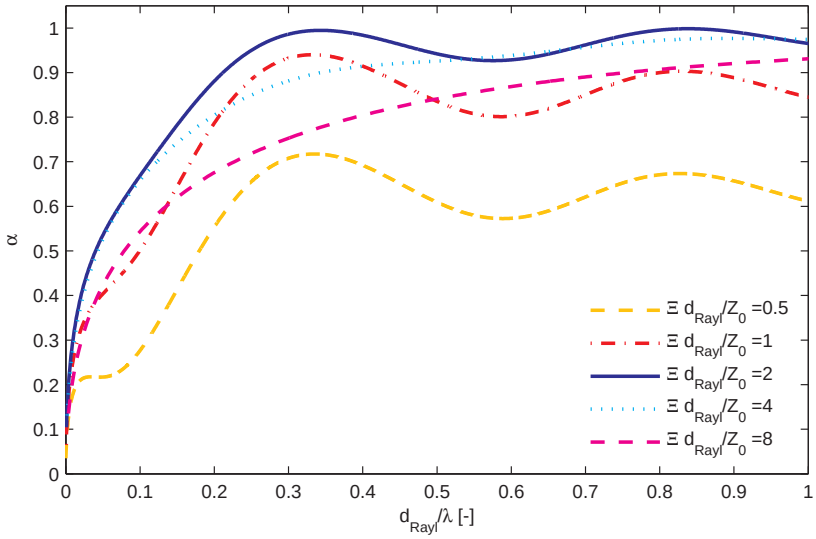

(b) *Rayleigh* model ($\kappa = 1$)

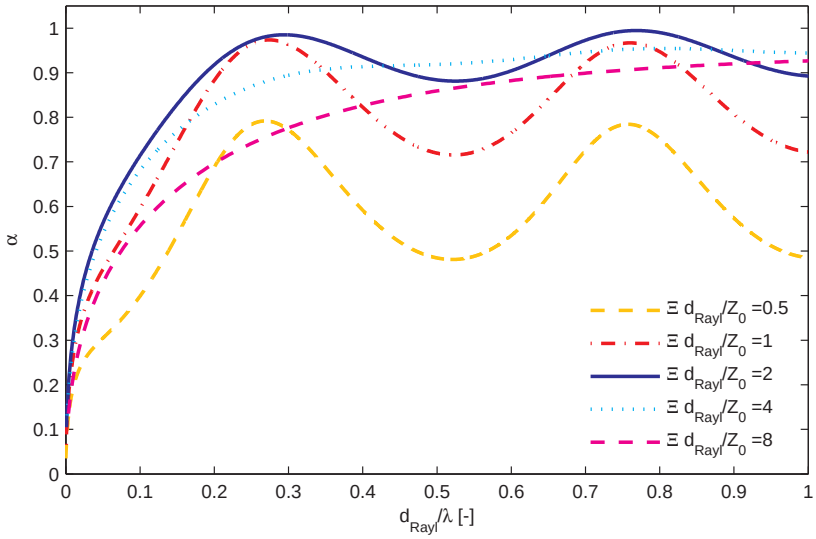

(c) *Rayleigh* model ($\kappa = 2$)

Figure 4.20: Absorption ratio α of porous layers on reflective walls for $\vartheta = 0$ and $n_g = 0.95$

The absorption ratio α is calculated out of the impedances Z with equation (4.35). The results are depicted in figure 4.20 depending on the ratio of the thickness of the layer and the wavelength in the acoustic fluid $\frac{d}{\lambda}$. The absorption ratio is, at first, increasing for increasing values of the flow resistance, because then more friction is activated between solid and fluid phase. For very high values of the flow resistance however, the sound waves are prevented from entering the porous material. The maximum values occur in both models for a thickness of the layer $\left(d > \frac{\lambda}{4}\right)$, because then the first velocity maximum of the wave is already covered by the absorber and the absorption is increasing for higher frequencies or higher ratios $\frac{d}{\lambda}$. It is also observed in both models, that the oscillations of α rise for decreasing values of the resistance. The factor, which is responsible for the extent of the oscillations in the *Rayleigh* model, is the structure factor κ. The effect is depicted in figures 4.20b and 4.20c. In the TPM-model a comparable adjusting screw does not exist. It would be possible to smooth the oscillations by specifying a macroscopic material damping loss factor η^D.

4.4.3 Elastic Plates

In this example a plate out of linear elastic material is analyzed. The basic characteristics of this system are visible in the model for the compound absorber, too. First of all the plate is modeled as a free supported system as sketched in figure 4.21. The Sommerfeld radiation condition is applied as a boundary condition in the system of linear equations (4.14). The structure is excited with waves in the acoustic fluid for varying angles of incidence, where the relation between the wavenumber and the angle of incidence is given in equation (4.28).

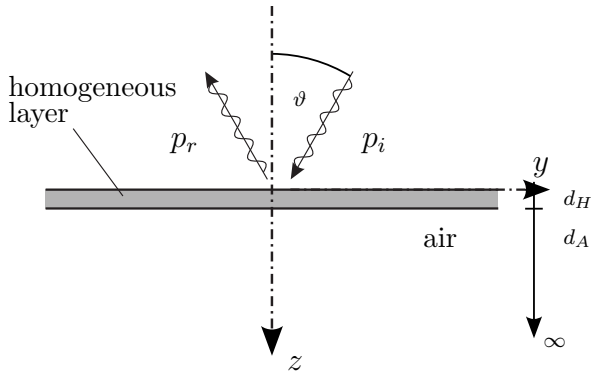

Figure 4.21: Infinite elastic layer

Having a look at the impedances and at the displacements, depicted in figure 4.22 the so called *trace matching* is observed, which is the spatial analogue of resonance [see Cremer

and Müller 1982]. This means, that the trace velocity of the exciting wave matches with the velocity of the bending waves of the plate.

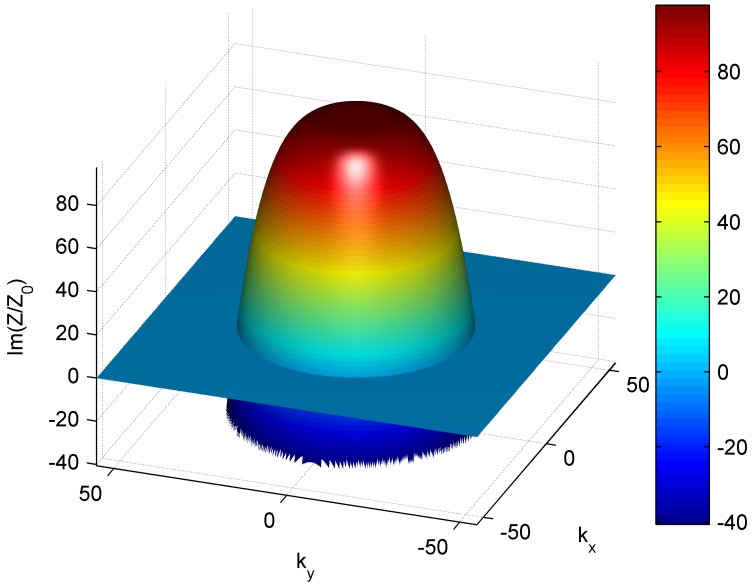

(a) imaginary part of the impedance $Z(k_x, k_y, \Omega)$ related to Z_0

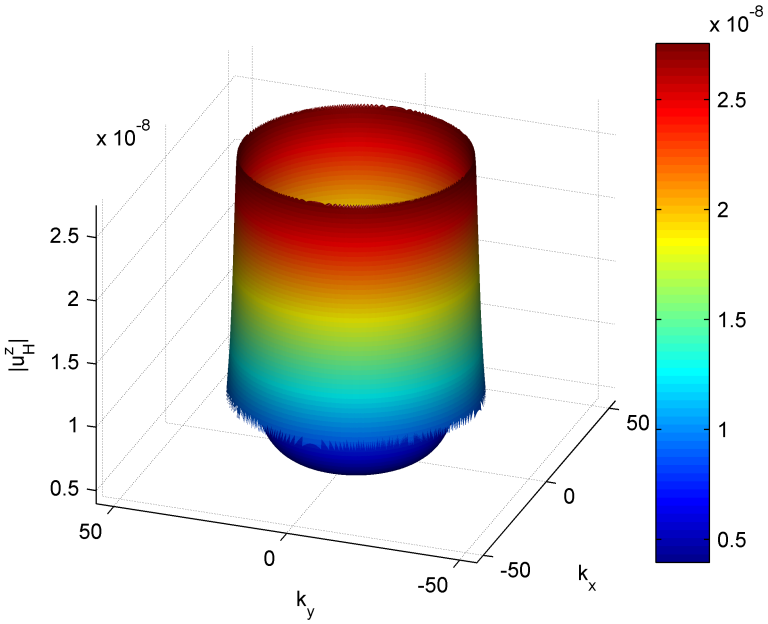

(b) transformed displacements $\hat{u}_H^z(k_x, k_y, \Omega)$

Figure 4.22: Trace matching for a frequency of $2000\,Hz$

The bending wavelength for a *Kirchhoff* plate with a thickness of $d_H = 8\,mm$, a bending

stiffness of $B' = 468.9\,Nm$ and a density of $\rho_H = 400\,\frac{kg}{m^3}$ is defined as:

$$\lambda_B = 2\,\pi \sqrt[4]{\frac{B'}{\rho_H\, d_H\, \Omega^2}} \tag{4.41}$$

This leads to a bending-wavenumber of $k_B = 32.22$ for a frequency of excitation of $2000\,Hz$, where the impedance $Z(k_x,\, k_y,\, \Omega)$ is equal to zero. There is a good agreement with the numerical results in figure 4.22.

Consequently the transformed displacements $\hat{u}_H^z(k_x,\, k_y,\, \Omega)$ tend to infinity if no damping is applied to the system. Then a total transmission of the incident wave occurs and no energy is absorbed. The results for the wavenumbers, which are linked to angles of incidence $\vartheta > 90°$ are not visualized in figure 4.22.

If a material damping factor η is defined, energy is dissipated. The absorption coefficient for this system is depicted in figure 4.24a for $\eta = 0.1$, which is quite a high value for elastic structures, used in engineering practice. Nevertheless the absorbing effect is quite poor and it is limited to a small range of wavenumber-frequency combinations. For the case of plane waves, where no bending waves are excited in the structure, an absorbing effect cannot be achieved at all.

To overcome this problem the elastic layer is mounted on an air cushion and a layer of porous material is arranged in the gap.

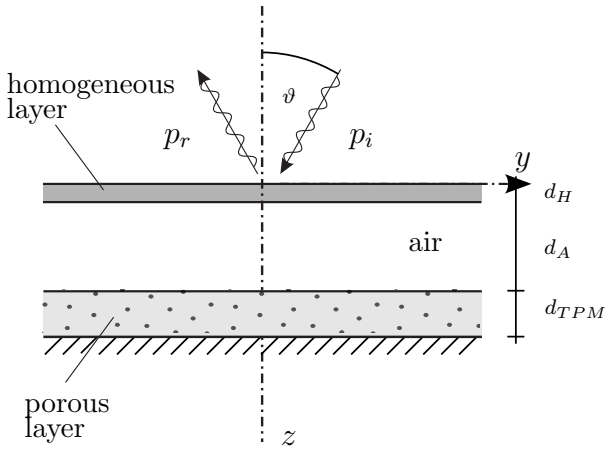

Figure 4.23: Infinite elastic layer with porous foam in the gap

Again the structure is excited with a combination of wavenumbers k_x, k_y and a circular frequency of excitation Ω, which fulfills the condition of trace matching between plate and acoustic fluid. Now, in spite of defining $\eta = 0$, a considerable amount of energy is dissipated

due to the absorber, as depicted in figure 4.24b, because the porous foam already observes a high absorptance in this frequency range.

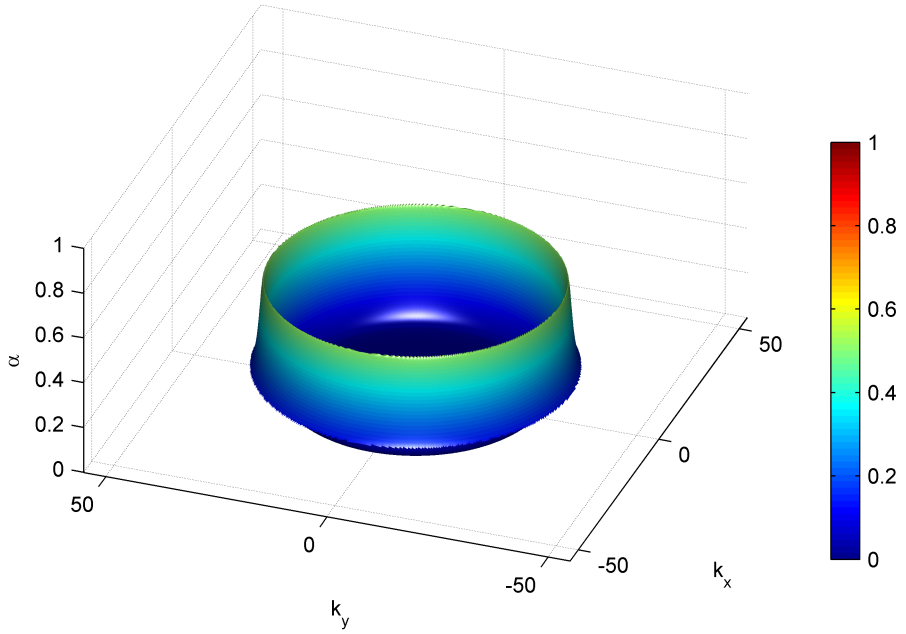

(a) without absorptive layer

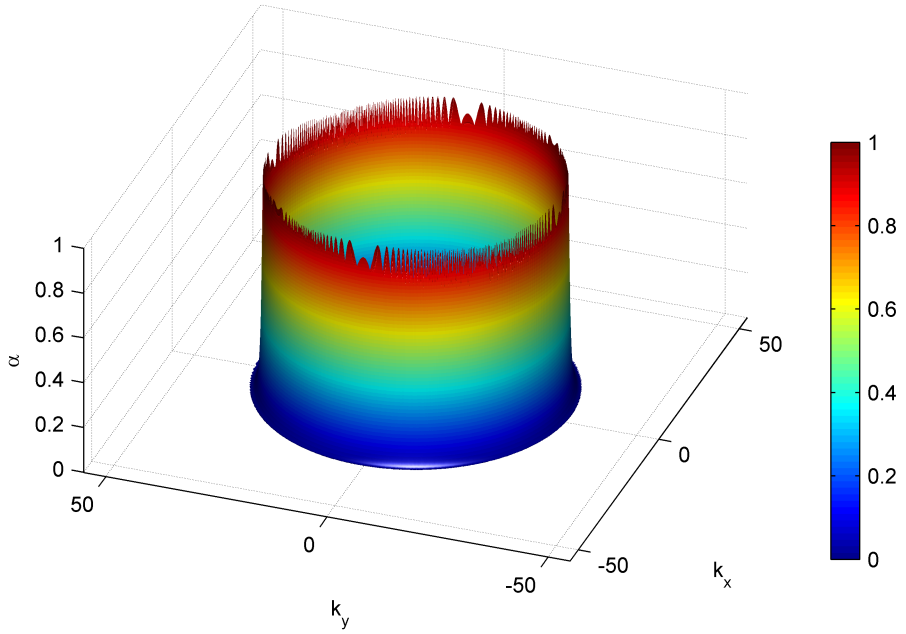

(b) with a $10.0\,cm$ layer of Melamine Foam

Figure 4.24: Absorption coefficient α at a frequency of excitation of $2000\,Hz$

4.4.4 Air Cushions in Front of Porous Sheets

The efficiency of porous absorbers is linked with the ratio of the velocity of the sound field in the cavity and the velocity within the layer, because the dissipation of energy is based on the difference velocity between solid and gas in the pores and the flow resistance (compare section 2.1.4). A possibility to take influence on the frequency-dependent characteristics is to mount the absorber on a layer of air to synchronize the location of the porous material and the peaks in the velocity field.

In the following the system of a porous layer with a thickness of $d_{TPM} = 10\,cm$ and a gap of $d_A = 10\,cm$ is compared with the porous layer without gap (figure 4.25). Plane waves are considered as well as waves of oblique incidence ($\vartheta = \frac{\pi}{4}$).

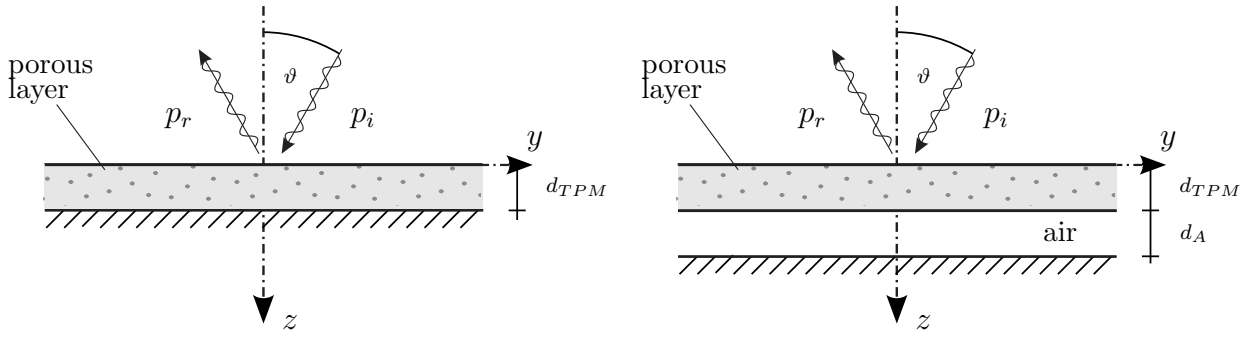

(a) without gap **(b)** with gap

Figure 4.25: Infinite porous layer

The same comparison was published by Allard [2009] using a theory, where a foam with a very high porosity is modeled with an equivalent fluid model based on the laws of Delany and Bazley [1970]. They did measurements for fibrous materials with a porosity close to 1 for large frequency ranges and established empirical equations for the complex wavenumber k and the characteristic impedance Z_c:

$$Z_c = \rho_A c_A \left(1 + \ 0.057 \left(\frac{\rho_A \Omega}{2\pi \Xi}\right)^{-0.754} - \ i\, 0.087 \left(\frac{\rho_A \Omega}{2\pi \Xi}\right)^{-0.732}\right) \tag{4.42}$$

$$k = \ \frac{\Omega}{c_A}\left(1 + 0.0978 \left(\frac{\rho_A \Omega}{2\pi \Xi}\right)^{-0.700} - \ i\, 0.189 \left(\frac{\rho_A \Omega}{2\pi \Xi}\right)^{-0.595}\right) \tag{4.43}$$

The model is similar to the *Rayleigh* model, discussed in section 4.4.2, with the difference, that it is based on measurement results instead of a structural model. It is valid for $0.01 < \frac{\rho_A \Omega}{2\pi \Xi} < 1.0$ and it can be used for a rough estimation of the acoustic characteristics of a porous material, but of course the quality of the results, predicted with such simple models is limited.

In the following a highly porous foam ($n_G = 0.94$) is modeled with the Theory of Porous Media assuming identical geometrical conditions and frequency bands as published in [Allard 2009, chapters 2.6 and 3.6]. Figures 4.26 and 4.27 show the a comparison of the impedances $Z(\Omega)$ for system with and without the gap applying waves of plane and oblique incidence respectively.

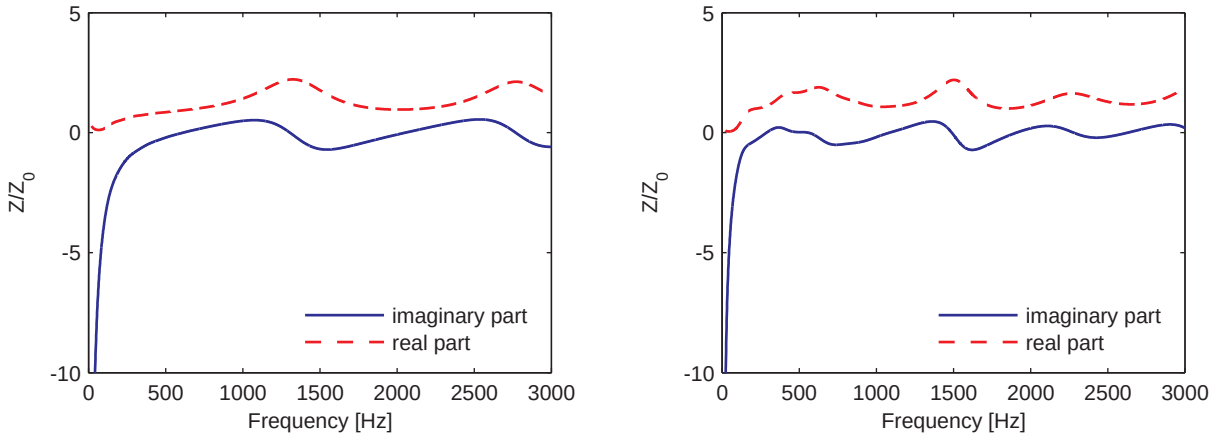

(a) without gap **(b)** with gap

Figure 4.26: Plane wave impedance $\frac{1}{Z_0} Z(k_x = 0,\, k_y = 0,\, \Omega)$ with $d_{TPM} = 10\,cm$, $d_A = 10\,cm$

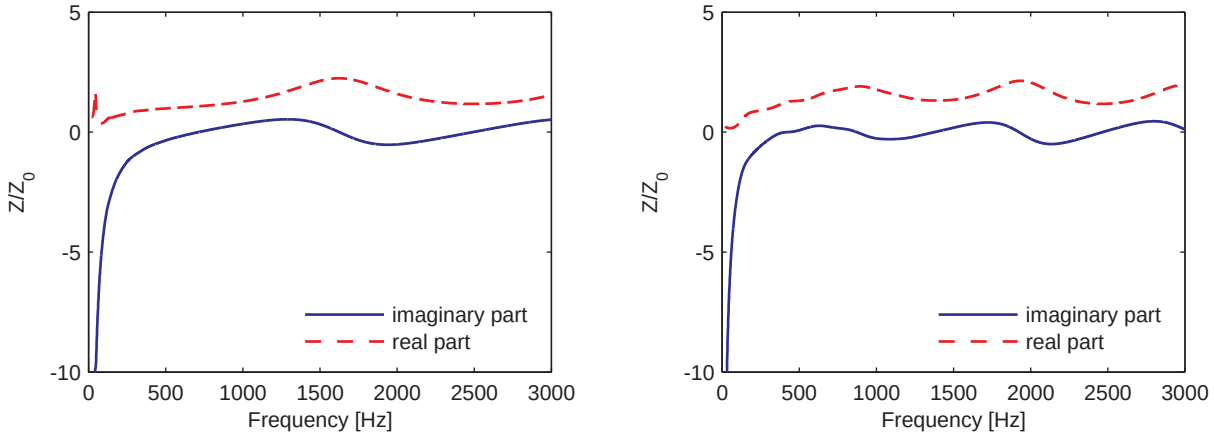

(a) without gap **(b)** with gap

Figure 4.27: Impedance ratio $\frac{1}{Z_0} Z(k_x = 0,\, k_y,\, \Omega)$ at oblique incidence $\vartheta = \frac{\pi}{4}$ with $d_{TPM} = 10\,cm$, $d_A = 10\,cm$

The results for the foam without gap for plane waves are comparable with the simulated impedances for a $10.3\,cm$ layer of mineral wool in section 4.4.1 as well as with the corresponding measurement results in the impedance tube.

The angle of incidence $\vartheta = \frac{\pi}{4}$ for the model underlying figure 4.27 is specified tuning the wavenumber k_y ($k_x = 0$) with respect to the circular frequency of excitation Ω according to equation (4.28) and the absorption ratio $\alpha(k_x = 0,\, k_y,\, \Omega)$ is computed out of the impedances $Z(k_x = 0,\, k_y,\, \Omega)$ with (4.35). The results are depicted in figure 4.28.

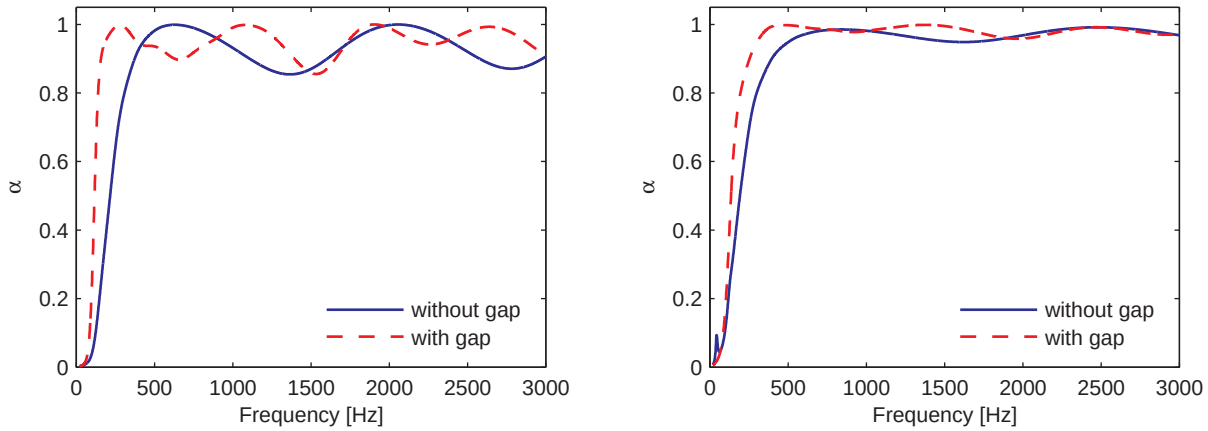

(a) $\vartheta = 0$ **(b)** $\vartheta = \frac{\pi}{4}$

Figure 4.28: Absorption coefficient $\alpha(k_x = 0,\, k_y,\, \Omega)$ – Comparison of plane waves and oblique incidence $\vartheta = \frac{\pi}{4}$ with $d_{TPM} = 10\,cm$, $d_A = 10\,cm$

The characteristics of the results are in a good accordance the results, published by Allard [2009], where however a detailed specification of the absorber is not given. One observes, that the gap is responsible for a faster increase of α for low frequencies. The maximum values in case of plane waves are linked to frequencies, where multiples of one half of the wavelength fit to the geometry of the absorptive layer, whereas in case of local minima of the absorption ratio multiples of the wavelength fit into the absorber. The serial connection with the layer of air yields a higher modal density in the discussed frequency band, which leads to an increasing amount of local extrema of α.

For oblique incidence the oscillations of the absorption ratio are less significant and the differences due to the gap are less intensive in the frequency band of the steep incline up to $500\,Hz$.

The method based on the Theory of Porous Media is able to capture the characteristics of porous materials in acoustics and agrees with common simplified models as well as with measurement results. More intensive studies concerning changes in the material parameters of the constituent parts of the absorber are done in the next sections.

4.4.5 Characteristics of Compound Absorbers

In the previous sections the ITM-based model was compared against measurements and simple numerical models, which are widely used in practice. The comparisons were presented for plane waves or for defined angles of incidence. Now the simulations are carried out varying both, the frequency of excitation and the angle of incidence in wide ranges.

The influence of changing acoustic parameters on the properties of the porous foam is discussed as well as the effects, which occur while combining individual acoustic components for models of compound absorbers.

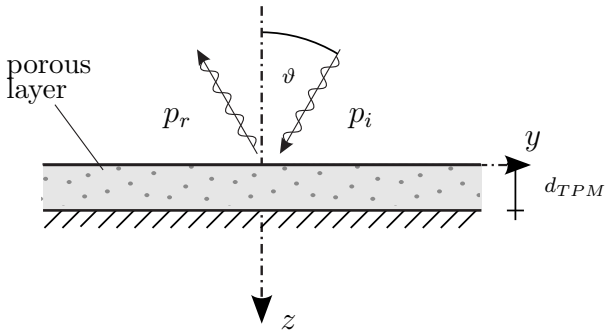

Figure 4.29: Infinite porous layer

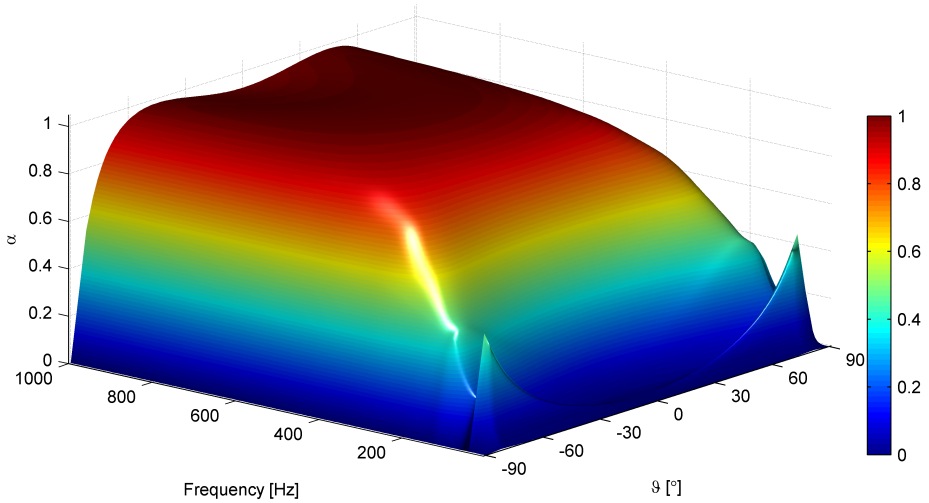

Figure 4.30: Porous layer - varying frequencies of excitation and angles of incidence

Results for the simple porous layer, sketched in figure 4.29 are presented in a 3D plot (figure 4.30) as well as for specific angles of incidence.

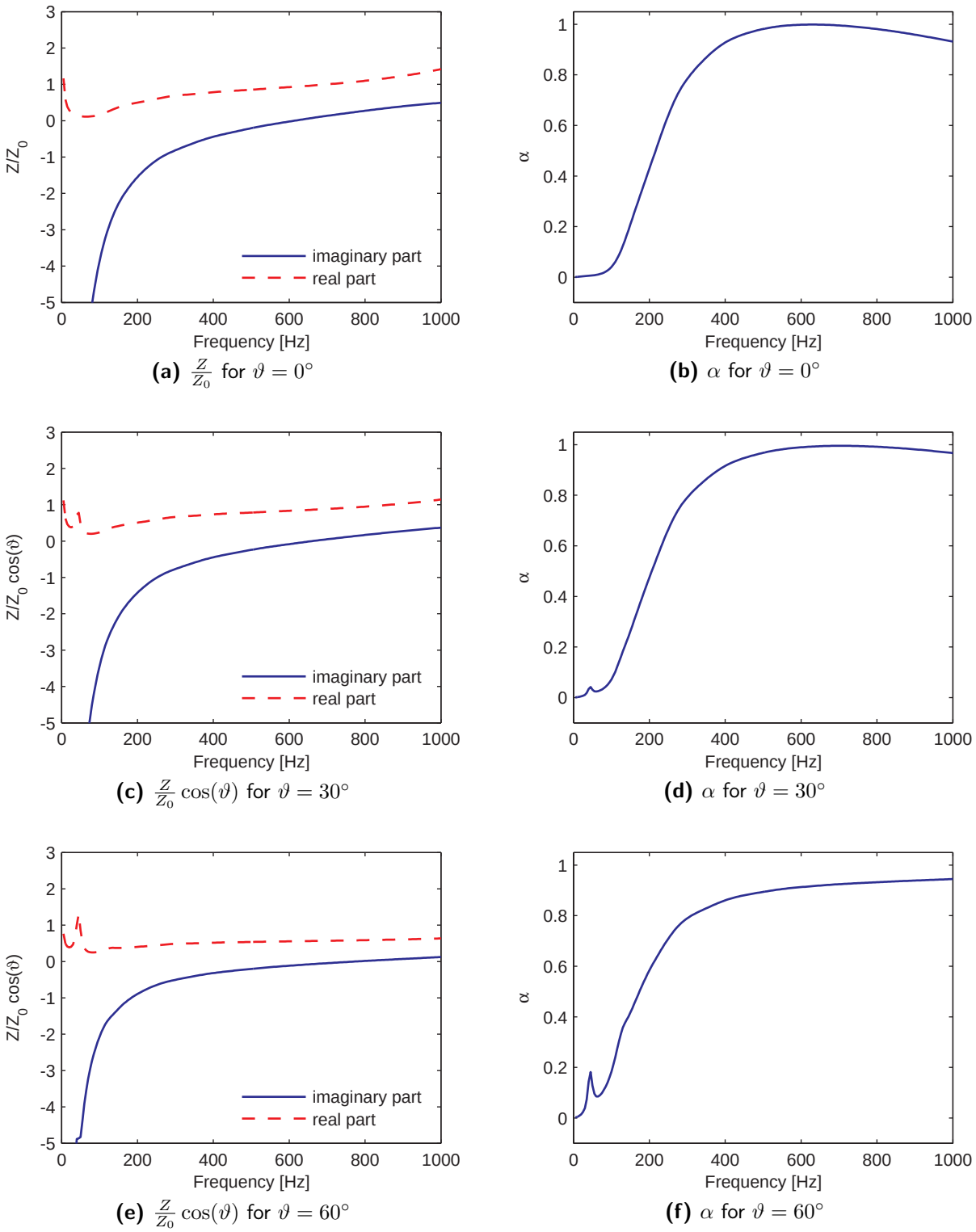

(a) $\frac{Z}{Z_0}$ for $\vartheta = 0°$ **(b)** α for $\vartheta = 0°$

(c) $\frac{Z}{Z_0}\cos(\vartheta)$ for $\vartheta = 30°$ **(d)** α for $\vartheta = 30°$

(e) $\frac{Z}{Z_0}\cos(\vartheta)$ for $\vartheta = 60°$ **(f)** α for $\vartheta = 60°$

Figure 4.31: Varying frequencies of excitation for constant angles of incidence

In figure 4.31 the ratio of the impedances $\frac{Z}{Z_0}$ and the corresponding absorption ratio α are depicted for the frequencies up to $1\,kHz$ for $\vartheta = 0°, 30°, 60°$. One observes the same characteristics as mentioned in section 4.4.1, where a comparison with measurement results was presented. As one can see in equation (4.35) the maximum absorption ratio $\alpha = 1$ is gained, if the imaginary part of the impedance vanishes and the real part of $\frac{Z}{Z_0}\cos(\vartheta) = 1$. The porous material depicted in figure 4.31 does not significantly absorb energy in the low frequency range. For increasing angles of incidence however local maxima are observed in the low frequency range for α, because of maxima in the real part of the impedance. Thus the differences of the measured data and the simulated data, mentioned in section 4.4.1, can be explained. Due to effects of resonance, occurring at the side walls of the impedance tube, waves of oblique incidence are obtained in the sound field of the measurement setup, which lead to peaks in the real parts of the impedance Z as one observes in figures 4.12, 4.14 and 4.16.

Porous materials are characterized by sets of parameters. In the simple *Rayleigh* model for example [see Möser 2007] only a few parameters are necessary to set up the system. One of the most important constants is the flow resistance Ξ (compare section 2.1.4). Amongst others Möser [2007] defines the range of Ξ, which is interesting for applications in acoustics, between $5\,Rayl/cm < \Xi < 100\,Rayl/cm$. In figures 4.33 and 4.34 the absorption ratio of a porous layer is sketched, where the flow resistance was varied. One observes, that the optimum ratio is about $5 - 10\,Rayl/cm$ for the chosen material. Defining very small values for Ξ leads to oscillations in Z and thus also in α, as one can see in figures 4.32a and 4.33a. Choosing very high values for Ξ, the sound wave is precluded from entering the porous foam and considerable impedance-maxima are observed between two resonances, resulting in a very inhomogeneous absorption efficiency (compare figures 4.32b and 4.34c).

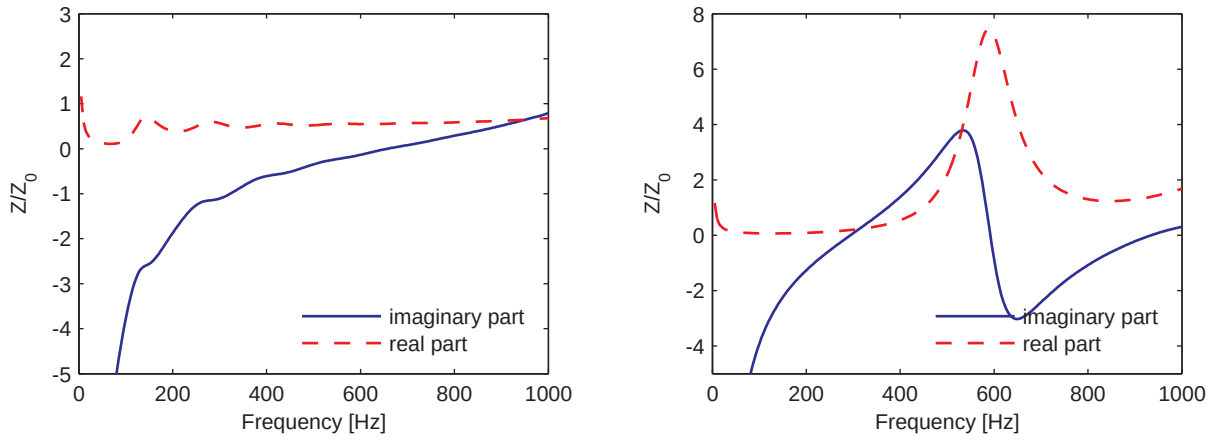

(a) $\Xi = 1\,\frac{\text{Rayl}}{\text{cm}}$ **(b)** $\Xi = 100\,\frac{\text{Rayl}}{\text{cm}}$

Figure 4.32: Impedance ratio $\frac{Z}{Z_0}$ for plane waves $\vartheta = 0°$ for inappropriate values of Ξ

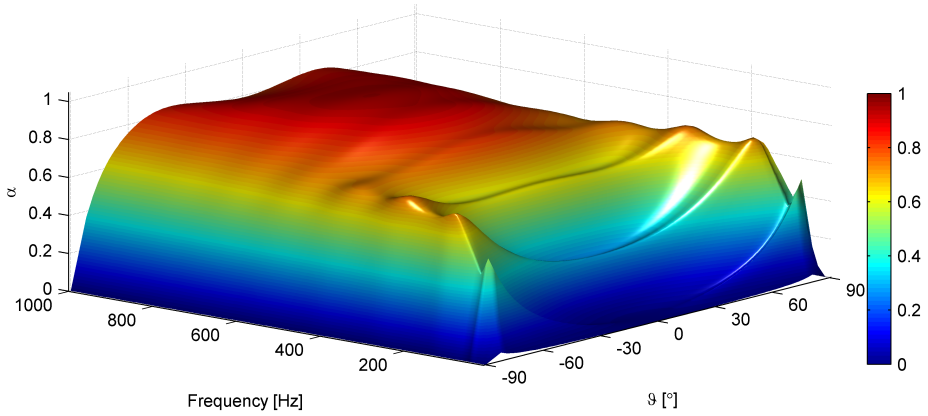

(a) $\Xi = 1 \frac{\text{Rayl}}{\text{cm}}$

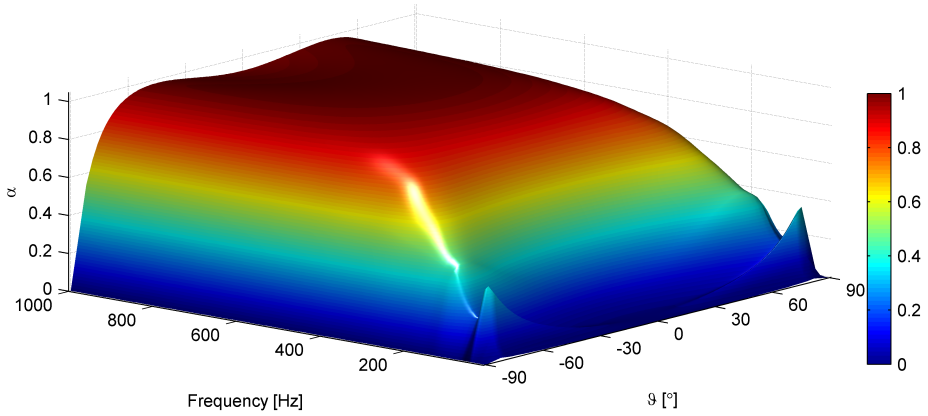

(b) $\Xi = 5 \frac{\text{Rayl}}{\text{cm}}$

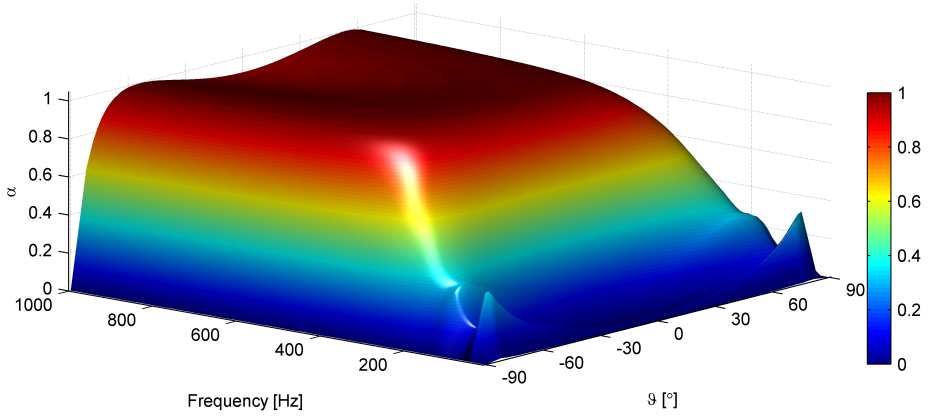

(c) $\Xi = 10 \frac{\text{Rayl}}{\text{cm}}$

Figure 4.33: Varying the flow resistance α of a $10.0\,cm$ porous layer

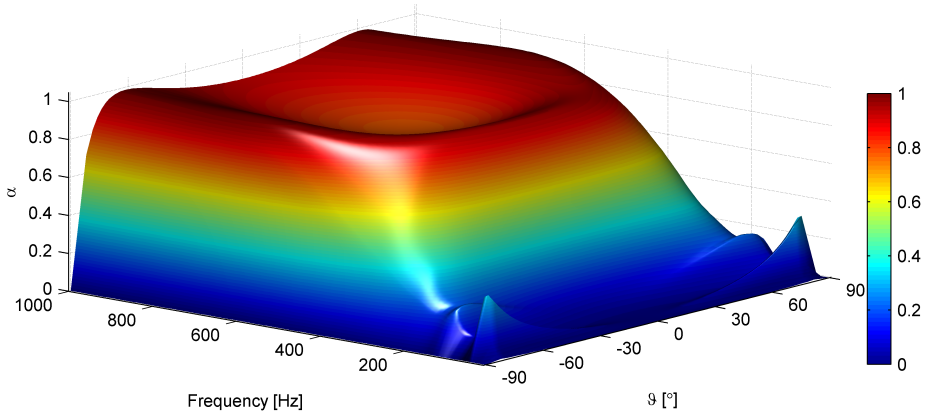

(a) $\Xi = 30\ \frac{\text{Rayl}}{\text{cm}}$

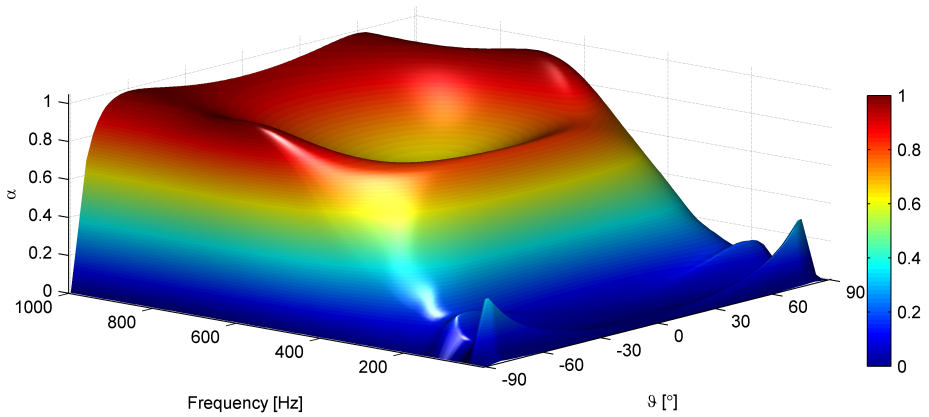

(b) $\Xi = 50\ \frac{\text{Rayl}}{\text{cm}}$

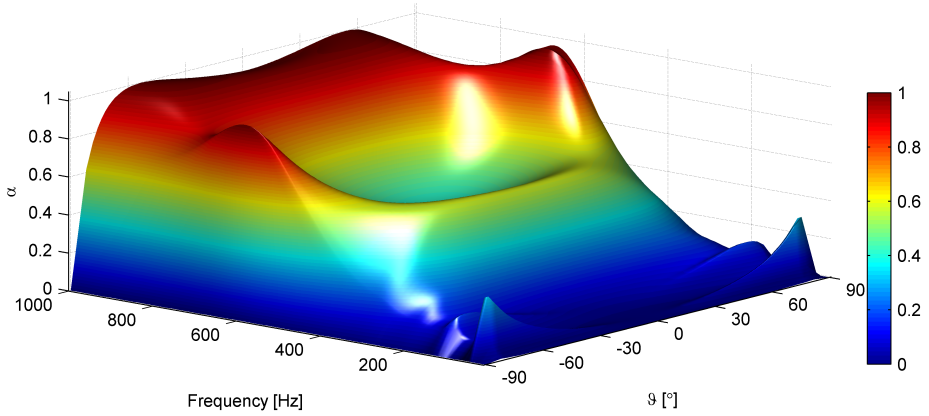

(c) $\Xi = 100\ \frac{\text{Rayl}}{\text{cm}}$

Figure 4.34: Varying the flow resistance α of a $10.0\,cm$ porous layer

The influence of air cushions behind thin porous layers, which increase the absorption ratio α in the low frequency range, was discussed in section 4.4.4 for selected angles of incidence. The simulation for oblique incidence is presented in figure 4.36 for the porous layer, which was used in the last examples in combination with an air cushion of a thickness $d_A = 10\,cm$.

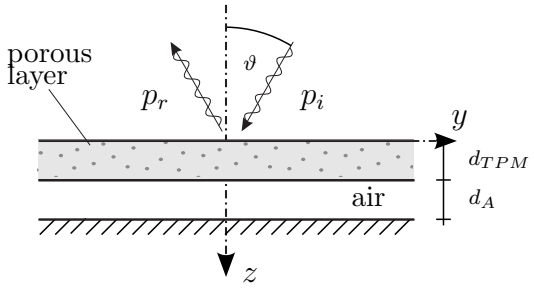

Figure 4.35: Infinite porous layer on air cushion

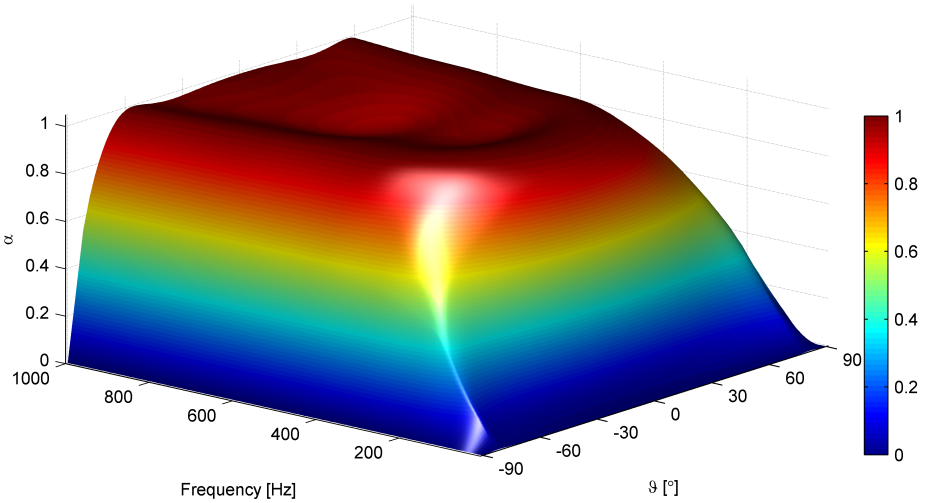

Figure 4.36: Porous layer on an air cushion - varying frequencies of excitation and angles of incidence

In order to affect different ranges of frequencies while optimizing the acoustic properties of rooms, various components are combined and act as compound absorbers. Porous layers can be coupled with elastic plates, which act as resonators, for instance. These resonators work mainly in their mass-spring resonance. Considering arbitrary angles of incidence, also effects at other frequencies are observed due to the trace matching properties, which were discussed in section 4.4.3. In the compound absorber the porous layer can be installed in the air cushion in order to dissipate if the plate is acting in resonance. A more efficient setup

can be achieved if the porous layer is coupled with the acoustic volume due to arrays of slits and holes. Such perforated plates cannot be built up in the model, derived in this work.

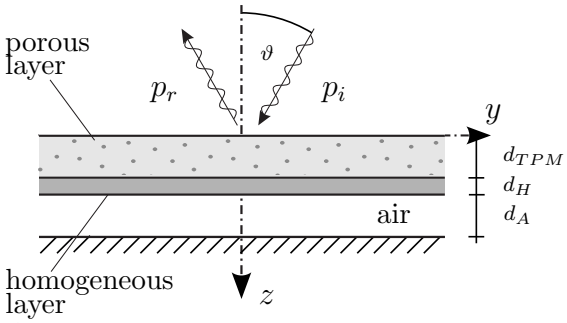

Figure 4.37: Infinite porous layer on elastic layer and air cushion

In order to model this effect anyhow, the porous layer is installed on an elastic layer (see figure 4.37), which is modeled as a wooden plate with a thickness of $d_H = 8\,mm$ in the following example.

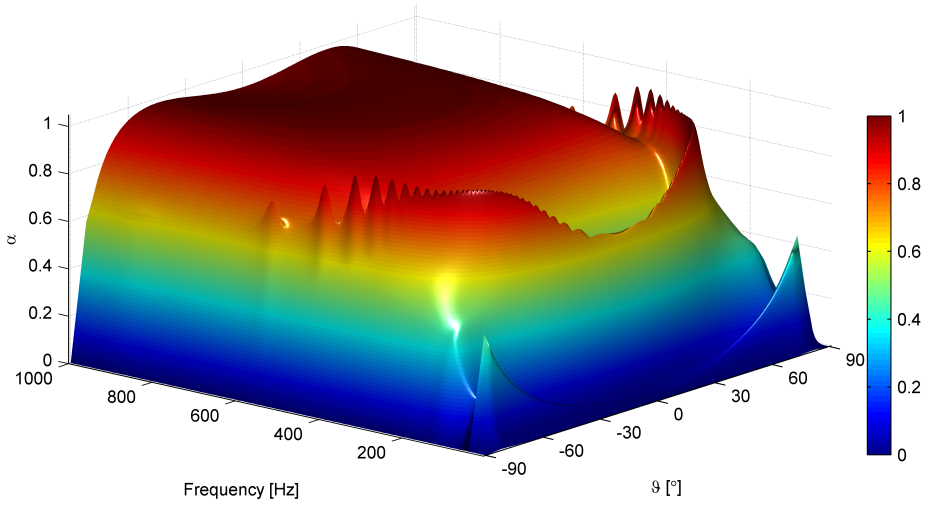

Figure 4.38: Porous layer on elastic layer and air cushion - varying frequencies of excitation and angles of incidence

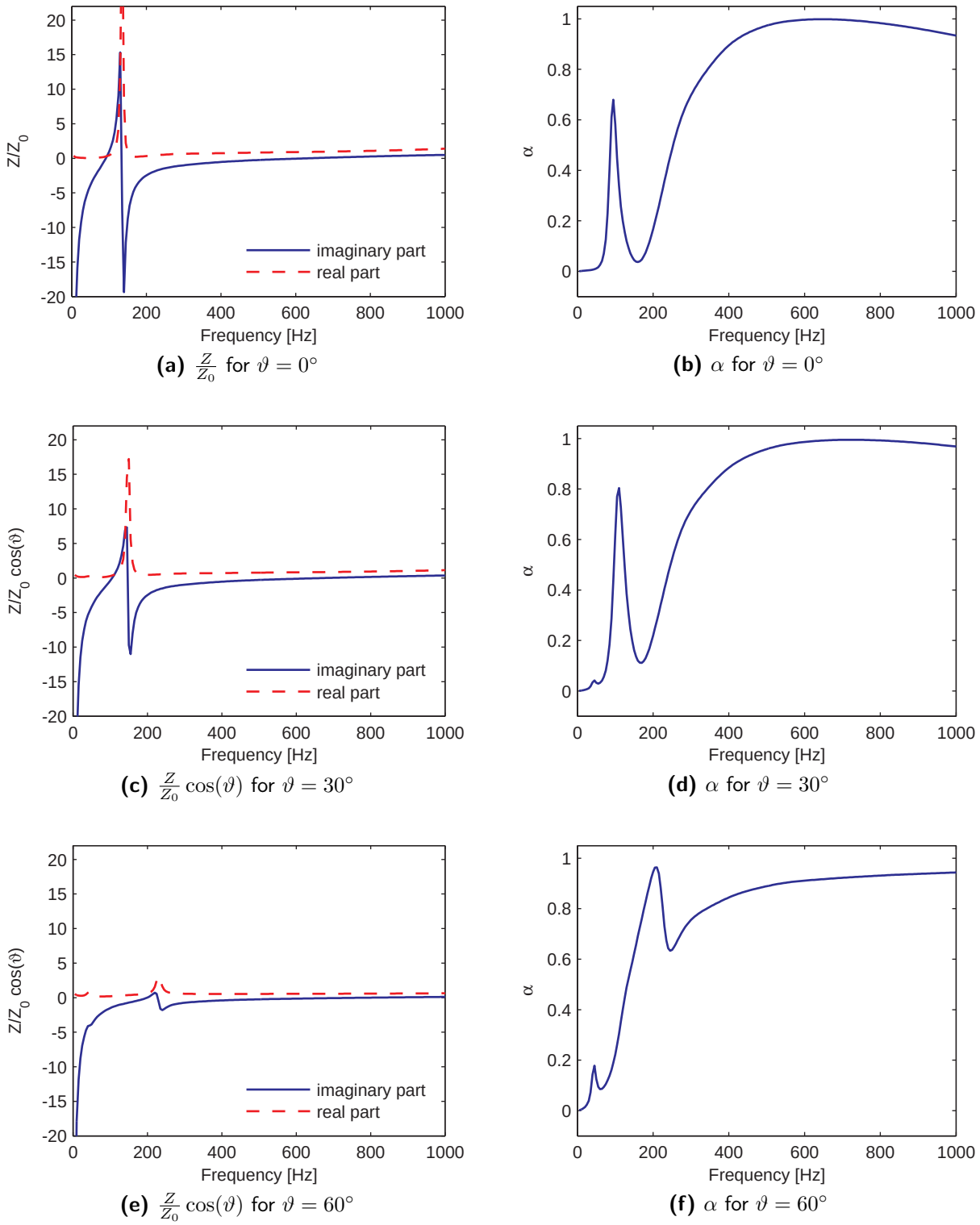

(a) $\frac{Z}{Z_0}$ for $\vartheta = 0°$ **(b)** α for $\vartheta = 0°$

(c) $\frac{Z}{Z_0}\cos(\vartheta)$ for $\vartheta = 30°$ **(d)** α for $\vartheta = 30°$

(e) $\frac{Z}{Z_0}\cos(\vartheta)$ for $\vartheta = 60°$ **(f)** α for $\vartheta = 60°$

Figure 4.39: Varying frequencies of excitation for constant angles of incidence

In figures 4.38 and 4.39 the absorption efficiency is sketched in the usual way. Besides the already known typical properties of the porous layer, the mechanical characteristics of the

elastic plate on a layer of air, which are the mass-spring resonance for $\vartheta = 0$ and the bending resonances for oblique incidence can be recognized in the results.

The mass-spring resonance of this system can be changed by varying the stiffness of the air cushion for instance. If it is raised by decreasing the thickness of the layer from $d_A = 10\,cm$ to $d_A = 5\,cm$ for example, an increase of the the mass-spring resonance is observed (figures 4.40 and 4.42).

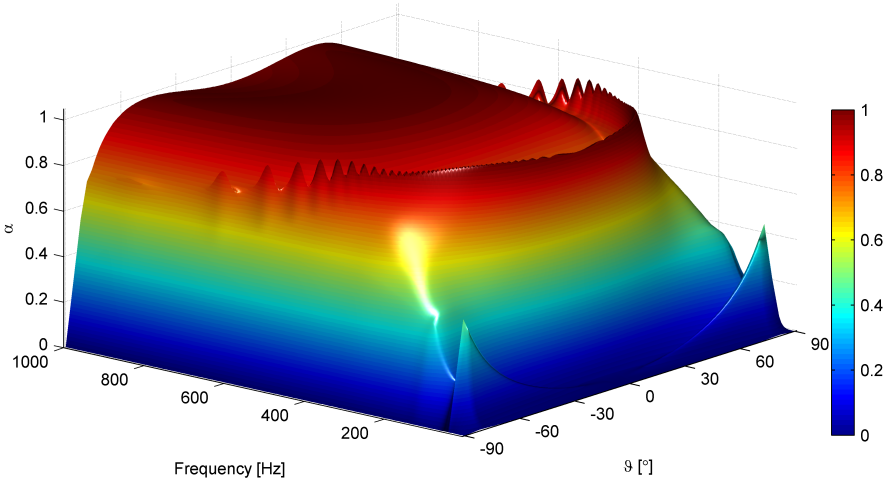

Figure 4.40: Porous layer on elastic layer and air cushion – tuning the stiffness of the elastic layer

One could also vary the mass of the elastic layer by changing the density ρ_H for instance. A shift towards lower frequencies is achieved by rising ρ_H. Figures 4.41 and 4.43 result out of a change from $\rho_H = 400\frac{kg}{m^3}$ to $\rho_H = 800\frac{kg}{m^3}$.

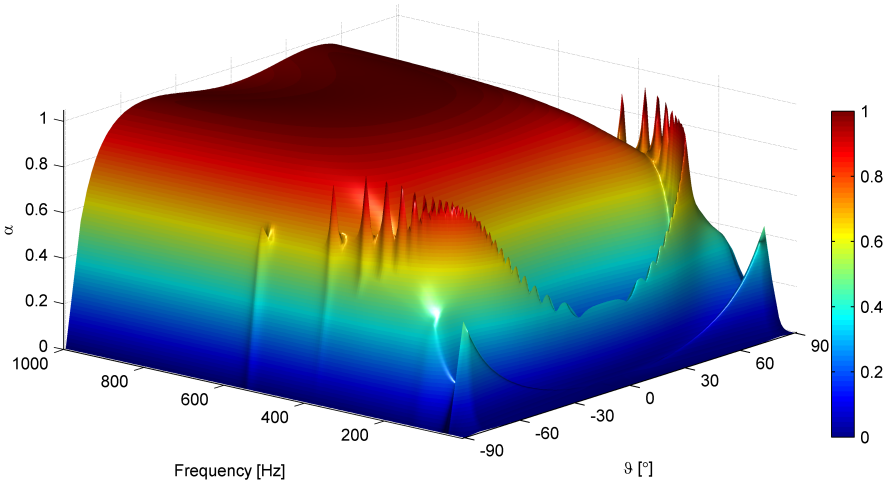

Figure 4.41: Porous layer on elastic layer and air cushion – tuning the density of the elastic layer

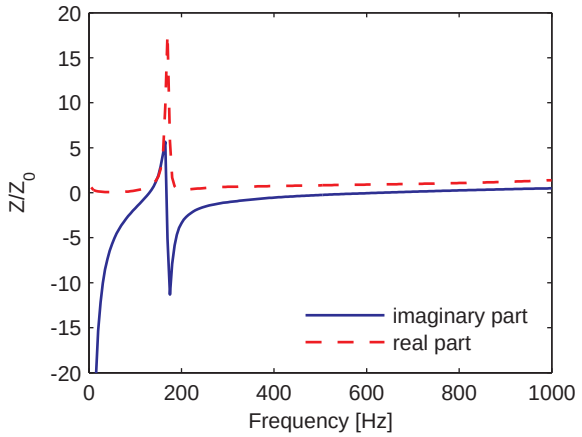

(a) $\frac{Z}{Z_0}$ for $\vartheta = 0°$

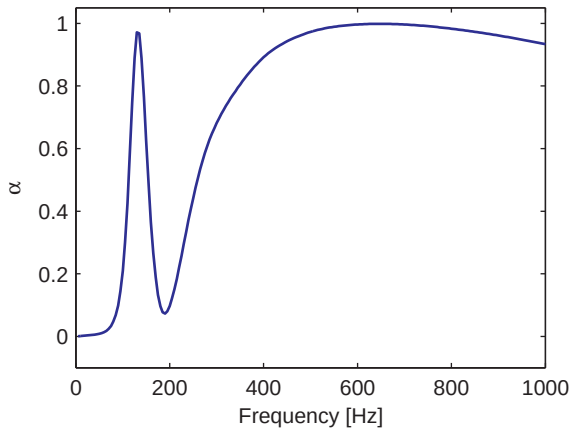

(b) α for $\vartheta = 0°$

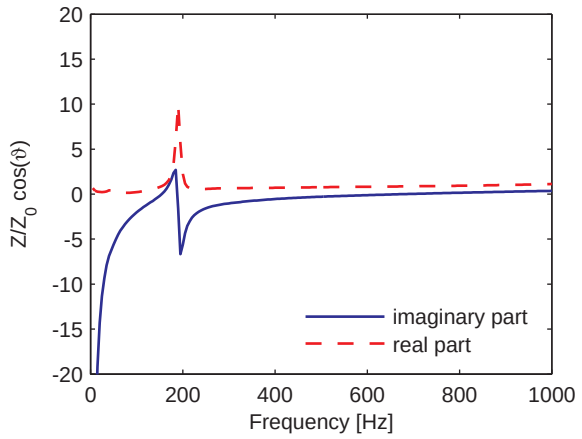

(c) $\frac{Z}{Z_0}\cos(\vartheta)$ for $\vartheta = 30°$

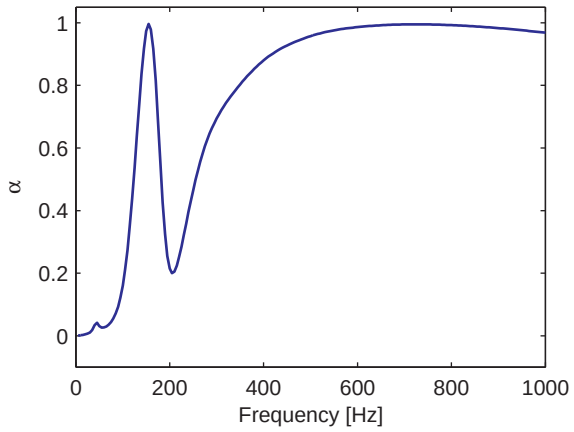

(d) α for $\vartheta = 30°$

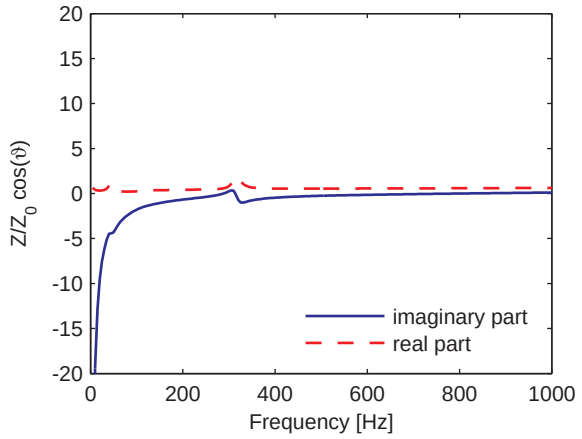

(e) $\frac{Z}{Z_0}\cos(\vartheta)$ for $\vartheta = 60°$

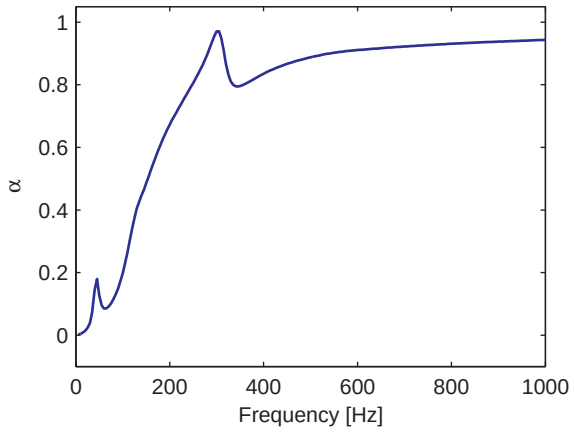

(f) α for $\vartheta = 60°$

Figure 4.42: Porous layer on elastic layer and air cushion – tuning the stiffness of the elastic layer and varying frequencies of excitation for constant angles of incidence

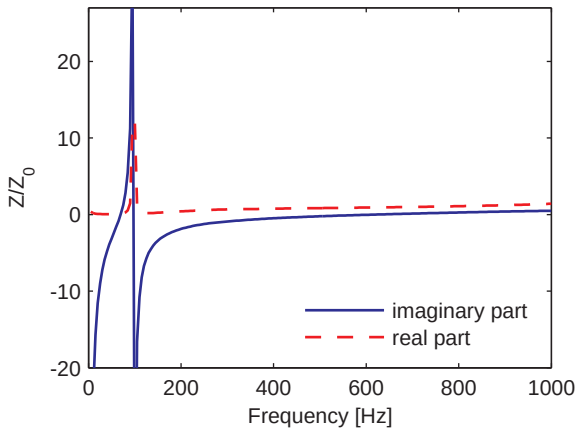

(a) $\frac{Z}{Z_0}$ for $\vartheta = 0°$

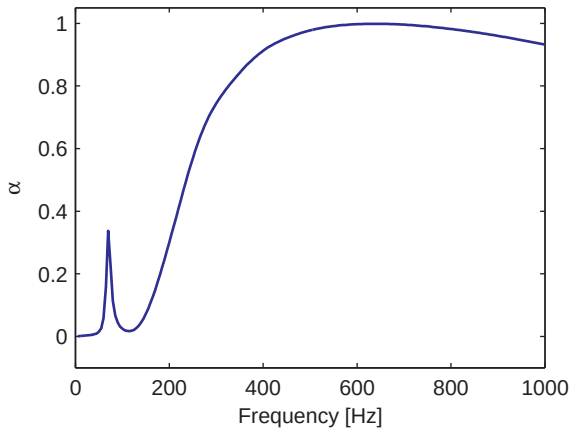

(b) α for $\vartheta = 0°$

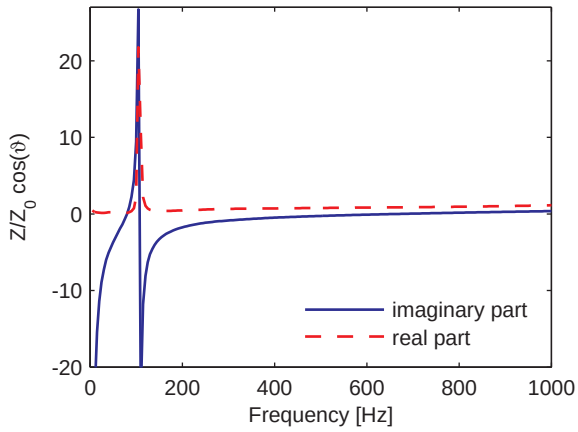

(c) $\frac{Z}{Z_0}\cos(\vartheta)$ for $\vartheta = 30°$

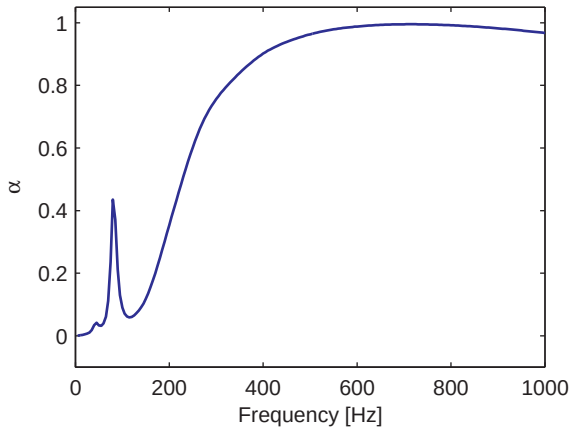

(d) α for $\vartheta = 30°$

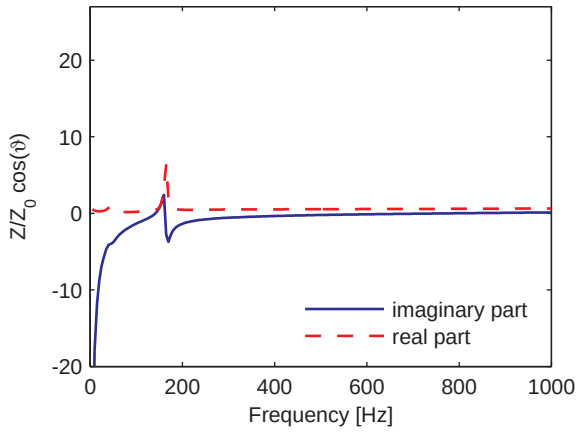

(e) $\frac{Z}{Z_0}\cos(\vartheta)$ for $\vartheta = 60°$

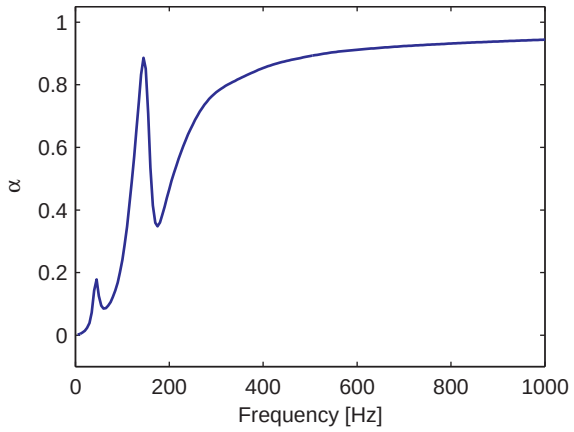

(f) α for $\vartheta = 60°$

Figure 4.43: Porous layer on elastic layer and air cushion – tuning the density of the elastic layer and varying frequencies of excitation for constant angles of incidence

Whereas due to changes of the thickness d_A of the air cushion in weakly coupled systems

just the mass-spring resonance of the system is affected, the latter modification has a major effect. According to equation (4.41) changes in the density or the stiffness of the elastic layer have an impact on the wavelength and therefore on the trace matching as well.

In order to illustrate this effect, two different models are used. A porous foam mounted on an elastic layer with a thickness of $d_H = 8\,mm$ and a layer of air with $d_A = 5\,cm$ (system 4.44a) is compared to a foam between two of these elastic layers (system 4.44b), where the acoustic fluid is not coupled to the porous foam and absorption just happens in case of trace matching.

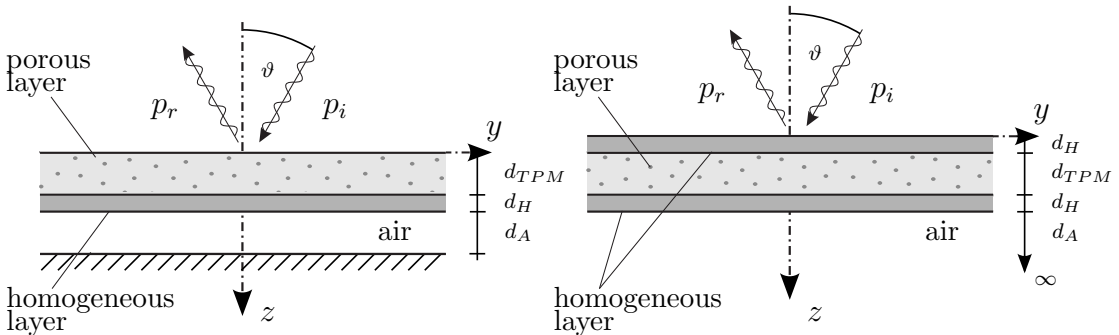

(a) Porous foam on elastic layer

(b) Porous foam between two elastic layers

Figure 4.44: Study on trace matching properties – system

The absorption ratio is computed for both models up to a frequency of $3\,kHz$, where the *Young*'s modulus is varied between $E_h = 1 \cdot 10^{10} \frac{N}{m^2}$ and $E_h = 1 \cdot 10^{12} \frac{N}{m^2}$.

In figure 4.45c the locus of the points, which fulfill the trace matching condition, because the trace velocity of the exciting wave matches with the velocity of the bending waves of the plate (compare section 4.4.3), is clearly visible starting from the coincidence frequency of ca $1590\,Hz$. This dispersion curve is also observed in figure 4.45b, whereas the porous characteristics dominate the result for higher frequencies.

The effect becomes more visible if higher values for the *Young*'s modulus E_h are defined, where the trace matching occurs for smaller angles ϑ. In figures 4.46b and 4.47b one observes clearly the transition from the mass-spring resonance for plane waves ($\vartheta = 0$) to the dispersion curve.

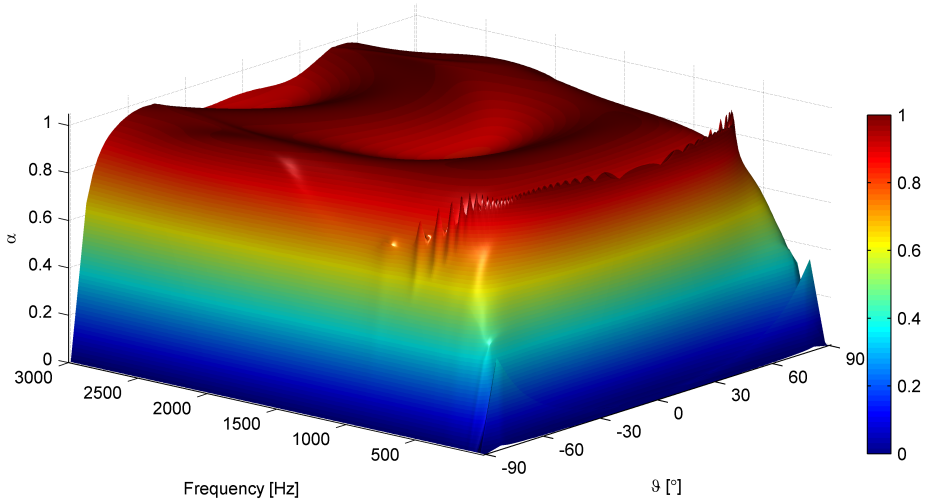

(a) Porous foam on elastic layer (compare figure 4.44a)

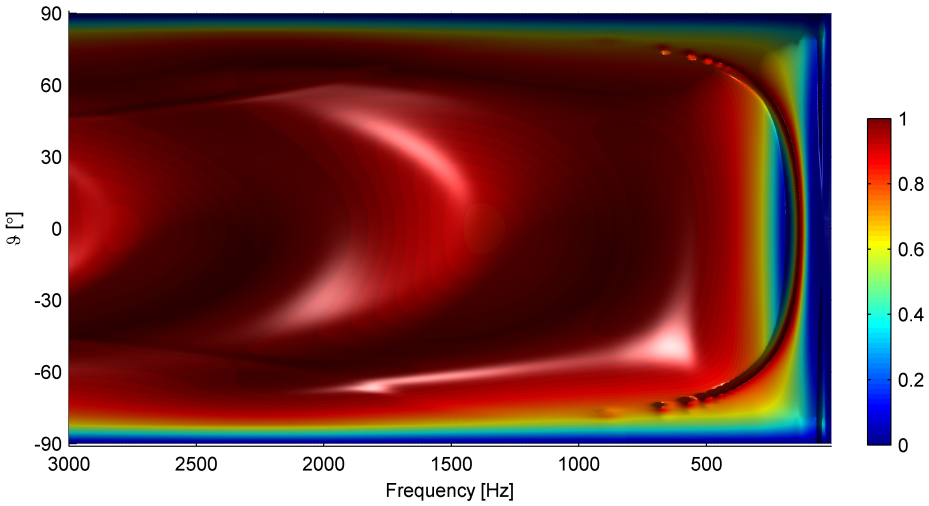

(b) Porous foam on elastic layer (compare figure 4.44a)

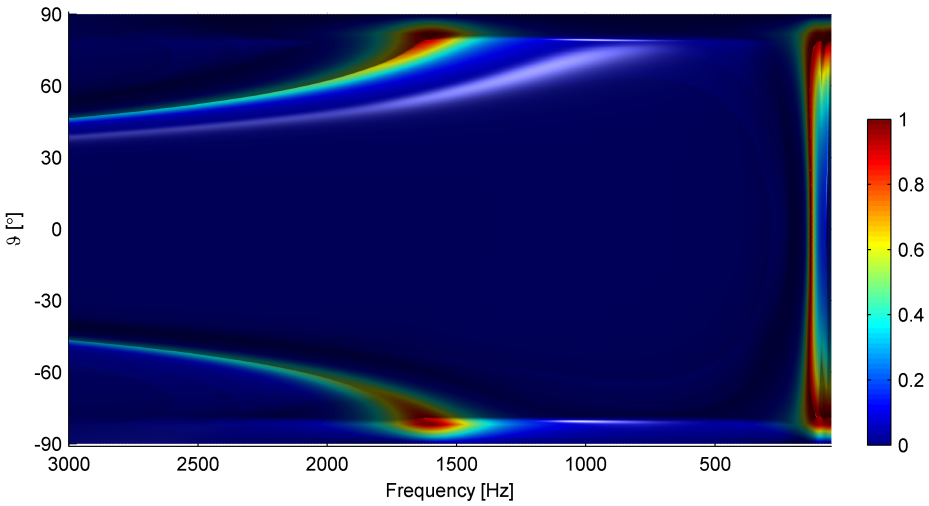

(c) Porous foam between two elastic layers (compare figure 4.44b)

Figure 4.45: Study on trace matching properties (dispersion diagram) – *Young*'s modulus $E_h = 10^{10}\frac{N}{m^2}$

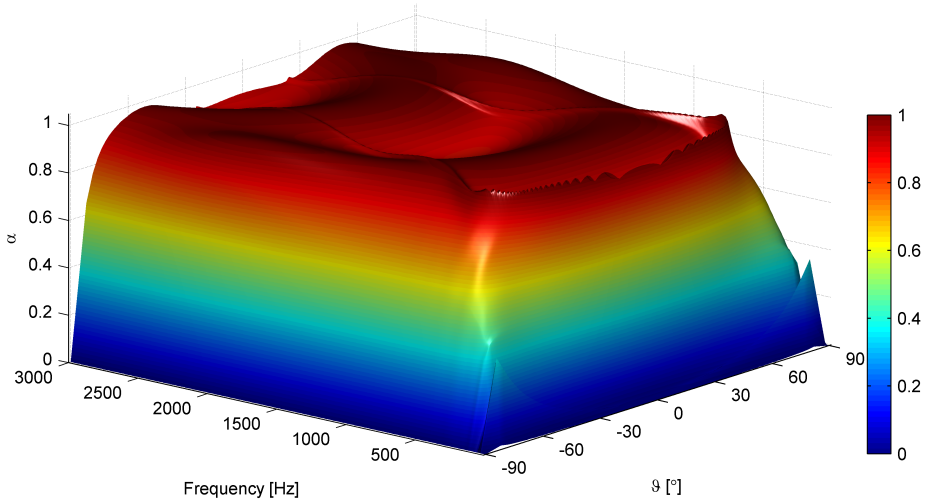

(a) Porous foam on elastic layer (compare figure 4.44a)

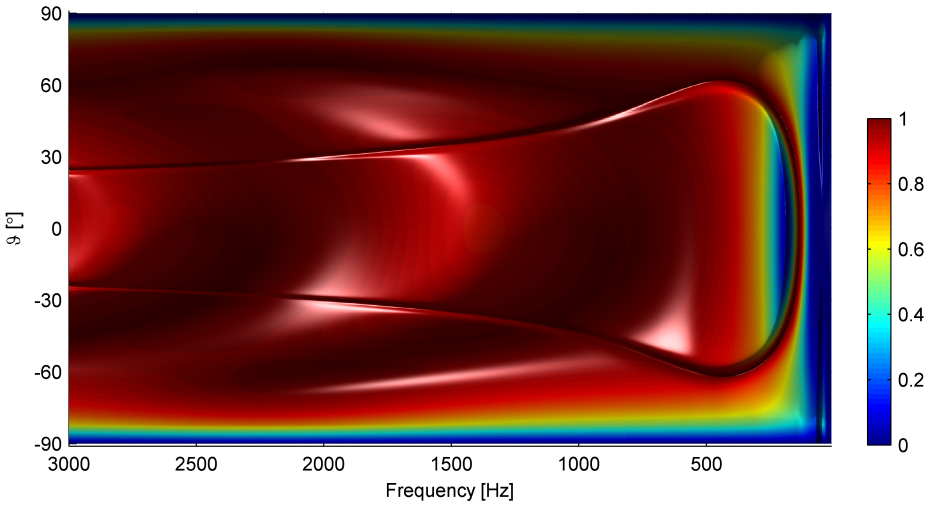

(b) Porous foam on elastic layer (compare figure 4.44a)

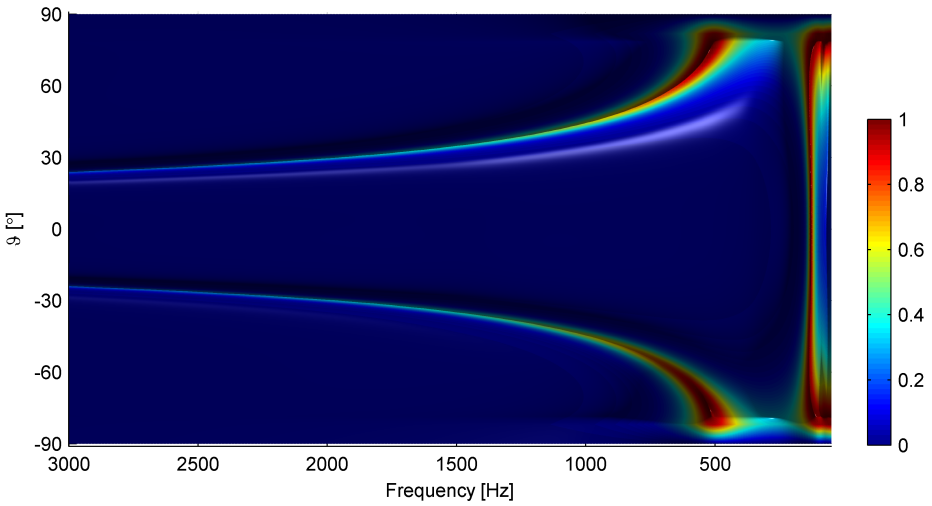

(c) Porous foam between two elastic layers (compare figure 4.44b)

Figure 4.46: Study on trace matching properties (dispersion diagram) – *Young*'s modulus $E_h = 10^{11} \frac{N}{m^2}$

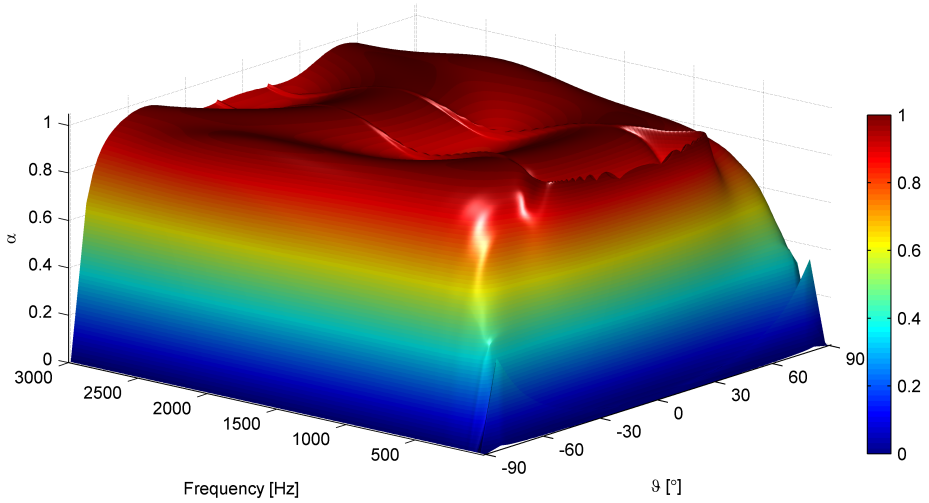

(a) Porous foam on elastic layer (compare figure 4.44a)

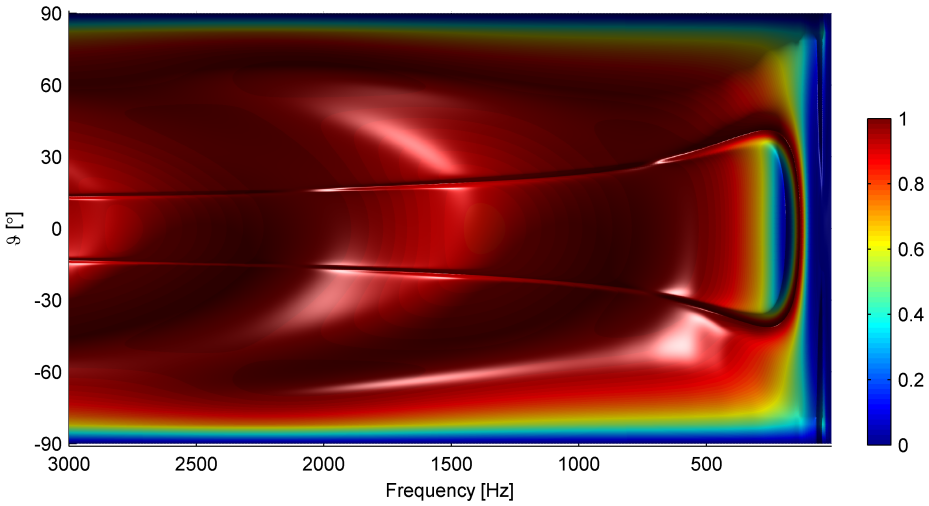

(b) Porous foam on elastic layer (compare figure 4.44a)

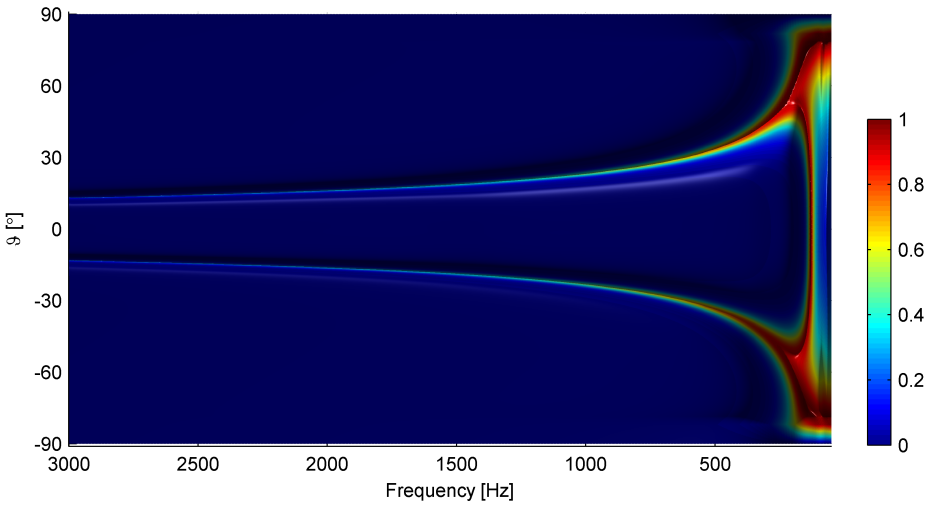

(c) Porous foam between two elastic layers (compare figure 4.44b)

Figure 4.47: Study on trace matching properties (dispersion diagram) – *Young*'s modulus $E_h = 10^{12} \frac{N}{m^2}$

In table 4.5 the material parameters and the geometry are specified for the examples, which were presented in the last sections.

			4.17	4.21	4.23	4.25a	4.25b	4.29	4.35	4.37	4.44a	4.44b
porous layer	n_G	$[-]$	var	–	0.94							
	ρ_s	$\left[\frac{kg}{m^3}\right]$	3.2	–	7.0							
	E_s	$\left[\frac{N}{m^2}\right]$	$5\,10^3$	–	$5\,10^3$							
	ν_s	$[-]$	0.05	–	0.05							
	ρ_g	$\left[\frac{kg}{m^3}\right]$	1.2	–	1.2							
	Ξ	$\left[\frac{\text{Rayl}}{\text{cm}}\right]$	var	–	6	5						
	d_{TPM}	$[cm]$	var	–	10							
elastic layer	ρ_H	$\left[\frac{kg}{m^3}\right]$	–	8.0		–	–	–	–	8.0		
	E_H	$\left[\frac{N}{m^2}\right]$	–	$1 \cdot 10^{10}$		–	–	–	–	$1 \cdot 10^{10}$		
	ν_H	$[-]$	–	0.3		–	–	–	–	0.3		
	d_H	$[mm]$	–	8		–	–	–	–	8		
air	d_A	$[cm]$	–	–	20	–	10	–	10	10	5	–

Table 4.5: Parameters for the compound absorber

5 Fluid Structure Interaction

In the next step the method for the fluid structure interaction (FSI) is derived for coupling the acoustic fluid and the boundary structures. As stated by Fahy [2007] for coupled systems impedance concepts are advantageous in case of simple systems, because they are efficient and refer to variables, which can directly be measured.

For applications in practice models for geometrical complex acoustical volumes coupled with finite plate absorbers have to be provided. Figure 5.1 specifies the FSI-problem underlaying this thesis. The acoustic volume is covered either by rigid walls or by flexible structures like compound absorbers. The structure is loaded by point sources. Excitations due to vibrating surfaces could be built up too.

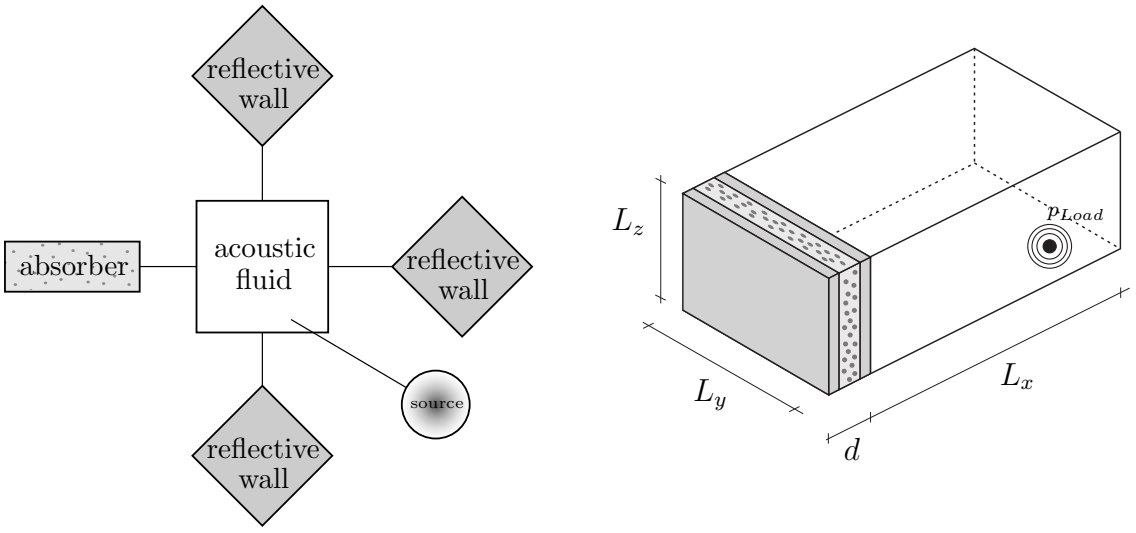

(a) Network Scheme **(b)** System

Figure 5.1: FSI-problem

For these systems analytic solutions, based on impedance models for example, are quite labor-intensive or even impossible. Therefore often variational methods like the FEM or the BEM are used, which lead to elegant expressions and allow an accurate prediction of the systems response [see e.g. Fahy 2007]. Existing Finite element formulations for the coupled

problem have to deal with huge numbers of unknowns, on the one hand side because of the three dimensional model of the acoustic fluid [see e.g. Fahy 2000] and on the other hand side because of the fact, that the porous foam has to be built up in the model of the absorber. Thus the velocity of both, the solid and the fluid component, and also the pore pressure have to be considered as state variables in the finite element description. In order to reduce this number of unknowns, impedance approaches can be used. Considering only plane wave impedances [see e.g. Larbi et al. 2009] the influence of different angles of incidence on the absorber cannot be captured.

In the scope of this work an idea for the FSI-coupling is pursued, which combines the advantages of impedance formulations and variational methods. Thus complex problems can be tackled with a reduced number of unknowns and a strict link to physical and measurable quantities. It is most variable concerning the aspects, which were mentioned above, applying the *Rayleigh-Ritz* method for the coupled problem. Therefore the most suitable discrete method for the description of the fluid, which could be the classic FEM or the Spectral Finite Element Method (SFEM) for example can be applied. The SFEM is convenient to deal with smooth solutions for acoustic problems in order to receive spectral convergence [see Pospiech et al. 2009; Pospiech 2011; Trefethen 2000]. Due to a strong coupling between fluid and absorber the approach could also be applied in case of liquids and flexible boundaries. An efficient semi analytical wavenumber dependent impedance formulation, which takes the angles of incidence of the sound waves into account, is implemented in the Ritz approach for plate-like compound absorbers, but also measured impedances could be used in this approach.

5.1 Hamilton's Principle and Rayleigh-Ritz Approach

For problems of practical significance, which are very often complex concerning geometry and material data, the equilibrium conditions for the FSI-problem cannot be fulfilled in a strong form. In a weak formulation the differential equations and the boundary conditions are considered implicitly in an integral expression [see Fahy 2007] and equilibrium is fulfilled in an averaged way. The principle of virtual work is known as *Lagrange-D'Alembert*-principle for vibrating continuum structures and considers the virtual work of the inertia forces $\delta W_{Inertia}$ in addition to the virtual strain energy δW_{Strain} for dynamic systems. Also external sound sources and internal damping effects are considered via their virtual work δW_{Load} and δW_{Damp}. For calculating the virtual work a virtual displacement δw is applied, while the time t is assumed to be frozen until the system reached the virtual position. The

Lagrange-D'Alembert-principle states, that

$$\delta W_{\text{Inertia}} + \delta W_{\text{Strain}} + \delta W_{\text{Damp}} + \delta W_{\text{Load}} = 0. \tag{5.1}$$

According to Wauer [2008] the fundamental variational principle of dynamics (*Hamilton*'s principle) can be obtained out of the *Lagrange-D'Alembert*-principle restricting the virtual displacements δw to result out of the displacements w by applying a variation δ and expressing the virtual work of the inertia forces $\delta W_{\text{Inertia}}$ as the variation δT of the kinetic energy T of the system. In elastodynamics a potential description is possible for the strain energy, and the virtual strain energy δW_{Strain} can be formulated as the variation δU of the potential energy U.

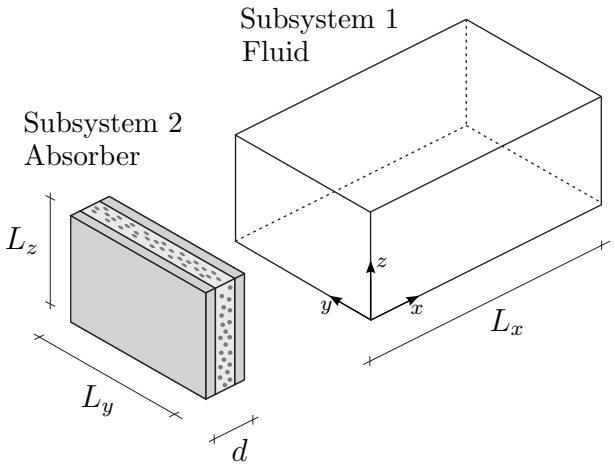

Figure 5.2: Subsystem definition

For the vibro-acoustical problem in this thesis a description, which is based on velocities, is preferred. The structure is divided into substructures (see figure 5.2), where the acoustic fluid and the boundary conditions are defined as subsystems respectively. According to *Hamilton*'s principle equilibrium is fulfilled by the velocity field, which meets the kinematic boundary conditions, the conditions at $t = t_1$ and $t = t_2$ and, in addition to that, satisfies

$$\int_{t_1}^{t_2} \delta\Big(L_A(t) + L_{\text{BC}}(t, Z) + \mathbf{R}^T \boldsymbol{\lambda}(t)\Big) + \delta W^{\text{nc}}_{\text{BC}}(t, Z) + \delta W^{\text{nc}}_{\text{Load}}(t)\, dt = 0. \tag{5.2}$$

In equation (5.2) δ specifies the first variation [see Elsgolc 2007] and L denotes the Lagrangian of a subsystem, which is defined for the air as the acoustic fluid as

$$L_A(t) = T_A(t) - U_A(t). \tag{5.3}$$

The kinetic energy T_A and the potential energy U_A are computed out of the state variables velocity and pressure

$$T_A(t) = \frac{\rho_A}{2} \int_V |\mathbf{v}_A(\mathbf{x},t)|^2 dV, \quad (5.4) \qquad U_A(t) = \frac{1}{2\rho_A c_A^2} \int_V |p_A(\mathbf{x},t)|^2 dV, \quad (5.5)$$

where ρ_A and c_A denote the density and the speed of sound for the acoustic fluid.

As mentioned above, non-conservative forces W^{nc}, for which a potential description is not possible, are introduced in *Hamilton*'s principle with their virtual work δW^{nc}. The virtual work of the sound source in the acoustic fluid is obtained as:

$$\delta W^{\mathrm{nc}}_{\mathrm{Load}}(t) = \int_{A_{\mathrm{Load}}} p_{\mathrm{Load}}(\mathbf{x},t)\, \mathbf{n}_{\mathrm{Load}}(\mathbf{x})\, \delta\mathbf{w}(\mathbf{x},t)\, dA \quad (5.6)$$

In equation (5.6) $\delta\mathbf{w}(\mathbf{x},t)$ is the function of the virtual displacement and $\mathbf{n}_{\mathrm{Load}}$ is the normal vector, defined with respect to the surface of the sound-source A_{Load}.

The calculation of the Lagrangian $L_{\mathrm{BC}}(t,Z)$ and the virtual work of the dissipation forces $\delta W^{\mathrm{nc}}_{\mathrm{BC}}(t,Z)$ for the absorptive boundary conditions are derived in section 5.3 using the impedance Z, modeled in section 4.

The kinematic coupling of the subsystems is considered in equation (5.2) as a constraint, where $\boldsymbol{\lambda}$ is the vector of *Lagrange* multipliers. It states, that these components of the velocity of the air in the acoustic cavity and the velocity at the absorber, which are perpendicular to the interface have to match.

In order to overcome the problem of solving the *Euler-Lagrange* equations resulting out of (5.2), a *Rayleigh-Ritz* approach is applied, where the state variables are approximated by a series of functions in space (see sections 5.2 and 5.3). Then the unknowns consist of a finite number of time-dependent functions and the task of solving partial differential equations is reduced to the solution of differential equations in time. In the scope of this thesis the focus is laid on Harmonic Analyses for steady-state solutions. Thus the variational problem in equation (5.2) can be reduced to a minimization problem and results in a system of linear equations.

5.2 Component Mode Synthesis

The Component Mode Synthesis is a substructuring technique for large coupled problems, which was introduced by Hurty [1960, 1965] to reduce the number of unknowns while keeping the physical characteristics of the structure. Further important improvements were done for example by Craig and Bampton [1968] and Craig and Chang [1976]. The structure is decomposed into individual components, where each component is described in the FEM with a set of basis functions consisting of normal modes and coupling modes. The normal modes result out of the eigenvalue problem for the component, defining either fixed or free interface boundary conditions. The coupling modes are the static solutions for unit displacements (constraint modes) or unit forces (attachment modes) at the interface nodes in the classical CMS methods. An overview of common CMS schemes as well as an application to room acoustical problems is presented by Hinke [2008] and Sremcevic [2011] for example.

The CMS, as well as the Guyan reduction [Guyan 1965] and modal reduction method, can be assigned to the *Rayleigh-Ritz* methods with certain *Ritz* basis vectors [see Hinke 2008; Sunar 2004]. This idea is picked up in this thesis for the definition of the test function used in the *Ritz* approach.

In order to approximate the steady state response of an acoustic volume (see figure 5.2) under a harmonic sound source the following approach is used in the *Ritz* method:

$$\mathbf{v}_A(\mathbf{x},t) \approx \sum_{m=1}^{m_{\max}} \mathbf{v}_m^N(\mathbf{x}) \left(\mathcal{A}_m e^{i\Omega t} + \overline{\mathcal{A}}_m e^{-i\Omega t}\right) + \sum_{n=1}^{n_{\max}} \mathbf{v}_n^C(\mathbf{x}) \left(\mathcal{B}_n e^{i\Omega t} + \overline{\mathcal{B}}_n e^{-i\Omega t}\right) \tag{5.7}$$

In equation (5.7) the velocity field is approximated by a linear combination of $m_{\max}$ normal modes $\mathbf{v}_m^N(\mathbf{x})$ and $n_{\max}$ coupling modes $\mathbf{v}_n^C(\mathbf{x})$. By the help of the conjugate complex quantities $\mathcal{A}$, $\overline{\mathcal{A}}$ and $\mathcal{B}$, $\overline{\mathcal{B}}$ the vibrations are specified with amplitudes and phase shifts. The model reduction is done by truncating the number of normal and coupling modes. The maximum number of modes, which has to be considered, depends on the related frequency of excitation and on the modal density of the system as well as on the geometry of the absorber in case of the coupling modes. The approximated velocity field converges with increasing the number of normal and coupling modes.

For the computation of the normal and the coupling modes, which is carried out in sections 5.2.1 and 5.2.2, the velocity potential $\Phi_A(\mathbf{x},t)$ is introduced:

$$\mathbf{v}_A(\mathbf{x},t) = \operatorname{grad} \Phi_A(\mathbf{x},t) \tag{5.8}$$

Whereas scalar and vector potentials were formulated for the displacement fields of the constituents of the absorber in chapter 2 and chapter 3, Φ_A refers to the scalar potential of the velocity field $\mathbf{v}_A$ for the acoustic volume. It has to fulfill the wave equation, introduced in section 3.2, which reads in a potential formulation:

$$\Delta\Phi_A(\mathbf{x},t) - \frac{1}{c_A^2}\frac{\partial^2\Phi_A(\mathbf{x},t)}{\partial t^2} = 0 \tag{5.9}$$

The time-variable t is transformed into the frequency domain ($t \circ\!\!-\!\!\bullet\ \omega$). This leads to the *Helmholtz* equation for the transformed velocity potential $\hat{\Phi}_A(\mathbf{x},\omega)$:

$$\Delta\hat{\Phi}_A(\mathbf{x},\omega) + \frac{\omega^2}{c_A^2}\,\hat{\Phi}_A(\mathbf{x},\omega) = 0 \tag{5.10}$$

The subscript A is omitted for the potential in the following. Applying the transformation to equation (5.8) the velocity is obtained in the *Fourier* domain:

$$\hat{\mathbf{v}}_A(\mathbf{x},\omega) = \operatorname{grad}\hat{\Phi}(\mathbf{x},\omega) \tag{5.11}$$

Transforming the relation between spatial changes in the velocity field and the change of the sound pressure in time, which is, in addition to *Newton*'s law, the fundamental equation for deriving the wave equation [see Cremer and Müller 1982], the pressure $\hat{p}_A(\mathbf{x},\omega)$ can be expressed in terms of the potential $\hat{\Phi}(\mathbf{x},\omega)$:

$$\begin{aligned}\hat{p}_A(\mathbf{x},\omega) &= -\frac{\rho_A c_A^2}{i\,\omega}\operatorname{div}\hat{\mathbf{v}}_A(\mathbf{x},\omega)\\ &= -\frac{\rho_A c_A^2}{i\,\omega}\Delta\hat{\Phi}(\mathbf{x},\omega)\end{aligned} \tag{5.12}$$

The calculation of the normal modes and the coupling modes, which are composed to build the trial function for the *Ritz* method in equation (5.7), is discussed in the following.

5.2.1 Normal Modes

There exist different possibilities for the definition of the normal modes in the classical CMS method. Most common are the fixed interface Craig-Bampton method [Craig and Bampton 1968] and the free interface Craig-Chang method [Craig and Chang 1976]. Fixed interface normal modes are the eigenvectors of the component defining the degrees of freedom at the interface as fixed in terms of displacements or velocities, whereas free interface normal modes result out of the eigenvalue problem with free interfaces. A detailed description of the FEM

formulation is given by Hinke [2008].

For the FSI-problem in this thesis the normal modes for the acoustic fluid are defined in terms of the velocity potential $\hat{\Phi}^N$ assuming fixed interfaces, which means reflective wall conditions for all boundaries of the fluid:

$$\operatorname{grad} \hat{\Phi}^N_m(\mathbf{x}, \omega_m) \cdot \mathbf{n}_{\mathrm{BC}} = 0 \tag{5.13}$$

This leads to the homogeneous *Helmholtz* equation for $\hat{\Phi}^N_m$:

$$\Delta \hat{\Phi}^N_m(\mathbf{x}, \omega_m) + \frac{\omega_m^2}{c_A^2} \hat{\Phi}^N_m(\mathbf{x}, \omega_m) = 0 \qquad \text{with } m = 1,\, 2, \ldots \tag{5.14}$$

For simple symmetric geometries the eigenvalue problem (5.14) can be solved analytically [see Cremer and Müller 1982]. For a fluid with a rectangular shape $[0, L_x] \times [0, L_y] \times [0, L_z]$ it reads

$$\left(-k_x^2 - k_y^2 - k_z^2 + \frac{\omega_m^2}{c_A^2} \right) \hat{\Phi}^N_m(\mathbf{x}, \omega_m) = 0 \tag{5.15}$$

$$\text{with } k_x = \frac{m_1\,\pi}{L_x},\; k_y = \frac{m_2\,\pi}{L_y},\; k_z = \frac{m_3\,\pi}{L_z},$$

where m is defined as a multi-index $m = (m_1, m_2, m_3)$. The analytical solution for the eigenvalues ω_m is gained out of equation (5.15) and reads

$$\omega_m = c_A \sqrt{\left(\frac{m_1\,\pi}{L_x}\right)^2 + \left(\frac{m_2\,\pi}{L_y}\right)^2 + \left(\frac{m_3\,\pi}{L_z}\right)^2}. \tag{5.16}$$

The related modeshapes are

$$\hat{\Phi}^N_m(\mathbf{x}, \omega_m) = \cos\left(\frac{m_1\,\pi}{L_x} x\right) \cos\left(\frac{m_2\,\pi}{L_y} y\right) \cos\left(\frac{m_3\,\pi}{L_z} z\right). \tag{5.17}$$

In case of arbitrary geometries the eigenvalue problem (5.14) has to be solved with numerical methods. In the scope of this work an algorithm based on the Spectral Finite Element Method (SFEM), developed by Pospiech [2011], is used. The method is discussed briefly in the appendix A.3. Figure 5.3 shows exemplarily fixed interface normal modes in terms of the velocity potential $\Phi^N_m(\mathbf{x})$ for the rectangular room, which is used to explain the FSI-coupling method in the following sections. In figure 5.4 the velocities in x-, y- and z-direction, computed out of $\Phi^N_{(4,3,2)}$ using equation (5.11), are depicted. In figures 5.4b to 5.4d one observes, that the reflective wall conditions are fulfilled.

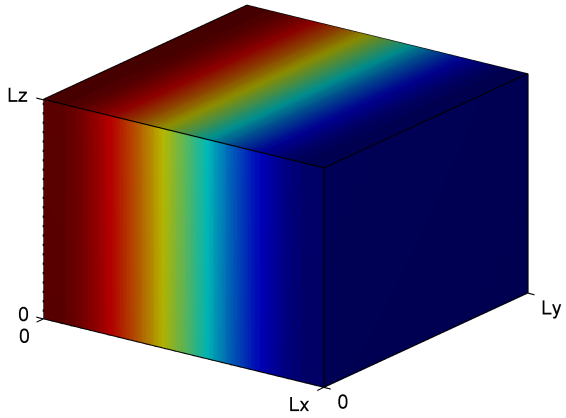

(a) $\Phi^N_{(1,0,0)}$

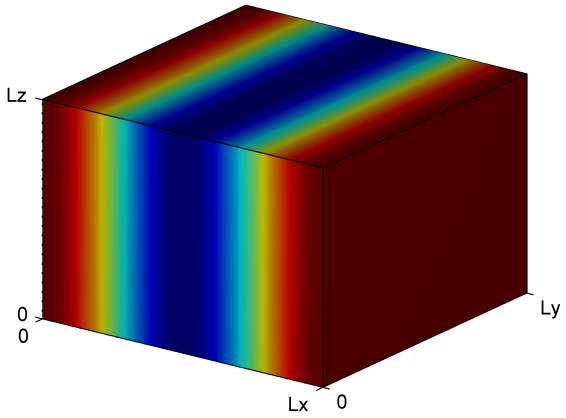

(b) $\Phi^N_{(2,0,0)}$

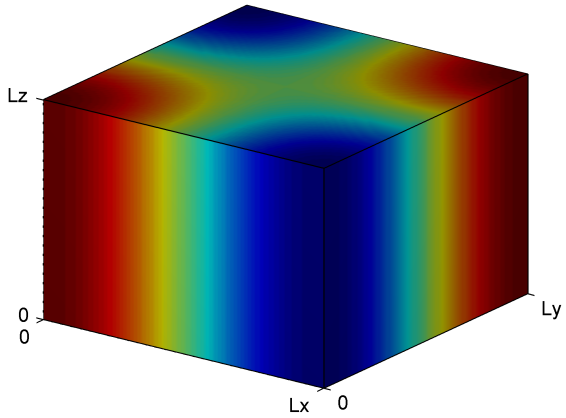

(c) $\Phi^N_{(1,1,0)}$

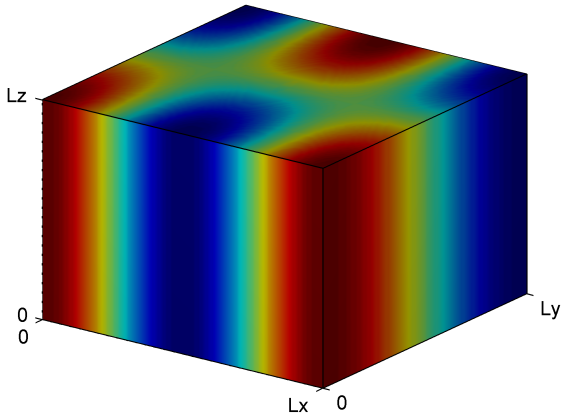

(d) $\Phi^N_{(2,1,0)}$

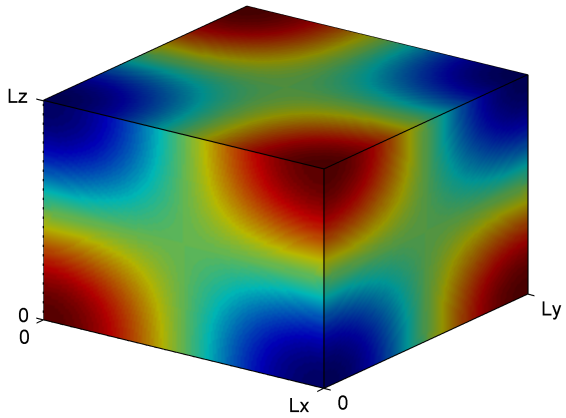

(e) $\Phi^N_{(1,1,1)}$

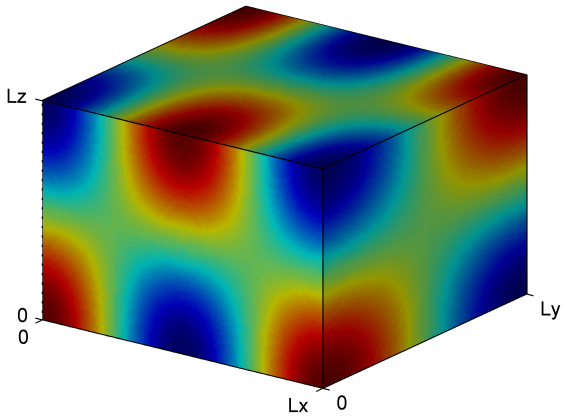

(f) $\Phi^N_{(2,1,1)}$

Figure 5.3: Normal modes $\Phi^N_m(\mathbf{x})$ for the velocity potential of the rectangular room $[0, L_x] \times [0, L_y] \times [0, L_z]$ with reflective walls for different multi-indices

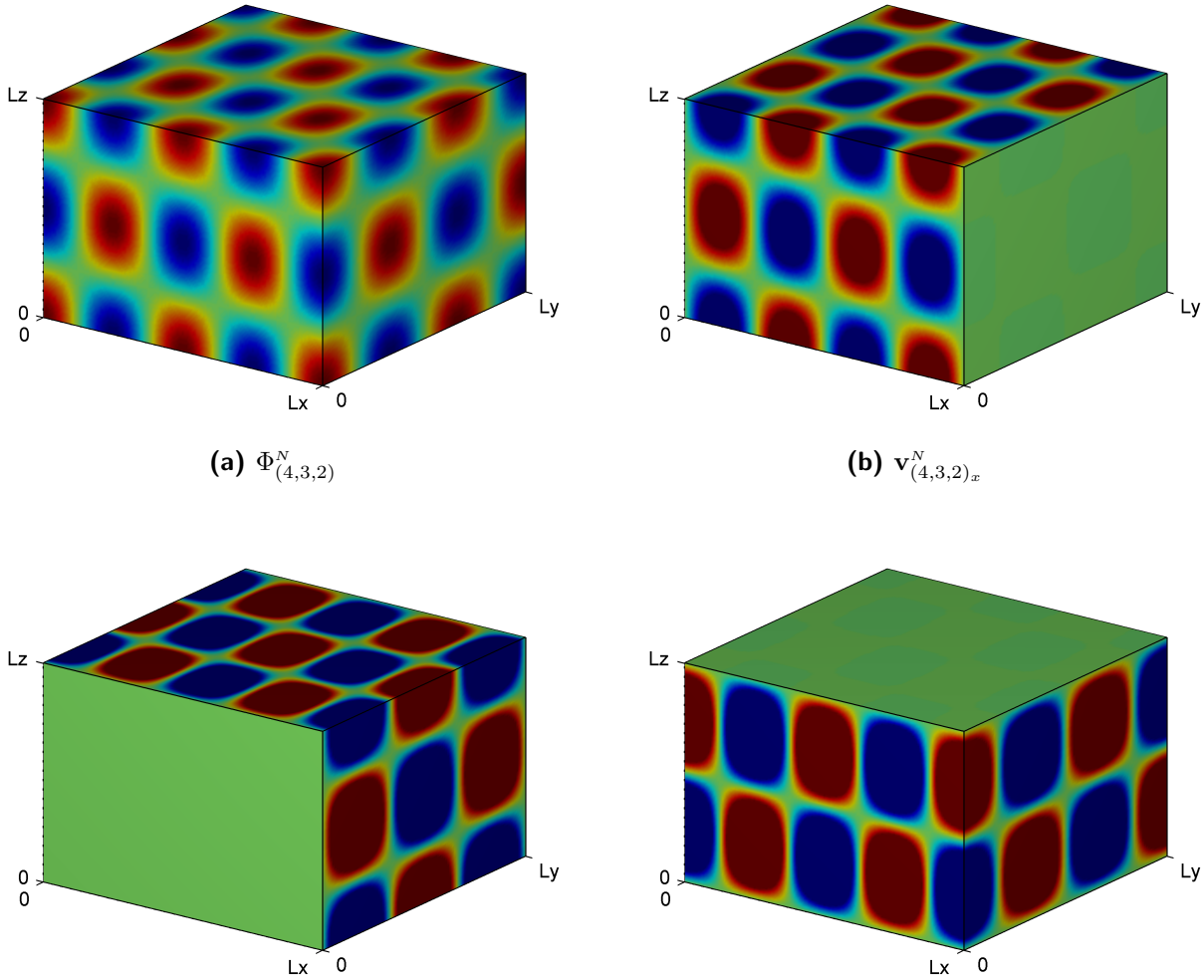

(a) $\Phi^N_{(4,3,2)}$ **(b)** $\mathbf{v}^N_{(4,3,2)_x}$

(c) $\mathbf{v}^N_{(4,3,2)_y}$ **(d)** $\mathbf{v}^N_{(4,3,2)_z}$

Figure 5.4: $\Phi^N_{(4,3,2)}(\mathbf{x})$ for the velocity potential and the related fluid velocities $\mathbf{v}^N_{(4,3,2)_x}(\mathbf{x})$, $\mathbf{v}^N_{(4,3,2)_y}(\mathbf{x})$ and $\mathbf{v}^N_{(4,3,2)_z}(\mathbf{x})$ for the rectangular room $[0, L_x] \times [0, L_y] \times [0, L_z]$ with reflective walls

5.2.2 Coupling Modes

The normal modes, which obey the reflective boundary conditions at the interface, are supplemented by coupling modes in order to define a valid set of trial functions for (5.7). These coupling modes enable velocities perpendicular to the coupling interface. They fulfill the reflective boundary conditions at all surfaces of the room, except for the interface, which is defined as $\mathbf{x}_{\mathrm{BC}}$ in the following.

In general one has to distinguish between different possibilities for the prescription of the interface displacements. In FEM-based methods very often a nodal definition is used. Then

the coupling modes are called constraint modes or attachment modes. In the first case displacements and in the second case forces are prescribed at the interfaces. This means, that for each node at the interface one coupling mode has to be considered. This results, especially in case of 3d FSI-problems with 2d interfaces, in a huge number of unknowns.

Here priority is given to a modal based definition of the coupling modes, which is used by Magalhaes [2004] for instance and reduces the number of unknowns significantly compared to nodal formulations. The normal velocity at this interface is prescribed with the function $g(\mathbf{x}_{\mathrm{BC}})$

$$\operatorname{grad} \hat{\Phi}_n^C(\mathbf{x}, \Omega) \cdot \mathbf{n}_{\mathrm{BC}} = g(\mathbf{x}_{\mathrm{BC}}). \tag{5.18}$$

This leads to an inhomogeneous *Helmholtz* equation for each coupling mode (compare appendix A.3). In equation (5.18) the index n marks the number of the coupling mode in the numerical solution. For the specification of the function $g(\mathbf{x}_{\mathrm{BC}})$ again a multi-index $n = (n_1, n_2)$ is defined with respect to the prescribed vibration pattern. In contrast to Magalhaes [2004], where static modes are defined assuming a linear decay normal to the interface, in this work the coupling modes are calculated as solutions of the dynamic problem in a harmonic analysis. Thus the number of coupling modes, which is considered in the calculation, can be chosen with respect to the physical properties of the system for reasons of efficiency.

Magalhaes [2004] and Magalhaes and Ferguson [2003, 2005] specified the coupling modes for the case, that one wall is covered completely by the interface. Furthermore they gave an outlook for coupling with just a part of a wall. In this thesis both cases are investigated. In order to exemplify the influence of the wavenumber, a rectangular room with reflective walls $[0, L_x = 6\,m] \times [0, L_y = 3\,m] \times [0, L_z = 2\,m]$ is considered and the coupling modes are calculated with the Spectral Finite Element formulation, implemented by Pospiech [2011].

Figure 5.5 shows the fluid velocity $\mathbf{v}_x^C$ in x-direction as well as the velocity potential Φ^C of the holohedral coupling modes, which cover the whole wall, when a sinusoidal vibration pattern is prescribed at the interface with a circular frequency of excitation $\Omega = 459\,\frac{rad}{s}$. The velocity $\mathbf{v}_x^C$ fulfills equation (5.18) at the interface and the boundary conditions at the reflective walls.

Comparing the velocity- and potential-fields for different multi-indices $n = (n_1, n_2)$ while keeping the frequency of excitation fixed, one observes far-fields, which means oscillating sinusoidal patterns, for small wavenumbers in the acoustic fluid, whereas with rising wavenumbers near-field solutions are obtained. They are characterized by an exponential decaying behavior perpendicular to the interface.

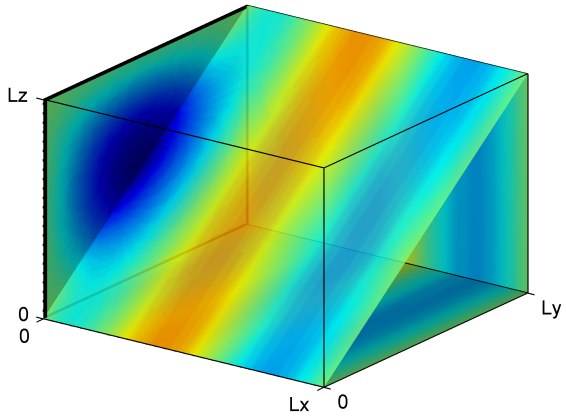

(a) $\mathbf{v}^C_{(1,1)_x}$

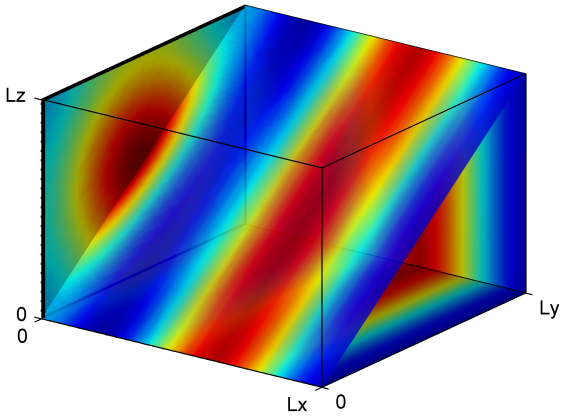

(b) $\Phi^C_{(1,1)}$

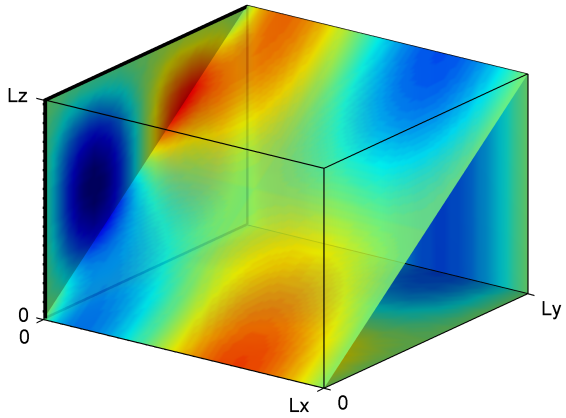

(c) $\mathbf{v}^C_{(2,1)_x}$

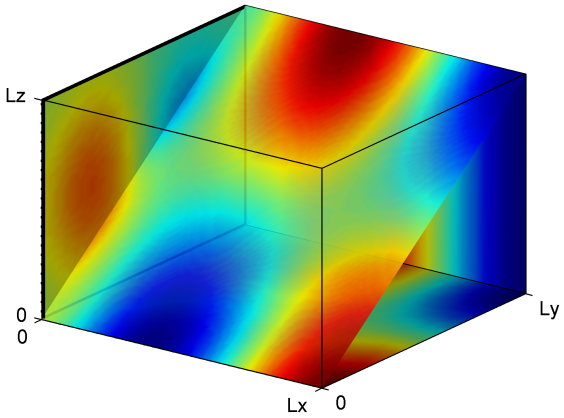

(d) $\Phi^C_{(2,1)}$

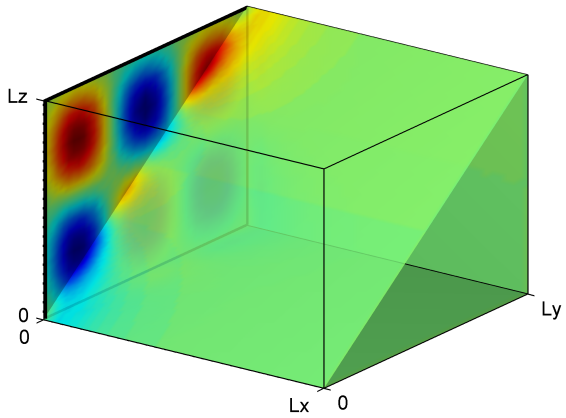

(e) $\mathbf{v}^C_{(3,2)_x}$

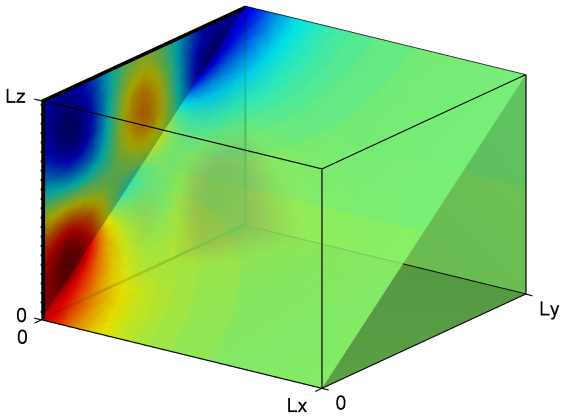

(f) $\Phi^C_{(3,2)}$

Figure 5.5: Holohedral coupling modes for the velocity potential $\Phi^C_n(\mathbf{x})$ and the fluid velocity $\mathbf{v}^C_{n_x}(\mathbf{x})$ perpendicular to the interface of the rectangular room with reflective walls $[0, L_x = 6\,m] \times [0, L_y = 3\,m] \times [0, L_z = 2\,m]$ for different multi-indices $n = (n_1, n_2)$ with $\Omega = 459\,\frac{rad}{s}$

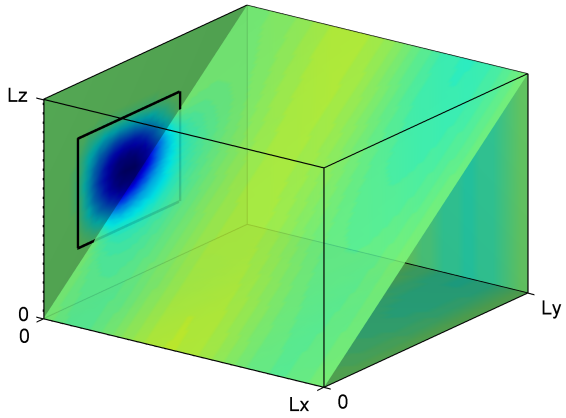

(a) $\mathbf{v}^C_{(1,1)_x}$

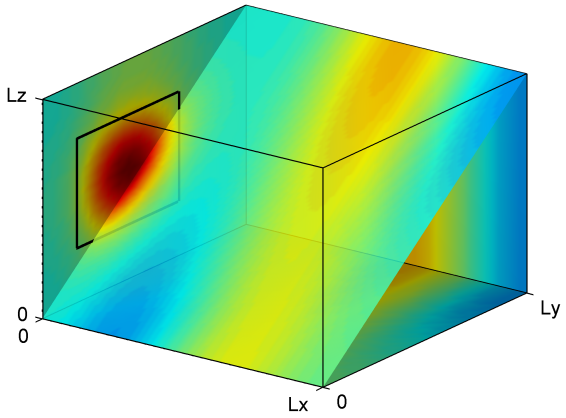

(b) $\Phi^C_{(1,1)}$

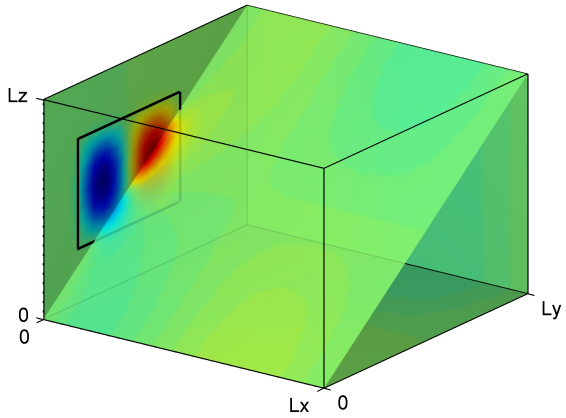

(c) $\mathbf{v}^C_{(2,1)_x}$

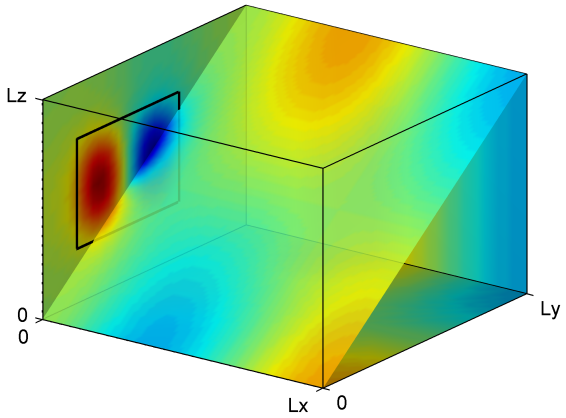

(d) $\Phi^C_{(2,1)}$

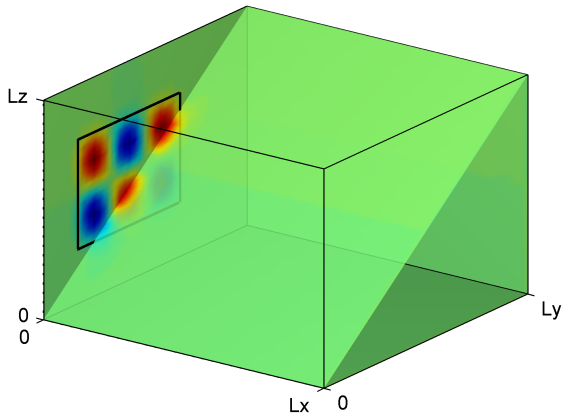

(e) $\mathbf{v}^C_{(3,2)_x}$

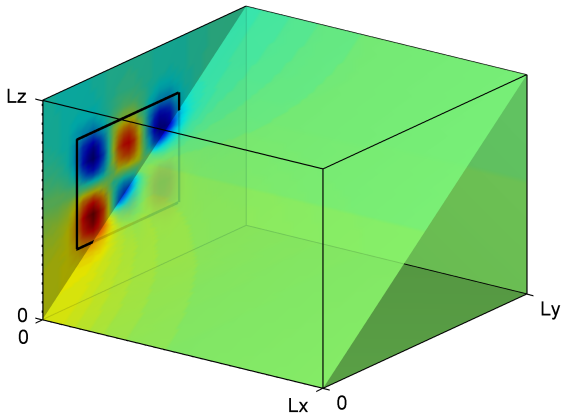

(f) $\Phi^C_{(3,2)}$

Figure 5.6: Subregional coupling modes for the velocity potential $\Phi^C_n(\mathbf{x})$ and the fluid velocity $\mathbf{v}^C_{n_x}(\mathbf{x})$ perpendicular to the interface of the rectangular room with reflective walls $[0, L_x = 6\,m] \times [0, L_y = 3\,m] \times [0, L_z = 2\,m]$ for different multi-indices $n = (n_1, n_2)$ with $\Omega = 459\,\frac{rad}{s}$

These near-field effects can be used to reduce the number of unknowns in the CMS approach. If the focus is laid on the sound field in the cavity, it is sufficient to consider just the coupling modes, which radiate far-fields into the acoustic volume.

In figure 5.6 the subregional coupling modes are depicted for the interface $y \in [0.5; 2.0]$ and $z \in [0.5; 1.5]$. Their impact on the acoustic fluid is smaller than in case of holohedral coupling modes (compare figure 5.5). Also concerning the decay characteristics one observes differences.

To define a sufficient number of coupling modes for an efficient numerical computation, this effect has to be predicted with low numerical effort. A calculation of the coupling modes with the SFEM in advance in order to investigate the decay characteristics would be too expensive.

In the following an efficient strategy for the selection of the coupling modes is developed. Applying Integral Transform Methods and filtering techniques in the spatial domain one can estimate these decay characteristics with negligible numerical effort. Starting from the wave equation in terms of displacements

$$\frac{\partial^2 u(x,y,z,t)}{\partial x^2} + \frac{\partial^2 u(x,y,z,t)}{\partial y^2} + \frac{\partial^2 u(x,y,z,t)}{\partial z^2} = \frac{1}{c_A^2}\frac{\partial^2 u}{\partial t^2} \tag{5.19}$$

a *Fourier* transformation is applied. For a start infinite dimensions of the interface are assumed and the spatial coordinates y and z, defining the plane of the interface, are transformed in the wavenumber domain. Furthermore the transformation into the frequency domain is carried out, considering vibrations in the steady state with a circular frequency of excitation Ω:

$$\frac{\partial^2 \hat{u}(x,k_y,k_z,\Omega)}{\partial x^2} + \left[\left(\frac{\Omega}{c_A}\right)^2 - k_y^2 - k_z^2\right] \hat{u}(x,k_y,k_z,\Omega) = 0 \tag{5.20}$$

The ordinary differential equation (5.20) is solved with the exponential approach

$$\hat{u}(x,k_y,k_z,\Omega) = A_1(k_y,k_z,\Omega)\, e^{\lambda x} + A_2(k_y,k_z,\Omega)\, e^{-\lambda x} \quad \text{where: } \lambda = \sqrt{k_y^2 + k_z^2 - \frac{\Omega^2}{c_A^2}}. \tag{5.21}$$

In this approximative method the rear panel is considered to be parallel to the interface. At the interface at $x = 0$ a vibration pattern $\hat{u}_0(k_y, k_z)$ is applied and at the rear panel (at $x = L_x$) rigid wall conditions are defined.

Thus one obtains the solution for the displacement field of the homogeneous problem:

$$\hat{u}(x,k_y,k_z,\Omega)=\begin{cases}\hat{u}_0(k_y,k_z)\,\left(\frac{-e^{-\lambda L_x}}{(e^{\lambda L_x}-e^{-\lambda L_x})}e^{\lambda x}+\frac{e^{\lambda L_x}}{(e^{\lambda L_x}-e^{-\lambda L_x})}e^{-\lambda x}\right), & \lambda\neq 0\\ \hat{u}_0(k_y,k_z)\,\left(1-\frac{x}{L_x}\right), & \lambda=0\end{cases} \tag{5.22}$$

Equation (5.22) contains all the information about the decay characteristics of the vibration pattern for each wavenumber-frequency combination. The ranges for the far-field, the near-field and the transition zone, where a linear decay is observed, are listed in (5.23).

$$k_y^2+k_z^2\begin{cases}< & \frac{\Omega^2}{c_A^2}, \quad \text{far-field}\\ > & \frac{\Omega^2}{c_A^2}, \quad \text{near-field}\\ = & \frac{\Omega^2}{c_A^2}, \quad \text{linear decay}\end{cases} \tag{5.23}$$

In the k_y, k_z-domain the transition zone marks a circle with the radius $\frac{\Omega}{c_A}$. Up to now infinite dimensions were assumed for the interface. In the practical problem finite absorbers with dimensions $L_x^{BC}\times L_z^{BC}$ have to be applied. Therefore the infinite vibration pattern $u_0(y,z)$ is multiplied with a filter function $\Theta(y,z)$ in the spatial domain:

$$u_0^{fin}(y,z)=u_0(y,z)\;\Theta(y,z) \tag{5.24}$$

$$\Theta(y,z)=\begin{cases}1, & -\frac{L_y^{BC}}{2}\leq y\leq\frac{L_y^{BC}}{2}\;\wedge\;-\frac{L_z^{BC}}{2}\leq z\leq\frac{L_z^{BC}}{2}\\ 0, & \text{else}\end{cases} \tag{5.25}$$

The multiplication with a 2d rectangular function in the spatial domain equals a convolution with a 2d *sinc*−function in the wavenumber domain.

$$\Theta(y,z)\;\circ\!\!-\!\!\bullet\;\frac{4}{k_y\,k_z}\,\sin\left(\frac{L_y^{BC}}{2}\,k_y\right)\,\sin\left(\frac{L_z^{BC}}{2}\,k_z\right) \tag{5.26}$$

In order to decide, whether a coupling mode has to be considered, just the *Fourier* transformation of the velocity pattern of the wall containing the interface $\mathbf{v}^C(x=0)_x$ has to be computed and evaluated according to condition (5.23). In figures 5.7 and 5.8 the results are depicted for the holohedral and the subregional coupling modes. The magenta colored circle specifies the transition zone. The wavenumbers within this circle refer to far-field solutions.

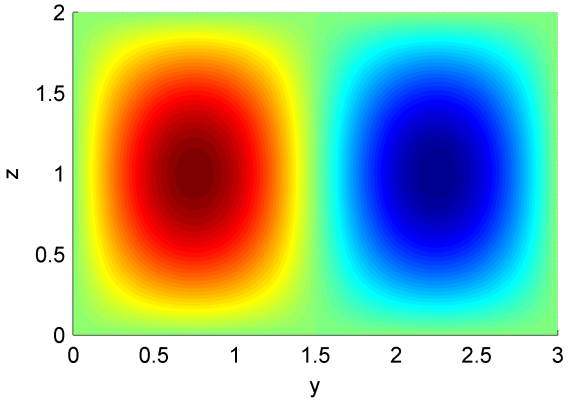

(a) $\mathbf{v}^C_{(2,1)}(x=0)_x$

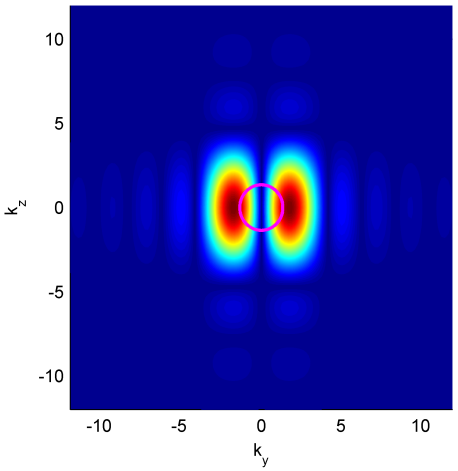

(b) $\mathcal{F}\left(\mathbf{v}^C_{(2,1)_x}(x=0)\right)$

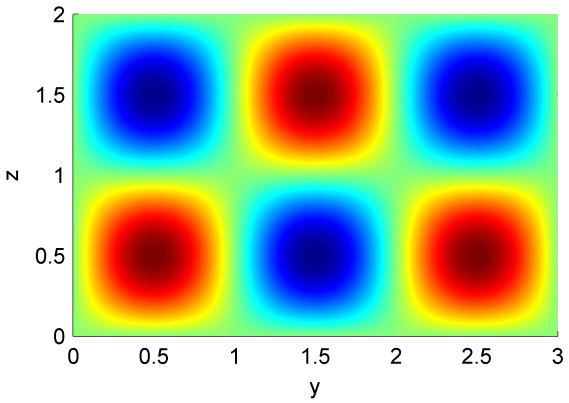

(c) $\mathbf{v}^C_{(3,2)_x}(x=0)$

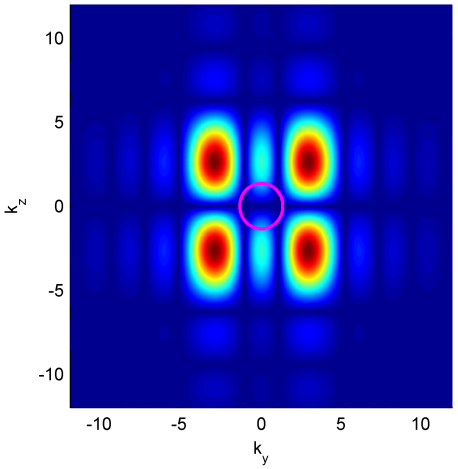

(d) $\mathcal{F}\left(\mathbf{v}^C_{(3,2)_x}(x=0)\right)$

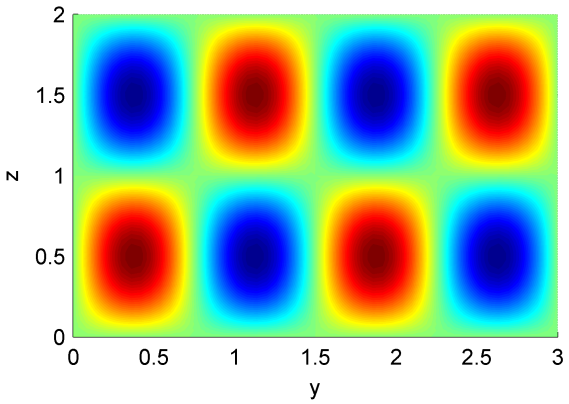

(e) $\mathbf{v}^C_{(4,2)_x}(x=0)$

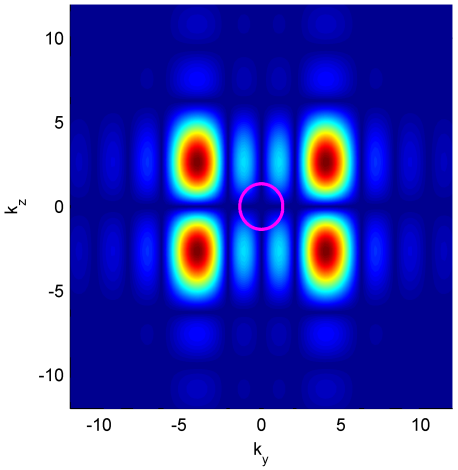

(f) $\mathcal{F}\left(\mathbf{v}^C_{(4,2)_x}(x=0)\right)$

Figure 5.7: Near-field effects of the holohedral coupling modes

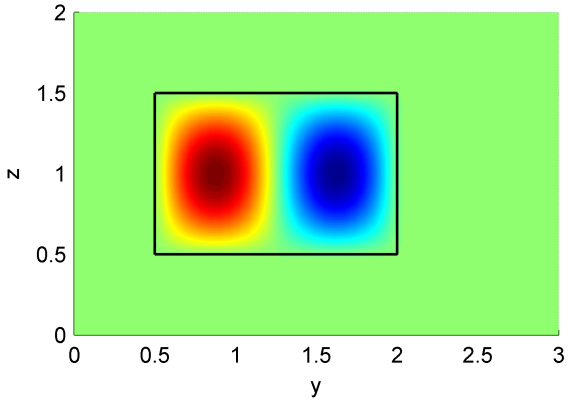

(a) $\mathbf{v}^C_{(2,1)_x}(x=0)$

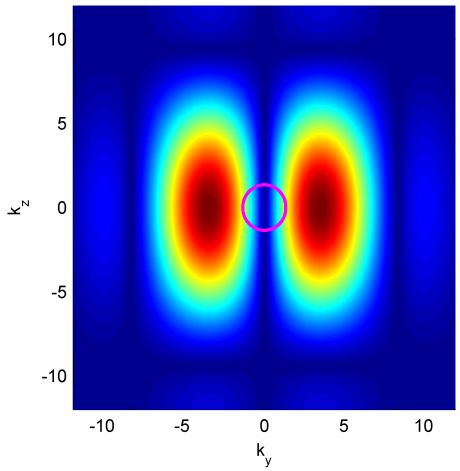

(b) $\mathcal{F}\left(\mathbf{v}^C_{(2,1)_x}(x=0)\right)$

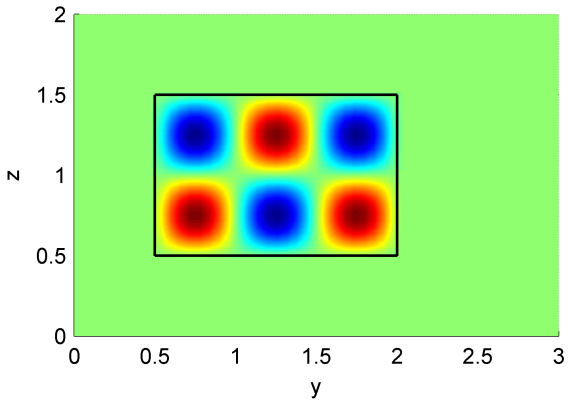

(c) $\mathbf{v}^C_{(3,2)_x}(x=0)$

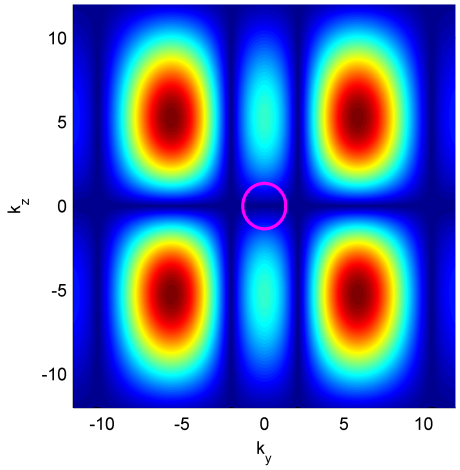

(d) $\mathcal{F}\left(\mathbf{v}^C_{(3,2)_x}(x=0)\right)$

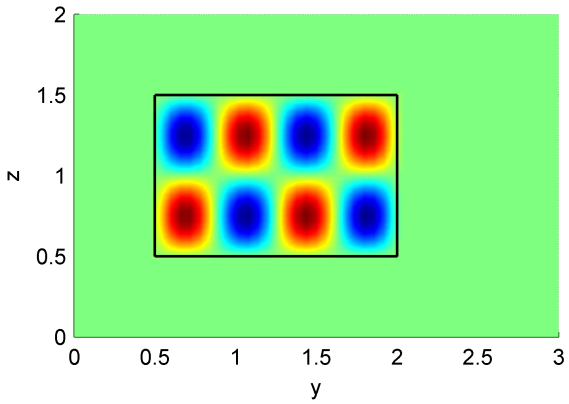

(e) $\mathbf{v}^C_{(4,2)_x}(x=0)$

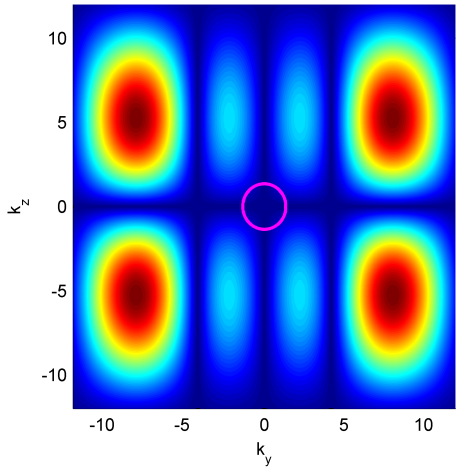

(f) $\mathcal{F}\left(\mathbf{v}^C_{(4,2)_x}(x=0)\right)$

Figure 5.8: Near-field effects of the subregional coupling modes

A comparison of the velocity fields and the potential fields in figures 5.5 and 5.6 with the corresponding transformed patterns of the interface velocities in figures 5.7 and 5.8 shows, that the coupling modes resulting in far-field solutions can be identified very well by this method.

For the subregional coupling modes the transition to near-fields is linked with smaller multi-index combinations than for the holohedral coupling modes (compare figures 5.5 and 5.6), because a fixed multi-index combination ((2, 1) or (3, 2) for instance) results in higher wavenumbers for the subregional than for the holohedral modes, as one observes comparing figures 5.7b and 5.8b as well as 5.7d and 5.8d.

Also the effect caused by the spatial limitation of infinite vibration patterns is clearly recognized. The infinite sinusoidal vibration patterns $u_0^{fin}(y, z)$ in figures 5.7e and 5.8a show the same wavenumber spectrum. The convolution effects, occurring due to the finite interface, depend on the size of the interface in relation to the wavelength. As one can see in equation (5.26), small filter functions cause broad sinc-functions in the transformed domain (see figures 5.7f and 5.8b). In figure 5.8b the maxima merge in k_z-direction due to the convolution and just one maximum is observed at $k_z = 0$. This leads to far-fields in the subregional modes, whereas mainly near-fields occur for the holohedral modes due to a wider filtering range. The phenomenon, that in case of filtering functions with a small range the hydrodynamic short-circuit cannot work efficiently, was explained by Cremer and Müller [1982] for instance.

The number of normal modes, which has to be considered, depends on the frequency of excitation Ω, if the load pattern is able to excite all modeshapes (in case of a randomly positioned spherical source for example). Then it is sufficient to consider the normal modes up to $1.5\,\Omega$. In case of load patterns, which excite individual vibration-patterns in particular, of course normal modes have to be taken into account, which are able to build up these patterns. The number of coupling modes can be limited efficiently selecting the far-fields in the wavenumber domain.

The kinetic and the potential energy can be evaluated with the help of (5.4) and (5.5) to represent the acoustic fluid in the *Hamilton* approach.

The implementation of the compound absorber in the FSI-formulation is discussed in the following sections.

5.3 Coupling with Impedances

For the coupled FSI-problem a weak formulation, based on variational principles, was chosen in section 5.1. Therefore the Lagrangian, which is the difference of kinetic and potential energy, has to be computed for each component respectively. For the acoustic fluid this was done in section 5.2, where the SFEM was applied for the spatial discretization.

For the porous compound absorber however, a model based on the ITM is much more efficient than a finite element description, where the velocity of the solid and the fluid component of the porous material and also the pore pressure would have to be considered as state variables in each node. Absorptive structures are implemented in the formulation of equilibrium (5.2) with the help of impedances. They can be computed with ITM and, by the way, they are measures of high engineering significance.

The idea of calculating the Lagrangian out of impedances was published already in 1959 for problems in Electrical Engineering. Meixner [1959] gave the proof, that the difference of electrical and magnetic energies coincides for equivalent terminal networks, which are loaded with identical electromotive forces. Equivalent networks are different systems, which have the same impedance. They show an identical current $I(t)$ for an individual voltage $U(t)$. Both systems have different electric energies at a specific time t. Also the magnetic energies are different, but the difference of both is the same for equivalent systems.

This idea was picked up in this work to compute the Lagrangian of the compound absorbers out of impedances. Vibrating systems have to fulfill the same differential equations as electrical oscillating circuits (RLC-circuit). They consist of a capacitor C, an inductor L and a resistor R. The capacitor is able to store electric charge and it is equivalent to a spring in a mechanical system. The inductor can be substituted by the mass and the resistor acts like a damper in vibrating systems.

Meixner [1959] stated, that the Lagrangian of the RLC-circuit is gained out of the imaginary part of the impedance and the electrical power, introduced into the network, can be included with its real part.

The derivation of the Lagrangian for plate-like compound absorbers and the computation of the virtual work of the non-conservative damping forces, which is equal to the variation of the work of the damping forces, is sketched in the following using the example of the *Kirchhoff* plate.

5.3.1 Lagrangian and Virtual Work

For the acoustic fluid the trial functions, which are essential elements in the *Ritz*-approach, were defined in section 5.2. Also for the impedance boundary conditions, which represent absorptive structures, elastic structures or compound absorbers consisting of several materials in practice, trial functions have to be prescribed. The velocity pattern $v_{\mathrm{BC}}(y,z,t)$ is chosen for a forced vibration in the steady state as the product of a spatial function $\psi_n(y,z)$ and a time dependent function representing the harmonic response for a circular frequency of excitation Ω. The displacement field $u_{\mathrm{BC}}(y,z,t)$ is derived out of $v_{\mathrm{BC}}(y,z,t)$.

$$v_{\mathrm{BC}}(y,z,t) = \sum_{n=1}^{n_{\max}} \psi_n(y,z)\ \left(\mathcal{C}_n e^{i\Omega t} + \overline{\mathcal{C}}_n e^{-i\Omega t}\right) \tag{5.27}$$

$$u_{\mathrm{BC}}(y,z,t) = \sum_{n=1}^{n_{\max}} \psi_n(y,z) \left(\frac{\mathcal{C}_n}{i\Omega} e^{i\Omega t} - \frac{\overline{\mathcal{C}}_n}{i\Omega} e^{-i\Omega t}\right) \tag{5.28}$$

In the following derivations the abbreviation $n_{\max} = N$ is used for the number of coupling modes. The trial functions are specified with the conjugate complex coefficients $\mathcal{C}_n$ and $\overline{\mathcal{C}}_n$. In the formulation of *Hamilton*'s principle the coupling of the acoustic fluid and the compound absorber is realized by *Lagrange* multipliers. If the same velocity pattern, which is chosen for the absorber in equation (5.27) is applied as a boundary condition at the absorber-interface in section 5.2.2 for the computation of the coupling modes, the coupling condition can be satisfied simply by substituting $\mathcal{C}_n = \mathcal{B}_n$ and $\overline{\mathcal{C}}_n = \overline{\mathcal{B}}_n$ in equations (5.27) and (5.28).

As the ITM, used for the model of the boundary conditions, provides results in terms of the wavenumbers k_y and k_z, it is convenient to approximate the spatial component of the trial function with a 2d *Fourier* series

$$\hat{\psi}_n(y,z) = \sum_{r=-r_{\max}}^{r_{\max}} \sum_{s=-s_{\max}}^{s_{\max}} E_{nrs}\, e^{i(k_y(r)y + k_z(s)z)}. \tag{5.29}$$

The range of the indices r and s in the *Fourier* series is defined to $r = -r_{\max} \ldots r_{\max}$ and $s = -s_{\max} \ldots s_{\max}$. In the following these ranges are no longer depicted explicitly. The complex *Fourier* coefficients are obtained, carrying out the 2d *Fourier* integrals for the lengths of repetition L_y^{rep} and L_z^{rep}:

$$E_{nrs} = \frac{1}{L_y^{\mathrm{rep}} L_z^{\mathrm{rep}}} \int_0^{L_z^{\mathrm{rep}}} \int_0^{L_y^{\mathrm{rep}}} \psi_n(y,z)\, e^{-i(k_y(r)\, y + k_z(s)\, z)}\, dy\, dz \tag{5.30}$$

$$\text{where:} \quad k_y(r) = \frac{r\, 2\pi}{L_y^{\mathrm{rep}}} \quad \text{and} \quad k_z(s) = \frac{s\, 2\pi}{L_z^{\mathrm{rep}}}$$

The definition of L_y^{rep} and L_z^{rep} is discussed in section 5.3.2 depending on the choice of the trial functions.

Inserting (5.29) into (5.27) and (5.28) one obtains for the approximative expressions $\hat{v}_{\mathrm{BC}}(y,z,t)$ and $\hat{u}_{\mathrm{BC}}(y,z,t)$.

$$\hat{v}_{\mathrm{BC}}(y,z,t) = \sum_{n=1}^{N} \hat{\psi}_n(y,z) \underbrace{\left(\mathcal{C}_n e^{i\Omega t} + \overline{\mathcal{C}}_n e^{-i\Omega t}\right)}_{\dot{y}_n(t)} \tag{5.31}$$

$$\hat{u}_{\mathrm{BC}}(y,z,t) = \sum_{n=1}^{N} \hat{\psi}_n(y,z) \underbrace{\left(\frac{\mathcal{C}_n}{i\Omega} e^{i\Omega t} - \frac{\overline{\mathcal{C}}_n}{i\Omega} e^{-i\Omega t}\right)}_{y_n(t)}. \tag{5.32}$$

The time depending functions $y_n(t)$ and $\dot{y}_n(t)$ are abbreviated with y_n and $\dot{y}_n$ in the following.

Lagrangian for plate-like flexible structures

The Lagrangian for the flexible part of the compound absorber is derived exemplarily using the example of the *Kirchhoff* plate in the following. The absorptive character will be considered by the virtual work of the damping forces later on. In order to simplify the expressions, in the following the spatial trial functions $\hat{\psi}_n(y,z)$ are abbreviated with $\hat{\psi}_n$.

Assuming a constant mass distribution μ the kinetic energy T_{BC} of the *Kirchhoff* plate is given in equation (5.33). The only requirement forced by the *Ritz* method is, that the trial functions have to fulfill the kinetic boundary conditions. The *Fourier* series of the trial functions (5.31) is introduced to approximate the kinetic energy (compare appendix A.5).

$$T_{\mathrm{BC}} = \frac{1}{2}\mu \int_0^{L_z}\int_0^{L_y} v_{\mathrm{BC}}^2 \, dy\, dz \tag{5.33}$$

$$T_{\mathrm{BC}} \approx \frac{1}{2}\mu \int_0^{L_z^{\mathrm{rep}}}\int_0^{L_y^{\mathrm{rep}}} \hat{v}_{\mathrm{BC}}^2 \, dy\, dz = \frac{1}{2}\mu \int_0^{L_z^{\mathrm{rep}}}\int_0^{L_y^{\mathrm{rep}}} \left[\sum_{n=1}^{N} \hat{\psi}_n \, \dot{y}_n\right]^2 dy\, dz \tag{5.34}$$

Henceforward the spatial integral over the domain of the *Fourier* series $\int_0^{L_z^{\mathrm{rep}}}\int_0^{L_y^{\mathrm{rep}}} dy\, dz$ is abbreviated with $\int_{A^{\mathrm{rep}}} dA$. The spatial integral in (5.34) is expanded according to equation (A.56),

given in the appendix.

$$\int\limits_{A^{\mathrm{rep}}} \left[\sum_{n=1}^{N} \hat{\psi}_n \, \dot{y}_n\right]^2 dA = \int\limits_{A^{\mathrm{rep}}} \sum_{n=1}^{N} \left(\hat{\psi}_n \, \dot{y}_n\right)^2 dA + 2 \int\limits_{A^{\mathrm{rep}}} \sum_{k=1}^{N-1} \sum_{l=k+1}^{N} \hat{\psi}_k \, \dot{y}_k \, \hat{\psi}_l \, \dot{y}_l \, dA$$
$$= \sum_{n=1}^{N} \dot{y}_n^2 \int\limits_{A^{\mathrm{rep}}} \hat{\psi}_n^2 \, dA + 2 \sum_{k=1}^{N-1} \sum_{l=k+1}^{N} \dot{y}_k \, \dot{y}_l \int\limits_{A^{\mathrm{rep}}} \hat{\psi}_k \, \hat{\psi}_l \, dA \tag{5.35}$$

The trial functions for u_{BC} and v_{BC} are real valued. This leads to conjugate complex *Fourier* coefficients E_{rs} in (5.30). The spatial integrals are computed with the help of the theorem of *Parseval*[1], which states, that the L^2 norm of a *Fourier* series can be calculated with the L^2 norm of the *Fourier* coefficients. A detailed description is given in the appendix A.6.

Inserting equations (A.59) and (A.60) in (5.34) and (5.35) the kinetic energy follows to

$$T_{\mathrm{BC}} \approx \frac{1}{2} \, \mu \, L_y^{\mathrm{rep}} L_z^{\mathrm{rep}} \left[\sum_{n=1}^{N} \dot{y}_n^2 \sum_r \sum_s |E_{nrs}|^2 + 2 \sum_{k=1}^{N-1} \sum_{l=k+1}^{N} \dot{y}_k \, \dot{y}_l \sum_r \sum_s E_{krs} \overline{E}_{lrs}\right]. \tag{5.36}$$

For the potential energy U_{BC} of the *Kirchhoff* plate one proceeds in a similar way. Starting from the general formulation (compare appendix A.5)

$$U_{\mathrm{BC}} = \frac{1}{2} \, B' \int_0^{L_z} \int_0^{L_y} \left(\frac{\partial^2 u_{\mathrm{BC}}}{\partial y^2} + \frac{\partial^2 u_{\mathrm{BC}}}{\partial z^2}\right)^2 - 2\,(1-\nu) \left[\frac{\partial^2 u_{\mathrm{BC}}}{\partial y^2} \, \frac{\partial^2 u_{\mathrm{BC}}}{\partial z^2} - \left(\frac{\partial^2 u_{\mathrm{BC}}}{\partial y \, \partial z}\right)^2\right] dy \, dz, \tag{5.37}$$

where B' is the bending stiffness of the plate and ν marks the *Poisson* ratio, and inserting the *Fourier* approximation (5.32), the derivatives of the spatial trial functions $\hat{\psi}_n$ have to be computed with respect to the coordinates y and z. The derivatives result in multiplications with the wavenumbers k_y and k_z. They are depicted in equation (5.38).

The products of the *Fourier* coefficients and the wavenumbers are expressed with the coefficients E''_{nrs}, E'''_{nrs} and E'''_{nrs} in order to simplify the derivations in the appendix A.6.

[1] M. A. Parseval, 1799

In the following the derivatives are abbreviated by $\hat{\psi}_n''$, $\hat{\psi}_n'''$ and $\hat{\psi}_n'^{\prime}$:

$$\begin{aligned}
\frac{\partial^2 \hat{\psi}_n}{\partial y^2} &= \sum_r \sum_s \underbrace{\left(-k_y^2\right) E_{nrs}}_{E''_{nrs}} e^{i(k_y y + k_z z)} = \hat{\psi}_n'' \\
\frac{\partial^2 \hat{\psi}_n}{\partial z^2} &= \sum_r \sum_s \underbrace{\left(-k_z^2\right) E_{nrs}}_{E'''_{nrs}} e^{i(k_y y + k_z z)} = \hat{\psi}_n''' \\
\frac{\partial^2 \hat{\psi}_n}{\partial y\, \partial z} &= \sum_r \sum_s \underbrace{\left(i\, k_y\right)\left(i\, k_z\right) E_{nrs}}_{E'^{\prime}_{nrs}} e^{i(k_y y + k_z z)} = \hat{\psi}_n'^{\prime}
\end{aligned} \tag{5.38}$$

Adding the time-dependent components of the approach

$$\frac{\partial^2 \hat{u}_{\mathrm{BC}}}{\partial y^2} = \sum_{n=1}^{N} \hat{\psi}_n''\, y_n; \qquad \frac{\partial^2 \hat{u}_{\mathrm{BC}}}{\partial z^2} = \sum_{n=1}^{N} \hat{\psi}_n'''\, y_n; \qquad \frac{\partial^2 \hat{u}_{\mathrm{BC}}}{\partial y\, \partial z} = \sum_{n=1}^{N} \hat{\psi}_n'^{\prime}\, y_n \tag{5.39}$$

equation (5.37) reads:

$$\begin{aligned}
U_{\mathrm{BC}} \approx \frac{1}{2} B' \Bigg[\int_{A^{\mathrm{rep}}} \Bigg[\sum_{n=1}^{N} \left(\hat{\psi}_n'' + \hat{\psi}_n''' \right) y_n \Bigg]^2 dA - \\
- 2\,(1-\nu) \int_{A^{\mathrm{rep}}} \sum_{n=1}^{N} \hat{\psi}_n'' y_n \sum_{n=1}^{N} \hat{\psi}_n''' y_n - \Big(\sum_{n=1}^{N} \hat{\psi}_n'^{\prime} y_n \Big)^2 dA \Bigg]
\end{aligned} \tag{5.40}$$

The second summand in equation (5.40) vanishes inserting the *Fourier* series and carrying out the integrals (compare equation (A.71) in section A.6).

$$U_{\mathrm{BC}} \approx \frac{1}{2} B' \int_{A^{\mathrm{rep}}} \Bigg[\sum_{n=1}^{N} \left(\hat{\psi}_n'' + \hat{\psi}_n''' \right) y_n \Bigg]^2 dA. \tag{5.41}$$

Inserting the derivatives of the *Fourier* members (5.38) one obtains with (A.61) to (A.63)

$$\begin{aligned}
U_{\mathrm{BC}} \approx \frac{1}{2} B'\, L_y^{\mathrm{rep}} L_z^{\mathrm{rep}} \Bigg[\sum_{n=1}^{N} y_n^2 \sum_r \sum_s \left(k_y^2 + k_z^2 \right)^2 |E_{nrs}|^2 + \\
+ \; 2 \sum_{k=1}^{N-1} \sum_{l=k+1}^{N} y_k\, y_l \sum_r \sum_s \left(k_y^2 + k_z^2 \right)^2 E_{krs} \overline{E}_{lrs} \Bigg].
\end{aligned} \tag{5.42}$$

In the variational formulation (5.2) the Lagrangian is integrated within an arbitrary time-range from t_1 to t_2.

Integrating over one time period T using (A.72) to (A.75) yields the Lagrangian

$$\begin{aligned}
\int_0^T L_{\mathrm{BC}}\, dt \;&=\; \int_0^T T_{\mathrm{BC}}\, dt - \int_0^T U_{\mathrm{BC}}\, dt \\
&\approx \frac{1}{2}\,\mu\, L_y^{\mathrm{rep}} L_z^{\mathrm{rep}} \left[\sum_{n=1}^{N} 2T\, \mathcal{C}_n \overline{\mathcal{C}}_n \sum_r \sum_s |E_{nrs}|^2 + \right. \\
&\qquad \left. + 2 \sum_{k=1}^{N-1} \sum_{l=k+1}^{N} T \left(\mathcal{C}_k \overline{\mathcal{C}}_l + \overline{\mathcal{C}}_k \mathcal{C}_l \right) \sum_r \sum_s E_{krs} \overline{E}_{lrs} \right] - \\
&\quad - \frac{1}{2}\, B'\, L_y^{\mathrm{rep}} L_z^{\mathrm{rep}} \left[\sum_{n=1}^{N} \frac{2T}{\Omega^2}\, \mathcal{C}_n \overline{\mathcal{C}}_n \sum_r \sum_s \left(k_y^2 + k_z^2 \right)^2 |E_{nrs}|^2 + \right. \\
&\qquad \left. + 2 \sum_{k=1}^{N-1} \sum_{l=k+1}^{N} \frac{T}{\Omega^2} \left(\mathcal{C}_k \overline{\mathcal{C}}_l + \overline{\mathcal{C}}_k \mathcal{C}_l \right) \sum_r \sum_s \left(k_y^2 + k_z^2 \right)^2 E_{krs} \overline{E}_{lrs} \right].
\end{aligned} \tag{5.43}$$

Substituting the impedance of the *Kirchhoff* plate

$$\mathrm{Im}\left(Z\left(r, s, \Omega \right) \right) = \mu\Omega - \frac{B'}{\Omega} \left(k_y(r)^2 + k_z(s)^2 \right)^2 \tag{5.44}$$

in equation (5.43) the formulation for the Lagrangian of plate-like flexible structures in terms of wavenumber- and frequency-dependent impedances is gained.

$$\begin{aligned}
\int_0^T L_{\mathrm{BC}}\, dt \;&\approx \frac{T}{\Omega} L_y^{rep} L_z^{rep} \left[\sum_{n=1}^{N} \mathcal{C}_n \overline{\mathcal{C}}_n \sum_r \sum_s \mathrm{Im}\left(Z\left(r, s, \Omega \right) \right) |E_{nrs}|^2 + \right. \\
&\qquad \left. + \sum_{k=1}^{N-1} \sum_{l=k+1}^{N} \left(\mathcal{C}_k \overline{\mathcal{C}}_l + \overline{\mathcal{C}}_k \mathcal{C}_l \right) \sum_r \sum_s \mathrm{Im}\left(Z\left(r, s, \Omega \right) \right) E_{krs} \overline{E}_{lrs} \right]
\end{aligned} \tag{5.45}$$

If the trial functions, which build up the velocity field of the absorber, are orthogonal, the off diagonal terms vanish and equation (5.45) can be simplified to

$$\int_0^T L_{\mathrm{BC}}\, dt \approx \frac{T}{\Omega} L_y^{rep} L_z^{rep} \left[\sum_{n=1}^{N} \mathcal{C}_n \overline{\mathcal{C}}_n \sum_r \sum_s \mathrm{Im}\left(Z\left(r, s, \Omega \right) \right) |E_{nrs}|^2 \right]. \tag{5.46}$$

In case of sinusoidal or cosinusoidal trial functions and a rectangular plate absorber the *Fourier* approximation is not necessary and would even cause errors (compare section 5.3.2). The simplified expression for the Lagrangian $L_{\mathrm{BC}}^{\mathrm{sin}}$, which is deduced from (5.46) is given in equation (5.59).

Virtual Work of the damping Forces

With the imaginary part of the impedance the flexible characteristics of the absorber can be modeled, as shown above. The absorptive characteristics, which are expressed by the real part of impedance (compare section 4.3), are considered in the variational formulation (5.2) with the virtual work of the non-conservative damping forces.

A virtual displacement $\delta\hat{w}(y,z,t)$ is applied to the system, which is assumed to be at rest during the process of application [see Wauer 2008].

$$\delta\hat{w}(y,z,t) = \sum_{n=1}^{N} \hat{\psi}_n(y,z) \underbrace{\left[\frac{\delta\,\mathcal{C}_n}{i\Omega}\,e^{i\Omega t} - \frac{\delta\,\overline{\mathcal{C}}_n}{i\Omega}\,e^{-i\Omega t}\right]}_{\delta y_n(t)} \tag{5.47}$$

Considering a plate-like structure with a damping coefficient c, the virtual work is gained out of the integral over the surface $dA = dy\,dz$ of the plate. As done for the Lagrangian in the last section, the integral over the time period T is calculated and the approximation with the *Fourier* series is applied according to (5.27) and (5.47):

$$\begin{aligned}
\int_0^T \delta W_{\mathrm{BC}}\; dt \;&=\; -\int_0^T \int_A c\, v_{\mathrm{BC}}\, \delta w\; dA\, dt \\
&=\; -\int_0^T \int_{A^{rep}} \sum_{n=1}^{N} c\;\hat{\psi}_n\,\dot{y}_n \sum_{n=1}^{N} \hat{\psi}_n\,\delta y_n\; dA\; dt
\end{aligned}$$

The application of (A.55), (A.59) and (A.76) yields:

$$\begin{aligned}
\int_0^T \delta W_{\mathrm{BC}}\; dt \;&=\; -\int_0^T \sum_{k=1}^{N}\sum_{l=1}^{N} \dot{y}_k\,\delta y_l \int_{A^{rep}} c\;\hat{\psi}_k\,\hat{\psi}_l\; dA\;\; dt \\
&\approx\; -\int_0^T L_y^{rep} L_z^{rep} \sum_{k=1}^{N}\sum_{l=1}^{N} \dot{y}_k\,\delta y_l \sum_r \sum_s c\; E_{krs}\overline{E}_{lrs}\;\; dt \\
&\approx\; -\frac{T}{i\Omega} L_y^{rep} L_z^{rep} \sum_{k=1}^{N}\sum_{l=1}^{N} \left(\overline{\mathcal{C}}_k\delta\mathcal{C}_l - \mathcal{C}_k\delta\overline{\mathcal{C}}_l\right) \sum_r \sum_s c\; E_{krs}\overline{E}_{lrs}
\end{aligned} \tag{5.48}$$

Substituting the real part of the impedance the virtual work of the damping forces for plate-like absorptive structures reads in terms of wavenumber- and frequency-dependent impedances:

$$\int_0^T \delta W_{\mathrm{BC}}\, dt \;\approx\; -\frac{T}{i\Omega} L_y^{rep} L_z^{rep} \sum_{k=1}^{N}\sum_{l=1}^{N} \left(\overline{\mathcal{C}}_k \delta\mathcal{C}_l - \mathcal{C}_k \delta\overline{\mathcal{C}}_l\right) \sum_r \sum_s \mathrm{Re}\left(Z\left(r,s,\Omega\right)\right)\; E_{krs}\overline{E}_{lrs} \tag{5.49}$$

In case of orthogonal trial functions again a simplified description is possible.

$$\int_0^T \delta W_{\mathrm{BC}}\, dt \;\approx\; -\frac{T}{i\Omega} L_y^{rep} L_z^{rep} \sum_{n=1}^{N} \left(\overline{\mathcal{C}}_n \delta\mathcal{C}_n - \mathcal{C}_n \delta\overline{\mathcal{C}}_n\right) \sum_r \sum_s \mathrm{Re}\left(Z\left(r,s,\Omega\right)\right)\; |E_{nrs}|^2 \tag{5.50}$$

In the same way as for the Lagrangian, in case of sinusoidal or cosinusoidal trial functions and a rectangular plate absorber an analytical solution is obtained for the virtual work of the non-conservative forces. The expression for $\delta W_{\mathrm{BC}}^{\mathrm{sin}}$, which is corresponding to (5.50) is given in equation (5.60).

Virtual Work of external Loads

The computation of the virtual work δW_{load} for the compound absorber is just required if this system is modeled as a single finite structure without coupling to the acoustic fluid or if a load is applied at the interface. In the second case δW_{load} can be computed using the FSI-coupling mode as well. Equation (5.52) shows the resulting expression for δW_{load}.

$$\int_0^T \delta W_{load}\, dt \;=\; \int_0^T \int_0^{L_z} \int_0^{L_y} p\left(y,z,t\right) \delta w \; dy\, dz\, dt \tag{5.51}$$

e.g. $p\left(y,z,t\right) \;=\; p\left(y,z\right)\, \cos\left(\Omega t\right)$

$$\begin{aligned} \int_0^T \delta W_{load}\, dt \;&=\; \int_0^T \int_0^{L_z} \int_0^{L_y} \frac{1}{2}\, p\left(y,z\right) \left(e^{i\Omega t} + e^{-i\Omega t}\right) \sum_{n=1}^{N} \delta\, y_n\, \hat{\psi}_n \; dy\, dz\, dt \\ &\approx\; \frac{T}{2i\Omega} \sum_{n=1}^{N} \left(\delta\mathcal{C}_n - \delta\overline{\mathcal{C}}_n\right) \int_0^{L_z^{rep}} \int_0^{L_y^{rep}} p\left(y,z\right) \sum_r \sum_s E_{nrs}\, e^{i(k_y y + k_z z)}\, dy\, dz \end{aligned} \tag{5.52}$$

5.3.2 Choice of the Trial Functions

The trial function $\psi_n(y,z)$ for the considered boundary conditions at the interface in a 3d acoustic volume is defined as the product of two one-dimensional functions

$$\psi_n(y,z) = \psi_{n_1}^{y}(y)\,\psi_{n_2}^{z}(z), \tag{5.53}$$

where n is defined as a multi-index $n = (n_1, n_2)$ in equation (5.53). For the implementation in the equilibrium formulation the *Fourier* series of the trial function $\hat{\psi}_n(y,z)$ is used. In this section properties of trial functions are discussed. Their individual advantages and disadvantages in the *Fourier* approach are analyzed and requirements are defined in order to reduce numerical errors. In the following four different types of functions are compared. The examinations are restricted to one dimension. Therefore just $\psi_{n_1}^{y}(y)$ is discussed.

For simply supported structures the fundamental system for the simply supported *Euler-Bernoulli* beam

$$\psi_{n_1}^{\sin}(y) = \sin\left(\frac{n_1\,\pi\,y}{L_y}\right) \tag{5.54}$$

could be applied for example. In case of the sinusoidal approach the computation of the Lagrangian could be carried out without a *Fourier* series as it is discussed later. Nevertheless the *Fourier* expansion is presented as an academic example in this section in order to exemplify the occurring phenomena.

In case of clamped compound absorbers for example the well known system out of hyperbolic functions [see Petersen 1996] could be implemented in the *Ritz* approach:

$$\psi_{n_1}^{\mathrm{hyp}}(y) = \sin(\lambda_{n_1}\,y) - \sinh(\lambda_{n_1}\,y) + \gamma_{n_1}\left[\cosh(\lambda_{n_1}\,y) - \cos(\lambda_{n_1}\,y)\right] \tag{5.55}$$

$$\lambda_{n_1} = \frac{n_1\,\beta_{n_1}}{L_y} \qquad \gamma_{n_1} = \frac{\sinh(\beta_{n_1}) - \sin(\beta_{n_1})}{\cosh(\beta_{n_1}) - \cos(\beta_{n_1})}$$

$$\beta_1 = 4.73004074 \qquad \beta_2 = 7.85320462$$

$$\beta_3 = 10.99560783 \qquad \beta_{n_1} = (n_1 + 0.5)\pi,\ n_1 > 3$$

In figures A.3 and A.4, which are depicted in the supplement A.7, the *Fourier* approximation of the trial functions, defined above, and also the first and second derivative of the *Fourier* series are depicted. The length of repetition for the periodic functions is defined to $L_y^{rep} = L$, where the most accurate results can be achieved for the energy-expressions, if the requirements, which are derived in this chapter, are fulfilled by the trial functions.

The rate of convergence of the *Fourier* series was discussed by Hamming [1973] for instance. It depends on the discontinuities of the function $\psi_n(y)$ itself and its derivatives $\frac{\partial^k \psi_n(y)}{\partial y^k}$. If corners occur, in case of the even sinusoidal modes for example, one has to consider *Fourier* members up to high wavenumbers for a good approximation of the function. For both, the sinusoidal and the hyperbolic modes, the function itself, which is introduced into the formulation of the kinetic energy T, is approximated with a sufficient accuracy. Having a look at the second derivatives of the hyperbolic modes $\frac{\partial^2 \psi_n^{\mathrm{hyp}}(y)}{\partial y^2}$, one recognizes a step in the function at the interval boundaries in case of odd modeshapes. Due to this step a uniform convergence of the *Fourier* series is not possible. The series converges pointwise. An overshoot occurs, which travels towards the discontinuity for rising wavenumbers. This effect is known as the *Gibbs* phenomenon [Gibbs 1899]. From the signal processing point of view the effect could be explained by a convolution of the function $\psi_n(y)$ with the inverse *Fourier* transformed of an ideal rectangular low pass filter (because just a finite number of wavenumbers can be considered).

Thus in case of hyperbolic trial functions the second derivatives of the odd modeshapes are described badly with the *Fourier* series (see figure A.4f). In case of the sinusoidal functions the effect occurs already in the approximation of the first derivatives. The second derivatives are described even worse as one can see in figure A.3e. This bad approximation leads to errors in the computation of the potential energies. The error analysis for a timber beam of a length $L_y = 5\,m$ with a *Young*'s modulus of $E = 1.2\,10^{10}\,\frac{N}{m^2}$, a density of $\rho = 380\,\frac{kg}{m^3}$ and a rectangular cross section $0.1\,m \cdot 0.15\,m$ ($EI = 3.375\,10^5\,Nm^2$) is presented in figure 5.9. The kinetic energy T is approximated well with the *Fourier* approach, whereas in case of sinusoidal modes an increasing number of wavenumbers has to be considered with an increasing number of modes.

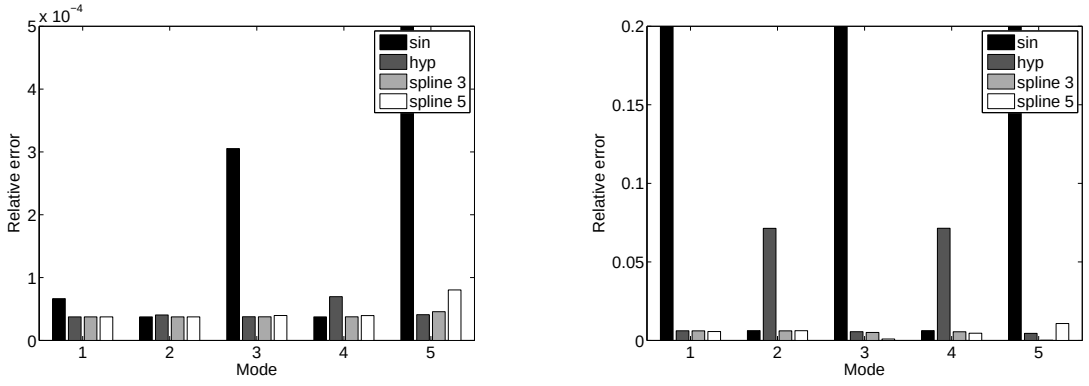

(a) Kinetic energy T **(b)** Potential energy U

Figure 5.9: Error analysis for the kinetic energy T and the potential energy U of the modeshapes for different trial functions, computed with the *Fourier* approximation with $r_{\mathsf{max}} = 10$ *Fourier* members and a frequency of excitation of $120\,Hz$

The potential energy U however cannot be expressed with a sufficient accuracy due to the bad approximation of the second derivatives. Very high error orders occur for the even sinusoidal modes and for the odd modes in case of the hyperbolic approach. The spline approaches, mentioned in figure 5.9, are introduced later on.

Different methods are applied in mathematics for reducing the oscillations due to the *Gibbs* phenomenon. The σ-approximation for example makes use of a modified computation of the *Fourier* coefficients introducing the sinc-function (*Lanczos-*σ factor), which is the inverse *Fourier* transformed of the ideal rectangular low pass filter and therefore responsible for the oscillations. The *Lanczos-*σ factor $\sigma_k(l) = \operatorname{sinc}\left(\frac{k}{l}\right)$ has to be introduced in equation (5.30) for both directions.

$$E^{\sigma}_{nrs} = E_{nrs} \operatorname{sinc}\left(\frac{r}{r_{\max}}\right) \operatorname{sinc}\left(\frac{s}{s_{\max}}\right) \tag{5.56}$$

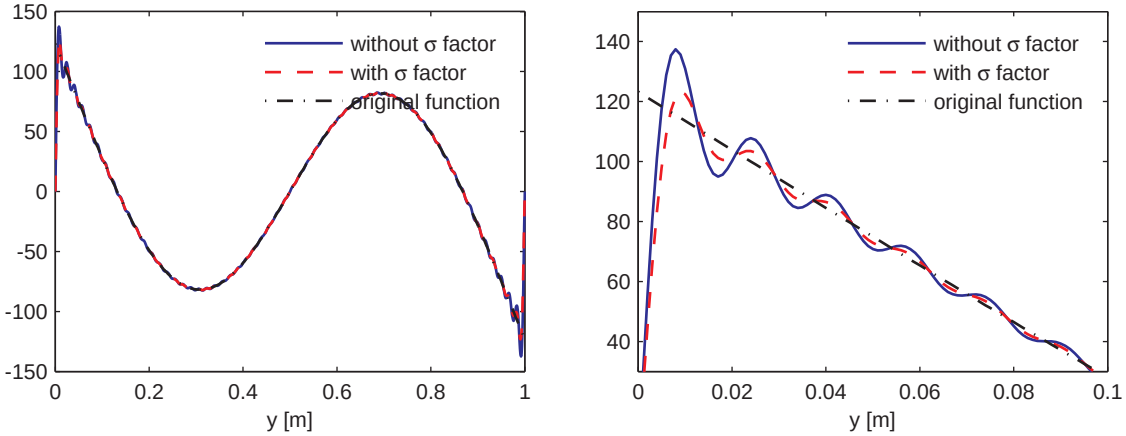

(a) $\frac{\partial^2 \psi_2^{\text{hyp}}(y)}{\partial y^2}$ **(b)** $\frac{\partial^2 \psi_2^{\text{hyp}}(y)}{\partial y^2}$ - excerpt

Figure 5.10: Reduction of *Gibb*'s phenomenon with the *Lanczos-*σ factor for a *Fourier* approximation of the second derivative for the hyperbolic approach $\psi_{n_1}^{\text{hyp}}(y)$ with $r_{\max} = 60$ *Fourier* members

In figure 5.10 the *Fourier* series of $\frac{\partial^2 \psi_2^{\text{hyp}}(y)}{\partial y^2}$ is sketched with $r_{\max} = 60$ *Fourier* members. The σ-approximation was applied to reduce the oscillations, where the *Lanczos-*σ factor was weighted by a power of four. *Fejer*'s method for example would eliminate the oscillations completely [compare Hamming 1973], but the absolute value of the function is underestimated and the partial sum rises very slow near the discontinuity. Thus both methods are not suitable. They are not able to approximate the trial functions well near the discontinuity and lead to significant errors in the potential energies (compare figures 5.14a and 5.14b).

The requirement for a good approximation up to the second derivative with a *Fourier* series is, that the trial functions are continuously differentiable up to the first derivative. If global functions should be applied, polynomials up to an order $6 + 2\,(n_{\max} - 1)$, where $n_{\max}$ marks the highest constraint mode to consider, would fulfill these requirements. The system of equations to specify the polynomial coefficients gets ill conditioned for higher modeshapes however.

Therefore the application of piecewise defined spline functions is discussed in the following. A spline of order three

$$\psi_{n_1}^{\text{spline }3}(y) = \sum_{i=1}^{n_1} a_i + b_i(x - x_{i-1}) + c_i(x - x_{i-1})^2 + d_i(x - x_{i-1})^3, \tag{5.57}$$

where the supporting points x_i $(i = 0, 1, \ldots, n_1)$ are distributed uniformly in $[0,\, L_y]$, is used at first. Considering $\psi_{n_1}(0) = \psi_{n_1}(L_y) = 0$ and $\frac{\partial^2}{\partial y^2}\psi_{n_1}(0) = \frac{\partial^2}{\partial y^2}\psi_{n_1}(L_y)$ the conditions for a good approximation are fulfilled, which can bee seen in figure A.5 in the appendix. This approach can just serve as an academic example and is without practical relevance, because it fulfills the kinetic boundary conditions of the clamped beam for even modeshapes and shows simply supported properties for odd modeshapes.

In order to simulate clamped conditions a spline of order five can be defined

$$\begin{aligned}\psi_{n_1}^{\text{spline }5}(y) = \sum_{i=1}^{n_1} a_i + b_i(x - x_{i-1}) + c_i(x - x_{i-1})^2 + d_i(x - x_{i-1})^3 + \\ + e_i(x - x_{i-1})^4 + f_i(x - x_{i-1})^5\end{aligned} \tag{5.58}$$

for the boundary conditions $\psi_{n_1}(0) = \psi_{n_1}(L_y) = 0$, $\frac{\partial}{\partial y}\psi_{n_1}(0) = \frac{\partial}{\partial y}\psi_{n_1}(L_y) = 0$ and $\frac{\partial^2}{\partial y^2}\psi_{n_1}(0) = \frac{\partial^2}{\partial y^2}\psi_{n_1}(L_y) = 0$. The corresponding *Fourier* expansion is sketched in figure A.6.

In the following example the four different types of trial functions are compared concerning their ability for the Fourier approach using the example of the simple *Euler-Bernoulli* beam:

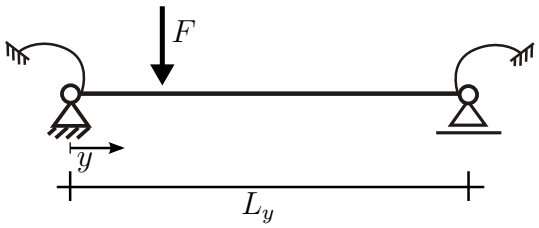

Figure 5.11: *Euler-Bernoulli* beam under a single load F

It is loaded by a single load F, which is able to excite all the modeshapes in the computed frequency band. The point of observation is defined following the same criterion. The frequency response function for the velocity is calculated with a *Ritz* approach, where the Lagrangian is computed out of the impedance of the *Euler-Bernoulli* beam according to equation (5.45). The virtual work of the single load results out of equation (5.49). Equilibrium is established with *Hamilton*'s principle.

In figures 5.12 and 5.13 the results are sketched for the spline of order five. The *Ritz*-method with an analytical calculation of the kinetic and potential energy out of the trial function is compared against the Fourier approach, where the Lagrangian is computed out of the impedance of the beam using the coefficients of the *Fourier* approximation of the trial functions. The energies are depicted in figure 5.12.

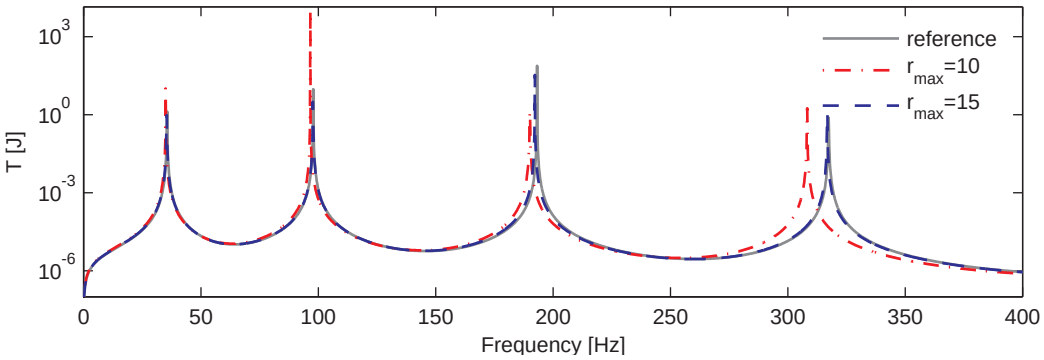

(a) Kinetic energy T

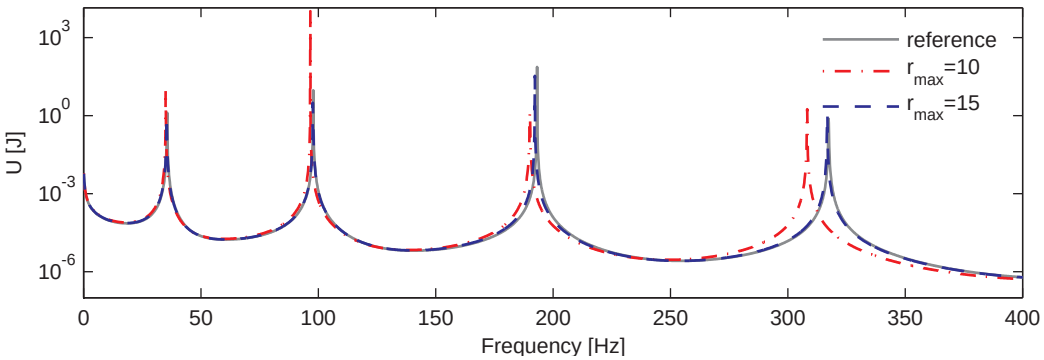

(b) Potential energy U

Figure 5.12: Results for the kinetic energy T and the potential energy U for the trial functions (spline of order 5), computed with the *Fourier* approximation (with $r_{\text{max}} = 10$ and $r_{\text{max}} = 15$ *Fourier* members) and comparison against the reference solution

The reference solution, which is the *Ritz*-approach using the trial function without a *Fourier* approach, can be approximated with sufficient accuracy, because both, the kinetic and the potential energy, are built up well. Only 15 *Fourier* members are necessary for a good

approximation of the frequency response function up to the fourth modeshapes as one can see in figure 5.13.

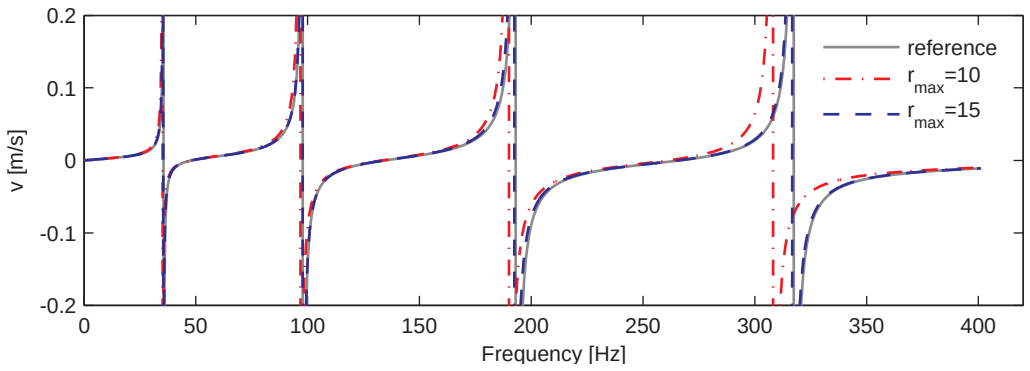

Figure 5.13: Frequency response function of the velocity $v(y)$, computed with the *Fourier* approximation (with $r_{\text{max}} = 10$ and $r_{\text{max}} = 15$ *Fourier* members) for splines of order 5 and comparison against the reference solution for this type of trial function $\psi(y)$

This example shows, that the idea to implement the boundary conditions via their impedances $Z(k_y, k_z, \Omega)$ and a *Fourier* series of the trial function $\hat{\psi}_n(y, z)$, which was suggested for the compound absorber, is applicable, if the requirements concerning the differentiability are fulfilled.

In figure 5.14 the frequency response functions for the different approaches, calculated with the *Fourier* series and the *Ritz* method, are compared against the analytical solution of the simply supported beam or the clamped beam in order to visualize the phenomena, discussed above. In figures 5.14a and 5.14b one observes, that in case of the sinusoidal (hyperbolic) trial functions the *Fourier* approach is not able to build up the even (odd) natural frequencies respectively. Having a look at the approximation of the second derivatives (figures A.3e and A.4f) one recognizes that the potential energy U is drastically overestimated for the sinusoidal functions and therefore the resonances are completely missed. In case of hyperbolic functions U is underestimated because of the jump in the second derivative, which cannot be built up accurately with the *Fourier* series, not even using a σ-approximation or *Fejer*'s method. Even if the results look better at first glance, this approach is unusable, with the exception of systems, where the mass is dominating the stiffness, because the results won't improve significantly considering more *Fourier* members and the approximation seams to have a lower energy level, than the analytical solution, which disagrees with the mechanical laws of conservation.

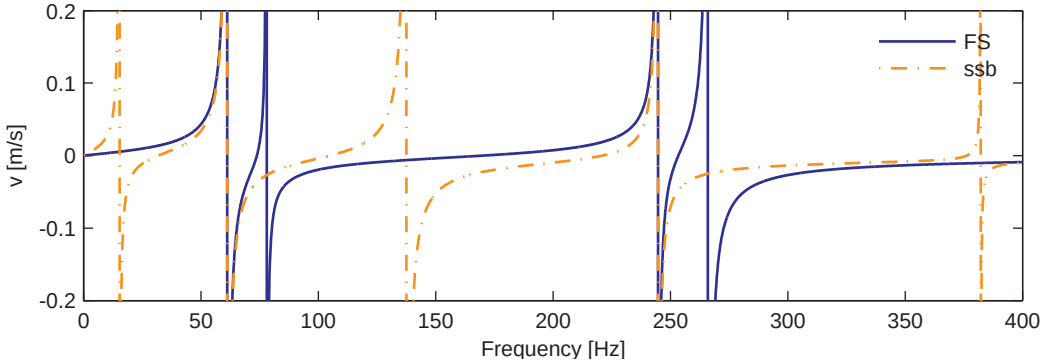

(a) Sinusoidal approach

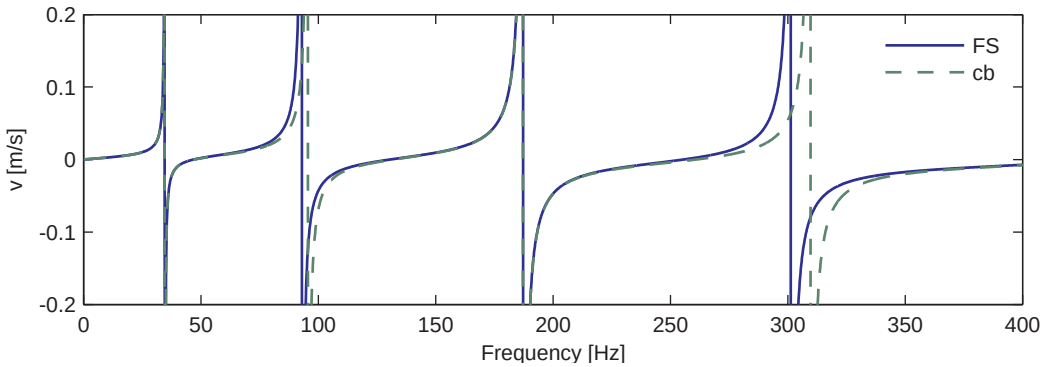

(b) Hyperbolic sine and hyperbolic cosine

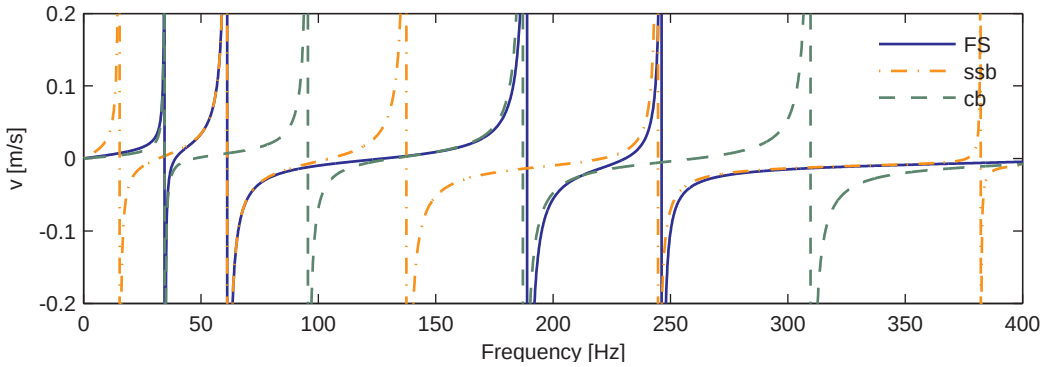

(c) Spline of order 3

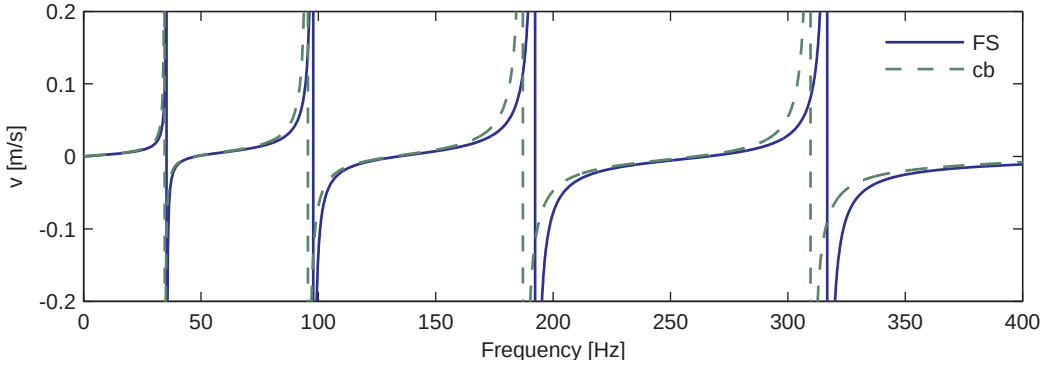

(d) Spline of order 5

Figure 5.14: Frequency response function of the velocity $v(y)$, computed with the *Fourier* approximation (FS) with $r_{\text{max}} = 10$ *Fourier* members for different types of trial functions $\psi(y)$ and comparison against the analytical solution for the clamped beam (cb) and the simply supported beam (ssb)

The spline of order three was just introduced in this academic example as the lowest order spline, which meets the requirements. As one observes in figure 5.14c this trial function approximates the clamped beam in case of even and the simply supported beam in case of odd modeshapes, because of the special characteristics of this spline function (compare figure A.5). Therefore it cannot be used in practice.

The spline of order five however, meets the requirements for the numerical approximation as well as the kinematic boundary conditions of a clamped structure. The result of the frequency response function is sketched in figure 5.14d. The numerical errors due to the *Fourier* approximation can be kept small by low costs (number of *Fourier* members), which was shown in figure 5.13. In this case the resonances are overestimated by the numerical approach (as one would expect). The quality of the prediction of course depends on the ability of the chosen approach to approximate the analytical solution. In view of the fact, that the trial functions, used in figures 5.14a and 5.14b, are the analytical solutions of the problem already, the approximation of the clamped structure with the spline of the order five is satisfactory.

Of course, as usual in the *Ritz* method, the internal forces of the beam should not be calculated out of the derivatives of the trial functions. Because of their definition the bending moment would vanish at the clamped support, which violates the laws of equilibrium. Instead, one has to calculate the internal forces out of the static problem considering the inertia forces, defined with the help of the accelerations out of the *Ritz* method.

For the room acoustical problems, underlying this thesis, the internal forces in the absorptive boundaries or the compound absorbers are not of relevance. Considering higher frequencies in acoustical simulations even the differences between simply supported or clamped boundaries are negligible.

The application of the Fourier series for the sinusoidal approach was just done for academic reasons in this section. If a sinusoidal or a cosinusoidal trial function, as defined in equations (5.53) and (5.54), should be used and if the compound absorber has got a rectangular shape, the Lagrangian and also the expressions for the virtual work can be computed analytically. Then errors due to the *Fourier* approximation based on $\frac{n_1 2\pi}{L_y}$ and $\frac{n_2 2\pi}{L_z}$ can be avoided.

The corresponding expressions can be deduced out of equations (5.46) and (5.50):

$$\int_0^T L_{\mathrm{BC}}^{\mathrm{sin}}\, dt = \frac{L_y\, L_z}{4}\frac{T}{\Omega}\sum_{n=1}^{N} \mathcal{C}_n \overline{\mathcal{C}}_n \,\mathrm{Im}\left[Z\left(\frac{n_1\,\pi}{L_y}, \frac{n_2\,\pi}{L_z}, \Omega\right)\right] \tag{5.59}$$

$$\int_0^T \delta W_{\mathrm{BC}}^{\mathrm{sin}}\, dt \;=\; -\frac{L_y\, L_z}{4}\frac{T}{i\Omega}\sum_{n=1}^{N} \left(\overline{\mathcal{C}}_n \delta\mathcal{C}_n - \mathcal{C}_n \delta\overline{\mathcal{C}}_n\right) \mathrm{Re}\left[Z\left(\frac{n_1\,\pi}{L_y}, \frac{n_2\,\pi}{L_z}, \Omega\right)\right] \tag{5.60}$$

5.4 System of Equations

As pointed out in section 5.1 *Hamilton*'s principle is applied for the formulation of the equilibrium of the coupled system. According to equation (5.2) the Lagrangian has to be set up for all components of the problem and the virtual work must be computed for the external forces as well as for the dissipative behavior of the absorbers.

Normal and coupling modes, which are specified in the CMS approach in equation (5.7), are computed for the acoustic fluid as trial functions in the scope of a *Ritz* approach and the Lagrangian of the fluid as well as the virtual work of the external loads are computed with equations (5.3)–(5.5) and (5.6) respectively. The Lagrangian of the compound absorber and the virtual work of the non-conservative damping forces are computed with (5.45) and (5.49) for instance.

The unknown complex coefficients $\mathcal{A}_i$ and $\mathcal{B}_i$ refer to the normal and the coupling modes in the acoustic volume, whereas $\mathcal{C}_i$ are the coefficients of the trial functions of the compound absorber. As pointed out in section 5.3.1 the coupling condition of the fluid and the absorber at the interface simply results in $\mathcal{B}_i = \mathcal{C}_i$ and $\bar{\mathcal{B}}_i = \bar{\mathcal{C}}_i$, because the same velocity pattern is chosen for the trial function of the absorber and for the boundary condition of the fluid at the absorber-interface. Thus the vectors for the unknown coefficients $\mathbf{x}$ and the corresponding conjugate complex values $\bar{\mathbf{x}}$ read:

$$\begin{aligned} \mathbf{x} &= \begin{bmatrix} \mathcal{A}_1 \cdots \mathcal{A}_{m_{\max}} & \mathcal{B}_1 \cdots \mathcal{B}_{n_{\max}} \end{bmatrix}^T \\ \bar{\mathbf{x}} &= \begin{bmatrix} \bar{\mathcal{A}}_1 \cdots \bar{\mathcal{A}}_{m_{\max}} & \bar{\mathcal{B}}_1 \cdots \bar{\mathcal{B}}_{n_{\max}} \end{bmatrix}^T \end{aligned} \tag{5.61}$$

The solution of the variational problem in equation (5.2) is reduced to a problem of minimization because of the *Ritz* approach. It is advantageous to express the conjugate complex coefficients with real and imaginary values in order to formulate the extremal problem:

$$\mathbf{x} = \left[\mathbf{x}^R + i\,\mathbf{x}^I\right]^T \qquad (5.62a) \qquad\qquad \bar{\mathbf{x}} = \left[\mathbf{x}^R - i\,\mathbf{x}^I\right]^T \qquad (5.62b)$$

The real and imaginary parts of the complex coefficients mark the new set of unknowns $\mathbf{y} = \left[\mathbf{x}^R \quad \mathbf{x}^I\right]^T$, where the total number of real valued unknowns is $2\,(m_{\max} + n_{\max})$. Here $m_{\max}$ and $n_{\max}$ are the maximum numbers of normal and coupling modes respectively.

$$\begin{aligned} \mathbf{x}^R &= \left[\mathcal{A}_1^R \cdots \mathcal{A}_{m_{\max}}^R \quad \mathcal{B}_1^R \cdots \mathcal{B}_{n_{\max}}^R\right]^T \\ \mathbf{x}^I &= \left[\mathcal{A}_1^I \cdots \mathcal{A}_{m_{\max}}^I \quad \mathcal{B}_1^I \cdots \mathcal{B}_{n_{\max}}^I\right]^T \end{aligned} \qquad (5.63)$$

For the consideration of the virtual work a vector $\delta\mathbf{y}$ is specified analogously. Carrying out the minimization of the Lagrangian one obtains a system of real valued linear equations

$$\mathbf{K}\,\mathbf{y} = \mathbf{F}, \qquad (5.64)$$

where the matrix of coefficients K_{ij} reads

$$K_{ij} = \frac{\partial^2 \int_0^T L_A \; dt}{\partial y_i \, \partial y_j} + \frac{\partial^2 \int_0^T L_{\mathrm{BC}}(Z) \; dt}{\partial y_i \, \partial y_j} + \frac{\partial^2 \int_0^T \delta W_{\mathrm{BC}}^{\mathrm{nc}}(Z) \; dt}{\partial\, \delta y_i \, \partial y_j} \qquad (5.65)$$

and the load vector $\mathbf{F} = \left[\mathbf{F}^R \quad \mathbf{F}^I\right]^T$ considers the external forces:

$$F_i = -\frac{\partial \int_0^T \delta W_{\mathrm{Load}}^{\mathrm{nc}} \; dt}{\partial\, \delta y_i} \qquad (5.66)$$

Defining submatrices $\mathbf{K}_{rs}$ for the matrix of coefficients, equation (5.64) reads:

$$\begin{bmatrix} \mathbf{K}_{11} & \mathbf{K}_{12} \\ \mathbf{K}_{21} & \mathbf{K}_{22} \end{bmatrix} \begin{bmatrix} \mathbf{x}^R \\ \mathbf{x}^I \end{bmatrix} = \begin{bmatrix} \mathbf{F}^R \\ \mathbf{F}^I \end{bmatrix} \qquad (5.67)$$

In consequence of the complex property of the unknown coefficients the relations

$$\mathbf{K}_{11} = \mathbf{K}_{22} \qquad (5.68)$$

$$\mathbf{K}_{21} = -\mathbf{K}_{12} \qquad (5.69)$$

hold for the submatrices. Of course the system of equations can be established with $m_{\max} +$

$n_{\max}$ unknown complex coefficients as well:

$$\left[\mathbf{K}_{11} + i\,\mathbf{K}_{21}\right]\,\mathbf{x} = \left[\mathbf{F}^R + i\,\mathbf{F}^I\right] \tag{5.70}$$

After solving the system of linear equations the sound field in the acoustic cavity, expressed with its primary variables $p_A(\mathbf{x}, t)$ and $\mathbf{v}_A(\mathbf{x}, t)$, is composed according to section 5.2.

5.5 Numerical Results for the FSI-problem

5.5.1 Application to 1d Structures

Comparison with reference solution for a SDOF impedance

In the following the FSI-approach, which was derived in the previous sections, is applied to the simple geometry $V = [0, L_x] \times [0, L_y] = [0, 8\,m] \times [0, 1\,m]$, which is sketched in figure 5.15. Plane waves are excited in the structure applying a pressure p_0 at $x = L_x$, which is harmonically oscillating in time with a circular frequency of excitation Ω.

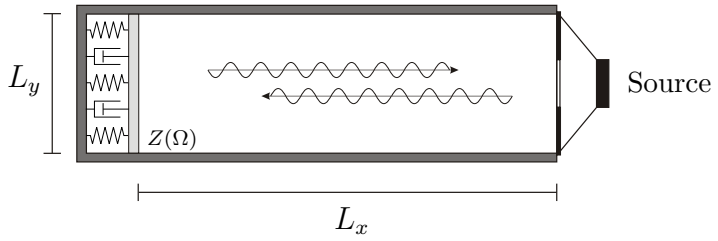

Figure 5.15: Geometry of the benchmark example

The boundary at $x = 0$ is described by the point impedance $Z(\Omega)$

$$Z(\Omega) = i\left(\Omega m - \frac{k}{\Omega}\right) + c\,, \tag{5.71}$$

where $m = 10\,kg$, $k = 10^4\,\frac{N}{m}$ and $c = 200\,\frac{Ns}{m}$ are the mass, the stiffness, and the damping coefficient of the impedance boundary condition. For this problem the analytical solution can be derived for the harmonic response. Starting from the fundamental system [see Fahy 2000]

$$p(x,t) = A\,e^{i\,(\Omega\,t - k_A\,x)} + B\,e^{i\,(\Omega\,t + k_A\,x)} \tag{5.72}$$

$$v_x(x,t) = \frac{1}{\rho_A\,c_A}\left[A\,e^{i\,(\Omega\,t - k_A\,x)} - B\,e^{i\,(\Omega\,t + k_A\,x)}\right] \tag{5.73}$$

the impedance at the interface $x = 0$ reads:

$$Z'(\Omega) = \frac{Z(\Omega)}{Z_0} = -\frac{p(x=0,t)}{v(x=0,t)\,\rho_0\,c} = -\frac{A+B}{A-B} \quad \Leftrightarrow \quad \frac{B}{A} = \frac{Z'-1}{Z'+1} \tag{5.74}$$

The complex coefficients A and B can be derived out of the boundary conditions

$$\begin{bmatrix} \frac{1+Z'}{1-Z'} & 1 \\ e^{-i\,k_A\,L_x} & e^{i\,k_A\,L_x} \end{bmatrix} \begin{bmatrix} A \\ B \end{bmatrix} = \begin{bmatrix} 0 \\ p_0 \end{bmatrix}. \tag{5.75}$$

For the numerical simulation the set of basis functions has to be defined. It consists of four normal and two coupling modes for the pressure $p(x, y, t)$ and the sound velocity $\mathbf{v}(x, y, t)$. The first coupling mode provides the coupling with the point impedance. The second one is necessary for the application of the loading at $x = L_x$, because the normal modes, which are computed for reflective wall conditions, prohibit any normal displacement at the boundaries. They are computed out of equation (A.34) obeying the boundary conditions (A.35, A.36).

The geometry is subdivided into eight equally sized elements. The normal and the coupling modes for the pressure and the sound velocity are computed with the SFEM as described in section A.3. The polynomial degree of the basis functions in each element is $P = 5$ and the number of quadrature points is $W = 7$.
In the following the spatial average of the transfer functions for the sound pressure L_{Amp}, as defined in equation (5.76), is computed for a harmonic excitation up to a frequency of excitation $150\,Hz$ and compared against the analytical solution.

$$L_{Amp} = 10\log\sqrt{\frac{1}{V}\int_V \left|\frac{p}{p_0}\right|^2 dV} \quad [dB] \tag{5.76}$$

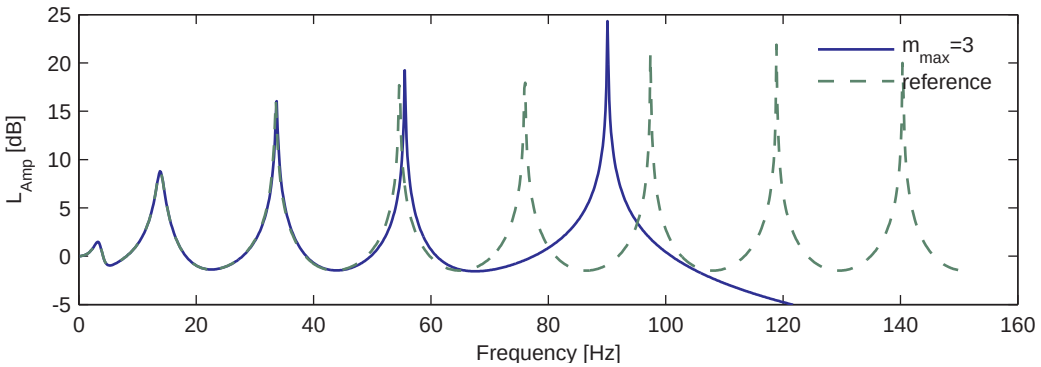

Figure 5.16: Comparison of analytical and numerical solution for the spatial average of the amplification factor of the sound pressure L_{Amp}

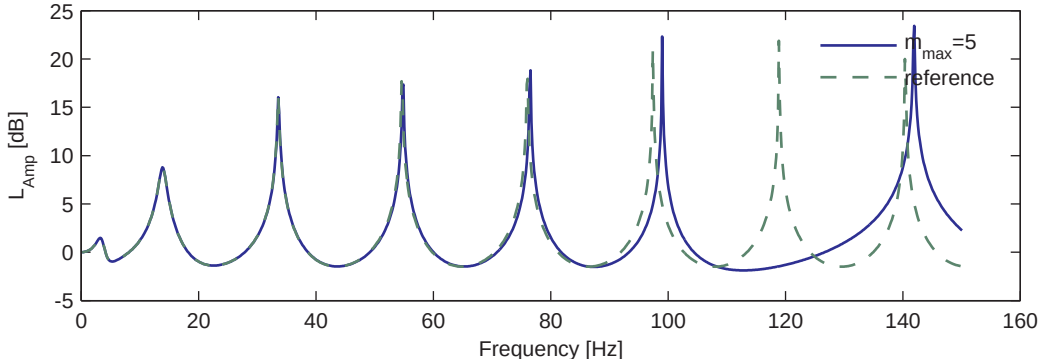

(a) $m_{\text{max}} = 5$ normal modes

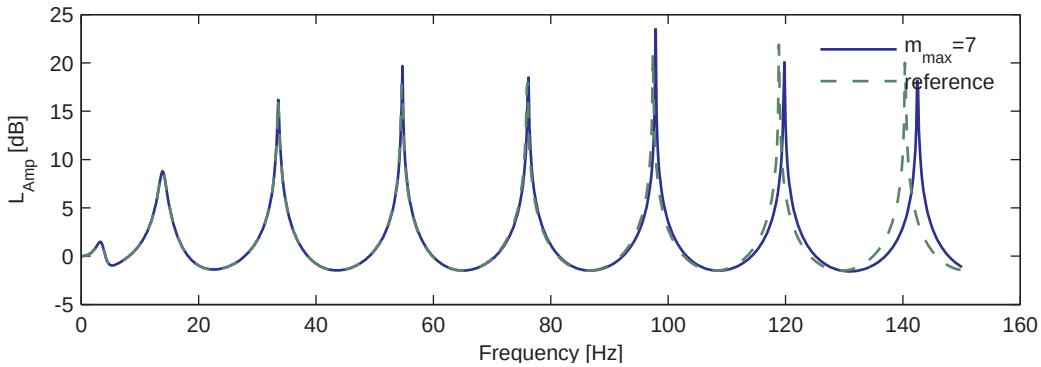

(b) $m_{\text{max}} = 7$ normal modes

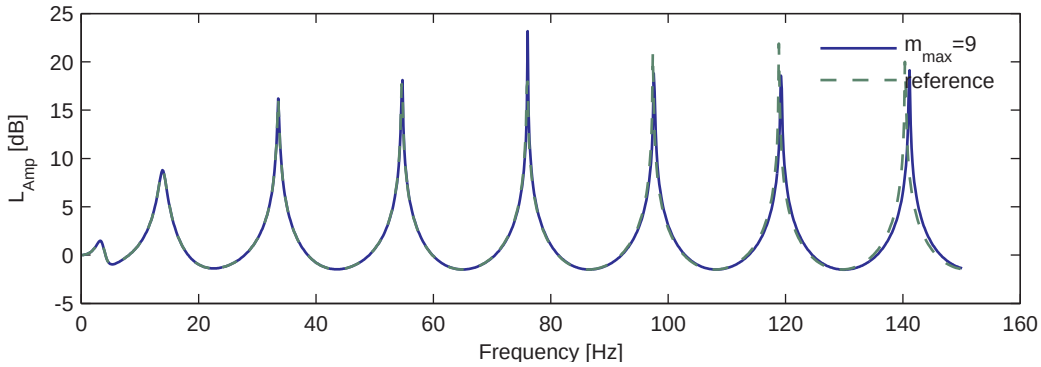

(c) $m_{\text{max}} = 9$ normal modes

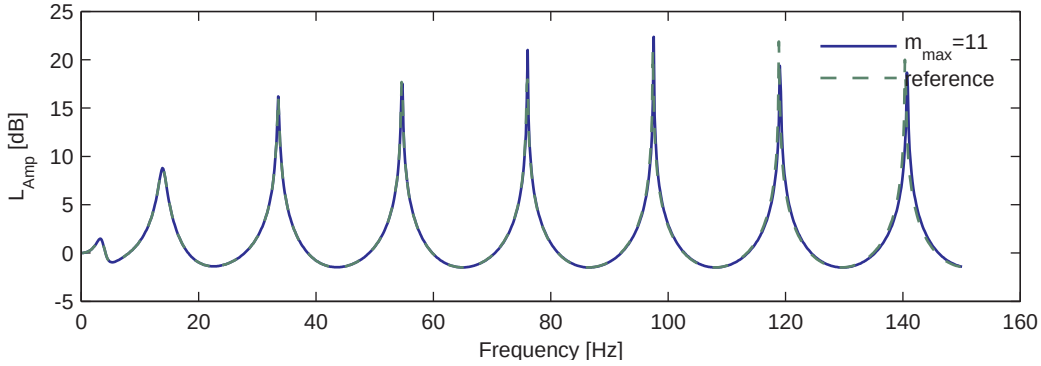

(d) $m_{\text{max}} = 11$ normal modes

Figure 5.17: Study on the number of normal modes considered in the CMS

In figure 5.16 the numerical results are depicted for three normal modes. One observes a good agreement of both solutions in the frequency range, which is covered by the set of trial functions. An increasing difference between the analytical and the numerical solution occurs from the third resonance on (around $53\,Hz$) and arises from the low number of normal modes in relation to the maximum frequency of excitation.

In figure 5.17 a comparison regarding the number of normal modes $m_{\max}$, considered in the SFEM, is depicted. In order to avoid the numerical error due to modal truncation it is recommended to consider normal modes up to a natural frequency, which is 50% above the maximum frequency of excitation. Following this rule of thumb, one has to consider $m_{\max} = 11$ normal modes for a maximum frequency of excitation of $150\,Hz$, where a good agreement with the analytical solution is achieved. If higher modeshapes are excited explicitly due to the pattern of the load, these patterns have to be considered in the computation as well.

In addition to the setup with $k = 1.0\,10^4$, where the impedance of the boundary condition was tuned to $5\,Hz$, another configuration, which is tuned to $65\,Hz$, is sketched in figure 5.18 in order to visualize the efficiency of the approach.

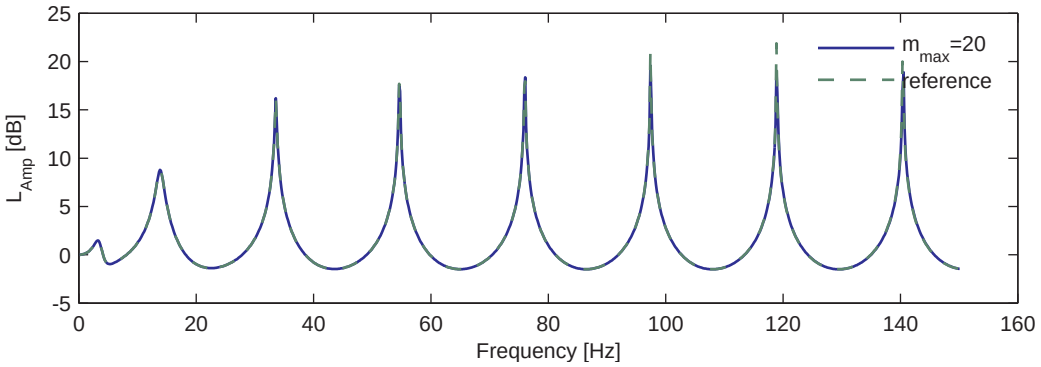

(a) $k = 1.0 \cdot 10^4$ - tuned to $5\,Hz$

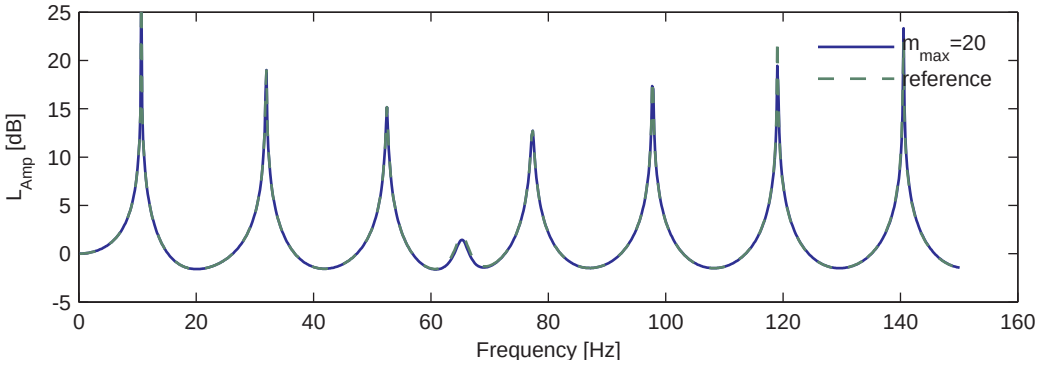

(b) $k = 1.7 \cdot 10^6$ - tuned to $65\,Hz$

Figure 5.18: Coupling with variously tuned impedances

Dissipation due to a porous absorber

In the following example the FSI of the acoustic fluid and porous absorbers is discussed in order to present the application of the method to measured impedances as well as to impedances out of numerical simulations. The rectangular acoustic volume, sketched in figure 5.19, with $V = [0, L_x] \times [0, L_y] = [0, 3\,m] \times [0, 1\,m]$ is modeled with Spectral Finite Elements as described in section A.3.

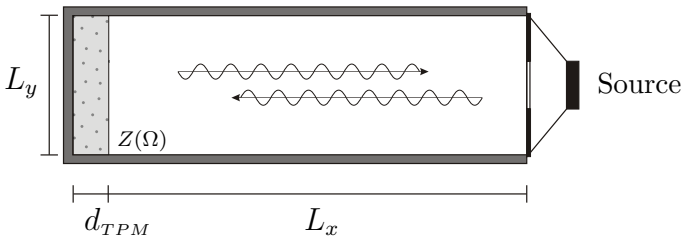

Figure 5.19: 1d structure with porous absorber

A layer out of porous material with a thickness d is mounted on the reflective wall at $x = 0$ and plane waves are excited in the system at $x = L_x$ in x-direction in the frequency range up to $275\,Hz$. The response of the sound pressure within the cavity is evaluated along the x-coordinate.

A layer of Melamine Foam with a thickness of $7.2\,cm$, a $10.2\,cm$ layer of Polyurethane Foam and a $10.3\,cm$ layer of Mineral Wool are used in this example to represent the porous sheet. These porous materials served as measured references in section 4.4.1, where the impedance $Z(\Omega)$ and the absorption ratio $\alpha(\Omega)$ were computed with the TPM-ITM-model (compare figures 4.12, 4.14, 4.16). In the following the measured values and the numerical impedances are applied as boundary conditions for the computation.

Figure 5.20 shows the transfer functions for the pressure, averaged over the acoustic volume according to equation (5.76). The results with the computed impedances Z_{sim} are plotted against the solution with measured impedances Z_{meas}.

A reduction of the amplitudes, especially at the location of the natural frequencies of the system, can be observed as well as the fact, that the porous absorber is working more efficiently for higher frequencies. Here the resulting wavelengths λ are shorter and therefore the sound velocity within the absorber compared to the maximum velocity is higher than for low frequencies of excitation.

The results also illustrate, that the simulation of the acoustic properties for porous foams with the TPM/ITM-model as a step of preprocessing for a FSI-simulation is suitable, because there is a good agreement between the results with the measured and the simulated impedances.

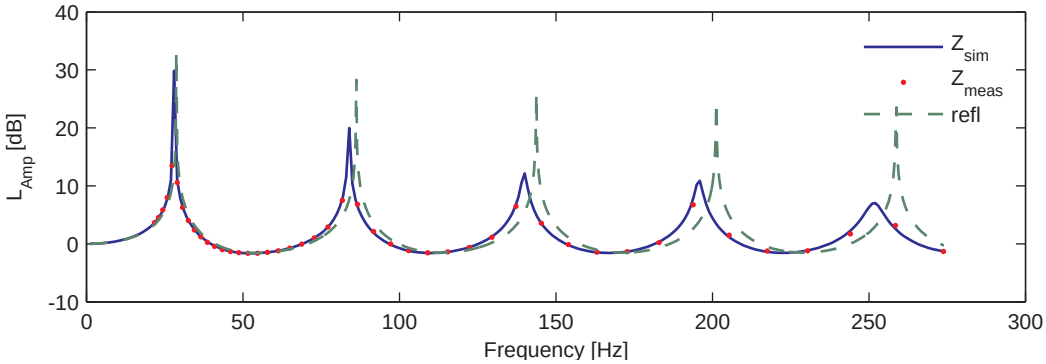

(a) $7.2\,cm$ layer of Melamine Foam

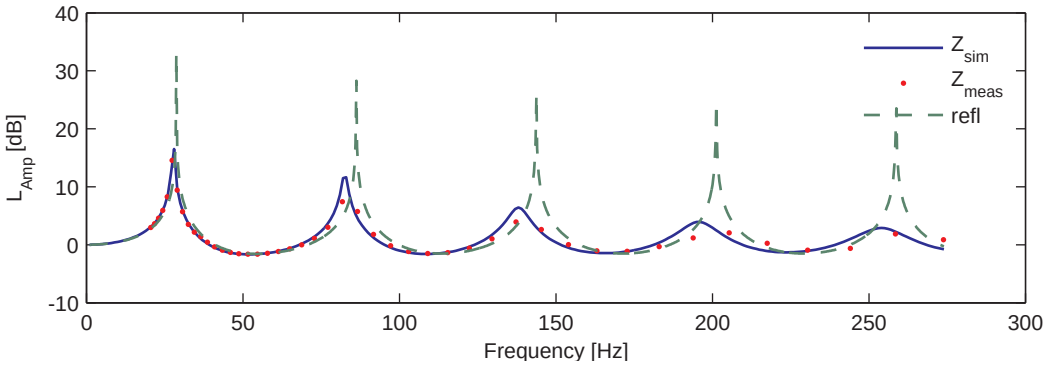

(b) $10.2\,cm$ layer of Polyurethane Foam

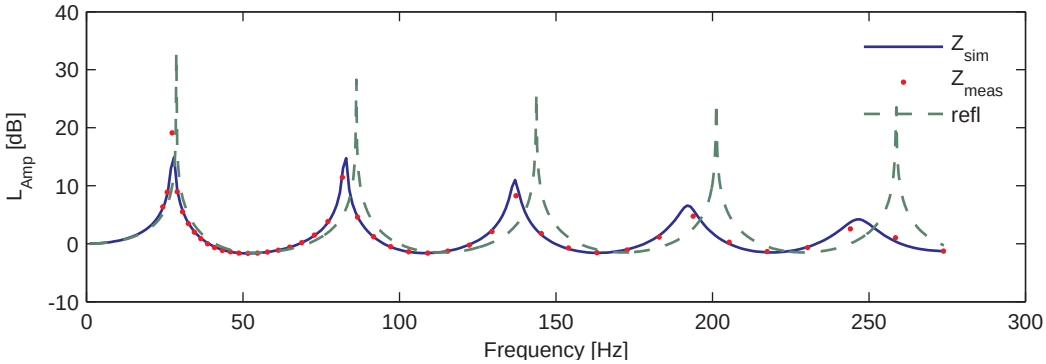

(c) $10.3\,cm$ layer of Mineral Wool

Figure 5.20: FSI-coupling with porous layers

The slight frequency shifts, which are observed between the results computed with Z_{sim} and Z_{meas} in case of the polyurethane foam, occur, because the imaginary part of the impedance,

which is sketched in figure 4.14b, is approximated worse than in case of the melamine foam and the mineral wool.

5.5.2 Application to 2d Structures

Holohedral and subregional coupling

In this section the FSI-model is applied to a 2d rectangular geometry $V = [0, L_x] \times [0, L_y] = [0, 6\,m] \times [0, 2\,m]$. The structure is modeled with 192 spectral finite elements and loaded by a harmonically oscillating point source with an amplitude $p_0 = 1\,[\mathrm{Pa}]$ at $x = 1.15\,m$ and $y = 0.77\,m$. A porous absorber is mounted at the interface $x = 0$, where sinusoidal coupling modes were specified (compare section 5.3.2).

Two different coupling techniques are compared (see figure 5.21). Whereas the holohedral coupling modes cover the whole interface, in case of the subregional coupling modes, which were introduced in section 5.2.2, just a part of the wall is covered with the absorber. In

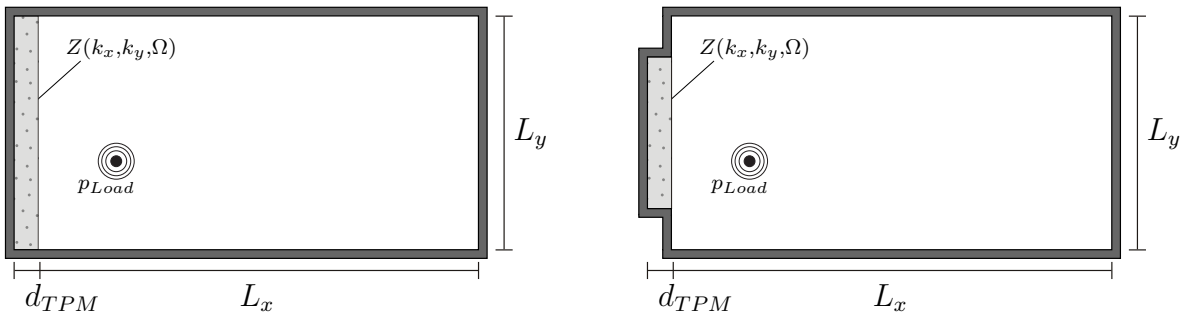

(a) holohedral coupling **(b)** subregional coupling

Figure 5.21: 2d structure with porous absorber

the first step frequency-response functions are computed. The location of the load is chosen arbitrarily in order to excite nearly all modeshapes. Analogously to the 1d case, the response for several points of observation is averaged according to equation (5.76) and the absorber is specified as a $7.2\,cm$ layer of Melamine Foam, a $10.2\,cm$ layer of Polyurethane Foam and a $10.3\,cm$ layer of Mineral Wool, where the numerical impedances out of the TPM-ITM computation are used.

The results for the averaged FRFs are depicted in figure 5.22 for the holohedral coupling modes. The subregional results are presented for an absorber with a length of $1\,m$ in figure 5.23. Both results are figured against the results for the reflective box. In contrast to the 1d case, the modal density is increasing for higher frequencies. Comparing the holohedral results

in figure 5.22 for the different porous materials, one again observes a different efficiency, which is linked to the absorption ratios $\alpha(\Omega)$ (compare figures 4.12, 4.14, 4.16). In addition to the dependency on frequencies, the absorption is depending on the angle of incidence of the wavenumber respectively (compare figure 4.30).

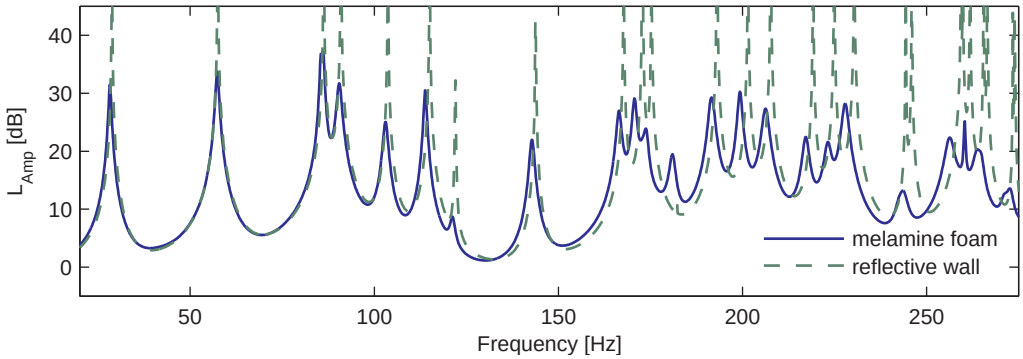

(a) $7.2\,cm$ Melamine Foam – compare figure 4.12

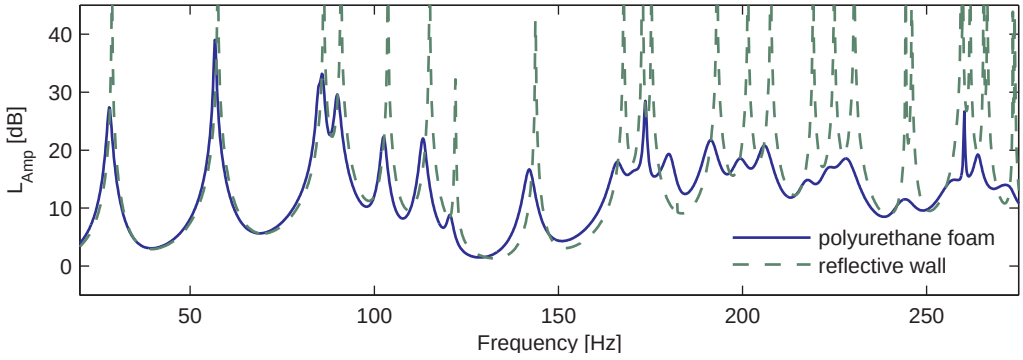

(b) $10.2\,cm$ layer of Polyurethane Foam – compare figure 4.14

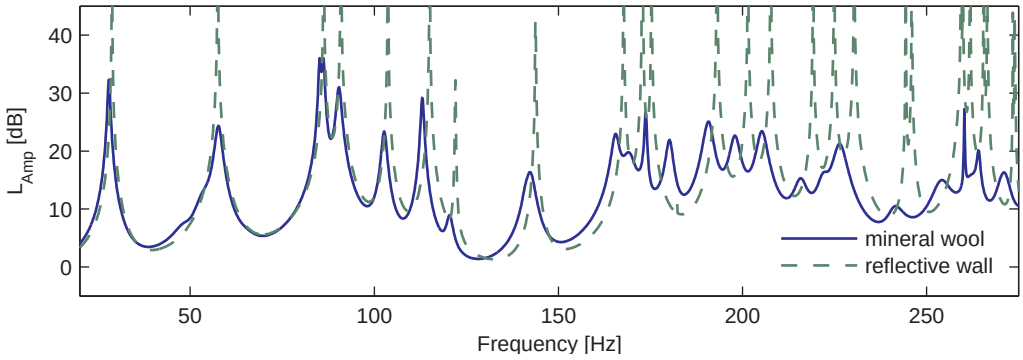

(c) $10.3\,cm$ layer of Mineral Wool – compare figure 4.16

Figure 5.22: FSI-Model with various porous absorbers - holohedral coupling

The results for the subregional coupling modes show the same characteristics. Due to the fact, that the absorptive area, which is totally installed in the room, is just one half of the

area, installed in the holohedral case, the resulting sound pressure level is higher. Due to the fact, that the absorptive interface is normal to the x-axis, modeshapes with dominant velocities in x-direction are reduced more efficiently, than modeshapes in y-direction. This is observed in figure 5.23a for example, where the resonances at $28\,Hz$ and $57\,Hz$ (the first and the second plane wave mode in x-direction) are reduced more significantly than the peaks at $86\,Hz$, $172\,Hz$ and $273\,Hz$. There the first modeshapes in y-direction occur in addition to modes in x-direction (multiple eigenvalues).

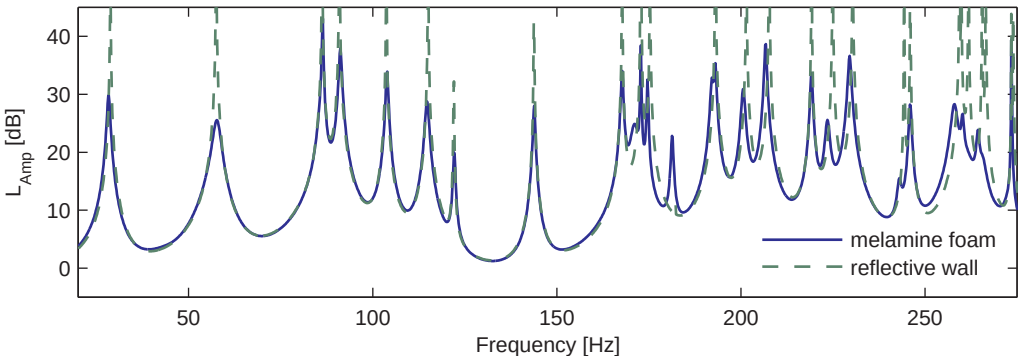

(a) $7.2\,cm$ Melamine Foam – compare figure 4.12

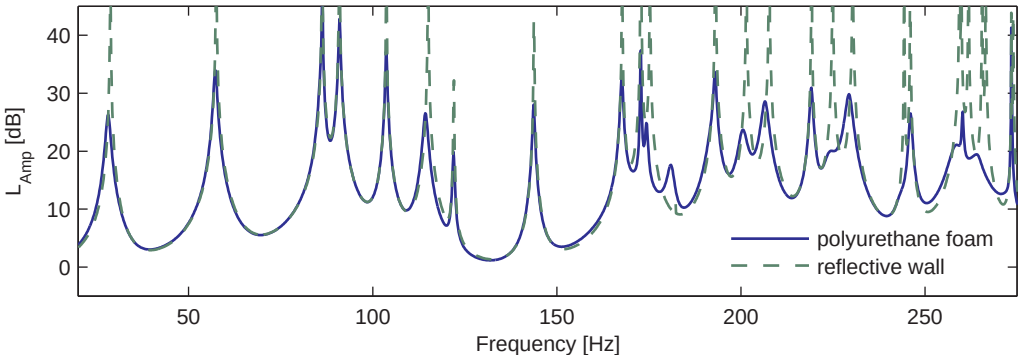

(b) $10.2\,cm$ layer of Polyurethane Foam – compare figure 4.14

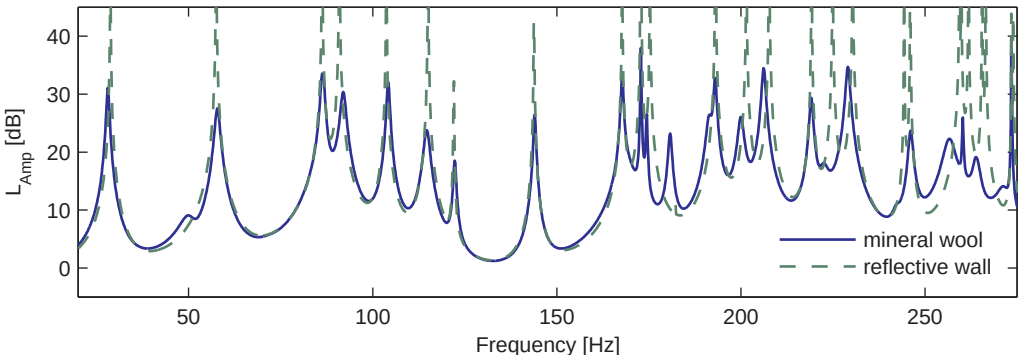

(c) $10.3\,cm$ layer of Mineral Wool – compare figure 4.16

Figure 5.23: FSI-Model with various porous absorbers - subregional coupling

In the second step the spatial resolution of the pressure and the velocity fields is computed for individual frequencies of excitation. The results are shown exemplarily for the Melamine Foam as porous material. The location of the sound source is marked with a white circle in figures 5.24 to 5.26 and the absorber is marked with a bold black line at $x = 0$.

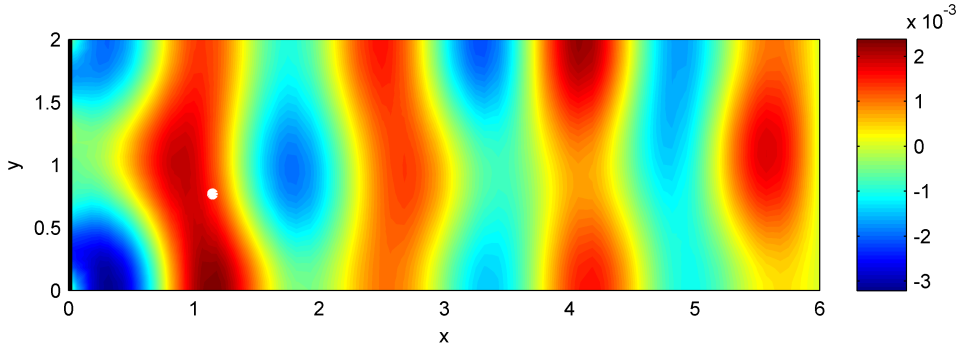

(a) Sound-velocity $v_x(x, y)$ [m/s] in x-direction

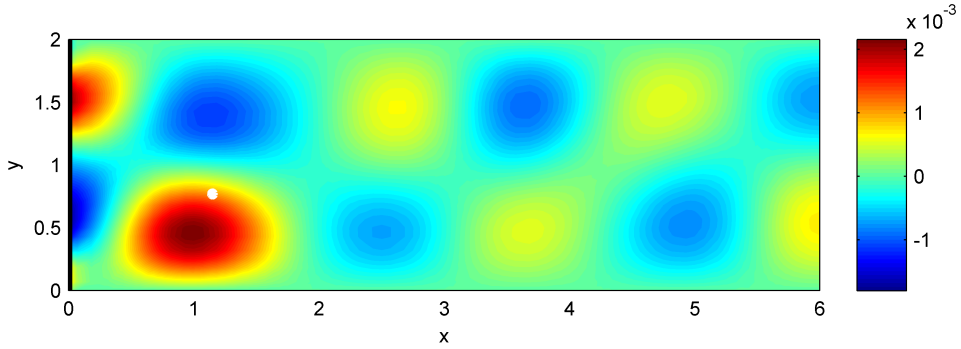

(b) Sound-velocity $v_y(x, y)$ [m/s] in y-direction

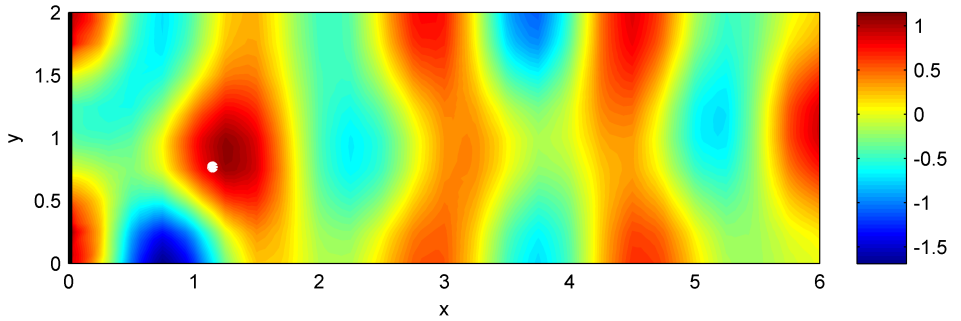

(c) Sound-pressure $p(x, y)$ [Pa]

Figure 5.24: FSI-Model with a $7.2\,cm$ Melamine Foam (holohedral coupling) – spatial resolution for an excitation with a unit point source at a frequency of $228\,Hz$

The system is excited with a frequency of $228\,Hz$, which is equal to the natural frequency of the $(8, 0)$-mode of the room with reflective walls. This modeshape dominates the harmonic

response for both coupling cases, whereas the small interface (5.25) "disturbs" the reflective modeshape less than the holohedral one does. Exciting the subregional system with $229.5\,Hz$ (see figure 5.26), the vibration pattern is already characterized by the $(5, 2)$-mode of the room with reflective walls due to the high modal density.

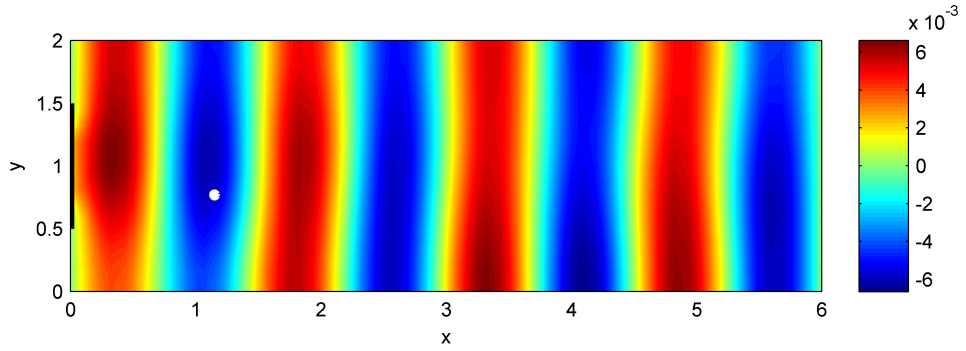

(a) Sound-velocity $v_x(x, y)$ [m/s] in x-direction

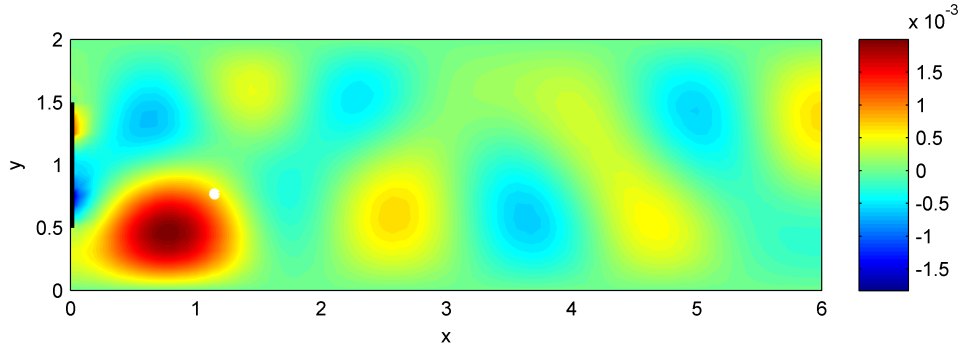

(b) Sound-velocity $v_y(x, y)$ [m/s] in y-direction

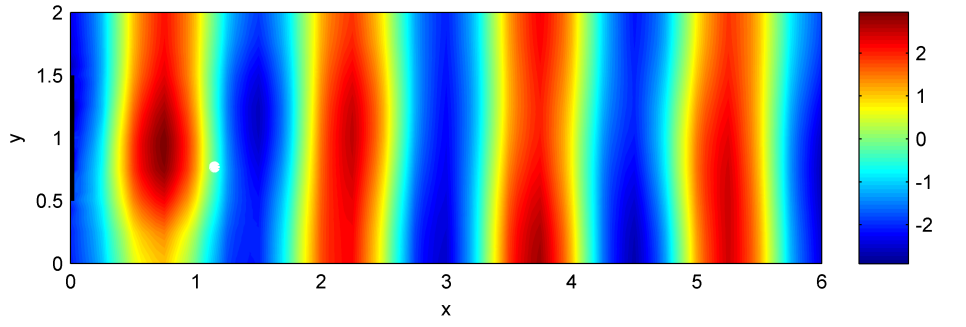

(c) Sound-pressure $p(x, y)$ [Pa]

Figure 5.25: FSI-Model with a $7.2\,cm$ Melamine Foam (subregional coupling) – spatial resolution for an excitation with a unit point source at a frequency of $228\,Hz$

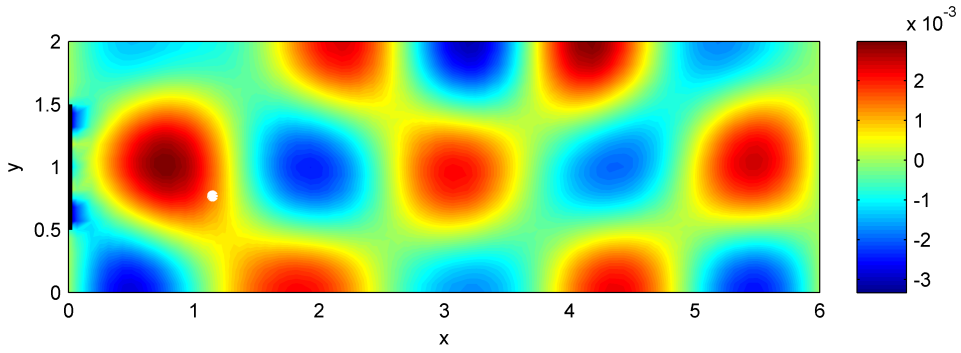

(a) Sound-velocity $v_x(x, y)$ $[\mathrm{m/s}]$ in x-direction

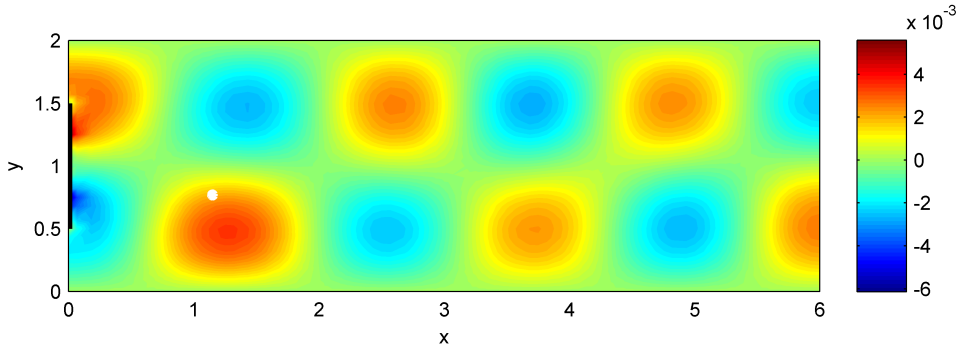

(b) Sound-velocity $v_y(x, y)$ $[\mathrm{m/s}]$ in y-direction

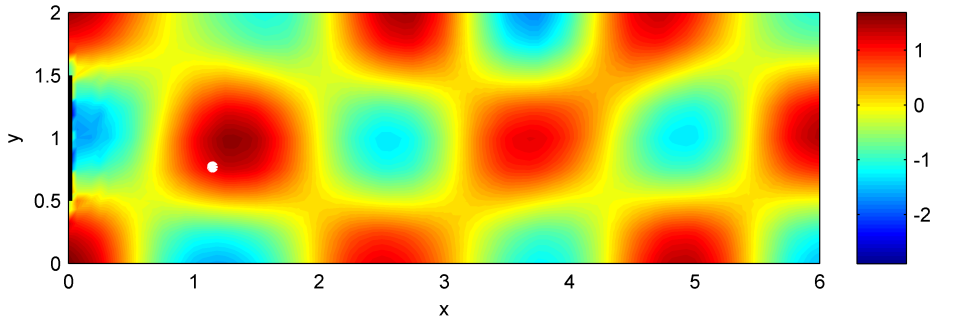

(c) Sound-pressure $p(x, y)$ $[\mathrm{Pa}]$

Figure 5.26: FSI-Model with a $7.2\,cm$ Melamine Foam (subregional coupling) – spatial resolution for an excitation with a unit point source at a frequency of $229.5\,Hz$

Inclined walls

The variability of the method concerning geometric modeling is shown, in principle, in the next example. The normal and coupling modes can be computed for arbitrary geometries with the SFEM. The only restriction, given by the application of the ITM for the Lagrangian of the absorber, is, that the interface has to be plain.

In the following the box model of the last example is modified by inclining the rear-wall. The wall containing the interface could be inclined as well. The geometry of the system is sketched in figure 5.27, where $L_x^1 = 6\,m$, $L_x^2 = 1.5\,m$ and $L_y = 2\,m$. The model is set up with 192 spectral finite elements. The interface is covered with a $7.2\,cm$ layer of Melamine Foam in analogy to the last example. Two different load cases are investigated. At first the unit point source is located at $x = 1.15\,m$ and $y = 0.77\,m$ and in a second computation the load is applied at $x = 5.89\,m$ and $y = 1.71\,m$, where the locations are chosen under the premise of exciting nearly all modeshapes.

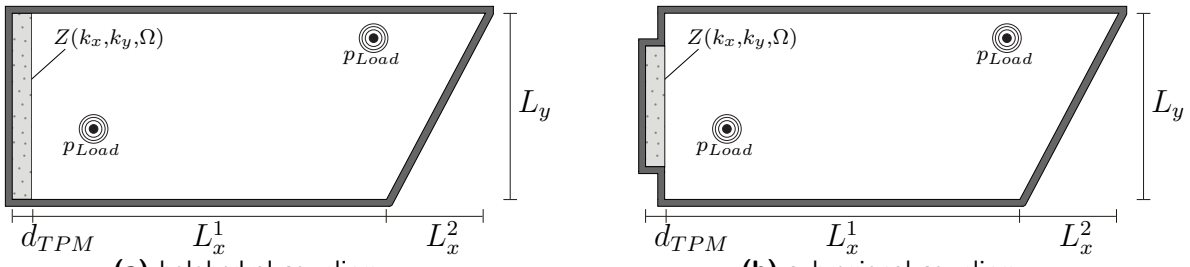

(a) holohedral coupling **(b)** subregional coupling

Figure 5.27: 2d structure with with inclined wall and porous absorber

In figures 5.28 and 5.29 the steady state response for the sound pressure level is sketched for both load cases. The different interface-specifications are compared against the system with reflective walls for a frequency of excitation of $163\,Hz$. Due to the fact, that the frequency of excitation is near to a natural frequency, one specific modeshape is excited and very high sound pressures occur in case of the undamped system (figures 5.28c and 5.29c). A significant reduction is achieved due to the application of the absorptive layer at the boundary. Comparing the results in figures 5.28a and 5.28b as well as in figures 5.29a and 5.29b one observes lower sound pressure levels for the holohedral case, because here the absorptive area, which is introduced into the system by the boundary condition, and therefore the dissipation of energy is higher than for subregional coupling.

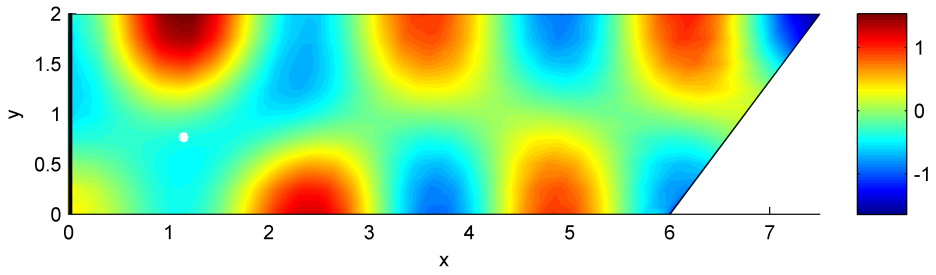

(a) $7.2\,cm$ Melamine Foam – holohedral coupling

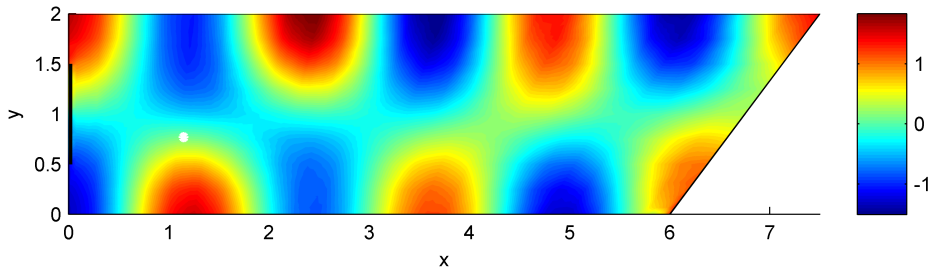

(b) $7.2\,cm$ Melamine Foam – subregional coupling

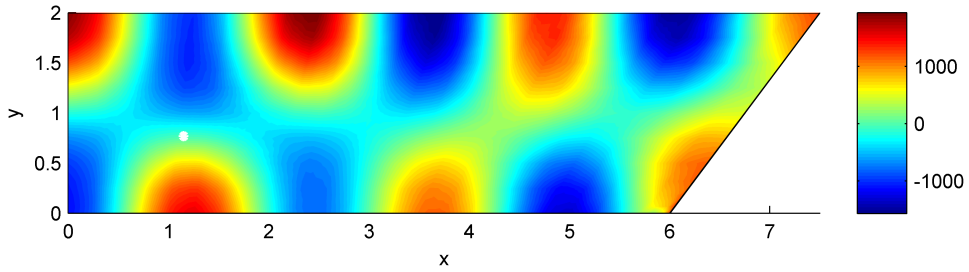

(c) System with reflective walls

Figure 5.28: Sound-pressure $p(x, y)$ [Pa] for a frequency of excitation of $163\,Hz$ – spatial resolution for a unit point source at $x = 1.15\,m$ and $y = 0.77\,m$

The point source, located at $x = 1.15\,m$ and $y = 0.77\,m$, yields higher sound pressure levels than the load, applied at $x = 5.89\,m$ and $y = 1.71\,m$. This results out of the modal load, which is higher for this load case as one can see from the velocity patterns in figures 5.30 and 5.31.

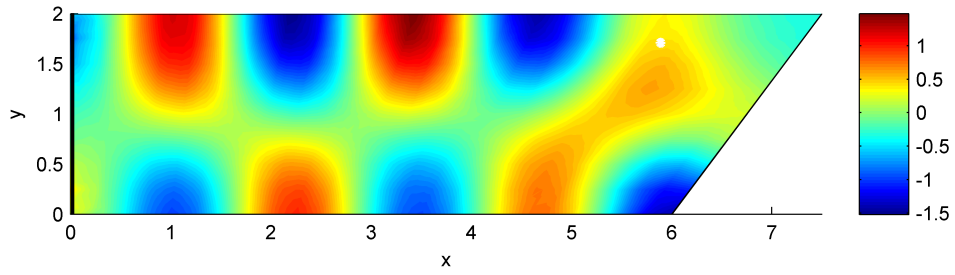

(a) $7.2\,cm$ Melamine Foam – holohedral coupling

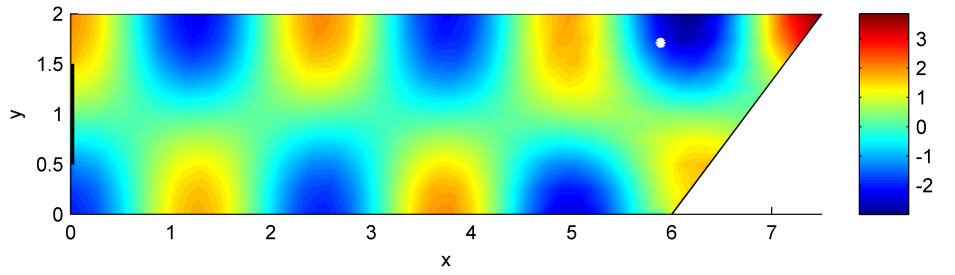

(b) $7.2\,cm$ Melamine Foam – subregional coupling

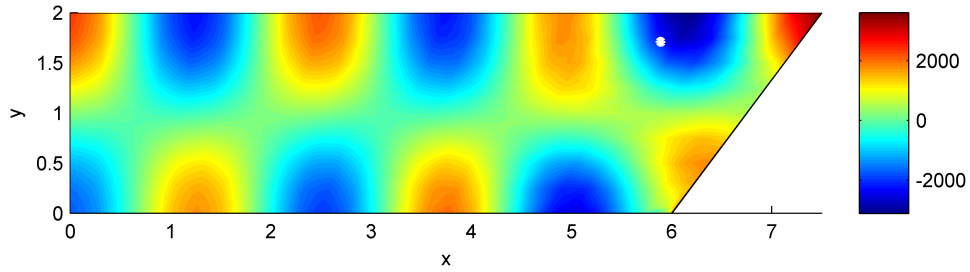

(c) System with reflective walls

Figure 5.29: Sound-pressure $p(x, y)$ [Pa] for a frequency of excitation of $163\,Hz$ – spatial resolution for a unit point source at $x = 5.89\,m$ and $y = 1.71\,m$

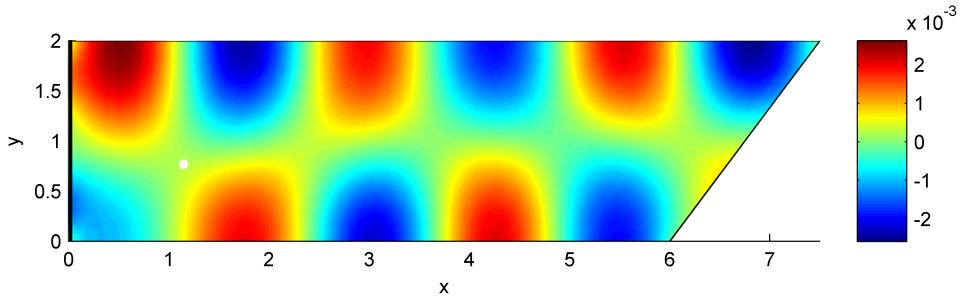

(a) Sound source at $x_L = 1.15\,m$, $y_L = 0.77\,m$ – holohedral coupling

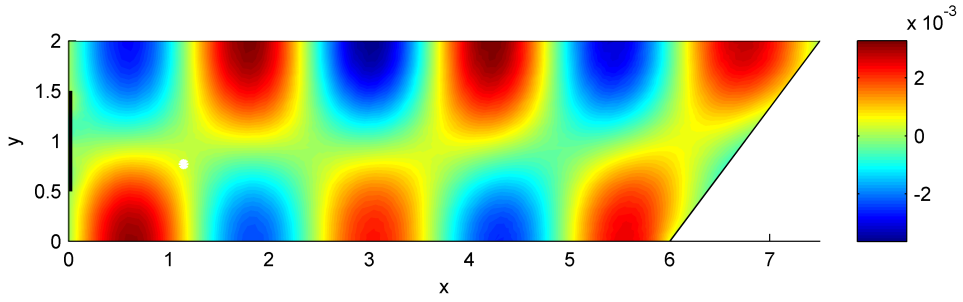

(b) Sound source at $x_L = 1.15\,m$, $y_L = 0.77\,m$ – subregional coupling

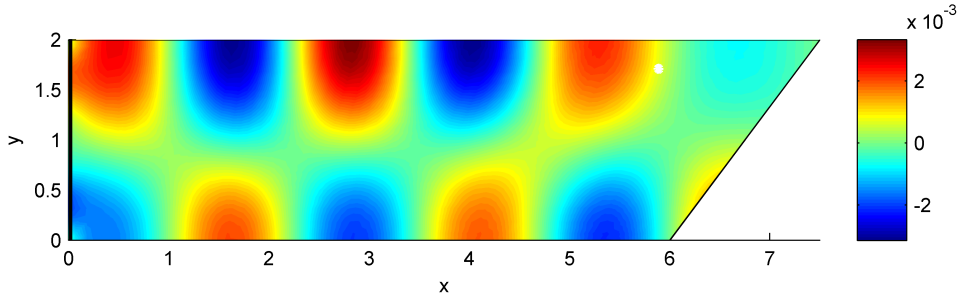

(c) Sound source at $x_L = 5.89\,m$, $y_L = 1.71\,m$ – holohedral coupling

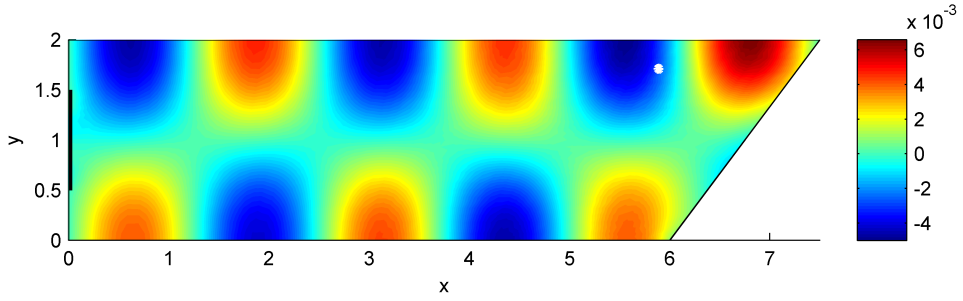

(d) Sound source at $x_L = 5.89\,m$, $y_L = 1.71\,m$ – subregional coupling

Figure 5.30: Sound-velocity $v_x(x, y)$ [m/s] in x-direction for an excitation with a unit point source at a frequency of $163\,Hz$ – spatial resolution

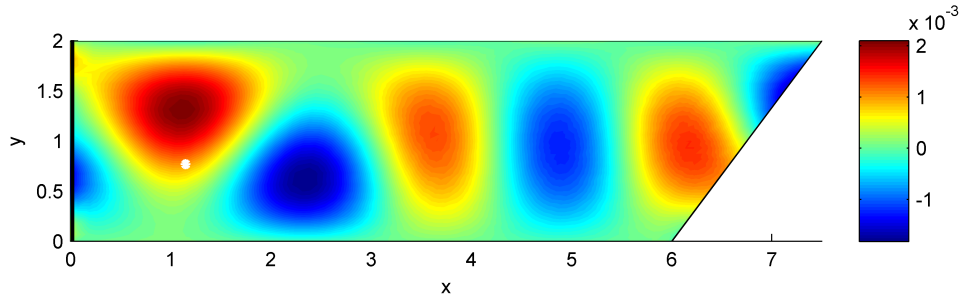

(a) Sound source at $x_L = 1.15\,m$, $y_L = 0.77\,m$ – holohedral coupling

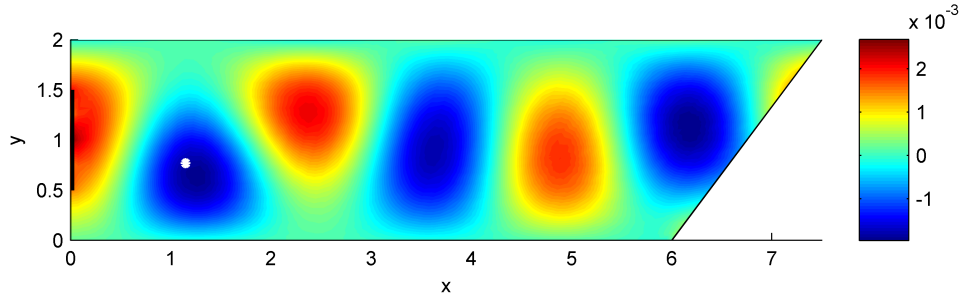

(b) Sound source at $x_L = 1.15\,m$, $y_L = 0.77\,m$ – subregional coupling

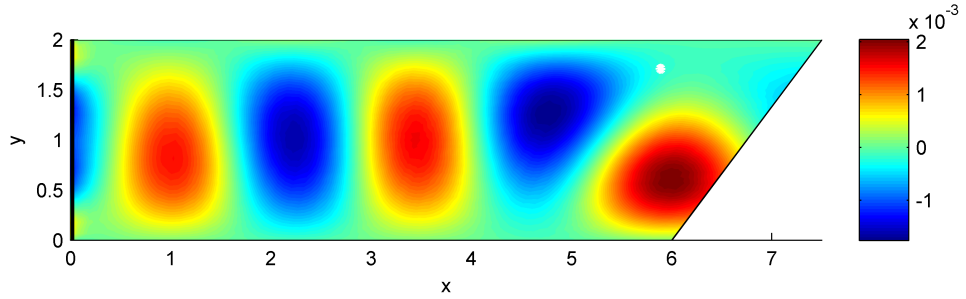

(c) Sound source at $x_L = 5.89\,m$, $y_L = 1.71\,m$ – holohedral coupling

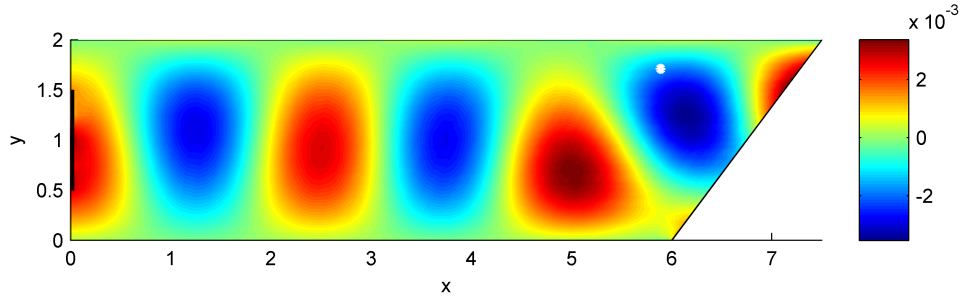

(d) Sound source at $x_L = 5.89\,m$, $y_L = 1.71\,m$ – subregional coupling

Figure 5.31: Sound-velocity $v_y(x, y)$ $[\mathrm{m/s}]$ in y-direction for an excitation with a unit point source at a frequency of $163\,Hz$ – spatial resolution

5.5.3 Application to 3d Structures

Finally the investigation of a 3d structure is presented. The rectangular geometry $V = [0, L_x] \times [0, L_y] \times [0, L_z] = [0, 6\,m] \times [0, 3\,m] \times [0, 2\,m]$, which is sketched in figure 5.32, is modeled with 288 spectral finite elements. In the CMS 50 normal and 6 coupling modes ($n_y = 2$ in y-direction and $n_z = 3$ in z-direction) are considered. A spherical unit pressure source is applied at $x = 0.5\,m$, $y = 1.3\,m$ and $z = 0.9\,m$. It is oscillating with a frequency of $122\,Hz$. The $7.2\,cm$ layer of Melamine Foam, which is known out of former examples is mounted at the interface and the boundary conditions for the interface are defined as line couplings. Thus sinusoidal trial functions can be used, where the expressions for the FSI-formulation are computed out of equation (5.59).

The absorber is mounted at $x = 0$. Whereas in case of the holohedral coupling the porous foam covers the whole interface, in the subregional case the absorber is located at $y \in [0.5\,m; 2.0\,m]$ and $z \in [0.5\,m; 1.5\,m]$. The spatial distribution of the resulting sound field is

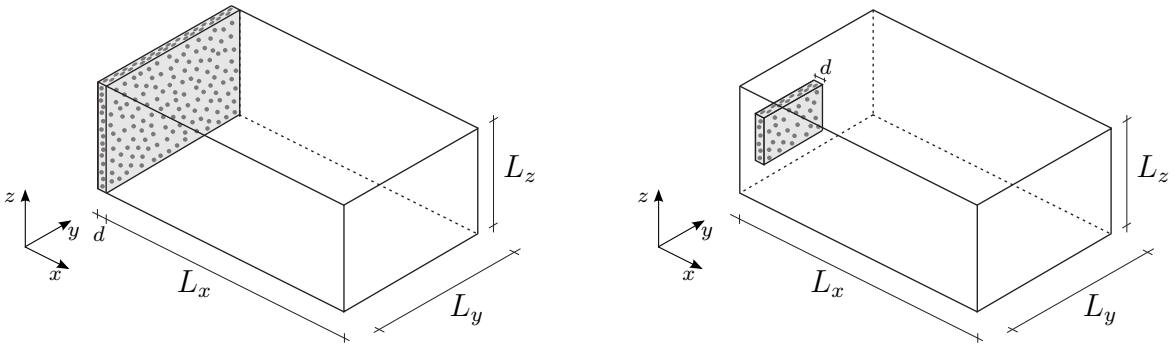

(a) holohedral coupling **(b)** subregional coupling

Figure 5.32: 3d structure with porous absorber

depicted in figures 5.34 and 5.36. The structure is excited at a frequency of $122\,Hz$, where a multiple eigenvalue of the system with reflective walls is located. The $(3, 0, 1)$ mode (three zero-crossings in the x-direction, none in the y-direction, and one in the z-direction for the pressure field) and the $(0, 1, 1)$ mode are at resonance there. One observes the contributions of these modes in the results.

As discussed in the 2d examples already, in case of subregional coupling the peak reduction due to the absorber is less significant, because less absorptive area is installed in the system and the modeshapes related to velocity patterns, which are dominant in the y- and z-direction are damped less than the patterns in x-direction because of the location of the absorber.

For acoustic design therefore is in inevitable to get the spatial information as well as the energetic values of the result.

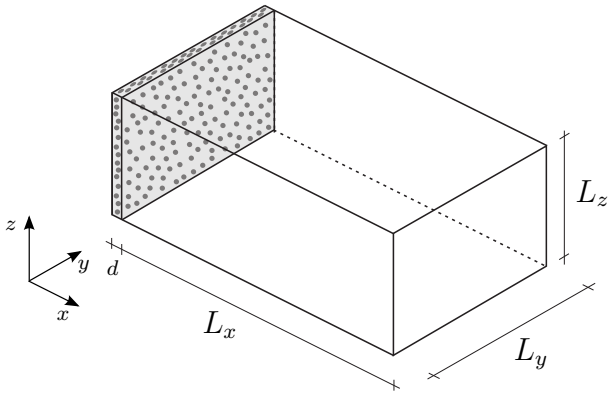

Figure 5.33: 3d structure with porous absorber – holohedral coupling

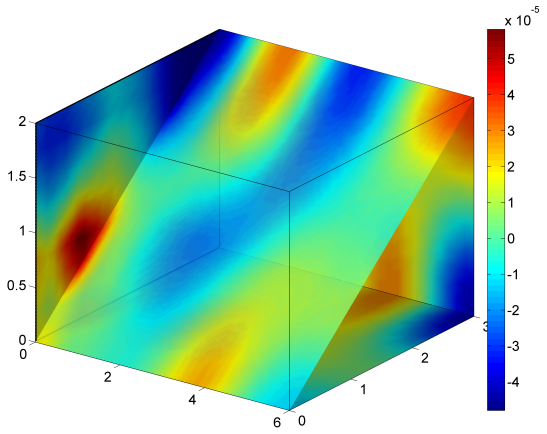

(a) $p(x, y, z)$ [Pa]

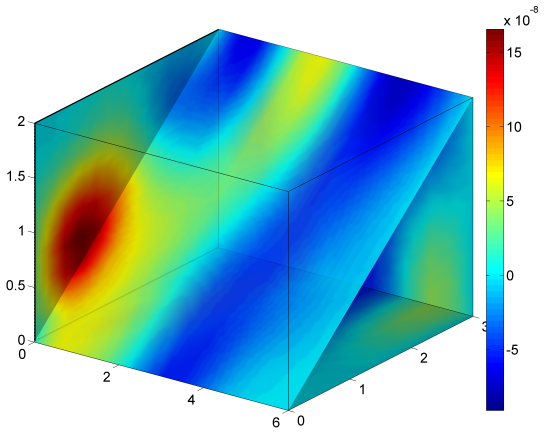

(b) $v_x(x, y, z)$ [m/s]

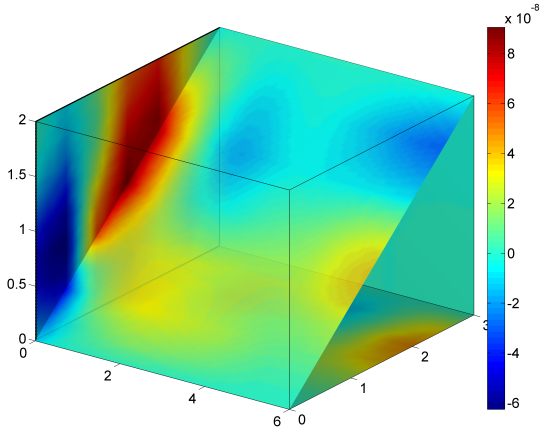

(c) $v_y(x, y, z)$ [m/s]

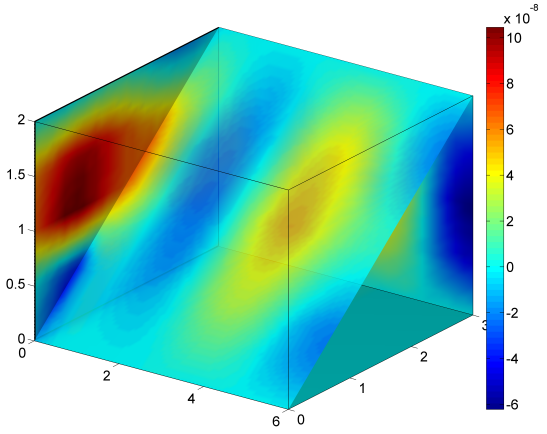

(d) $v_z(x, y, z)$ [m/s]

Figure 5.34: $7.2\,cm$ Melamine Foam (holohedral coupling) – Response for an excitation with a unit point source at a frequency of $122\,Hz$

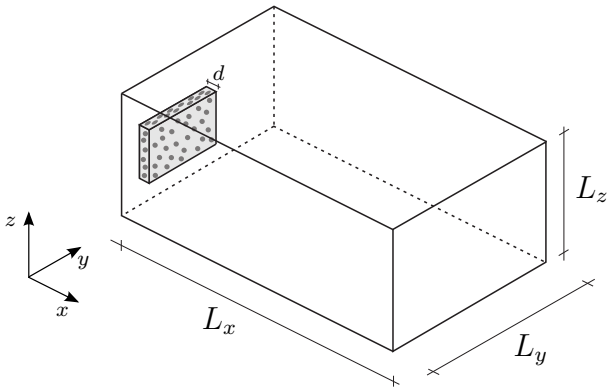

Figure 5.35: 3d structure with porous absorber – subregional coupling

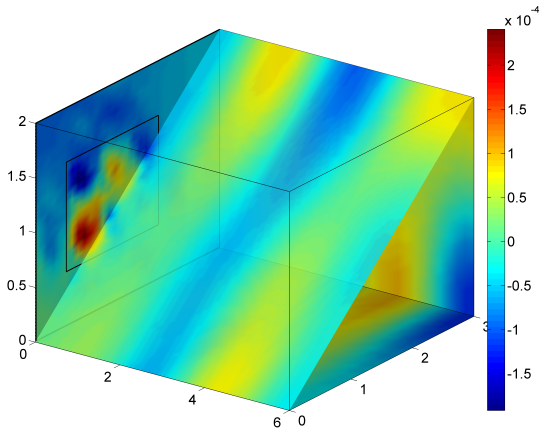

(a) $p(x, y, z)$ [Pa]

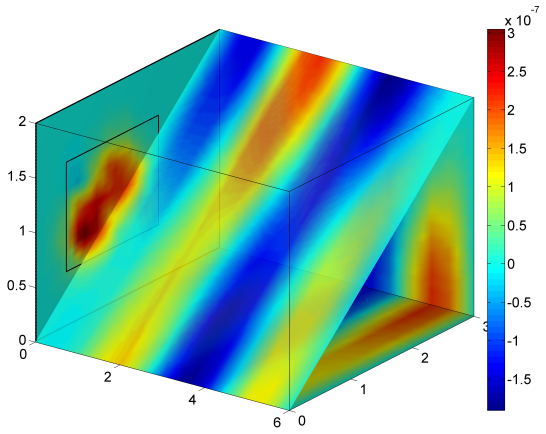

(b) $v_x(x, y, z)$ [m/s]

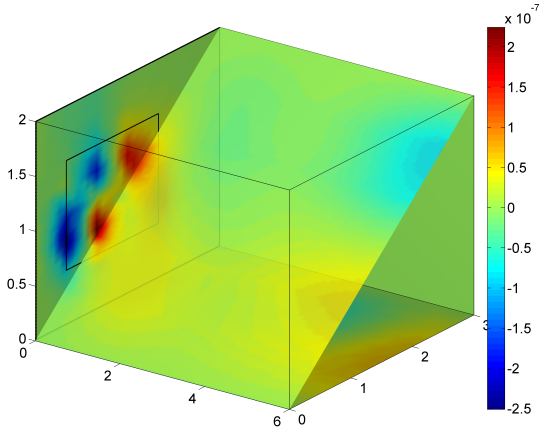

(c) $v_y(x, y, z)$ [m/s]

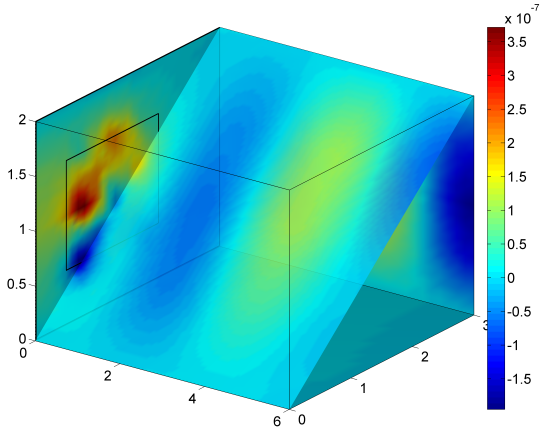

(d) $v_z(x, y, z)$ [m/s]

Figure 5.36: $7.2\,cm$ Melamine Foam (subregional coupling) – Response for an excitation with a unit point source at a frequency of $122\,Hz$

Conclusions and Outlook

In the field of engineering acoustics the simulation of sound fields in cavities with absorptive boundaries is an important task, especially if the spatial resolution of the sound field is of interest. The application of commercial FE-methods is often limited for such applications. The number of unknowns is increasing significantly with increasing frequencies, on the one hand side, because of the grid-refinement to build up the short wavelengths, occurring in this range, and on the other hand side, because of the huge effort to consider the porous material with a high level model. If porous foams would have to be modeled with FEM, unknowns for the displacements of the constituents and for the pressure would have to be introduced in the model. For porous materials, which are used for acoustical optimization in civil engineering and automotive design, often measurement results are available for characteristic parameters, like impedances for instance.

On the one hand side the method, which has been derived in this work, allows to investigate porous absorbers or compound absorbers, consisting of porous and elastic layers, numerically in order to deduce measures like impedances or absorption ratios, on the other hand side these absorbers can be considered in a coupled model with acoustic fluids for computations in the steady state.

The model is based on a Component Mode Synthesis, where the normal and coupling modes, as well as the energies in the fluid and the virtual work of the load, are computed with the SFEM. This method is advantageous for smooth solutions like they occur in acoustics and provides a high accuracy at comparable low costs. Test functions are applied at the interface between acoustic fluid and absorber. After a spectral decomposition of the trial functions, the Lagrangian of the absorber and the virtual work of the dissipative forces, which are considered in the *Hamilton* principle, are computed at the basis of impedances in the wavenumber-frequency-domain. The quality of the approximation of the energetic expressions with the impedance-based computation has been discussed for several trial functions and criteria for the choice of the trial functions have been defined. Because wavenumbers are linked to the angle of incidence of a sound wave, hitting the respective surface, wavenumber- and

frequency-dependent impedances are able to express the absorber concerning all properties, which are necessary for the coupling.

These impedances can be gained directly out of measurements and used for the coupling method. Measurement results for plain-wave impedances have been presented and introduced into the coupling algorithm.

On the other hand the impedances for compound absorbers can be computed with numerical models. Therefore a method, based on the ITM has been derived in this thesis, where the equations of motion are established for the different materials and then transformed into the wavenumber- and frequency domain applying a *Fourier* transformation. For the description of the porous material the Theory of Porous Media has been applied, which is strictly based on the mechanical laws of conservation and provides a wide range of possibilities to specify the porous foam. In the scope of the TPM a rigid solid phase is modeled in combination with a compressible gas in the pores. The friction between the constituents depends on the seepage velocity and the permeability constant. In this thesis a relation between the permeability and the specific flow resistance – a well known quantity in acoustics – is given. The fundamental system is computed in the transformed domain after applying a *Helmholtz*-decomposition, and the transformed stresses and displacements are established. The solutions for foams, elastic layers and air cushions are combined to compound absorbers, observing the boundary condition at the interfaces of the individual layers. Applying an incident sound wave for arbitrary wavenumber-frequency combinations the impedance is obtained at the surface of the absorber.

The method has been validated by simulating compound absorbers in several examples. The results have been discussed in the light of common engineering models for porous foams and additionally compared against measurements. The impedance-based FSI formulation for coupled problems of acoustic fluids and absorbers has been validated with analytical solutions for simple problems. In addition to that the application of the method has been presented for 2d- and 3d-structures computing the pressure and velocity fields as well as the frequency response functions for different load cases.

In the scope of this work topics out of various engineering disciplines like material mechanics, structural dynamics, technical acoustics and room acoustics have been discussed and several methods e.g. Integral Transform methods, impedance approaches, Finite Element Methods or measurements have been used. Consequently links to future research topics result for all of these disciplines and methods.

In the material mechanical formulation of the porous absorber the damping-losses of porous

materials coupled with the acoustic fluid due to the flow resistance and heat conduction effects (for high frequencies) can be a part of future research, where experimental tests can be applied to enrich the optimization of the model. In addition, the wavenumber-dependence of the damping characteristics of foams can be investigated with the help of the ITM model and accompanying measurements in the free field for varying angles of incidence.

The limits of the method in the mid-frequency range are of special interest, too. Since the modal density of the acoustic volume is increasing rapidly for high frequencies, even the CMS-based approach is getting numerically expensive because of an increasing number of modeshapes, which has to be considered. In addition, the number of degrees of freedom for the computation of the normal and coupling modes with the SFEM is increasing, because a very fine spatial discretization is required for the acoustic fluid in this frequency range.

Due to the use of the ITM, the FSI-method is restricted to models with plane interfaces between absorber and acoustic fluid. This is sufficient for most of the applications in civil engineering. In case of very complex geometries, which have to be modeled for specific problems in automotive engineering for instance, an expansion of the method is necessary. Applying mapping techniques at the interface, curved geometries can be modeled (up to a certain limit, which is depending on the frequency range) with SFEM, where the impedance of the absorber still can be computed with the ITM assuming a plane geometry.

Even impulse response functions, which are usually computed with ray tracing methods in the time domain, can be computed out of the results in the frequency domain if an inverse *Fourier* transform is applied. The efficiency of the method for this application is linked to the frequency range, which has to be considered, and the required sampling interval as well as to the volume of the system.

A Appendix

A.1 Vector Calculus

In the derivation of the TPM balance equations for the porous medium in section 2.2 the expressions are defined and simplified with the help of vector calculus. The definition of the operators as well as the relations, which are used for the simplification are sketched below.

Differential operators

$u, \dots$ scalar field $\quad \mathbf{v}, \dots$ vector field $\quad \mathbf{T}, \dots$ tensor field (of 2^{nd} order)

$$\begin{aligned} \text{grad } u &= \nabla \otimes u \\ &= \mathbf{g}^i \frac{\partial}{\partial \theta^i} \otimes u \\ &= u_{,k}\ \mathbf{g}^k \\ &= u|_k\, \mathbf{g}^k \end{aligned} \tag{A.1}$$

$$\begin{aligned} \text{grad } \mathbf{v} &= \nabla \otimes \mathbf{v} \\ &= \mathbf{g}^i \frac{\partial}{\partial \theta^i} \otimes \mathbf{v} \\ &= \mathbf{g}^i \frac{\partial}{\partial \theta^i} \otimes \left(v^j\ \mathbf{g}_j \right) \\ &= v^j|_i\, \mathbf{g}^i \otimes \mathbf{g}_j \\ &= \left(v^j{}_{,i} + v^k \Gamma_{ki}{}^j \right) \mathbf{g}^i \otimes \mathbf{g}_j \end{aligned} \tag{A.2}$$

$$
\begin{aligned}
\text{grad } \mathbf{T} &= \nabla \otimes \mathbf{T} \\
&= \mathbf{g}^i \frac{\partial}{\partial \theta^i} \otimes \mathbf{T} \\
&= \mathbf{g}^i \frac{\partial}{\partial \theta^i} \otimes t^{ij}\, \mathbf{g}_j \otimes \mathbf{g}_j \\
&= t^{ij}|_k\, \mathbf{g}^k \otimes \mathbf{g}_i \otimes \mathbf{g}_j \\
&= \left(t^{ij}{}_{,k} + t^{nj}\Gamma_{nk}{}^i + t^{in}\Gamma_{nk}{}^j\right) \mathbf{g}^k \otimes \mathbf{g}_i \otimes \mathbf{g}_j
\end{aligned}
\tag{A.3}
$$

$$
\begin{aligned}
\text{div } \mathbf{v} &= \nabla \cdot \mathbf{v} \\
&= \mathbf{g}^i \frac{\partial}{\partial \theta^i} \cdot \mathbf{v} \\
&= \mathbf{g}^i \frac{\partial}{\partial \theta^i} \cdot \left(v^j\, \mathbf{g}_j\right) \\
&= v^j|_i\, \mathbf{g}^i \cdot \mathbf{g}_j \\
&= v^j|_i\, \delta^i_j \\
&= v^j|_j \\
&= v^j{}_{,j} + v^k \Gamma_{kj}{}^j
\end{aligned}
\tag{A.4}
$$

$$
\begin{aligned}
\text{div } \mathbf{T} &= \nabla \cdot \mathbf{T} \\
&= \mathbf{g}^i \frac{\partial}{\partial \theta^i} \cdot \mathbf{T} \\
&= \mathbf{g}^i \frac{\partial}{\partial \theta^i} \cdot t^{ij}\, \mathbf{g}_i \otimes \mathbf{g}_j \\
&= t^{ij}|_k\, \left(\mathbf{g}^k \cdot \mathbf{g}_i\right) \otimes \mathbf{g}_j \\
&= t^{ij}|_k\, \delta^k_i\, \mathbf{g}_j \\
&= t^{ij}|_i\, \mathbf{g}_j \\
&= \left(t^{ij}{}_{,i} + t^{nj}\Gamma_{ni}{}^i + t^{in}\Gamma_{ni}{}^j\right) \mathbf{g}_j
\end{aligned}
\tag{A.5}
$$

$$
\begin{aligned}
\text{rot } \mathbf{v} &= \nabla \times \mathbf{v} \\
&= \mathbf{g}^i \frac{\partial}{\partial \theta^i} \times \mathbf{v} \\
&= \mathbf{g}^i \frac{\partial}{\partial \theta^i} \times \left(v_j\, \mathbf{g}^j\right) \\
&= v_j|_i\, \mathbf{g}^i \times \mathbf{g}^j \\
&= v_j|_i\, \varepsilon^{ijk}\, \mathbf{g}_k \\
&= \left(v_{j,i} - v_m \Gamma_{ij}{}^m\right) \varepsilon^{ijk}\, \mathbf{g}_k
\end{aligned}
\tag{A.6}
$$

Relations for differential operators

$u,\ \rho,\ \lambda, \ldots$ scalars $\quad \mathbf{a},\ \mathbf{b},\ \mathbf{v}, \ldots$ vectors $\quad A,\ B,\ V, \ldots$ tensors of 2^{nd} order

$$\text{grad}\ (c\,u) = c\ \text{grad}\, u \tag{A.7}$$

$$\text{grad}\ (u_1\, u_2) = u_1\, \text{grad}\, u_2 + u_2\, \text{grad}\, u_1 \tag{A.8}$$

$$\nabla \otimes (u_1 u_2) = u_1 \nabla \otimes u_2 + u_2 \nabla \otimes u_1 \tag{A.9}$$

$$\text{div}\ (\mathbf{a} + \mathbf{b}) = \text{div}\ \mathbf{a} + \text{div}\ \mathbf{b} \tag{A.10}$$

$$\nabla \cdot (\mathbf{a} + \mathbf{b}) = \nabla \cdot \mathbf{a} + \nabla \cdot \mathbf{b} \tag{A.11}$$

$$\text{div}\, c\,\mathbf{v} = c\, \text{div}\, \mathbf{v} \tag{A.12}$$

$$\text{div}\, \mathbf{I} = \mathbf{0} \tag{A.13}$$

$$\text{div}\ \text{grad}\, \mathbf{v} = \nabla \cdot \nabla \otimes \mathbf{v} = \nabla^2 \otimes \mathbf{v} = \Delta \mathbf{v} = v_{i,kk} e_i \tag{A.14}$$

$$\text{div}\ (\text{grad}\, \mathbf{v})^T = \text{grad}\, \text{div}\, \mathbf{v} \tag{A.15}$$

$$\text{div}\ \text{grad}\, \mathbf{v} = \text{grad}\, \text{div}\ \mathbf{v} - \text{rot}\ \text{rot}\ \mathbf{v} \tag{A.16}$$

$$\text{rot}\ (\mathbf{a} + \mathbf{b}) = \text{rot}\ \mathbf{a} + \text{rot}\ \mathbf{b} \tag{A.17}$$

$$\nabla \times (\mathbf{a} + \mathbf{b}) = \nabla \times \mathbf{a} + \nabla \times \mathbf{b} \tag{A.18}$$

$$\text{rot}\ (c\,\mathbf{v}) = c\, \text{rot}\ \mathbf{v} \tag{A.19}$$

$$\text{rot}\ (u\,\mathbf{v}) = u\, \text{rot}\ \mathbf{v} - \mathbf{v} \times \text{grad}\, u \tag{A.20}$$

$$\nabla\ \times\ (u\,\mathbf{v}) = u \nabla\ \times\ \mathbf{v} - \mathbf{v}\ \times\ \nabla \otimes u \tag{A.21}$$

$$\text{div}\ (\rho\,\mathbf{v}) = \rho\, \text{div}\ \mathbf{v} + \mathbf{v} \cdot \text{grad}\, \rho \tag{A.22}$$

$$\nabla \cdot (\rho\,\mathbf{v}) = \rho\, \nabla \cdot \mathbf{v} + \mathbf{v} \cdot \nabla \otimes \rho \tag{A.23}$$

$$\text{div}\ \text{rot}\ \mathbf{v} = \nabla \cdot \nabla \times \mathbf{v} = 0 \tag{A.24}$$

$$\text{div}\ (\mathbf{v}_1 \times \mathbf{v}_2) = \mathbf{v}_2 \cdot \text{rot}\ \mathbf{v}_1 - \mathbf{v}_1 \cdot \text{rot}\ \mathbf{v}_2 \tag{A.25}$$

$$\text{rot}\ \text{grad}\, u = \nabla \times \nabla \otimes u = 0 \tag{A.26}$$

$$\text{div}\, \mathbf{v} = \frac{1}{2} \left(\text{grad}\, \mathbf{v} + (\text{grad}\, \mathbf{v})^T \right) \cdot \mathbf{I} \tag{A.27}$$

A.2 Fourier Transform - Short Summary

Definition

The function $f\left(x,y,z,t\right)$ is transformed from the original into the *Fourier* domain $\hat{f}\left(k_x,k_y,z,\omega\right)$ via

$$f\left(x,y,z,t\right) \quad \circ\!\!-\!\!\bullet \quad \hat{f}\left(k_x,k_y,z,\omega\right)$$

$$\hat{f}\left(k_x,k_y,z,\omega\right) = \int_{-\infty}^{\infty}\int_{-\infty}^{\infty}\int_{-\infty}^{\infty}\left(\left(f\left(x,y,z,t\right)e^{-ik_x x}\,dx\right)e^{-ik_y y}\,dy\right)e^{-i\omega t}\,dt \tag{A.28}$$

The z-coordinate is not transformed in equation (A.28) in order to enable layered structures in this direction.

The inverse transform follows equation (A.29)

$$\hat{f}\left(k_x,k_y,z,\omega\right) \quad \bullet\!\!-\!\!\circ \quad f\left(x,y,z,t\right)$$

$$f\left(x,y,z,t\right) = \frac{1}{\left(2\pi\right)^3}\int_{-\infty}^{\infty}\int_{-\infty}^{\infty}\int_{-\infty}^{\infty}\left(\left(\hat{f}\left(k_x,k_y,z,\omega\right)e^{ik_x x}\,dk_x\right)e^{ik_y y}\,dk_y\right)e^{i\omega t}\,d\omega \tag{A.29}$$

Derivatives

The derivative of a function $f\left(x,y,z,t\right)$ with respect to a parameter, which is transformed according to (A.28), which means with respect to x, y or t is simplified to a multiplication with the transformed variables k_x, k_y and ω respectively.

$$\frac{d^n}{dt^n}f\left(x,y,z,t\right) \quad \circ\!\!-\!\!\bullet \quad \left(i\,\omega\right)^n\hat{f}\left(k_x,k_y,z,\omega\right) \tag{A.30}$$

$$\frac{d^n}{dx^n}f\left(x,y,z,t\right) \quad \circ\!\!-\!\!\bullet \quad \left(i\,k_x\right)^n\hat{f}\left(k_x,k_y,z,\omega\right) \tag{A.31}$$

$$\frac{d^n}{dy^n}f\left(x,y,z,t\right) \quad \circ\!\!-\!\!\bullet \quad \left(i\,k_y\right)^n\hat{f}\left(k_x,k_y,z,\omega\right) \tag{A.32}$$

A detailed introduction into the *Fourier* transformation method as well as a summary of the rules of calculation and examples for its application are provided by Buchschmid [2010] for instance.

A.3 Spectral Finite Element Method

The normal and the coupling velocity potential modes Φ_j^N and Φ_k^C, which were introduced in the FSI-formulation in chapter 5 are numerically computed with the Spectral Finite Element Method (SFEM). The Spectral Finite Element Method as well as the Spectral Method are convenient to deal with very smooth solutions for acoustic problems to receive spectral convergence [Trefethen 2000; Pospiech and Rentrop 2009; Buchschmid et al. 2010; Pospiech 2011].

The SFEM is used to compute the modes, which formulate the Lagrangian function of the air (5.3), that means the normal and coupling modes of the pressure $p_A(\mathbf{x})$ and the sound velocity $\mathbf{v}_A(\mathbf{x})$. After transforming the wave equation (5.9) with the help of the *Fourier* transformation from the time domain into the frequency domain, the *Helmholtz* equation (5.10) is obtained. Multiplying (5.10) with test functions $\nu(\mathbf{x})$ and integrating by parts one yields the weak formulation of the *Helmholtz* equation.

$$\int_V \nabla\Phi\nabla\nu \, - k^2\Phi\nu dV = \int_{\partial V} \nabla\Phi\nu ds \tag{A.33}$$

The solution of equation (A.33) is computed with the SFEM. After the domain partition and an approximation of Φ with basis functions, which are equal to the test functions, equation (A.33) ends up in the global matrix vector formulation

$$\left(\mathbf{K} - k^2\mathbf{M}\right)\widetilde{\Phi} = \mathbf{F}, \tag{A.34}$$

where $\mathbf{K}$ stands for the global stiffness matrix, $\mathbf{M}$ for the global mass matrix, $\mathbf{F}$ incorporates the normal derivative of Φ at the domain boundaries, and $\widetilde{\Phi}$ is the vector of the global coefficients of the basis functions in each element.

To find a solution for the coefficients in equation (A.34), boundary conditions for the related normal and coupling modes $\left\{\Phi_j^N, \Phi_k^C\right\}$ have to be enforced at the domain boundaries. For the $m_{\max}$ normal modes homogeneous Neumann boundary conditions have to be fulfilled everywhere, due to the totally reflecting walls. These boundary conditions end up in a right-hand side $\mathbf{F} = \mathbf{0}$ and consequently in a general eigenvalue problem. The resulting normal modes of the potential $\Phi_1^N, \Phi_2^N, ..., \Phi_{m_{\max}}^N$ are related to the complex coefficients $\mathcal{A}_1, \mathcal{A}_2, ..., \mathcal{A}_{m_{\max}}$ in (5.7). For the potential coupling modes Φ_k^C a boundary condition must be defined. This boundary condition can be an inhomogeneous Neumann boundary condition on Γ_N (A.35)

or a given inhomogeneous Dirichlet boundary condition on Γ_D (A.36).

$$\frac{\partial \Phi_k^C(\mathbf{x})}{\partial \mathbf{n}} = g_k(\mathbf{x}), \qquad \forall\, \mathbf{x} \in \Gamma_N \subset \partial V \tag{A.35}$$

$$\Phi_k^C(\mathbf{x}) = h_k(\mathbf{x}), \qquad \forall\, \mathbf{x} \in \Gamma_D \subset \partial V \tag{A.36}$$

Because of the inhomogeneous Neumann or Dirichlet boundary conditions equation (A.34) has a nonzero right-hand side $\mathbf{F}$. Therefore a system of linear equations has to be solved for each coupling mode. The coupling modes belong to the coefficients $\mathcal{B}_1, \mathcal{B}_2, ..., \mathcal{B}_{n_{\max}}$ in (5.7). According to Karniadakis and Sherwin [2005] the basis functions for the SFEM on the reference interval $\xi \in [-1, 1]$ result from the modal continuous C^0 expansion of polynomials from degree 1 to Q.

$$N_q(\xi) = \begin{cases} \frac{1-\xi}{2} & , \; q = 0 \\ (\frac{1-\xi}{2})(\frac{1+\xi}{2}) J_q^{1,1}(\xi) & , \; 0 < q < Q \\ \frac{1+\xi}{2} & , \; q = Q \end{cases} \tag{A.37}$$

$J_q^{1,1}$ in (A.37) denotes the Jacobi polynomial with parameters $\alpha = 1$, $\beta = 1$ and polynomial degree q. In three dimensions the related hexahedral tensor product expansion is defined for the reference domain $[-1, 1]^3$ with $\{\xi_1, \xi_2, \xi_3\} \in [-1, 1]$.

$$N_{qrs}(\xi) = N_q(\xi_1) N_r(\xi_2) N_s(\xi_3), \quad 0 \leq q, r, s \leq Q \tag{A.38}$$

In two dimensions for instance there exist 4 vertex-modes, $4\,(Q-1)$ edge-modes, and $(Q-1)^2$ interior-modes. They are depicted in figure A.1.

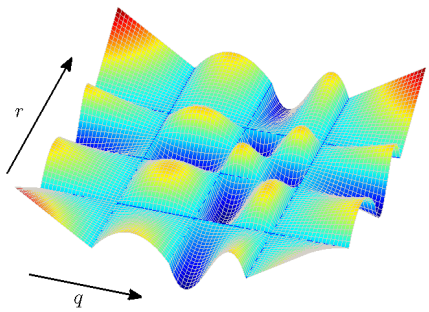

Figure A.1: 2d Legendre basis functions N_{qr} for a polynomial degree $Q = 3$

Thereby the modal face orientation and connectivity has to be considered at the boundaries between adjacent elements. For the integrals in every element of the domain the Gauss-Lobatto-Legendre quadrature with the quadrature points ξ_j and weights $w_j^{0,0}$ is applied.

$$\xi_j = \begin{cases} -1 & , \ j = 1 \\ \xi_{j-2,W-2}^{1,1} & , \ j = 2, ..., W-1 \\ 1 & , \ j = W \end{cases} \tag{A.39}$$

$$w_j^{0,0} = \frac{2}{W(W-1)\left(J_{j-2}^{1,1}(\xi_j)\right)^2} \quad , \ j = 1, ..., W$$

The quadrature points $\xi_{j-2,W-2}^{1,1}$, which are clustered and symmetrically distributed in $[-1, 1]$, are the $(W-2)$ zeros of the $(W-2)$ th-order Jacobi polynomial $J_{W-2}^{1,1}$. When using the Gauss-Lobatto-Legendre quadrature of order W, a polynomial $u(\xi) \in P_{2W-3}$ is integrated exactly. Consequently for basis functions up to order Q the number of quadrature points $W = Q + 2$ is chosen for integration. For the kinetic and the potential energy in equations (5.4) and (5.5) and for the load in equation (5.6) the same quadrature rule is used as for the computation of the modes.

A.4 Preconditioning

Modification of the System of Equations

There occur different magnitudes for one individual coefficient in the equations of (4.14) and also for the coefficients within one individual equation. This leads to an ill conditioned system of equations. Therefore a scaling of rows and columns is applied as a preconditioning using diagonal matrices $\mathbf{D}_\mathrm{R}$ and $\mathbf{D}_\mathrm{C}$ for rows and columns respectively.

$$\mathbf{D}_\mathrm{R} = \begin{bmatrix} \frac{1}{\max|K_{11..1m}|} & \cdots & 0 \\ \vdots & \ddots & \vdots \\ 0 & \cdots & \frac{1}{\max|K_{n1..nm}|} \end{bmatrix} \qquad \mathbf{D}_\mathrm{C} = \begin{bmatrix} \frac{1}{\max|[\mathbf{D}_\mathrm{R}\,\mathbf{K}]_{11..n1}|} & \cdots & 0 \\ \vdots & \ddots & \vdots \\ 0 & \cdots & \frac{1}{\max|[\mathbf{D}_\mathrm{R}\,\mathbf{K}]_{1m..nm}|} \end{bmatrix} \tag{A.40}$$

The elements of (4.14) are scaled with the help of (A.40).

$$\mathbf{D}_\mathrm{R}\,\mathbf{K}\,\mathbf{x} = \mathbf{D}_\mathrm{R}\,\mathbf{f} \tag{A.41}$$

$$\mathbf{D}_\mathrm{R}\,\mathbf{K}\,\mathbf{D}_\mathrm{C}\,\mathbf{D}_\mathrm{C}^{-1}\,\mathbf{x} = \mathbf{D}_\mathrm{R}\,\mathbf{f} \tag{A.42}$$

Substituting $\mathbf{K}^\star = \mathbf{D}_\mathrm{R}\,\mathbf{K}\,\mathbf{D}_\mathrm{C}$, $\mathbf{f}^\star = \mathbf{D}_\mathrm{R}\,\mathbf{f}$ and $\mathbf{x}^\star = \mathbf{D}_\mathrm{C}^{-1}\,\mathbf{x}$ one obtains a system of equations (A.43), which is well conditioned. This system is solved for the transformed vector of unknowns $\mathbf{x}^\star$. The inverse transform in order to gain $\mathbf{x}$ is carried out with the help of (A.44).

$$\mathbf{K}^\star\,\mathbf{x}^\star = \mathbf{f}^\star \tag{A.43}$$

$$\mathbf{x} = \mathbf{D}_\mathrm{C}\,\mathbf{x}^\star \tag{A.44}$$

Alternative Definition of the Scalar and Vector Potentials

If thick layers are defined in the absorber model, big arguments occur in the exponential functions. This leads to ill conditioned systems of equations, which cannot be improved sufficiently applying the method, outlined above. Then it is reasonable to rearrange the definitions of the scalar and vector potentials in equations (2.73)–(2.76) for the porous foams, (3.8) and (3.9) for the homogeneous layers as well as in (3.22) for the air before defining the system of equations.

The argument in the exponential function $e^{\lambda z}$ is expressed as $e^{\lambda (z-h)}$ with respect to a constant h, where $h > z$ holds. It is suitable to choose the thickness of the layer for the

constant h. The procedure is presented exemplarily for the homogeneous material [see e.g. Lieb 1997].

The potentials out equations (3.8) and (3.9) are redefined as:

$$C_1\, e^{\kappa_1 z} \;=\; C_1\, e^{\kappa_1 d_H}\, e^{-\kappa_1 d_H}\, e^{\kappa_1 z} \;=\; \overline{C}_1\, e^{\kappa_1 (z-d_H)} \tag{A.45}$$

$$D_{1x}\, e^{\kappa_2 z} = D_{1x}\, e^{\kappa_2 d_H}\, e^{-\kappa_2 d_H}\, e^{\kappa_2 z} \;=\; \overline{D}_{1x}\, e^{\kappa_2 (z-d_H)} \tag{A.46}$$

$$D_{1y}\, e^{\kappa_2 z} = D_{1y}\, e^{\kappa_2 d_H}\, e^{-\kappa_2 d_H}\, e^{\kappa_2 z} \;=\; \overline{D}_{1y}\, e^{\kappa_2 (z-d_H)} \tag{A.47}$$

The displacements in the transformed domain read after the transformation analogously to equation (3.16):

$$\begin{bmatrix} \hat{u}_H^x \\ \hat{u}_H^y \\ \hat{u}_H^z \end{bmatrix} = \begin{bmatrix} ik_x e^{\kappa_1 (z-d_H)} & ik_x e^{-\kappa_1 z} & 0 & 0 & -\kappa_2 e^{\kappa_2 (z-d_H)} & \kappa_2 e^{-\kappa_2 z} \\ ik_y e^{\kappa_1 (z-d_H)} & ik_y e^{-\kappa_1 z} & \kappa_2 e^{\kappa_2 (z-d_H)} & -\kappa_2 e^{-\kappa_2 z} & 0 & 0 \\ \kappa_1 e^{\kappa_1 (z-d_H)} & -\kappa_1 e^{-\kappa_1 z} & -ik_y e^{\kappa_2 (z-d_H)} & -ik_y e^{-\kappa_2 z} & ik_x e^{\kappa_2 (z-d_H)} & ik_x e^{-\kappa_2 z} \end{bmatrix} \begin{bmatrix} \overline{C}_1 \\ C_2 \\ \overline{D}_{1x} \\ D_{2x} \\ \overline{D}_{1y} \\ D_{2y} \end{bmatrix} \tag{A.48}$$

A.5 Linear Structural Model for the Kirchhoff Plate

In section 5.3 the calculation of the Lagrangian for a plate structure based on an impedance description is deduced using the example of the *Kirchhoff* plate. The derivation of the energy expressions, which are used there, is sketched in the following [see Wauer 2008; Petersen 1982, 1996].

Mechanical models for 3d structures, which can be expressed with less than three metric parameters are deduced from continuum models by introducing kinematic relations, where in general two approaches are used [see Wauer 2008]. In a systematic approach the condensation is achieved step by step. Primary variables, which are displacements in the mid-surface of plates or shells for instance, are defined and introduced into the displacement field, which simplified via ansatz-functions over the condensed dimension. The simplified displacement field is then used in the mechanical laws of conservation. Near to this systematic approach a direct method is often used in engineering practice, where the kinematic relations are introduced heuristically and analytical, mechanical principles, like *Hamilton*'s principle are applied.

The direct method is used to deduce the energetic expressions for the rectangular *Kirchhoff* plate starting from a plane load-bearing structure. An infinitesimal element is sketched in figure A.2, where the y, z-plane of the reference frame is defined in the mid-surface of the plate.

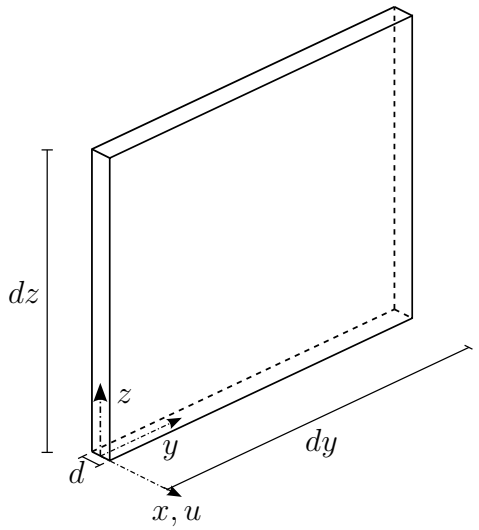

Figure A.2: Infinitesimal plate element

In the y, z-plane tension/compression and shear occur whereas perpendicular to the mid-surface bending is carried. In this plane state of stresses σ_x as well as τ_{yx}, τ_{zx} vanish.

Potential Energy

The potential energy of the internal forces U can be written in terms of σ_y, σ_z and τ_{yz}.

$$U = \frac{1}{2} \int_V \sigma_z \epsilon_z + \sigma_y \epsilon_y + \tau_{yz} \gamma_{yz} \, dV \tag{A.49}$$

Assuming a linear elastic material *Hooke*'s law is applied and the stresses are defined in terms of the strains:

$$\begin{aligned} \sigma_y &= \frac{E}{1-\nu^2} (\epsilon_y + \nu \epsilon_z) \\ \sigma_z &= \frac{E}{1-\nu^2} (\epsilon_z + \nu \epsilon_y) \\ \tau_{yz} &= G \gamma_{yz} = \frac{E}{2(1+\nu)} \gamma_{yz} = \frac{E(1-\nu)}{2(1-\nu^2)} \gamma_{yz} = \frac{E}{1-\nu^2} \frac{1}{2} (1-\nu) \gamma_{yz} \end{aligned} \tag{A.50}$$

Inserting the relations for σ_y, σ_z and τ_{yz} in equation (A.49) one obtains

$$\begin{aligned} U &= \frac{1}{2} \frac{E}{1-\nu^2} \int_V \epsilon_y^2 + 2\nu \epsilon_y \epsilon_z + \epsilon_z^2 + \frac{1}{2}(1-\nu) \gamma_{yz}^2 \, dV \\ &= \frac{1}{2} \frac{E}{1-\nu^2} \int_V (\epsilon_y + \epsilon_z)^2 - 2(1-\nu) \left(\epsilon_y \epsilon_z - \frac{1}{4} \gamma_{yz}^2 \right) dV \end{aligned} \tag{A.51}$$

for the potential energy of the internal forces. As pointed out by Bauchau and Craig [2009], in the scope of the *Kirchhoff* theory it is assumed, that the normal material line is rigid, straight and normal to the deformed mid-plane during the deformation, i.e. plain cross sections, which are perpendicular to the mid-plane, remain plain during the process of deformation.

Restricting the system to the bending problem and neglecting higher order effects, the strains are defined to:

$$\begin{aligned} \epsilon_y &= -x \frac{\partial^2 u}{\partial y^2} = -x \, u'' \\ \epsilon_z &= -x \frac{\partial^2 u}{\partial z^2} = -x \, u'' \\ \gamma_{yz} &= -2x \, u'' \end{aligned} \tag{A.52}$$

The angles occurring due to bending are linked to the out of plane displacement u via its derivatives u' and $u\backslash$.

Inserting the strains into (A.51) one finally obtains

$$\begin{aligned} U &= \frac{1}{2}\frac{E}{1-\nu^2}\int\limits_A\int\limits_d x^2\left[\left(u''+u\backslash\backslash\right)^2-2\left(1-\nu\right)\left(u''u\backslash\backslash-u'\backslash^2\right)\right]\,dx\;dA \\ &= \frac{1}{2}\underbrace{\frac{Ed^3}{12\left(1-\nu^2\right)}}_{B\text{`}}\int\limits_A\left(u''+u\backslash\backslash\right)^2-2\left(1-\nu\right)\left(u''u\backslash\backslash-u'\backslash^2\right)\,dA \end{aligned} \tag{A.53}$$

where B‘ is the abbreviation for the bending stiffness of the plate.

Kinetic Energy

Within the Kirchoff theory the rotational inertia is neglected and for the bending problem just velocities perpendicular to the plate have to be considered. Then one obtains for the kinetic energy T

$$T = \frac{1}{2}\int\limits_A \mu\left(\frac{\partial u}{\partial t}\right)^2 dA \quad \text{with:} \quad \mu = \rho\, d \tag{A.54}$$

where μ is the mass distribution and ρ is the density of the homogeneous material. As the result of the condensation the plate is described with the help of two metric parameters y and z.

A.6 Supplement: Coupling with Impedances

Integrating in space

The calculation of the Lagrangian of the absorptive component out of impedances is done in section 5.3.1, where also non-orthogonal trial functions have to be considered. The velocities and displacements of the substructure are defined as sums in a *Fourier* series. In order to obtain the virtual work of the damping forces and energies for the formulation of the Lagrangian for the *Ritz* approach, products of these sums have to be computed via

$$\sum_{n=1}^{N} a_n \sum_{n=1}^{N} b_n = \sum_{k=1}^{N}\sum_{l=1}^{N} a_k\, b_l = \sum_{n=1}^{N} a_n\, b_n + \sum_{k=1}^{N-1}\sum_{l=k+1}^{N} a_k\, b_l + \sum_{k=1}^{N-1}\sum_{l=k+1}^{N} b_k\, a_l \tag{A.55}$$

$$\left(\sum_{n=1}^{N} a_n\right)^2 = \sum_{n=1}^{N} a_n^2 + 2\sum_{k=1}^{N-1}\sum_{l=k+1}^{N} a_k\, a_l \tag{A.56}$$

The integration over the surface of the boundary layer in equations (5.35) and (5.41) is done in dependence of the *Fourier* coefficients using the theorem of *Parseval*.

Parseval Theorem

$f(t)$ and $g(t)$ are continuous functions, which are periodic in $[0, T]$. The theorem of *Parseval*[1] [compare Beerends et al. 2003; Meyberg and Vachenauer 2001] states that:

$$\frac{1}{T}\int_0^T f(t)\,\overline{g}(t)\;dt = \sum_{k=-\infty}^{\infty} c_k\,\overline{d}_k \tag{A.57a}$$

$$\frac{1}{T}\int_0^T |f(t)|^2\;dt = \sum_{k=-\infty}^{\infty} |c_k|^2 \tag{A.57b}$$

$f(t)$ and $g(t)$ are expressed as $f(t) = \sum_{k=-\infty}^{\infty} c_k\, e^{i(k\,\omega\,t)}$ and $g(t) = \sum_{k=-\infty}^{\infty} d_k\, e^{i(k\,\omega\,t)}$ using a *Fourier* series. In section 5.3 a 2-D *Fourier* series is used to build up the trial functions for velocity and displacements in equations (5.31) and (5.32). In case of surface integrals,

[1] M. A. Parseval, 1799

equations (A.57a) and (A.57b) read

$$\int_0^{L_z^{\mathrm{rep}}} \int_0^{L_y^{\mathrm{rep}}} f(y,z)\,\overline{g}(y,z)\;dy\,dz \;=\; L_y^{\mathrm{rep}} L_z^{\mathrm{rep}} \sum_{-r_{\max}}^{r_{\max}} \sum_{-s_{\max}}^{s_{\max}} C_{rs}\,\overline{D}_{rs} \tag{A.58a}$$

$$\int_0^{L_z^{\mathrm{rep}}} \int_0^{L_y^{\mathrm{rep}}} |f(y,z)|^2\;dy\,dz \;=\; L_y^{\mathrm{rep}} L_z^{\mathrm{rep}} \sum_{-r_{\max}}^{r_{\max}} \sum_{-s_{\max}}^{s_{\max}} |C_{rs}|^2 \tag{A.58b}$$

where the functions $f(y,z)$ and $g(y,z)$ are replaced by $\hat{\psi}_k$ and $\hat{\psi}_l$ in (5.35). The integrals appearing during the derivation in section 5.3.1 can be calculated with equations (A.58a) and (A.58b). The results are listed below:

$$\int_{A^{\mathrm{rep}}} \hat{\psi}_k\,\hat{\psi}_l dA = L_y^{\mathrm{rep}} L_z^{\mathrm{rep}} \sum_r \sum_s E_{krs}\overline{E}_{lrs} \tag{A.59}$$

$$\int_{A^{\mathrm{rep}}} \left(\hat{\psi}_n\right)^2 dA = L_y^{\mathrm{rep}} L_z^{\mathrm{rep}} \sum_r \sum_s |E_{nrs}|^2 \tag{A.60}$$

With equations (A.55) and (A.56) equation (5.41) is transformed.

$$\begin{aligned}\int_{A^{\mathrm{rep}}} \left[\sum_{n=1}^{N} \left(\hat{\psi}_n'' + \hat{\psi}_n'''\right) y_n\right]^2 dA &= \sum_{n=1}^{N} y_n^2 \int_{A^{\mathrm{rep}}} \left(\hat{\psi}_n'' + \hat{\psi}_n'''\right)^2 dA + \\ &+ 2\sum_{k=1}^{N-1} \sum_{l=k+1}^{N} y_k\,y_l \int_{A^{\mathrm{rep}}} \left(\hat{\psi}_k'' + \hat{\psi}_k'''\right)\left(\hat{\psi}_l'' + \hat{\psi}_l'''\right) dA\end{aligned} \tag{A.61}$$

The surface-integrals in (A.61) are solved in equations (A.62) and (A.63), introducing the abbreviations defined in (5.38) and applying (A.59) and (A.60).

$$\begin{aligned}&\int_{A^{\mathrm{rep}}} \left(\hat{\psi}_k'' + \hat{\psi}_k'''\right)\left(\hat{\psi}_l'' + \hat{\psi}_l'''\right) dA \\ &\quad= L_y^{\mathrm{rep}} L_z^{\mathrm{rep}} \sum_r \sum_s \left(E_{krs}''\overline{E}_{lrs}'' + E_{krs}''\overline{E}_{lrs}''' + E_{krs}'''\overline{E}_{lrs}'' + E_{krs}'''\overline{E}_{lrs}'''\right) \\ &\quad= L_y^{\mathrm{rep}} L_z^{\mathrm{rep}} \sum_r \sum_s \left(k_y^4 + 2\,k_y^2\,k_z^2 + k_z^4\right) E_{krs}\overline{E}_{lrs} \\ &\quad= L_y^{\mathrm{rep}} L_z^{\mathrm{rep}} \sum_r \sum_s \left(k_y^2 + k_z^2\right)^2 E_{krs}\overline{E}_{lrs}\end{aligned} \tag{A.62}$$

Analogously one obtains setting $k = n$ and $n = l$ in (A.62).

$$\int\limits_{A^{\mathrm{rep}}} \left(\hat{\psi}_n'' + \hat{\psi}_n^{\mathrm{IV}}\right)^2 dA = L_y^{\mathrm{rep}} L_z^{\mathrm{rep}} \sum_r \sum_s \left(k_y^2 + k_z^2\right)^2 |E_{nrs}|^2 \tag{A.63}$$

Proof of Equation (5.41)

In section 5.3.1 the potential energy of the *Kirchhoff*-plate is formulated defining a *Fourier* series for the velocity field. Starting from the formulation in (5.37) the *Fourier* series and its derivatives are inserted according to (5.29) and (5.38).

$$U_{\mathrm{BC}} = \frac{1}{2} B' \int\limits_0^{L_z} \int\limits_0^{L_y} \left(\frac{\partial^2 u_{\mathrm{BC}}}{\partial y^2} + \frac{\partial^2 u_{\mathrm{BC}}}{\partial z^2}\right)^2 - 2\,(1-\nu) \left(\frac{\partial^2 u_{\mathrm{BC}}}{\partial y^2}\,\frac{\partial^2 u_{\mathrm{BC}}}{\partial z^2} - \left(\frac{\partial^2 u_{\mathrm{BC}}}{\partial y\,\partial z}\right)^2\right) dy\,dz$$

$$\begin{aligned} U_{\mathrm{BC}} \approx \frac{1}{2} B' \Bigg[& \int\limits_0^{L_z^{\mathrm{rep}}} \int\limits_0^{L_y^{\mathrm{rep}}} \left[\sum_n \left(\hat{\psi}_n'' + \hat{\psi}_n^{\mathrm{IV}}\right) y_n\right]^2 dy\,dz - \\ & - 2\,(1-\nu) \int\limits_0^{L_z^{\mathrm{rep}}} \int\limits_0^{L_y^{\mathrm{rep}}} \sum_n \hat{\psi}_n'' y_n \sum_n \hat{\psi}_n^{\mathrm{IV}} y_n - \left(\sum_n \hat{\psi}_n^{\mathrm{IV}\prime} y_n\right)^2 dy\,dz \Bigg] \end{aligned} \tag{A.64}$$

The second summand in (A.64)

$$\int\limits_{A^{\mathrm{rep}}} \sum_n \hat{\psi}_n'' y_n \sum_n \hat{\psi}_n^{\mathrm{IV}} y_n - \left(\sum_n \hat{\psi}_n^{\mathrm{IV}\prime} y_n\right)^2 dA \tag{A.65}$$

is discussed in detail in the following. It is splitted up in two integrals (A.66) and (A.67).

$$\begin{aligned} \int\limits_{A^{\mathrm{rep}}} \sum_n \hat{\psi}_n'' y_n \sum_n \hat{\psi}_n^{\mathrm{IV}} y_n\, dA &= \sum_{k=1}^{N} \sum_{l=1}^{N} y_k\, y_l \int\limits_{A^{\mathrm{rep}}} \hat{\psi}_k''\, \hat{\psi}_l^{\mathrm{IV}}\, dA \\ &= \sum_{n=1}^{N} y_n^2 \int\limits_{A^{\mathrm{rep}}} \hat{\psi}_n''\, \hat{\psi}_n^{\mathrm{IV}} dA + \sum_{k=1}^{N-1} \sum_{l=k+1}^{N} y_k\, y_l \int\limits_{A^{\mathrm{rep}}} \hat{\psi}_k''\, \hat{\psi}_l^{\mathrm{IV}}\, dA + \sum_{k=1}^{N-1} \sum_{l=k+1}^{N} y_k\, y_l \int\limits_{A^{\mathrm{rep}}} \hat{\psi}_k^{\mathrm{IV}}\, \hat{\psi}_l''\, dA \end{aligned} \tag{A.66}$$

$$\int\limits_{A^{\mathrm{rep}}} \left(\sum_n \hat{\psi}_n^{\mathrm{IV}\prime} y_n\right)^2 dA = \sum_{n=1}^{N} y_n^2 \int\limits_{A^{\mathrm{rep}}} \left(\hat{\psi}_n^{\mathrm{IV}\prime}\right)^2 dA + 2 \sum_{k=1}^{N-1} \sum_{l=k+1}^{N} y_k\, y_l \int\limits_{A^{\mathrm{rep}}} \hat{\psi}_k^{\mathrm{IV}\prime}\, \hat{\psi}_l^{\mathrm{IV}\prime}\, dA \tag{A.67}$$

Expression (A.67) is transformed to obtain an assembly, which is similar to (A.66)

$$\begin{aligned}\int_{A^{\mathrm{rep}}} \Big(\sum_n \hat{\psi}_n^{\prime\prime} y_n\Big)^2 dA &= \sum_{n=1}^{N} y_n^2 \int_{A^{\mathrm{rep}}} \left(\hat{\psi}_n^{\prime\prime}\right)^2 dA + \\ &+ \sum_{k=1}^{N-1}\sum_{l=k+1}^{N} y_k\, y_l \int_{A^{\mathrm{rep}}} \hat{\psi}_k^{\prime\prime}\ \hat{\psi}_l^{\prime\prime}\, dA + \sum_{k=1}^{N-1}\sum_{l=k+1}^{N} y_k\, y_l \int_{A^{\mathrm{rep}}} \hat{\psi}_k^{\prime\prime}\ \hat{\psi}_l^{\prime\prime}\, dA\end{aligned} \tag{A.68}$$

Equation (A.65) is calculated finally evaluating the corresponding terms in (A.66) and (A.68).

$$\begin{aligned}&\int_{A^{\mathrm{rep}}} \hat{\psi}_n^{\prime\prime\prime}\, \hat{\psi}_n^{\prime\prime\prime}\, dA - \int_{A^{\mathrm{rep}}} \left(\hat{\psi}_n^{\prime\prime}\right)^2 dA = \\ &\quad = L_y^{\mathrm{rep}} L_z^{\mathrm{rep}} \sum_r \sum_s \left(E_{nrs}^{\prime\prime\prime} \overline{E}_{nrs}^{\prime\prime\prime} - E_{nrs}^{\prime\prime} \overline{E}_{nrs}^{\prime\prime} \right) \\ &\quad = L_y^{\mathrm{rep}} L_z^{\mathrm{rep}} \sum_r \sum_s \Big(\left(-k_y^2\right)\left(-k_z^2\right) - (i\,k_y)\,(i\,k_z)\,(i\,k_y)\,(i\,k_z) \Big)\, E_{nrs} \overline{E}_{nrs} \\ &\quad = 0\end{aligned} \tag{A.69}$$

$$\begin{aligned}&\int_{A^{\mathrm{rep}}} \hat{\psi}_k^{\prime\prime\prime}\, \hat{\psi}_l^{\prime\prime\prime}\, dA - \int_{A^{\mathrm{rep}}} \hat{\psi}_k^{\prime\prime}\, \hat{\psi}_l^{\prime\prime} dA = \\ &\quad = L_y^{\mathrm{rep}} L_z^{\mathrm{rep}} \sum_r \sum_s \left(E_{krs}^{\prime\prime\prime} \overline{E}_{lrs}^{\prime\prime\prime} - E_{krs}^{\prime\prime} \overline{E}_{lrs}^{\prime\prime} \right) \\ &\quad = L_y^{\mathrm{rep}} L_z^{\mathrm{rep}} \sum_r \sum_s \Big(\left(-k_y^2\right)\left(-k_z^2\right) - (i\,k_y)\,(i\,k_z)\,(i\,k_y)\,(i\,k_z) \Big)\, E_{krs} \overline{E}_{lrs} \\ &\quad = 0\end{aligned} \tag{A.70}$$

Since (A.65) vanishes, equation (A.64) can be simplified.

$$U_{\mathrm{BC}} \approx \frac{1}{2} B' \int_{A^{\mathrm{rep}}} \left[\sum_n \left(\hat{\psi}_n^{\prime\prime} + \hat{\psi}_n^{\prime\prime\prime} \right) y_n \right]^2 dA \tag{A.71}$$

Integrating in time

In the variational formulation (5.2) the Lagrangian functions L_{BC} and the virtual work of the non-conservative forces $\delta W_{\mathrm{BC}}^{\mathrm{nc}}$ have to be integrated for the boundary conditions within an arbitrary time-range from t_1 to t_2. In the scope of this work, the integral is computed over one time period T in equations (5.43) and (5.48). The results are listed below. The

results are used in section 5.3.1.

$$\begin{aligned}\int_0^T \dot{y}_k(t)\ \dot{y}_l(t)\ dt &= \int_0^T \mathcal{C}_k\,\mathcal{C}_l\,e^{2i\Omega t} + \mathcal{C}_k\overline{\mathcal{C}}_l + \overline{\mathcal{C}}_k\mathcal{C}_l + \overline{\mathcal{C}}_k\,\overline{\mathcal{C}}_l\,e^{-2i\Omega t}\ dt \\ &= T\ \left(\mathcal{C}_k\overline{\mathcal{C}}_l + \overline{\mathcal{C}}_k\mathcal{C}_l\right)\end{aligned} \tag{A.72}$$

$$\int_0^T \left[\dot{y}_n(t)\right]^2\ dt\ =\ 2T\,\mathcal{C}_n\overline{\mathcal{C}}_n \tag{A.73}$$

$$\begin{aligned}\int_0^T y_k(t)\ y_l(t)\ dt &= \int_0^T -\frac{\mathcal{C}_k\,\mathcal{C}_l}{\Omega^2}e^{2i\Omega t} + \frac{\mathcal{C}_k\overline{\mathcal{C}}_l}{\Omega^2} + \frac{\overline{\mathcal{C}}_k\mathcal{C}_l}{\Omega^2} - \frac{\overline{\mathcal{C}}_k\,\overline{\mathcal{C}}_l}{\Omega^2}e^{-2i\Omega t}\ dt \\ &= \frac{T}{\Omega^2}\ \left(\mathcal{C}_k\overline{\mathcal{C}}_l + \overline{\mathcal{C}}_k\mathcal{C}_l\right)\end{aligned} \tag{A.74}$$

$$\int_0^T \left[y_n(t)\right]^2\ dt = \frac{2T}{\Omega^2}\,\mathcal{C}_n\overline{\mathcal{C}}_n \tag{A.75}$$

$$\begin{aligned}\int_0^T \dot{y}_k(t)\,\delta y_l(t)\ dt &= \int_0^T \frac{\mathcal{C}_k\,\delta\mathcal{C}_l}{i\,\Omega}e^{2i\Omega t} - \frac{\mathcal{C}_k\delta\overline{\mathcal{C}}_l}{i\,\Omega} + \frac{\overline{\mathcal{C}}_k\delta\mathcal{C}_l}{i\,\Omega} - \frac{\overline{\mathcal{C}}_k\,\delta\overline{\mathcal{C}}_l}{i\,\Omega}e^{-2i\Omega t}\ dt \\ &= \frac{T}{i\,\Omega}\ \left(\overline{\mathcal{C}}_k\delta\mathcal{C}_l - \mathcal{C}_k\delta\overline{\mathcal{C}}_l\right)\end{aligned} \tag{A.76}$$

A.7 Supplement: Fourier Approximation of the Trial Functions and its Derivatives

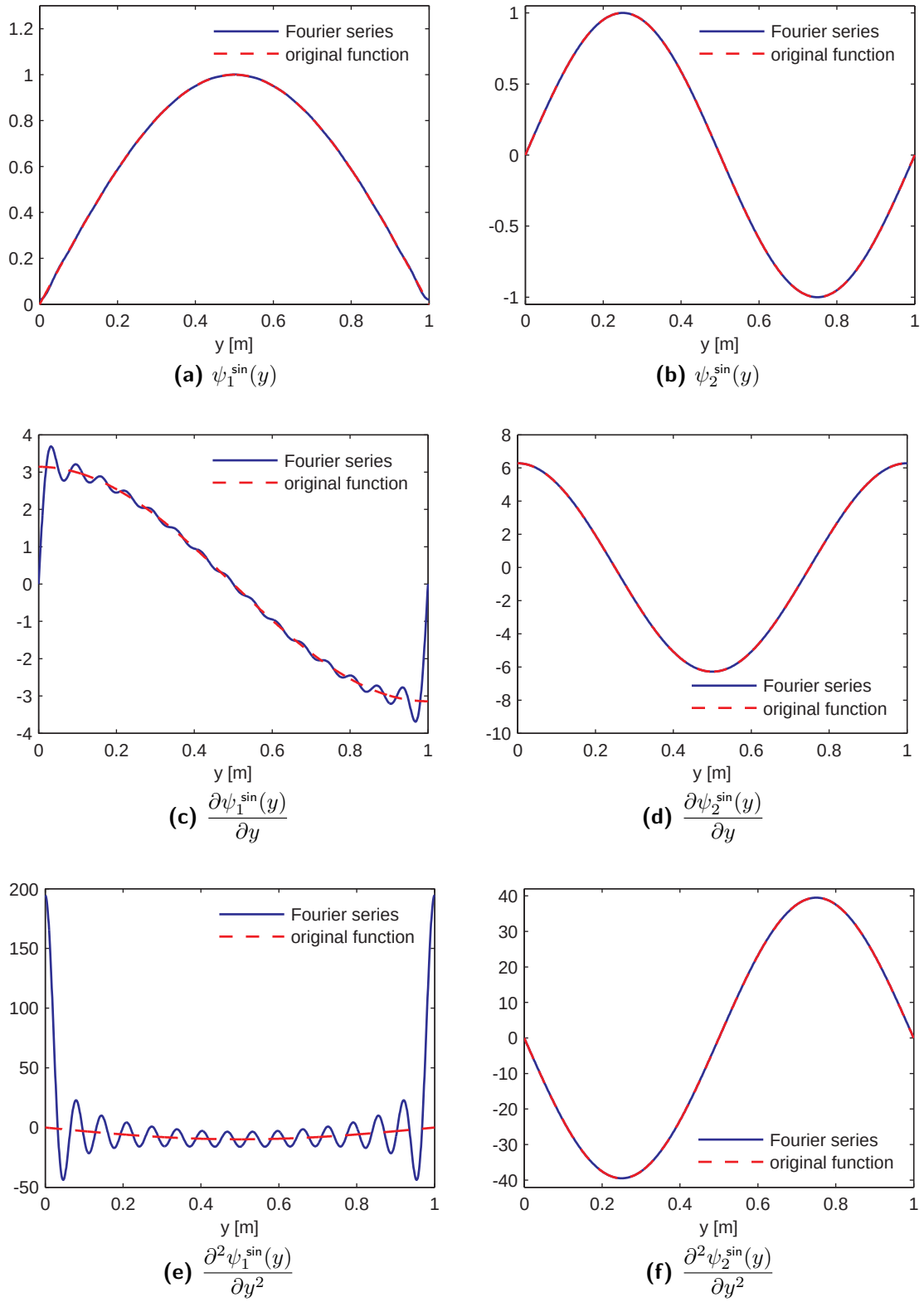

(a) $\psi_1^{\sin}(y)$ **(b)** $\psi_2^{\sin}(y)$

(c) $\frac{\partial \psi_1^{\sin}(y)}{\partial y}$ **(d)** $\frac{\partial \psi_2^{\sin}(y)}{\partial y}$

(e) $\frac{\partial^2 \psi_1^{\sin}(y)}{\partial y^2}$ **(f)** $\frac{\partial^2 \psi_2^{\sin}(y)}{\partial y^2}$

Figure A.3: *Fourier* approximation of the original trial function and its derivatives for a sinusoidal approach $\psi_{n_1}^{\sin}(y)$ with $r_{\max} = 15$ Fourier members

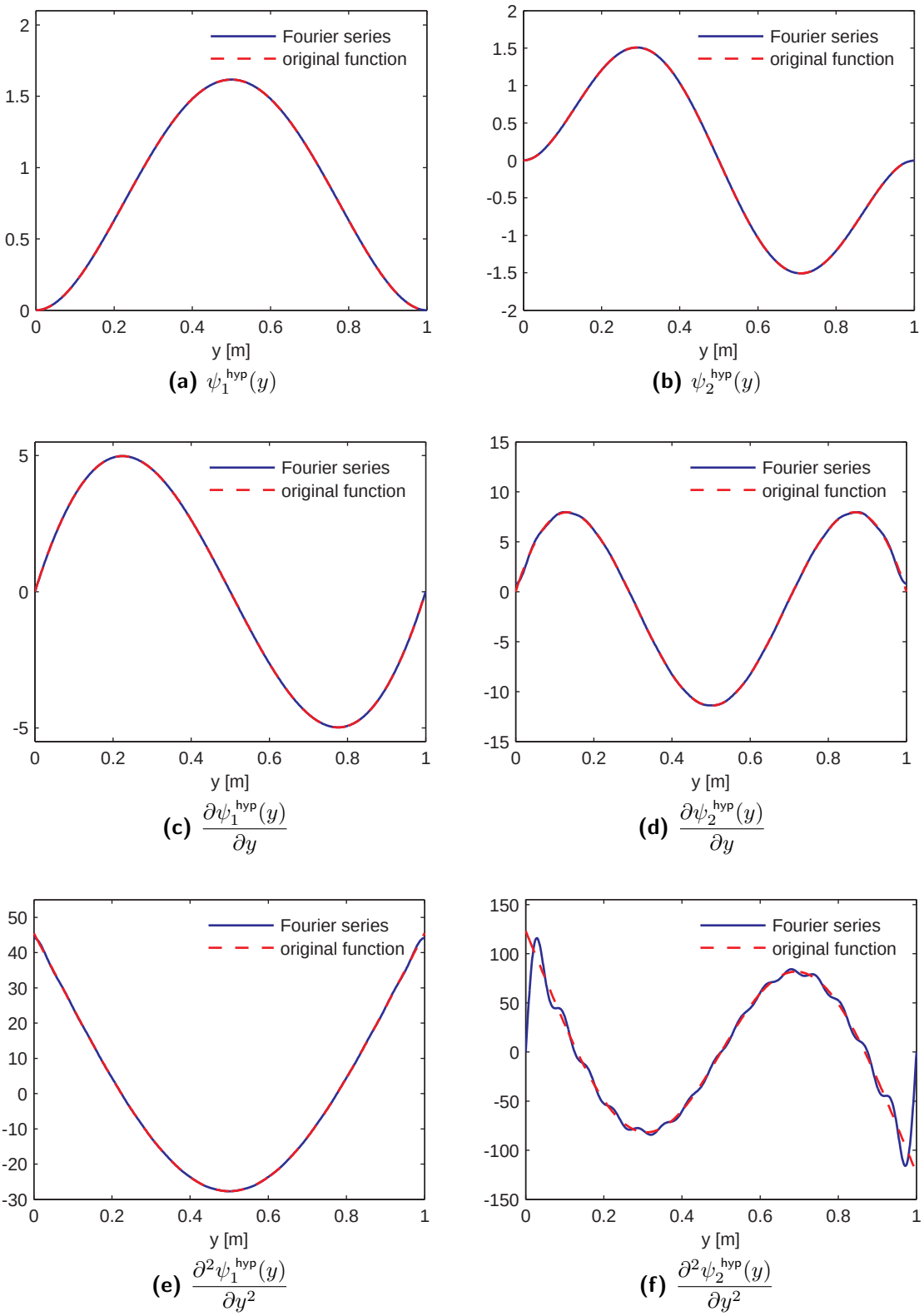

(a) $\psi_1^{\text{hyp}}(y)$ **(b)** $\psi_2^{\text{hyp}}(y)$

(c) $\frac{\partial \psi_1^{\text{hyp}}(y)}{\partial y}$ **(d)** $\frac{\partial \psi_2^{\text{hyp}}(y)}{\partial y}$

(e) $\frac{\partial^2 \psi_1^{\text{hyp}}(y)}{\partial y^2}$ **(f)** $\frac{\partial^2 \psi_2^{\text{hyp}}(y)}{\partial y^2}$

Figure A.4: *Fourier* approximation of the original trial function and its derivatives for a hyperbolic sine and cosine approach $\psi_{n_1}^{\text{hyp}}(y)$ with $r_{\text{max}} = 15$ Fourier members

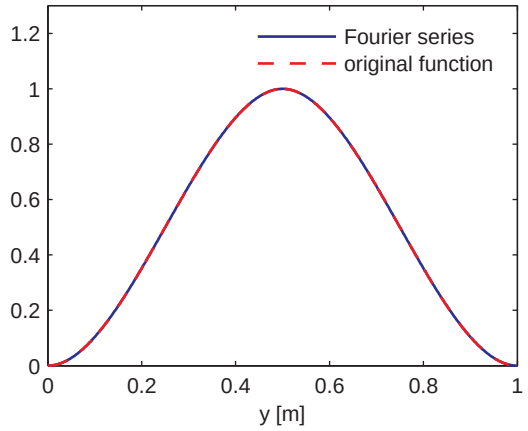

(a) $\psi_1^{\text{spline }3}(y)$

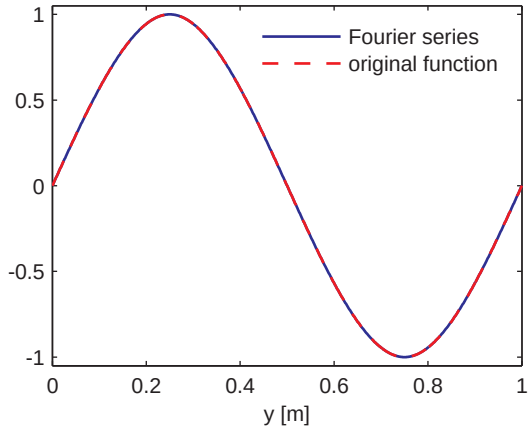

(b) $\psi_2^{\text{spline }3}(y)$

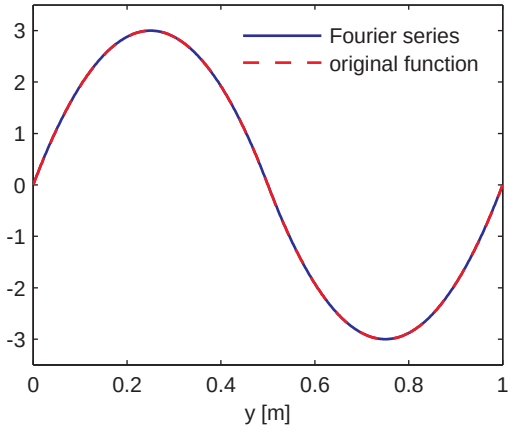

(c) $\dfrac{\partial \psi_1^{\text{spline }3}(y)}{\partial y}$

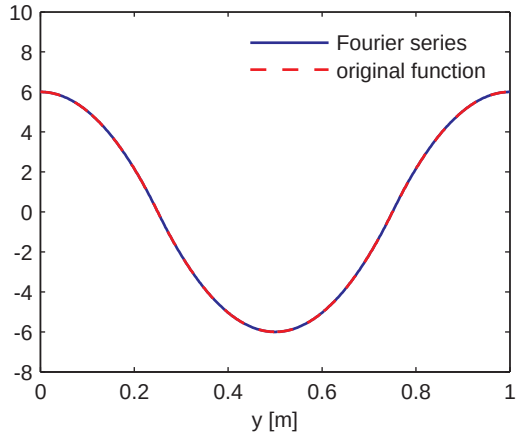

(d) $\dfrac{\partial \psi_2^{\text{spline }3}(y)}{\partial y}$

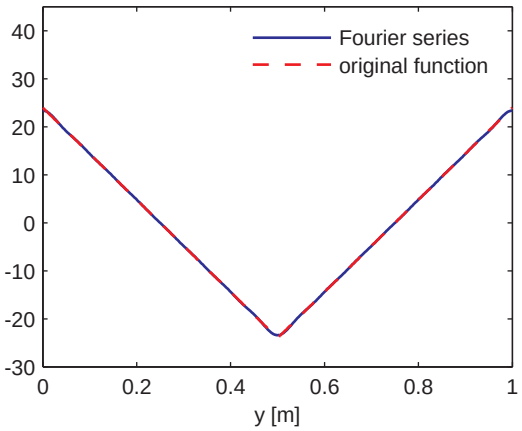

(e) $\dfrac{\partial^2 \psi_1^{\text{spline }3}(y)}{\partial y^2}$

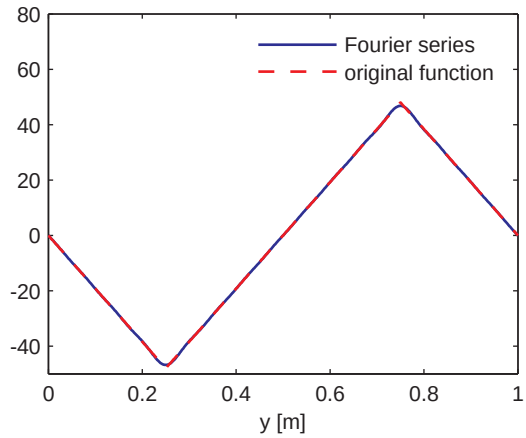

(f) $\dfrac{\partial^2 \psi_2^{\text{spline }3}(y)}{\partial y^2}$

Figure A.5: *Fourier* approximation of the original trial function and its derivatives for a spline of order 3 $\psi_{n_1}^{\text{spline }3}(y)$ with $r_{\max} = 15$ Fourier members

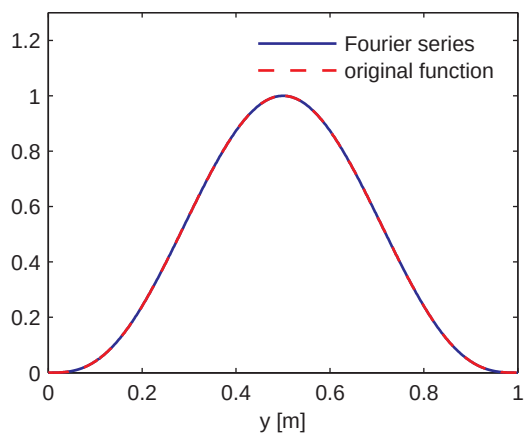

(a) $\psi_1^{\text{spline }5}(y)$

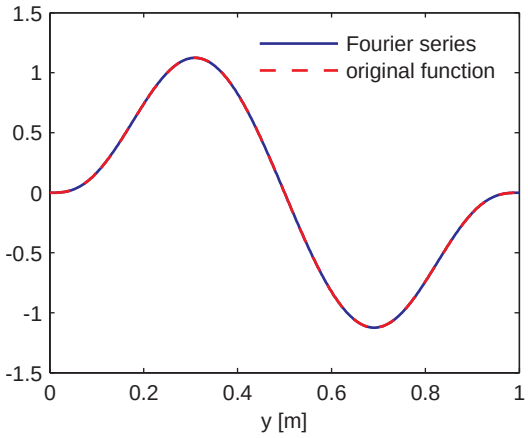

(b) $\psi_2^{\text{spline }5}(y)$

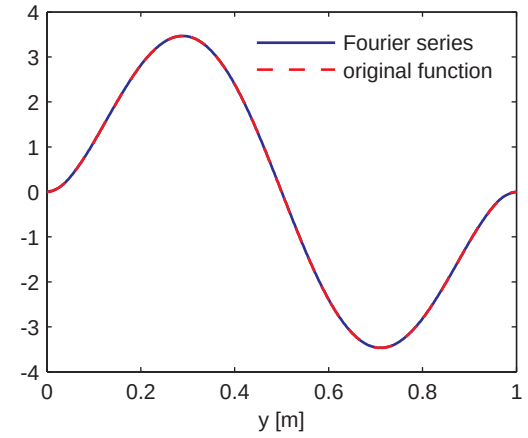

(c) $\dfrac{\partial \psi_1^{\text{spline }5}(y)}{\partial y}$

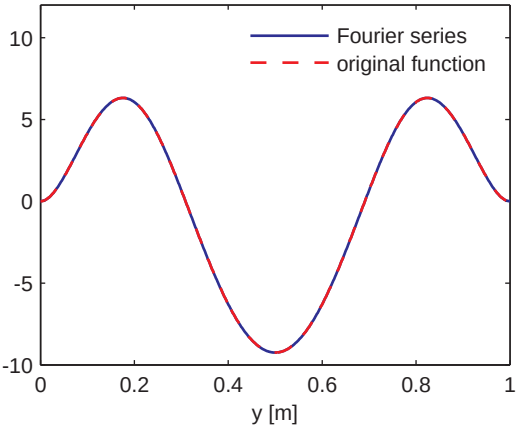

(d) $\dfrac{\partial \psi_2^{\text{spline }5}(y)}{\partial y}$

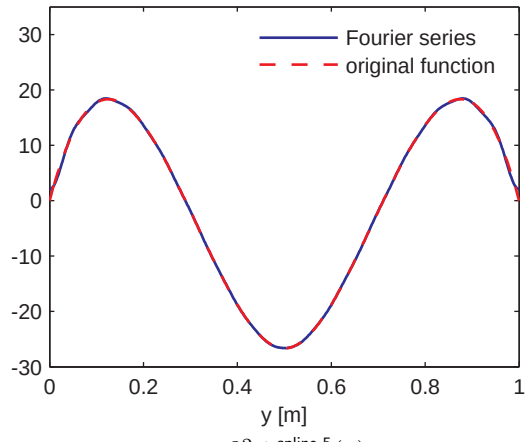

(e) $\dfrac{\partial^2 \psi_1^{\text{spline }5}(y)}{\partial y^2}$

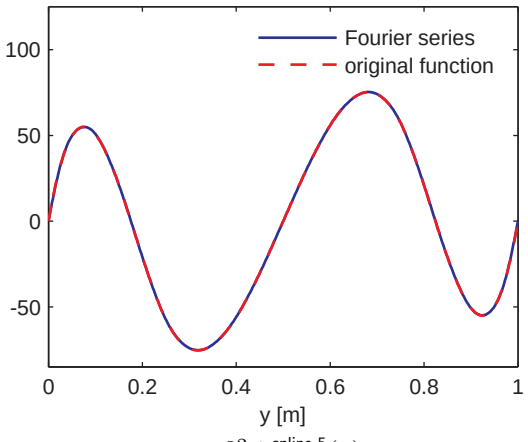

(f) $\dfrac{\partial^2 \psi_2^{\text{spline }5}(y)}{\partial y^2}$

Figure A.6: *Fourier* approximation of the original trial function and its derivatives for a spline of order 5 $\psi_{n_1}^{\text{spline }5}(y)$ with $r_{\text{max}} = 15$ Fourier members

List of Figures

Bibliography

[Allard 2009] Allard, J.-F.: *Propagation of Sound in Porous Media: Modelling Sound Absorbing Materials*. Wiley, 2009

[Aoutou and Savin 2011] Aoutou, S. ; Savin, É.: Discontinuous finite element solution of transport equations for high-frequency power flows in slender structures. In: *EURODYN Conference* (2011), p. 3222–3229

[Arfken 1985] Arfken, G.: *Mathematical Methods for Physicists*. Chap. Helmholtz's Theorem, p. 78–84, Academic Press, 1985

[Babuška et al. 1997a] Babuška, I. ; Ihlenburg, F. ; Strouboulis, T. ; Gangaraj, S.K. ; Posteriori, A.: Error Estimation for Finite Element Solutions of Helmholtz' Equation. Part I: The Quality of local Indicators and Estimators. In: *International Journal for Numerical Methods in Engineering* 40 (1997), p. 3443–3462

[Babuška et al. 1997b] Babuška, I. ; Ihlenburg, F. ; Strouboulis, T. ; Gangaraj, S.K. ; Posteriori, A.: Error Estimation for Finite Element Solutions of Helmholtz' Equation. Part II: Estimation of the Pollution Error. In: *International Journal for Numerical Methods in Engineering* 40 (1997), p. 3883–3900

[Babuška and Sauter 1997] Babuška, I. ; Sauter, S.: Is the pollution effect of the FEM avoidable for the Helmholtz equation considering high wave numbers. In: *SIAM Journal on Numerical Analysis* 34 (1997), p. 2392–2423

[Baer and Nunziato 1986] Baer, M. R. ; Nunziato, J. W.: A two-phase mixture theory for the deflagration-to-detonation transition (DDT) in reactive granlar materials. In: *International Journal of Multiphase Flow* 12 (1986), p. 861–889

[Bauchau and Craig 2009] Bauchau, O. A. ; Craig, J. I.: *Structural Analysis*. Springer, 2009

[Beerends et al. 2003] Beerends, R.J. ; Morsche, H.G. ; Berg, J.C. van den: *Fourier and Laplace Transforms*. Cambridge University Press, 2003

[Beranek 1947] Beranek, L.: Acoustical Properties of Homogeneous, Isotropic Rigid Tiles and Flexible Blankets. In: *The Journal of the Acoustical Society of America* 19 (1947), p. 556–568

[Biot 1941a] Biot, M.A.: Consolidation settlement under a rectangular load distribution. In: *Journal of Applied Physics* 12 (1941), p. 426–430

[Biot 1941b] Biot, M.A.: General Theory of Three-Dimensional Consolidation. In: *Journal of Applied Physics* 12 (1941), p. 55–164

[Biot 1955] Biot, M.A.: Theory of Elasticity and Consolidation for a Porous Anisotropic Solid. In: *Journal of Applied Physics* 26 (1955), p. 182–185

[Biot 1956a] Biot, M.A.: Theory of Deformation of a Porous Viscoelastic Anisotropic Solid. In: *Journal of Applied Physics* 27 (1956), p. 459–467

[Biot 1956b] Biot, M.A.: Theory of propagation of elastic waves in a fluid saturated porous solid. I Low frequency range. In: *The Journal of the Acoustical Society of America* 28 (1956), p. 168–178

[Biot 1956c] Biot, M.A.: Theory of propagation of elastic waves in a fluid saturated porous solid. II Higher frequency range. In: *The Journal of the Acoustical Society of America* 28 (1956), p. 179–191

[Biot 1961] Biot, M.A.: Mechanics of Deformation and Acoustic Propagation in Porous Media. In: *Journal of Applied Physics* 33 (1961), p. 1482–1498

[Biot 1962] Biot, M.A.: Generalized Theory of Acoustic Propagation in Porous Dissipative Media. In: *Journal of the Acoustical Society of America* 34 (1962), p. 1254–1264

[Biot and Willis 1957] Biot, M.A. ; Willis, D. G.: The elastic coefficients of the theory of consolidation. In: *Journal of Applied Mechanics* 24 (1957), p. 594–601

[Bitsie 1996] Bitsie, F.: *The structural acoustic energy finite element method and energy boundary element method*, Purdue University , USA, Ph.D. thesis, 1996

[Bluhm 1997] Bluhm, J.: *A consistent model for saturated and empty porous media*, Fachbereich Bauwesen, Universität-Gesamthochschule Essen, Habilitation, 1997

[Bluhm 2002] Bluhm, J.: *Porous Media: Theory, Experiments and Numerical Applications*. Chap. Modelling of saturated thermoelastic porous solids with different temperatures, p. 87 – 118, Springer, 2002

[Bluhm and de Boer 1997] Bluhm, J. ; Boer, R. de: The volume fraction concept in the porous media theory. In: *ZAMM - Journal of Applied Mathematics and Mechanics* 77 (1997), p. 563–577

[de Boer 1992] Boer, R. de: Development of porous media theories - A brief historical review. In: *Transport in Porous Media* 9 (1992), p. 155–164

[de Boer 2000] Boer, R. de: *Theory of Porous Media. Highlights in Historical Development and Current State*. Springer, 2000

[de Boer 2005a] Boer, R. de: *The Engineer and the Scandal: A Piece of Science History*. Springer, 2005

[de Boer 2005b] Boer, R. de: *Trends in Continuum Mechanics of Porous Media. Theory and Applications of Transport in Porous Media*. Springer, 2005

[de Boer and Didwania 2004] Boer, R. de ; Didwania, A. K.: Two-Phase Flow and the Capillarity Phenomenon in Porous Solids - A Continuum Thermomechanical Approach. In: *Transport in Porous Media* 56 (2004), p. 137–170

[de Boer and Ehlers 1986] Boer, R. de ; Ehlers, W.: Theorie der Mehrkomponentenkontinua mit Anwendungen auf bondemechanische Probleme, Teil I. / Fachbereich Bauwesen, Universität-Gesamthochschule Essen. 1986. – Research Report

[Boskovic 2005] Boskovic, L.: *Halbraumdynamik nach der Theorie Poröser Medien und Einfluss der Horizontalverschiebungsbehinderung unter einem auf dem klassischen halbraum gebetteten Balken*, TU München, Ph.D. thesis, 2005

[Boskovic et al. 2003] Boskovic, L. ; Buchschmid, M. ; Trommer, E.: Erschütterungsweiterleitung im Zweikomponenten-Halbraum: Vergleichende Untersuchungen unterschiedlicher Modellierungsansätze im Hinblick auf baupraktische Belange / Deutsche Forschungsgemeinschaft. 2003. – Research Report

[Bowen 1980] Bowen, R. M.: Incompressible porous media models by use of the theory of mixtures. In: *International Journal of Engineering Science* 18 (1980), p. 1129–1148

[Bowen 1982] Bowen, R. M.: Compressible porous media models by use of the theory of mixtures. In: *International Journal of Engineering Science* 20 (1982), p. 697–735

[Buchschmid 2010] Buchschmid, M.: *Integral Transform Methods – Theory and Application.* Lecture Notes, TU München, 2010

[Buchschmid and Müller 2008] Buchschmid, M. ; Müller, G.: Modeling of Wave Number Dependent Absorptive Characteristics with the Help of the Theory of Porous Media. In: *EURODYN Conference*, 2008

[Buchschmid et al. 2009a] Buchschmid, M. ; Müller, G. ; Kropp, A.: Closing the Mid-Frequency-Gap: Acoustic BIW Design using a Hybrid SEA-FEA Approach. In: *The 16th International Congress on Sound and Vibration, Krakow, Poland, ICSV16*, 2009

[Buchschmid et al. 2010] Buchschmid, M. ; Pospiech, M. ; Müller, G.: Coupling impedance boundary conditions for absorptive structures with spectral finite elements in room acoustical simulations. In: *Computing and Visualization in Science* 13 (2010), p. 355–363

[Buchschmid et al. 2009b] Buchschmid, M. ; Pospiech, M. ; Müller, G.: ITM-based FSI-Models for applications in room acoustics. In: *COMPDYN Conference*, 2009

[Champoux and Allard 1991] Champoux, Y. ; Allard, J.-F.: Dynamic tortuosity and bulk modulus in air-saturated porous media. In: *Journal of Applied Physics* 70 (1991), p. 1975–1979

[Coussy 2004] Coussy, O.: *Poromechanics.* Wiley, 2004

[Craig and Bampton 1968] Craig, R.R.J. ; Bampton, M.C.C.: Coupling of Substructures for Dynamic Analyses. In: *AIAA* 6 (7) (1968), p. 1313–1319

[Craig and Chang 1976] Craig, R.R.J. ; Chang, C.J.: Free-interface methods of substructure coupling for dynamic analysis. In: *AIAA Journal of Computational Physics* 14 (1976), p. 1633–1635

[Cremer and Müller 1982] Cremer, L. ; Müller, H. A.: *Principles and applications of room acoustics*. Applied Science, 1982

[Deü et al. 2006] Deü, J.-F. ; Larbi, W. ; Ohayon, R.: *Dissipative interface modeling for vibroacoustic problems - A new symmetric formulation*. p. 413–428, Springer, 2006

[Delany and Bazley 1970] Delany, M.E. ; Bazley, E.N.: Acoustical properties of fibrous materials. In: *Applied Acoustics* 3 (1970), p. 105–116

[Depollier et al. 1988] Depollier, C. ; Allard, J.-F. ; Lauriks, W.: Biot theory and stress-strain equations in porous sound-absorbing materials. In: *The Journal of the Acoustical Society of America* 84 (1988), p. 2277–2279

[Diebels 2000] Diebels, S.: *Mikropolare Zweiphasenmodelle: Formulierung auf der Basis der Theorie Poröser Medien*, Universität Stuttgart, Habilitation, 2000

[DIN EN 29053 1991] DIN EN 29053: *Acoustics; Materials for acoustical applications; Determination of airflow resistance*. Beuth, 1991

[DIN EN ISO 10534-1 2001] DIN EN ISO 10534-1: *Acoustics; Determination of sound absorption coefficient and impedance in impedance tubes - Part 1: Method using standing wave ratio*. Beuth, 2001

[DIN EN ISO 10534-2:2001-10 2001] DIN EN ISO 10534-2:2001-10: *Acoustics; Determination of sound absorption coefficient and impedance in impedance tubes - Part 2: Transfer-function method*. Beuth, 2001

[DIN ISO 13472-1 2002] DIN ISO 13472-1: *Acoustics; Measurement of sound absorption properties of road surfaces in situ*. Beuth, 2002

[DIN ISO 354 2003] DIN ISO 354: *Acoustics; Measurement of sound absorption in a reverberation room*. Beuth, 2003

[Ehlers 1989] Ehlers, W.: *Poröse Medien: Ein kontinuumsmechanisches Modell auf der Basis der Mischungstheorie*, Fachbereich Bauwesen, Universität-Gesamthochschule Essen, Habilitation, 1989

[Ehlers and Bluhm 2002] Ehlers, W. ; Bluhm, J.: *Porous Media: Theory, Experiments and Numerical Applications*. Springer, 2002

[Ehlers and Kubik 1994] Ehlers, W. ; Kubik, J.: On finite dynamic equations for fluid-saturated porous media. In: *Acta Mechanica* 105 (1994), p. 101–117

[Elsgolc 2007] Elsgolc, L.D.: *Calculus of Variations*. Dover Publications, 2007

[von Estorff et al. 2008] Estorff, O. von ; Petersen, S. ; Dreyer, D.: *Computational Acoustics of Noise Propagation in Fluids - Finite and Boundary Element Methods*. Chap. Efficient Infinite Elements on Jacobi Polynomials, Springer, 2008

[Fahy 2000] Fahy, F. J.: *Foundations of Engineering Acoustics*. Academic Press, 2000

[Fahy 2007] Fahy, F. J.: *Sound and Structural Vibration*. Academic Press, 2007

[Farhat et al. 2002] Farhat, C. ; Harari, I. ; Hetmaniuk, U.: A discountinuous Galerkin method with Lagrange multipliers for the Helmholtz problems in the mid-frequency regime. In: *Computer Methods in Applied Mechanics and Engineering* 192 (2002), p. 1389–1419

[Fillunger 1913] Fillunger, P.: Der Auftrieb in Talsperren. In: *österr. Wochenschrift für den öffentlichen Baudienst* (1913), p. 532–556, 567–570

[Föllinger 2003] Föllinger, O.: *Laplace- Fourier- und z- Transformation.* Hüthig-Verlag, Heidelberg, 2003

[Franck 2006] Franck, A.: FEM-Simulation raumakustischer Übertragungsfunktion mit Padé-Lanczos-Verfahren. In: *DAGA, 32th annual convention for acoustics, Braunschweig*, 2006

[Franck and Hafner 2005] Franck, A. ; Hafner, M.: Numerical methods for high wave number acoustical FEM simulation. In: *7th International Conference on Theoretical and Computational Acoustics (ICTCA), Hangzhou, China*, 2005

[Freymann 2000] Freymann, R.: *Advanced Numerical and Experimental Methods in the Field of Vehicle Structural Acoustics*, Fakultät für Maschinenwesen, Technische Universität München, Habilitation, 2000

[Freymann and Stryczek 2000] Freymann, R. ; Stryczek, R.: A New Optimization Approach in the Field of Structural Acoustics. In: *SAE 2000 Word-Congress*, 2000

[Frühe 2011] Frühe, Georg: *Überlagerung von Grundlösungen in der Elastodynamik zur Behandlung der dynamischen Tunnel-Boden-Bauwerk-Interaktion*, TU München, Ph.D. thesis, 2011

[Fuchs 2006] Fuchs, H. V.: *Schallabsorber und Schalldämpfer: Innovative akustische Konzepte und Bauteile mit praktischen Anwendungen in konkreten Beispielen.* Springer, 2006

[Gaul and Wagner 1998] Gaul, L. ; Wagner, M.: Formulation of fluid-structure-interaction by hybrid boundary integral method. In: *ZAMM - Journal of Applied Mathematics and Mechanics* 78 (1998), p. 93–96

[Gerdes and Ihlenburg 1999] Gerdes, K. ; Ihlenburg, F.: On the pollution effect in FE solutions of the 3D-Helmholtz equation. In: *Journal of Computer Methods in Applied Mechanics and Engineering* 170 (1999), p. 155–172

[Gibbs 1899] Gibbs, J.W.: Fourier's Series. In: *Nature* 59 (1899)

[Guyan 1965] Guyan, R. J.: Reduction of stiffness and mass matrices. In: *AIAA Journal* 3 (2) (1965), p. 380

[Hall and Hoff 2002] Hall, C. ; Hoff, W.: *Water Transport in Brick, Stone and Concrete.* Spon Press, 2002

[Hamming 1973] Hamming, R.W.: *Numerical methods for scientists and engineers.* McGraw-Hill, New York, 1973

[Heckl and Müller 1995] Heckl, M. ; Müller, H. A.: *Taschenbuch der Technischen Akustik*. Springer, 1995

[Hinke 2008] Hinke, L.: *Modelling approaches for the low-frequency analysis of built-up structures with non-deterministic properties*, University of Southampton, Faculty of Engineering, Science and Mathematics, Institute of Sound and Vibration Research, Ph.D. thesis, 2008

[Hüppe and Kaltenbacher 2009] Hüppe, A. ; Kaltenbacher, M.: Limits of Finite Element Methods in the Mid-Frequency Range. In: *NAG/DAGA , 35th annual convention for acoustics, Rotterdam*, 2009

[Hurty 1960] Hurty, W.C.: Vibrations of Structural Systems by Component-Mode Synthesis. In: *Journal of Engineering Mechanics (ASCE)* 86(4) (1960), p. 51–69

[Hurty 1965] Hurty, W.C.: Dynamic analysis of structural systems using component modes. In: *AIAA Journal* 3 (4) (1965), p. 678–685

[Johnson et al. 1978] Johnson, K.L. ; Koplik, J. ; R., Dashen: Theory of dynamic permeability and tortuosity in fluid-saturated porous media. In: *Journal of Fluid Mechanics* 176 (1978), p. 379–402

[Karniadakis and Sherwin 2005] Karniadakis, G. E. ; Sherwin, S.: *Spectral/hp Element Methods for computational Fluid Dynamics*. Volume 2. Oxford University Press, 2005

[Kuttruff 2009] Kuttruff, H.: *Room Acoustics*. Spon Press, 2009

[Lafarge 2006] Lafarge, D.: *Materiaux et acoustique*. Chap. Propagation des Ondes Acoustiques, Lavoisier, Paris, 2006

[Lafarge et al. 1997] Lafarge, D. ; Lemarinier, P. ; Allard, J.-F. ; Tarnov, V.: Dynamic compressibility of air in porous structures at audible frequencies. In: *Journal of the Acoustical Society of America* 102 (1997), p. 1995–2006

[Lambert 1983] Lambert, R.F.: Propagation of sound in highly porous open-cell elastic foams. In: *The Journal of the Acoustical Society of America* 4 (1983), p. 1131–1138

[Langer et al. 2009] Langer, S. ; Al-Kharabsheh, D. ; Wulkau, M.: On the Sensitiveness of Absorption Coefficient to Changes in Material Parameters. In: *Proceedings in Applied Mathematics and Mechanics* 9 (2009), p. 513 – 514

[Langhe 2007] Langhe, K. D.: Modeling for Mid-frequency Vibration Transmission. In: *DAGA, 33th annual convention for acoustics, Stuttgart*, 2007

[Langley 2008] Langley, R. S.: Recent Advances and remaining Challenges in the Statistical Energy Analysis. In: *EURODYN*, 2008

[Larbi et al. 2009] Larbi, W. ; Deü, J.-F. ; Ohayon, R.: Finite Element Formulations for structural-acoustic internal problems with poroelastic treatment. In: *COMPDYN Conference*, 2009

[Li 2011] Li, X.: A scaling approach for high-frequency vibration analysis of built-up systems. In: *EURODYN Conference* (2011), p. 3193–3197

[Lieb 1997] Lieb, M.: *Adaptive numerische Fouriertransformation in der Bodendynamik unter Verwendung einer Waveletzerlegung*, TU München, Ph.D. thesis, 1997

[Long 1967] Long, C. F.: On the completeness of Lamé potentials. In: *Acta Mechanica* 3 (1967), p. 371–375

[Lyon 1983] Lyon, R.H.: Progressive Phase Trends in Multi-Degree-of-Freedom Systems. In: *Journal of the Acoustical Society of America* 73 (1983), p. 1223–1228

[Lyon 1984] Lyon, R.H.: Range and Frequency Dependence of Transfer Function Phase. In: *Journal of the Acoustical Society of America* 76 (1984), p. 1433–1437

[Lyon and DeJong 1995] Lyon, R.H. ; DeJong, R.G.: *Theory and Application of Statistical Energy Analysis*. 2. Butterworth-Heinemann, Boston, 1995

[Mace and Shorter 2000] Mace, B. ; Shorter, P.J.: Energy Flow Models from Finite Element Analysis. In: *Journal of Sound and Vibration* 233 (2000), p. 369–389

[Magalhaes 2004] Magalhaes, M. D. C.: *Improved model for the prediction of sound transmission through partitions at low freqencies*, University of Southampton, Ph.D. thesis, 2004

[Magalhaes and Ferguson 2003] Magalhaes, M. D. C. ; Ferguson, N.S.: Acoustic–structural interaction analysis using the component mode synthesis method. In: *Applied Acoustics* 64 (2003), p. 1049–1067

[Magalhaes and Ferguson 2005] Magalhaes, M. D. C. ; Ferguson, N.S.: The development of a Component Mode Synthesis (CMS) model for three-dimensional fluid-structure interaction. In: *Acoustical Society of America* 118 (2005), p. 3679–3690

[Makert 2005] Makert, B.: *Porous Media Viscoelasticity with Application to Polymeric Foams*, Universität Stuttgart, Ph.D. thesis, 2005

[Manning 1999] Manning, J.E.: *IUTAM Symposium on Statistical Energy Analysis*. Chap. SEA-coupling factors for regular and irregular structures, 1999

[Marburg and Nolte 2008] Marburg, S. ; Nolte, B.: *Computational Acoustics of Noise Propagation in Fluids - Finite and Boundary Element Methods*. Springer, 2008

[Mechel 1976] Mechel, F. P.: Ausweitung der Absorberformel von Delany und Bazley zu tiefen Frequenzen. In: *Acustica* 35 (1976), p. 210–213

[Mechel 1989] Mechel, F. P.: *Schallabsorber, Bd.1, Äußere Schallfelder, Wechselwirkungen*. Hirzel, Stuttgart, 1989

[Mechel 1995a] Mechel, F. P.: *Schallabsorber, Bd.2, Innere Schallfelder, Strukturen*. Hirzel, Stuttgart, 1995

[Mechel 1995b] Mechel, F. P.: *Schallabsorption*. in "Taschenbuch der Technischen Akustik" [Heckl and Müller 1995], Springer, 1995

[Mechel 2008] Mechel, F. P.: *Formulas of Acoustics*. Springer, 2008

[Mehdizadeh and Paraschivoiu 2003] Mehdizadeh, O.Z. ; Paraschivoiu, M.: Investigation of a Three-Dimensional Spectra Element Method of Helmholtz's Equation. In: *Lecture Notes in Computer Science (LNCS)* 2668 (2003), p. 819–825

[Meixner 1959] Meixner, J.: Impedanz und Lagrange-Funktion linearer dissipativer Systeme. In: *Zeitschrift für Physik* 156 (1959), p. 200–210

[Meyberg and Vachenauer 2001] Meyberg, K. ; Vachenauer, P.: *Höhere Mathematik 2 - Differentialgleichungen, Funktionentheorie, Fourier-Analyse, Variationsrechnung*. Springer, 2001

[Müller 1989] Müller, G.: *Ein Verfahren zur Erfassung der Fundament-Boden Wechselwirkung unter Einwirkung periodischer Lasten*, TU München, Ph.D. thesis, 1989

[Müller et al. 2006] Müller, G. ; Buchschmid, M. ; Guggenberger, J.: *Baudynamik*. Chap. Modellbildung zur Körperschallausbreitung in Tragstrukturen unter Berücksichtigung des Einflusses von Innenausbauten, p. 59–70, VDI Verlag, 2006

[Müller et al. 2008] Müller, G. ; Buchschmid, M. ; Seipelt, S. ; Müller, K.: Soil-structure interaction of tunnel-structures under consideration of far- and near-field effects. In: *Proceedings in Applied Mathematics and Mechanics* (2008), p. 10317–10318

[Müller and Möser 2003] Müller, G. ; Möser, M.: *Taschenbuch der Technischen Akustik*. Springer, 2003

[Moens et al. 1998] Moens, I. ; Vandepitte, D. ; Sas, P.: Vibro-acoustic energy flow models implemented by finite elements. In: *International conference on Noise and Vibration Engineering, ISMA* (1998), p. 853–858

[Mohammed and Fahy 1990] Mohammed, A.D. ; Fahy, F.J.: A study of uncertainty in applications of statistical energy analysis to one-dimensional and two-dimensional structural systems. In: *Proceedings of the Institute of Acoustics* 12 (1990), p. 543–549

[Mommertz 1995] Mommertz, E.: Angle-dependent in-situ measurements of reflection coefficients using a subtraction technique. In: *Applied Acoustics* 46 (1995), p. 251–263

[Möser 2007] Möser, M.: *Technische Akustik*. Springer, 2007

[Naka et al. 2004] Naka, Y. ; Oebrai, A. ; Shinn-Cunningham, B.: The Finite Element Method with the Dirichlet-to Neumann Map for Sound-Hard Rectangular Rooms. In: *International Congress on Acoustics ICA, Kyoto*, 2004

[Olny and Panneton 2008] Olny, X. ; Panneton, R.: Acoustical determination of the parameters governing thermal dissipation in porous media. In: *Journal of the Acoustical Society of America* 123 (2008), p. 814–824

[Panneton and Olny 2006] Panneton, R. ; Olny, X.: Acoustical determination of the parameters governing viscous dissipation in porous media. In: *Journal of the Acoustical Society of America* 119 (2006), p. 2027–2040

[Petersen 1982] Petersen, C.: *Statik und Stabilität der Baukonstruktionen*. Vieweg, 1982

[Petersen 1996] Petersen, C.: *Dynamik der Baukonstruktionen*. Vieweg, 1996

[Pospiech 2011] Pospiech, M.: *Numerical Simulations in Room Acoustics using direct coupling Techniques and finite Elements*, TU München, Ph.D. thesis, 2011

[Pospiech et al. 2009] Pospiech, M. ; Buchschmid, M. ; Müller, G.: Spectral Approaches for Room Acoustics. In: *The 16th International Congress on Sound and Vibration, Krakow, Poland, ICSV16*, 2009

[Pospiech et al. 2010] Pospiech, M. ; Buchschmid, M. ; Rentrop, P. ; Müller, G.: Modal-based fluid structure coupling in room acoustics considering non-deterministic properties. In: *Proceedings in Applied Mathematics and Mechanics* (2010), p. 507–508

[Pospiech and Rentrop 2009] Pospiech, M. ; Rentrop, P.: Boundary Conditions in Linear 3d-Aeroacoustic Numerical Simulation. In: *MATHMOD*, 2009

[Pride et al. 1993] Pride, S.R. ; Morgan, F.D. ; Gangi, F.A.: Drag forces of porous media acoustics. In: *Physical Review B* 47 (1993), p. 4964–4975

[Rabold et al. 2010] Rabold, A. ; Buchschmid, M. ; Düster, A. ; Müller, G. ; Rank, E.: Modelling the excitation force of a standard tapping machine on lightweight floor structures. In: *Journal of Building Acoustics* 17 (2010), p. 175–197

[Rayleigh 1878] Rayleigh, J. W. S.: *The Theory of Sound*. Cambridge, 1878

[Ricken 2002] Ricken, T.: *Kapillarität in porösen Medien – theoretische Untersuchung und numerische Simulation*, Fachbereich Bauwesen, Universität-Gesamthochschule Essen, Ph.D. thesis, 2002

[Sabine 1922] Sabine, W. C.: *Collected Papers On Acoustics*. Harvard University Press, 1922

[Schanz and Diebels 2003] Schanz, M. ; Diebels, S.: A comparative study of Biot's theory and the linear Theory of Porous Media for wave propagation problems. In: *Acta Mechanica* 161 (2003), p. 213–235

[Shorter and Bremner 1999] Shorter, P.J. ; Bremner, P.G.: A hybrid method for the vibration analysis of complex structural-acoustic systems. In: *Journal of the Acoustical Society of America* 105 (1999), p. 1657–1671

[Shorter and Langley 2005a] Shorter, P.J. ; Langley, R.S.: Modeling structure-borne noise with the hybrid FE-SEA method. In: *EURODYN*, 2005

[Shorter and Langley 2005b] Shorter, P.J. ; Langley, R.S.: On the reciprocity relationship between direct field radiation and diffuse reverberant loading. In: *Journal of the Acoustical Society of America* 117 (2005), p. 85–95

[Shorter and Langley 2005c] Shorter, P.J. ; Langley, R.S.: Vibro-Acoustic analysis of complex systems. In: *Journal of Sound and Vibration* 288 (2005), p. 669–699

[Sommerfeld 1949] Sommerfeld, A.: *Partial differential equations in physics*. Academic Press, 1949

[Sremcevic 2011] Sremcevic, J.: *Model Reduction Methods in Room Acoustical Simulations*, TU München, Ph.D. thesis, 2011

[Stein and Barthold 1996] Stein, E. ; Barthold, F.-J.: *Der Ingenieurbau*. Chap. Elastizitätstheorie, p. 165–428, Ernst & Sohn, Berlin, 1996

[Struckmeier 2007] Struckmeier, V.: *A computational model for seismically induced liquefaction*, Technische Universität Braunschweig, Ph.D. thesis, 2007

[Sunar 2004] Sunar, M.: *Encyclopedia of Vibration, Theory of vibration*. Chap. Substructuring, p. 1332–1335, Academic Press, 2004

[Trefethen 2000] Trefethen, L. N.: *Spectral Methods in Matlab*. SIAM, 2000

[Truesdell 1984] Truesdell, C.: *Thermodynamics of diffusion*. Springer, 1984

[Truesdell and Toupin 1960] Truesdell, C.A. ; Toupin, R.: *Flügge's Handbuch der Physik*. Chap. The classical field theories, p. 226–793, Springer, 1960

[Vorländer 2007] Vorländer, M.: *Fundamentals of Acoustics, Modelling, Simulation, Algorithms and Acoustic Virtual Reality*. Springer Berlin Heidelberg, 2007

[Wagner et al. 2004] Wagner, M. ; Gaul, L. ; Dumont, N.A.: The hybrid boundary element method in structural acoustics. In: *ZAMM - Journal of Applied Mathematics and Mechanics* 84 (2004), p. 780–796

[Wauer 2008] Wauer, J.: *Kontinuumsschwingungen*. Vieweg+Teubner, 2008

[Wilson 1993] Wilson, K.: Relaxation-matched modeling of propagation through porous media, including fractal pore structure. In: *Journal of the Acoustical Society of America* 94 (1993), p. 1136–1145

[Zwikker and Kosten 1949] Zwikker, C. ; Kosten, C.W.: *Sound Absorbing Materials*. Elsevier, 1949

Index

T

V

W